THREE DIMENSIONAL FLOW IN AN AXIAL FLOW IMPELLER

by

KRISHNA SWAROOP GUPTA

THESIS SUBMITTED FOR THE DEGREE OF DOCTOR OF PHILOSOPHY

OF THE UNIVERSITY OF EDINBURGH, EDINBURGH,

IN THE FACULTY OF SCIENCE.

SEPTEMBER 1970.

ACKNOWLEDGEMENTS

The author wishes to acknowledge his indebtedness to Dr. S. Soundranayagam, under whose supervision this study was carried out. Thanks are due to the staff of the workshop of the Mechanical Engineering Department for their assistance in making the instruments etc., to the North of Scotland Hydro-Electric Board for providing financial assistance for a part period of this study and to the University of Jodhpur, Jodhpur (India) for sanctioning the leave of absence for the period of this study.

SUMMARY

This study reports experimental and theoretical work on a high specific speed low hub tip radius ratio axial flow impeller.

The concept of a constant slip factor was examined and shown to be unfounded. For performance prediction on a two dimensional basis, the slip and deviation approaches are shown to be in no way contradictory. They are both essentially the same in that they each take into consideration the deviation of the flow from the blade.

Two dimensional fluid flow outlet angles at different flow coefficients and different radius ratios were obtained by potential flow solution of the cascades. The flow was analysed by simple radial equilibrium methods based on the assumption that the flow was in radial equilibrium shortly after the blade row. The use of two dimensional potential flow angles showed only fair agreement with the experimental results in the prediction of the outlet axial velocity distribution. When the effect of secondary flows and axial velocity ratio was taken into consideration, good agreement was obtained at all flow coefficients in the unstalled region of flow.

A simple method for the calculation of the loss in relative total pressure from hot wire anemometer readingsof wake R.M.S. voltage has been suggested, and the losses obtained by this method are compared to the losses derived from pitot tube measurements. The proposed method is seen to work satisfactorily.

The predicted head rise coefficients at different radius ratios and the integrated overall head rise coefficients are compared with experimentally obtained values at different flow coefficients. Good agreement was obtained.

To study the behaviour of the impeller, extensive aerodynamic

measurements were made in front of and behind the impeller at different flow coefficients in the unstalled and stalled region of flow. Pictures of blade wakes were also obtained from hot wire anemometer traces. It was observed that the behaviour of the impeller suddenly changed when the flow was reduced from the mean flow coefficient where the overall efficiency was a maximum. It was found that this mean flow coefficient could be predicted using the Betz "loading factor" criteria.

It was concluded that it is possible to design a low pressure rise impeller of small hub tip radius ratio and moderately large space chord ratio at the tip in the same way as conventional compressors are designed, provided correct estimation of the outlet angles can be made at different flow coefficients, as at large space chord ratios, the outlet angle is not constant with incidence angle.

TABLE OF CONTENTS

NOMENCLATURE

A_1, A_2, A_3	quantities as described in Chapter III.
A_i	inlet area of venturimeter sq. ft.
A_T	throat area of the venturimeter sq. ft.
A_t	constant as given by Mellor for blade thickness effect
A_a	constant as given by Mellor for cascade influence factor (same as the Weinig factor).
a, b, d, e, ℓ	quantities as described in Fig. 6.2
C	absolute velocity ft./sec.
c	blade chord ft.
C_x	axial velocity ft./sec.
C_θ	tangential velocity ft./sec.
C_r	radial velocity ft./sec.
C_b	constant describing blade camber
C_{b1}	modification of C_b due to axial velocity change
C_b^*	$C_b - C_{b1}$
C_H	slip coefficient
C_L	lift coefficient
C_P	coefficient of pitch angle
C_T	coefficient of total pressure
C_S	coefficient of static pressure
C_{DS}	annulus drag coefficient
C_d	coefficient of discharge of venturimeter
d	boundary layer thickness ft.
g	gravitational constant ft./sec^2
H	total head ft.

H_i	ideal total head ft.
h	static head ft.
h_b	blade height ft.
h_w	dynamic head in ft. of water.
I	$p + \frac{1}{2}\rho W_1^2 - \frac{1}{2}\rho U^2$
i	incidence angle
K	Weinig factor
k	axial velocity ratio
L	lift force lbs.
N	revolutions/minute
N_s	specific speed
P_o	total pressure lbs./ft^2.
P_1, P_2, P_3	readings of pressure at orifice 1, 2 and 3 of the three dimensional probe.
p	static pressure lbs./ft^2.
Q_i	flow calculated by venturi pressure differential ft^3/min.
Q_T	flow calculated by traversing the throat ft^3/min.
Q_V	$C_d \cdot Q_i$ ft^3/min.
q	loss in total pressure lbs./ft^2
$\bar{q}_t$	space averaged total pressure loss lbs./ft^2. at traverse plane
R	principal radius of curvature of the relative streamline ft.
R_T	radius of the throat of the venturimeter ft.
r	any radius ft.
r_h	hub radius ft.
s	space ft.
s"	distance along the streamline ft.

S''	$s \cos \beta_2$ ft.
T_A	aerodynamic torque ft. lbs.
T_m	net mechanical torque ft. lbs.
$\frac{t}{c}$	thickness ratio
U	blade speed at any radius ft./sec.
U_t	blade tip speed ft./sec.
u, v	induced velocities due to cascade blades ft./sec.
u', v'	induced velocities due to axial velocity change ft./sec.
V	mean velocity voltage on D.C. voltmeter readings on
V_o	zero velocity voltage on D.C. voltmeter constant temp-
V_{RMS}	reading of R.M.S. voltmeter erature anemometer.
W	relative velocity ft./sec.
W_v	relative streamwise vorticity radians/sec.
w_v	absolute streamwise vorticity radians/sec.
w_o	induced velocity normal to cascade ft./sec. corresponding to axial velocity change
x	distance in axial direction ft.
y	distance along tangential direction ft.
y_c	camber line ordinates
α	absolute angle
α_a	angle of attack from the no lift direction of the blade.
β	relative angle
β_n	no lift angle of the blade
β_{ni}	no lift angle of an isolated aerofoil
β_p	pitch angle
Γ	circulation $ft^2/sec.$
Δ	increment in any quantity

γ	angle between the direction of curvature of the relative streamline and $(\frac{\nabla I}{\rho}) \wedge \vec{W}$
γ_a	specific weight of air lbs./ft^3
γ_w	specific weight of water lbs./ft^3
δ	deviation angle
δ'	angle between no lift direction of the blade and outlet velocity
δ''	angle between $\vec{\Omega}$ and $\frac{\nabla I}{\rho}$
η	efficiency
η_H	total head efficiency of the blade element (blade element efficiency)
θ	angle between vector mean velocity W_m and W_2, also camber angle.
θ_m	angle of attack of W_m measured from chord
λ	stagger angle
ρ	density lbs./ft^3
ϕ	flow coefficient
ψ	work coefficient
ψ_E	theoretical work coefficient for infinite number of blades
ψ_{ES}	theoretical work coefficient for infinite number of blades (based on static pressure rise)
ψ_S	work coefficient based on static pressure rise.
$\mathcal{V}$	head rise coefficient
Ω	angular velocity radians/sec.
w	loss in relative total head ft.

Subscripts

b	blade
M	maximum
m	vector mean values

1	inlet to the impeller
2	outlet of the impeller
3	outlet of the impeller where blade wakes have mixed out.

Superscripts

*	asterisk to distinguish 2d flow with reduced circulation
'	prime to distinguish a flow with axial velocity variation
‾	mean values

CHAPTER I

INTRODUCTION

The most conventional design of axial flow impellers is based on the assumption of free vortex flow distribution downstream from the impeller. In free vortex flow the tangential component of velocity varies inversely as the radius and the axial component is uniform throughout the flow. There is no radial component of velocity, and the streamlines lie on circular, cylindrical surfaces which are axisymmetric. The specific work done by the moving blade row is invariant with radius, the circulation being constant along the blade length. The blade therefore sheds no vorticity into the flow, which remains free from vorticity. Hence it was thought that this type of flow led to greater efficiency.

The design point is only one condition on the performance curve. At other points the impeller works at "off design" conditions. When an impeller designed for free vortex distribution is operating at an off design condition, a radial variation of axial flow velocity appears in transit through the impeller and the flow ceases to remain irrotational. In such a case, radial equilibrium will be achieved some distance downstream, but only after a redistribution of streamlines takes place. The meridional streamlines become parallel again but are no longer uniform, and the co-axial cylindrical stream surfaces downstream are found at radii different from those upstream. The redistribution of streamlines is accompanied by radial flow. Because of the axial and radial velocity changes, the tangential vorticity components assume finite values and thus the circulation along the blade must change. This involves changes in the whirl distribution, which no longer follows the free vortex law.

When a larger quantity of flow is to be handled by an axial impeller smaller hub tip ratios have to be employed. A free vortex design leads to an impeller blade which is twisted along its span, and on which the incident velocity varies considerably from hub to tip. In order to have a straighter blade, design methods other than "free vortex" have to be employed. Also, even a nominal "free vortex" design impeller has three dimensional flow except at the so called design point. The general problem of the design of impellers under conditions of three dimensional flow becomes important.

Along with three dimensional flows, secondary flows are also generated by the turning of a non-uniform inlet stream through the blade row passage. These flows are the result of boundary layer growth on the casing wall of the impeller which in turn is the result of viscosity. This turning of the boundary layer produces a transfer of vorticity from a direction perpendicular to the stream to a direction parallel to the main stream flow.

The development of high pressure rise axial compressors, especially those employed in aircraft propulsion engines, has resulted in an extensive study of all aspects of three dimensional flow in such impellers. These impellers are of low specific speed and are characterised by a close spacing of the blades and a large hub to tip ratio. Axial impellers of high specific speed which are characterised by large throughputs and a consequent low hub to tip ratio, and greater blade spacing, have been comparatively neglected. Such impellers are widely used in industry.

The large blade spacing of such impellers raises the question of whether conventional blade cascade design methods used in high pressure rise impellers could be successfully employed here. Also the small hub to tip ratio would tend to accentuate the effects of three dimensional flow. This

study reports on an investigation into the flow in a nine bladed axial impeller with a hub to tip ratio of 0.33. Extensive experimental measurements were made to determine the flow patterns over a wide range of operating conditions. Predictions of performance are compared with experimental measurements showing good agreement. An assessment of the flow losses had to be made for performance prediction and this was done by the use of a hot wire anemometer measuring the velocity variation in the blade wakes. Allowance for changes in axial velocity was made when estimating the fluid flow angles.

CHAPTER II

REVIEW OF LITERATURE AND PROPOSED PROGRAMME OF WORK

The head rise along a streamline in the relative flow of an incompressible fluid through an impeller is given by the elementary equation

$$H_2 - H_1 = \frac{1}{g} \Omega (r_2 C_{\theta 2} - r_1 C_{\theta 1}) \qquad (2.1)$$

Ω being the angular velocity of the impeller and r the radius. See Fig. 2.1 for the definitions of quantities associated with the flow in an impeller. This is often referred to as the Euler turbomachine equation. This implies that r_2 is known for a given r_1 and that the tangential velocities $C_{\theta 2}$ and $C_{\theta 1}$ are known. It also assumes that there are no losses.

In any given design situation the problems have been the determination of r_2 for a given r_1, the accurate estimation of the angles of the flow relative to the impeller together with the determination of the axial velocities C_{x1} and C_{x2} before and after the impeller so that $C_{\theta 2}$ and $C_{\theta 1}$ may be calculated, and in accounting for the flow losses so that the actual rather than an ideal performance may be predicted. The problem is made more difficult by the existance of additional three dimensional effects due to boundary layer secondary flows and tip clearance flows.

If the flow is assumed to be cylindrical, which at first sight is reasonable in an axial flow impeller, r_1 is always equal to r_2. The flow in any cylindrical plane can be assumed to be the same as the two dimensional flow in a flat plane which is the development of the cylindrical surfaces. The blades of the axial impellers are now represented in the flat plane as an infinite cascade of blades.

Assuming that the flow is always cylindrical and that the angle of flow β_2 (Fig. 2.1) is equal to the blade outlet angle (sometimes identified

as the blade no lift angle) the calculation is straight forward and the result is referred to as simple Euler theory. For a single impeller with a uniform axial inlet velocity the work flow characteristic of the impeller is given by

$$\psi = 2(1 - \phi \tan \beta_2) \qquad (2.2)$$

where ψ is the work coefficient and ϕ the flow coefficient.

A slip factor C_H is introduced to allow for the fact that the actual flow would leave at an angle other than the blade outlet angle, the flow however still remaining cylindrical. Wislicenus [1] has calculated the magnitude of C_H in terms of blade spacing and cascade influence factor K, obtaining

$$C_H = \frac{2}{(\frac{s}{c})(\frac{2}{\pi K})(\text{Sec } \beta_n) + 1} \qquad (2.3)$$

where β_n is the no lift angle of the blade.

The cascade influence factor K, introduced by Weinig [2] attempts to relate the circulation around a blade in cascade arrangement (as in turbomachines) to the circulation around an isolated blade if it were at the same angle of attack in the same mean stream. There is considerable doubt about the validity of the concept of a constant slip factor C_H. This is discussed in detail in Chapter III.

The assumption of cylindrical flow is in error and at the very best can only be an approximate to the real state of affairs. As the flow proceeds through the impeller the tangential velocities C_θ change. Radial pressure gradients are set up and the flow moves radially inwards or outwards until ultimately the radial pressure gradients are exactly balanced by the centrifugal forces of the swirling flows.

There is a very limited set of conditions under which there is no radial shift of the streamlines in passing through the impeller. One of these is the so called free vortex flow where the tangential component of velocity varies inversely with radius, the axial velocity remaining unchanged when the total pressure is invariant with radius. This implies equal work addition at all radii. Free vortex design results in highly twisted blades for small hub tip radius ratio impellers. In order to have straighter blades other designs were tried. In most of these designs an attempt is made to satisfy the condition of radial equilibrium by balancing the radial pressure gradient with the centripetal acceleration due to the tangential component of velocity of whirl. The aim is to render radial flow negligible. Cohen and White [3] derived an equation for the calculation of flow in an axial compressor assuming that the flow had reached radial equilibrium at the trailing edge of the blade. In their derivation they assumed that the radius of streamline at outlet is the same as at inlet i.e. $r_2 = r_1 = r$ (fig. 3.5). They neglected interference from other blade rows. Bowen, Sabersky and Rannie [4] improved upon the radial equilibrium theory of Cohen and White by omitting the approximation that $r_2 = r_1 = r$. They also assumed that the flow had reached radial equilibrium immediately downstream of the impeller. They neglected any interaction of the blade rows in a multistage machine. Experimental verification of this theory for the prediction of outlet axial velocity and the work flow coefficient at different radii was obtained at design and off design conditions of flow. For experimental verification two single stage compressors of hub tip radius ratio 0.6 were used. The first compressor was designed for free vortex whirl distribution and the other for solid body whirl distribution, i.e. where the tangential

velocity is directly proportional to the radius.

For both compressors, the agreement between the experimentally obtained and theoretically calculated values of axial velocity was good except in the boundary layer regions. The agreement between the work-flow coefficient was only fair for both compressors. The effect of secondary flows was not taken into consideration. Thwaites [5] has compared the outlet axial velocity as predicted by the methods of Cohen and White and of Bowen, Sabersky and Rannie for the first stage rotor of a multistage compressor. Both methods have given nearly the same result.

In a blade row where the aspect ratio is high (ratio of blade height to axial blade length) it has been observed that radial equilibrium is not obtained at the trailing edge of the blade and is not necessarily established between the rows of blades. An alternative to the radial equilibrium type of analysis is one in which it is no longer assumed that the radial movement of streamlines takes place only within the impeller. The blade row is replaced by a disc of infinitely small axial thickness, across which a sudden change in tangential velocity and vorticity takes place. Radial equilibrium exists far upstream and far downstream of the disc but not necessarily in between these stations. Rudan [6] was the first to suggest the use of this actuator disc model. He showed that upon the assumption of an infinite number of infinitely thin blades, and a system of trailing vortices that extended downstream to infinity in concentric cylinders, the effective axial velocity at the blade is the mean of the axial velocities at points upstream and downstream where equilibrium exists. To know the variation of axial velocity inbetween the points of equilibrium far upstream and far downstream, Marble [7] introduced the so called "exponential approximation" to the

throughflow. Bragg and Hawthorne [8] derived an actuator disc equation in terms of stagnation enthalpy and stream function. They obtained some exact solutions for the equation under special restrictive conditions. Horlock [9, 10], Hawthorne and Horlock [11] have obtained general solutions for single and for any number of closely packed discs including the interference effect of discs. They have used this theory for flow analysis in an isolated rotor and in a complete stage of a compressor of hub tip radius ratio of 0.4. In an isolated rotor axial velocities were measured at different chord lengths downstream and compared with the values for different positions calculated by the "exponential decay" equations obtained by them. Good agreement was obtained except in the boundary layer regions at hub and tip. They have also predicted axial velocities at very low flow rate with appreciable stall for a complete stage after allowing for losses. This has been compared with experimental results. The theory was able to predict the trend of the profile correctly though the agreement was only fair. To obtain an actuator disc solution it is necessary that an approximate position of the disc should be selected. Marble [7] suggested that the actuator disc should be located at the centre of pressure of the blade. Horlock and Deverson [12] conducted some experiments on the flow through an isolated rotor row and suggested that the disc should be located within the blade row, and may be placed 30 to 40 percent of the chord ahead of the trailing edge of the blade row. Hawthorne and Horlock [11] have suggested that for simplicity it may be placed mid way through the blade row except in the case of stalled blade row, when the disc is better located at the leading edge. Lewis [13] has suggested that the location of actuator disc is related to the processes of shedding of the bound vorticity of the blades and that

it should be located at a third of the blade chord from the leading edge. Also the bound and shed circulation distribution varied with flow coefficient; thus the best location for the actuator disc will also slightly vary over the operating range.

Both radial equilibrium and actuatorndisc methods are simplified views of the general problem of flow in turbomachines. Wu [14] derived the general equations governing the flow through turbo machines. Streamline curvature and matrix throughflow methods are used to obtain the general solution of flow through turbomachines. Marsh [15] has pointed out that both the methods are based on the same mathematical model. For both these methods high speed computers are necessary. Marsh [16] has written a general programme for the matrix flow method which is stored at The National Physical Laboratory.

Any method to be used for flow analysis depends upon the type of the machine and the facilities available. In the simple radial equilibrium equation it was assumed that radial equilibrium is attained at the blade trailing edge or very near the blade trailing edge and does not take into consideration the interaction of blade rows. Therefore this method is more suitable for an isolated rotor while the actuator disc equation which takes into consideration the effect of interaction of the blade rows will be more suitable in a stage than the simple radial equilibrium equations. To obtain solutions with the streamline curvature method and matrix flow method, high speed computers are necessary and for the matrix flow method variation of angle from inlet to outlet throughout the blade passage should also be known.

Many investigations have been made on both high and low pressure

rise impellers which have been designed on the basis of free vortex whirl distribution as well as many other types of distribution of the tangential velocity. The design analysis being carried out either on a simple two dimensional basis or based on one of the three methods discussed. In accord with the interests of the present investigation attention will mainly be concentrated on low pressure rise impellers.

Ruden [6] designed three axial flow fans using the various charts given by him. For the design of these fans the cascade influence factor and thickness factor was taken into consideration. The axial velocity at the rotor was taken as the mean of the axial velocity far upstream and far downstream. The upstream axial velocity was assumed constant and the downstream axial velocity was calculated from the simple differential equations obtained by him. He designed the fans for constant energy additions at all radii. The design operating point and the hub tip radius ratio was the same for all the three fans. However, the chord distribution was different. In the first case it was decreasing from hub to tip, in the second it was constant and in the third it was increasing. For all the rotors, good agreement has been shown between the theoretically calculated and experimentally obtained pressure rise coefficients for different flow coefficients except near the hub and the tip. The sharp decrease in pressure rise coefficient and efficiency near the tip was attributed to tip clearance losses and near the hub to secondary flow losses. Besides the total pressure rise coefficient and efficiency, no other experimental details are given and as such, not much information can be obtained.

Khane [17] applied Ruden's [6] theory that the axial velocity at the rotor is the mean of the axial velocity far upstream and far downstream of

the rotor, in conjunction with two dimensional cascade data to design two axial flow fans. One fan was designed for approximately uniform and the other for solid body whirl distribution downstream of the impeller. The fans were of 0.6 hub tip radius ratio and of unity space chord ratio from hub to tip. Extensive aerodynamic measurements were made in front of and behind the impellers at different flow coefficients. In the solid body design tip clearance effects were also investigated. Comparison with theory has been shown only at design point operation. Outside the boundary layer region good agreement has been obtained for axial velocity and pressure rise coefficient, He concluded that high efficiency fans can be designed incorporating three dimensional flows to obtain higher pressures. For the calculation of outlet axial velocity, he used Ruden's equations in simplified way.

Mikhail [18] designed and tested four fans. The first was of low hub tip radius ratio of 0.29 and large space chord ratio of four at the tip. This was designed by simple aerofoil theory without taking into consideration the cascade influence factor. For this rotor free vortex whirl distribution was selected. The second fan was designed for non-free vortex whirl distribution with increasing blade circulation from hub to tip. The hub tip radius ratio was 0.5 with space chord ratio decreasing from hub to tip. At the tip it was 0.75. The third fan was of free vortex design with constant blade circulation. The hub tip radius ratio was 0.5 and the space chord ratio increased from hub to tip being two at the tip. The fourth fan had a non-free vortex flow with decreasing blade circulation towards the tip. In this case the hub tip radius ratio was 0.5 with a space chord ratio of 1.5 at the tip. The last three machines

were designed by the cascade method. In the cascade design method, up to a limited space chord ratio which is generally 1.5, the outlet fluid angle is calculated by semi-empirical rules. Mikhail used Constant's deviation rule. All the four fans were made of 1 mm. thick sheet metal. The aim of these tests was to check the validity of the fact that the axial velocity at the rotor plane is the mean of the axial velocities far upstream and far downstream where equilibrium exists, and to investigate losses in non-free vortex machines. Results have been plotted at the maximum efficiency point for all the fans. He concluded that for lightly loaded machines designed for free vortex whirl distribution, the above fact was established. But for highly loaded machines, tests did not give enough evidence to establish the accuracy of the above theory. He further concluded that properly designed non-free vortex machines have values of total efficiency comparable to that of free vortex machines. He also observed that radial equilibrium was reached at a place not very far from the rotor and before the measuring plane, but he has not given the distance of the measuring plane from the rotor. He observed that the difference between the measured outlet angles and those predicted by Constant's rule was due to secondary flows. However, in the middle region also the agreement is only fair. Barna [19] conducted tests on an axial flow fan of hub tip radius ratio of 0.5 and with four blades of decreasing blade chord from hub to tip. The fan was designed by aerofoil theory for free vortex whirl distribution and uniform axial velocity from inlet to outlet. R.A.F. 6E Section was used for blades. The tests were conducted at two blade settings and four different speeds and at different flow coefficients. The flow was varied by providing wire screens of varying mesh sizes at the outlet of the tunnel. Aerodynamic surveys were made in

front of and behind the impeller. No comparison has been shown with design values as the main purpose of the tests were to observe the behaviour of the fan at design and at off design conditions. From these tests he concluded that at the design operation point, the fan satisfies the requirements of irrotational flow except near the hub and the tip, but at off design conditions, the flow pattern was considerably altered and the flow ceased to be irrotational. He further recommended that special attention should be given to the hub and tip regions while designing the fan. Miller, Crouse and Sandercock [20] tested three isolated rotors in water. These rotors were designed by N.A.C.A. Diffusion Factor D. This factor is a blade loading criterion. It is suggested that the separation will occur on the suction surface of the cascade aerofoil when the value of "Diffusion factor" D given by

$$D = \left(1 - \frac{W_2}{W_1}\right) + \frac{\Delta C_\theta}{2W_1} \cdot \frac{s}{c} \qquad (2.4)$$

will increase a certain value. Originally, this was suggested to be 0.6 as given by Horlock [21]. The first rotor was of hub tip radius ratio of 0.4 and a blade tip D factor of 0.223, second rotor of hub tip radius ratio of 0.7 and tip D factor of 0.426 and the third rotcr of hub tip radius ratio of 0.8 and tip diffusion factor of 0.664. The space chord ratio increased from hub to tip and was unity at the tip in all the three cases. All the rotors were designed for free vortex whirl distribution. In general, the tests were aimed at studying the flow conditions of axial flow pump blading over a range of basic design parameters, that is, blade loading, flow coefficient, hub tip radius ratio etc. Detailed overall performance and blade element performance at tip, mean and hub are given. It was concluded that three dimensional flows were present in all the rotors and deviation angles were

different from the design values. They suggested that the three dimensional effects on reference incidence and deviation angles must be accounted for in design procedures. The method they suggested is to modify two dimensional deviation and reference incidence angles with three dimensional correction factor based on data from tests on similar rotors in the form $i_{ref} = i_{2D} + (i_{ref} - i_{2D})$ and $\delta_{ref} = \delta_{2D} + (\delta_{ref} - \delta_{2D})$ where i_{2D} and δ_{2D} are the two dimensional incidence and deviation angles respectively and i_{ref} and δ_{ref} are the minimum loss values of incidence and deviation angle obtained for each blade element from the tests. As this correction factor was based on experimental results and varied considerably for the three rotors, no general rule can be made. Miller and Sandercock [22] have given similar results for a rotor designed for tip D factor of 0.66, where the hub tip radius ratio was 0.8 and the space chord ratio unity at the tip. Conclusions were the same as in the previous case.

For accurate performance prediction, it is essential that the loss of relative stagnation pressure should be known. Many empirical rules of Howell [23], Lieblien [24], Vavra [25], Fujie [26] and Balje [27] are available to calculate the profile, secondary and tip clearance losses. However, these rules do not give identical results as shown by Laxminarayana and Horlock [28] and are in any case, of limited value outside the range of empirical data which was used to obtain them.

In the design of an impeller, the blade loading is estimated by the use of aerofoil theory in conjunction with a cascade influence factor or by the use of cascade data. In the cascade design method, a knowledge of the flow outlet angle is essential. Generally it is obtained by semi-empirical rules as given by Constant, Howell and Carter and summarized by Horlock [21]

These rules are basically for circular arc and parabolic arc profiles. By these rules nominal deviation is obtained, nominal conditions being defined as the point where deflection is 80 percent of maximum stalling deflection. These semi-empirical rules are applicable up to medium space-chord ratio of about 1.5 and in the region of moderate stagger angles. They are of very limited use in the region of larger space-chord ratios and higher staggers as are encountered in low pressure rise impellers.

The value of the outlet angles as given by the semi-empirical rules is based on cascade data and they are for two dimensional flows. But in an impeller secondary flows are developed when the boundary layer at the annulus and the hub containing vorticity perpendicular to streamline direction is deflected by a blade row are associated with a component of vorticity which is produced in the direction of the stream. Squire and Winter [29] considered the flow in a symmetrical impulse cascade and obtained the simple result $w_v = -2(\alpha_1 - \alpha_2) \frac{d\, C_{x1}}{dr}$ for the magnitude of the stream-wise secondary vorticity where $\frac{d\, C_{x1}}{dr}$ is the velocity variation in the inlet boundary layer and $(\alpha_1 - \alpha_2)$ the deflection. Hawthorne [30] produced a more general method for the calculation of streamwise vorticity. An essential feature of Hawthorne's theory was that the gradient of total pressure is related to the growth of the streamwise component of vorticity. The fact that total pressure is constant along a streamline for invisid flow makes it possible to treat this relationship. In rotating passages the total pressure is not constant along a streamline. Smith [31] obtained a quantity $I(= p + \frac{1}{2}\rho W_1^2 - \frac{1}{2}\rho U^2)$ which is constant along a streamline passing through the rotor, and derived an equation for the calculation of the streamwise component of relative vorticity in rotating passages for an isolated rotor. Horlock [32]

has given a simple method of tracing the secondary vorticity in a complete stage of a compressor. In this method the boundary layer was assumed to be small in comparison with tip radius and remains constant through the stage. The trailing vorticity shed by the blades was neglected. Hawthorne [33] has obtained series solution for the change in mean outlet angles due to secondary flows.

Besides the secondary flows, there is a redistribution of axial velocity due to the lack of radial equilibrium. This redistribution flow affects the outlet angle. This has been studied analytically and experimentally by many workers. Pollard and Horlock [34] have studied this problem analytically and considered that as the axial velocity ratio, which is defined as the ratio of outlet axial velocity to inlet axial velocity at the same radius, increases through the cascade, deviation decreases. Mani and Acosta [35] in another analytical study have concluded that there may not always be a decrease in the deviation angle due to increase in axial velocity ratio. Pollard and Costelow [36] in an experimental study through a compressor cascade have suggested that increase in axial velocity reduces the deviation angle linearly. Shaalan [37] has suggested that the linear law may not be taken as a general rule. The manner in which deviation will vary depends upon the value of axial velocity ratio, cascade geometry and change in circulation. Horlock [38] has recommended that in any flow analysis, the effect of axial velocity ratio on deviation should be taken into consideration.

When the space chord ratio is more than 1.5, no experimental or semi-empirical rules are available to estimate the outlet angle. Therefore, generally, such impellers are designed by aerofoil theory. For designing

such impellers by aerofoil theory, experimentally obtained lift coefficients for single aerofoils are used. But the lift of the aerofoil in cascade is not the same as the lift of the single aerofoil. To account for this, generally the Weinig factor is used. The Weinig factor is given for straight and parallel vanes, but generally it is assumed that this can also be used when the blades have finite thickness and are curved. But the thickness has a definite effect on the no lift angle of the blade. Wislicenus [1] has suggested a method for estimating no lift angle for curved vanes with finite thickness in cascade. This graphical method is merely a suggestion with no theoretical or experimental backing. Thus the use of the Weinig factor as such can only give approximate values of the lift coefficient in cascade.

Hutton [39] carried out extensive experiments on an impeller with a small hub tip radius ratio of 0.33 and a space chord ratio of 3 at the tip to verify the applicability of the usual design methods to such a low pressure rise impeller. The experimentally obtained head rise coefficients at different radii have been compared with those calculated by slip theory as given by Wislicenus [1], and cascade theory. The purpose of slip theory and cascade theory is the same, that is to take into consideration the effect of deviation of the fluid from the blade. Therefore both methods should give the same results. Moreover, at zero flow, the cascade theory gives a head rise coefficient as 2, but from the slip theory, different values have been obtained at different radii, which seems rather contradictory. The concept of constant slip coefficient is critically examined in Chapter III and shown to be untenable.

Hutton observed that the slip theory gave only a very rough prediction of blade performance and similarly, the cascade theory gave poor agreement

between theory and experiment as, due to the three dimensional flows, the deviation angle was not the same as predicted by using two dimensional rules. He has commented that the cascade rules are being applied to a situation very different from normal gas turbine practice. It was further assumed that the deviation is invariant with flow coefficient. He has suggested a modified aerofoil theory in which the axial velocity at the impeller was taken as the mean of the axial velocity at inlet and outlet where radial equilibrium exists. This method gave better agreement than the previous two methods. However, in this method it seems that the experimentally obtained head rise coefficients have been compared with the work coefficients obtained by the modified aerofoil theory as blade efficiency has not been taken into consideration. If the efficiency would have been taken into consideration, perhaps agreement would have been better at the tip, and deteriorated at the other two radii for which results are given.

In the discussion of Hutton's work, Numachi [40] has suggested an equation for work coefficient, which gave better agreement for the impeller tested by Hutton. Numachi gave neither theoretical basis nor derivation for his equation. As shown in Appendix "A", it is based on the static pressure rise and there is no justification for using it to predict the total pressure rise coefficient. The apparent agreement in this particular case is merely fortuitous.

Turner [41] has pointed out the desirability of formulating a unified design method which could be applied to the whole range of staggers and space chord ratios likely to be encountered in fans and compressors. It was suggested that the cascade approach could provide a basis for the formulation of a unified design method. It was suggested that this would

require testing and performance analysis of typical fans.

In this investigation it was decided to make a thorough exploration of the flow in a high specific speed impeller of small hub tip radius ratio over a wide range of flow rates to obtain a physical picture of the flow phenomena. The impeller blade number was to be such as to give a blade spacing of a magnitude where aerofoil methods are usually considered appropriate in design. An attempt was to be made to predict the performance of the impeller using cascade methods of assessing outlet angles in this situation of wide blade spacing. The effect of secondary flows and changes in axial velocity on the outlet angles were to be taken into account.

An attempt was to be made to take efficiency into account by estimating the losses in the flow. If the losses were to be experimentally determined, a method was to be sought that did not involve inferring loss from direct measurement of total pressure rise in the impeller.

It was decided to use a commercial impeller of 24 inches outside diameter and 8 inches hub diameter with 9 blades. It was decided to keep the blade tip clearance and stagger setting constant throughout the study. Some details of the impeller are given in Appendix "D" and Fig. 4.9.

The experimental value of $N_s = N.\frac{Q_v^{\frac{1}{2}}}{H^{3/4}}$ at maximum head rise coefficient was about 3000 r.p.m. where N is the revolutions per minute, Q_v the cubic feet of air per minute and H is the head in feet of air. Its dimensionless specific speed is 1.05, based on the Eckert equation as given by Hutton [39].

CHAPTER III

THEORETICAL APPROACH TO THE PROBLEM

3.1 Performance prediction by two dimensional theories

For an impeller with moderate hub tip radius ratio Where the flow is two dimensional, performance can be predicted remarkably well by an analysis based on cascade characteristics at mid blade height. Where the hub tip radius ratio is small, but the flow is two dimensional, the overall performance can be predicted by integrating the performance over the blade height.

3.1.1 Euler's equation

The head rise through an isolated rotor with zero swirl at inlet is given by Euler's turbine equation,

$$\Delta H = \frac{U}{g} \cdot C_{\theta 2} \qquad (3.1)$$

and in non dimensional form as

$$\psi = 2(1 - \phi \tan \beta_2) \qquad (3.2)$$

where ψ is the work coefficient defined as $\frac{2g.\Delta H}{U^2}$ and ϕ the flow coefficient as $\frac{C_x}{U}$, U being the blade speed. If there are an infinite number of blades, the flow would leave at the blade outlet angle β_{2b} (sometimes identified as the blade no lift angle β_n) and a result is obtained often referred to as simple Euler theory.

$$\psi_E = 2(1 - \phi \tan \beta_{2b}) \qquad (3.3)$$

or $$\psi_E = 2(1 - \phi A_1) \qquad (3.4)$$

where $A_1 = \tan \beta_{2b}$

This equation gives a straight line work flow characteristic as shown in Fig. 3.1 and the slope is $-2A_1$.

In practice there is a deviation of the fluid from the blades. To predict the correct work flow characteristic, this deviation of the fluid should be accounted for. The deviation of the fluid from the blade depends upon the blade shape, solidity, stagger and the incidence angle. Where solidity is high it can be assumed with a fair degree of accuracy, that the deviation δ does not vary with incidence angle.

Then $\beta_2 = (\beta_{2b} + \delta)$ and $\tan(\beta_{2b} + \delta) = A_2$ and $A_2 > A_1$.

Then $$\psi = 2(1 - \phi A_2) \qquad (3.5)$$

The work flow coefficient line will again be a straight line but its slope will be $-2A_2$, which is greater than in the previous case and is shown in Fig. 3.1.

When the solidity is low, the deviation angle does not remain constant and varies with the incidence angle.

In this case, the outlet angle can be written as suggested by Rannie [42]

$$\tan \beta_2 = A_3 + F \tan \beta_1 \qquad (3.6)$$

$$= A_3 + F \left(\frac{1}{\phi}\right)$$ for no inlet swirl where A_3 is a constant and F is some function of β_1.

This gives $$\psi = 2(1 - F) - 2 \phi A_3 \qquad (3.7)$$

If F is constant and equal to B, then

$$\psi = 2(1 - B) - 2 \phi A_3 \qquad (3.8)$$

This is also a straight line relation and its slope is $-2A_3$ and as

B is not zero, A_3 must be less than A_2, therefore the slope of work flow coefficient line is less than the case where δ is constant.

At a certain inlet angle β_1, the outlet angle β_2 will be the same for both the above cases, hence ψ will also be the same.

The relation $\tan \beta_2 = A_3 + B \tan \beta_1$ can hold only in a small region of β_1, otherwise β_2 will be equal to 90° when $\beta_1 = 90^\circ$ at $\phi = 0$. In a cascade, β_2 will be of the order of β_{2b} for all values of β_1. Therefore where $\beta_1 = 90^\circ$ ($\tan \beta_1 = \infty$), B must be zero, if it is not equal to 90°.

Therefore at $\phi = 0$, the intercept on the ψ axis must be equal to 2.0. This will be valid for all values of F, whether equal to a constant B (for a limited range of β_1) or otherwise. The flow is of course assumed to remain two dimensional at all flow rates.

3.1.2 Slip theory

To account for the same effect of the fluid deviation from the blade, the work coefficient ψ_E is multiplied by a slip factor C_H to give

$$\psi = C_H \psi_E \qquad (3.9)$$

The slip factor C_H is treated as a constant and gives the work flow characteristic shown in Fig. 3.1 which is at variance with the work flow characteristic of the previous sections. The work coefficient at zero ϕ is not equal to 2.0. The seeming anomaly is resolved if one examines the concept of a constant slip factor. It follows from the definition of slip factor from Eqn. 3.9.

$$C_H = \frac{\psi}{\psi_E}$$

$$= \frac{2(1 - \phi \tan(\beta_{2b} + \delta)}{2(1 - \phi \tan \beta_{2b})}$$

$$= \frac{1 - \phi \tan(\beta_{2b} + \delta)}{1 - \phi \tan \beta_{2b}} \qquad (3.10)$$

Thus C_H is seen not to be a constant but a function of ϕ. At $\phi = 0$, $C_H = 1$, which gives $\psi = 2$ at $\phi = 0$ irrespective of the value of β_2 which conforms with the result of the previous section.

Wislicenus [1] has derived an expression for the slip factor as given in Chapter II by the equation 2.3, i.e.

$$C_H = \frac{2}{\frac{s}{c}\left(\frac{2}{\pi K}\right)(\sec \beta_n) + 1}$$

where K is the Weinig factor and β_n the no lift angle of the blade. Eqn. 2.3 makes C_H a constant. C_H of course is not constant and seeming contradiction of Eqn. 2.3 must be resolved.

The derivation of Eqn. 2.3 is dependent on the assumption that for a blade in cascade it is possible to write

$$C_L = 2\pi K \sin \alpha_a \qquad (3.11)$$

where α_a is the angle of attack measured from the no lift direction. A well known result for the lift coefficient is

$$C_L = \frac{2 \Delta C_\theta}{W_m} \cdot \frac{s}{c} \qquad (3.12)$$

But $\frac{\Delta C_\theta}{2} = \frac{W_m \sin \theta}{\cos \beta_2}$ (θ is the angle between W_m and W_2 as shown in Fig. 3.2)

which gives

$$C_L = 4 \frac{s}{c} \frac{\sin \theta}{\cos \beta_2}$$

$$\therefore \quad C_L = 4 \frac{s}{c} \frac{\sin(\beta_m - \beta_2)}{\cos \beta_2} \qquad (3.13)$$

β_n, the no lift angle, is less than β_2.

Let $\beta_n = \beta_2 - \delta'$, where δ' is the angle between no lift direction and W_2.

Then $\theta = \alpha_a - \delta'$ or $\alpha_a = (\theta + \delta')$

or $$C_L = 4 \frac{s}{c} \frac{\sin(\alpha_a - \delta')}{\cos \beta_2} \qquad (3.14)$$

or $$C_L = 4 \frac{s}{c} \left[\frac{\sin \alpha_a \cos \delta'}{\cos \beta_2} - \frac{\cos \alpha_a \sin \delta'}{\cos \beta_2}\right] \qquad (3.15)$$

The assumption of Eqn. 3.11 is thus seen to be unjustified. However, in the case where the blades are so closely spaced, then $\beta_2 = \beta_n$ at all incidences.

Then $$C_L = 4 \frac{s}{c} \frac{\sin \alpha_a}{\cos \beta_n}$$

and in this case C_L is proportional to $\sin \alpha_a$.

$$\therefore C_L = 2\pi K \sin \alpha_a = 4 \frac{s}{c} \frac{\sin \alpha_a}{\cos \beta_n}$$

giving $$K = \frac{2}{\pi} \cdot \frac{s}{c} \sec \beta_n \qquad (3.16)$$

Let the no lift direction of isolated blade = β_{ni}, the lift on it would be given by

$$C_L = 2\pi \sin(\beta_m - \beta_{ni}) \qquad (3.17)$$

Even assuming that the lift on a cascade blade would be given by the right hand side of the Eqn. 3.17 multiplied by K, there is the additional difficulty that β_{ni} is in general, not equal to β_n.

It is easily shown from calculation of work coefficient ψ, that the slip factor C_H can be written as

$$C_H = \frac{\tan \beta_1 - \tan \beta_2}{\tan \beta_1 - \tan \beta_n} \qquad (3.18)$$

From Fig. 3.2

$$C_x[\tan\beta_1 - \tan\beta_n] = \frac{C_x}{2}[\tan\beta_1 - \tan\beta_2] + \frac{W_m \sin\alpha_a}{\cos\beta_n}$$

$$\frac{\tan\beta_1 - \tan\beta_n}{\tan\beta_1 - \tan\beta_2} = \tfrac{1}{2} + \frac{W_m \sin\alpha_a}{C_x \cos\beta_n[\tan\beta_1 - \tan\beta_2]}$$

$$= \tfrac{1}{2} + \frac{\sin\alpha_a}{\cos\beta_n[\tan\beta_1 - \tan\beta_2]\cos\beta_m} \qquad (3.19)$$

Here we cannot substitute for $\sin\alpha_a$ from $C_L = 2\pi K \sin\alpha_a$ even for a flat plate cascade if δ' is not zero.

$$\therefore \frac{\tan\beta_1 - \tan\beta_n}{\tan\beta_1 - \tan\beta_2} = \tfrac{1}{2} + \frac{\sin\alpha_a}{\cos\beta_n \dfrac{C_L}{2\dfrac{s}{c}}},$$

using $C_L = 2\dfrac{s}{c}(\tan\beta_1 - \tan\beta_2)\cos\beta_m$

substituting for C_L from eqn. 3.13

$$\frac{\tan\beta_1 - \tan\beta_n}{\tan\beta_1 - \tan\beta_2} = \tfrac{1}{2} + \frac{\sin\alpha_a \cdot \cos\beta_2}{\cos\beta_n . 2\sin(\beta_m - \beta_2)}$$

$$= \frac{\cos\beta_n \cdot \sin(\beta_m - \beta_2) + \sin\alpha_a \cos\beta_2}{2\cos\beta_n \sin(\beta_m - \beta_2)}$$

$$\therefore C_H = \frac{2\cos\beta_n \sin(\beta_m - \beta_2)}{\cos\beta_n \sin(\beta_m - \beta_2) + \sin\alpha_a \cos\beta_2}$$

$$= \frac{2}{1 + \dfrac{\sin\alpha_a \cos\beta_2}{\cos\beta_n \sin(\beta_m - \beta_2)}}$$

$$= \frac{2}{1 + \frac{\cos \beta_2}{\cos \beta_n} \cdot \frac{\sin (\beta_m - \beta_n)}{\sin (\beta_m - \beta_2)}}$$

$$= \frac{2}{1 + \frac{\cos \beta_2}{\cos \beta_n} \cdot \frac{\sin \beta_m \cos \beta_n - \cos \beta_m \sin \beta_n}{\sin \beta_m \cos \beta_2 - \cos \beta_m \sin \beta_2}} \qquad (3.20)$$

which should be the correct version of Eqn. 2.3.

When $\emptyset = 0$, $\beta_1 = 90^\circ$ and $\beta_m = 90^\circ$

Then

$$C_H = \frac{2}{1 + \frac{\cos \beta_2}{\cos \beta_n} \cdot \frac{\cos \beta_n}{\cos \beta_2}} = 1 \qquad (3.21)$$

This agrees with the deviation approach of section 3.1.1 for the correction of the work flow characteristic and with the result of Eqn. 3.10 for $\emptyset = 0$, as for infinite blades $\beta_n = \beta_{2b}$. In the case of a flat plate cascade where it may be assumed that there is no deviation of the fluid, C_H should be equal to unity.

In Eqn. 3.19, $C_L = 2 \pi K \sin \alpha_a$ can be used for $\sin \alpha_a$ as $\delta' = 0$.

Then

$$C_H = \frac{2}{1 + 2\left(\frac{s}{c} \cdot \frac{1}{\pi K}\right) \sec \beta_n}$$

which is Wislicenus' result of Eqn. 2.3.

Substituting for K from equation 3.16

$$C_H = \frac{2}{1 + 2\left[\frac{\frac{s}{c}}{2 \cdot \frac{s}{c} \cdot \sec \beta_n}\right] \sec \beta_n} = 1 \qquad (3.22)$$

Eqn. 2.3 is valid only for flat plate cascades with zero deviation. When

there is no deviation there should be no slip and the concept of slip factor (as given by eqn. 2.3) has no meaning.

In Fig. 3.3, values of C_H calculated from eqn. 3.20 for $\beta_n = \beta_{2b} = 45^\circ$ and $\delta' = \delta = 2^\circ\ 44'$ are plotted against ϕ and in Fig. 3.4 it has been shown that the deviation method and variable slip factor method give identical results. This resolves the contradiction between the two approaches mentioned by Hutton in reference [39].

In the discussion of ref. [39], Numachi has suggested an equation for the work coefficient as

$$\psi = 2\,C_H\left[1 - \frac{C_H}{2}\left(1 - \sqrt{1 - \psi_E}\right)\right]\left(1 - \sqrt{1 - \psi_E}\right) \qquad (3.23)$$

which apparently gave good agreement with Hutton's [39] experimental results. Numachi gave no derivation of his equation. A derivation is given in Appendix "A" of this thesis from which it is evident that Numachi based his work coefficient on the static pressure rise in the impeller and the suggestion that it allows for three dimensional effect is unfounded. The agreement with Hutton's results which are based on total pressure rise is purely fortuitous. Using the subscript s to denote quantities associated with static pressure rise it is seen from Appendix "A" that Eqn. 3.23 should really be

$$\psi_s = 2\,C_H\left[1 - \frac{C_H}{2}\left(1 - \sqrt{1 - \psi_{ES}}\right)\right]\left(1 - \sqrt{1 - \psi_{ES}}\right) \qquad (3.24)$$

3.2 Head rise coefficient

The work coefficient applies to work input to the rotor. The efficiency of the processes is not taken into consideration. The most

commonly used term is head rise coefficient ψ which is defined as

$$\psi = \eta_H \psi \qquad (3.25)$$

where η_H is the total head rise efficiency. Equation 3.25 is based on the total head rise actually achieved. If there are no losses, head rise coefficient will be equal to work coefficient i.e. $\psi = \psi$. If the losses in an impeller are known, efficiency can be calculated as given in Appendix "B".

3.3 Three dimensional approach to the problem

Various methods of allowing for the radial shift in the streamlines can be used in flow analysis. Thwaites [5] has shown that the flow behind actuator disc settles within 50 percent of its final value at a distance of about one fifth of a blade height downstream of an actuator disc and within about ten percent at a distance of about three quarters of a blade height downstream. In the case of an isolated rotor, where the axial width is comparable with the height of the blade, if the row is replaced by an actuator disc at a third of its axial width from leading edge, the flow has already nearly reached its final downstream conditions at the plane of the trailing edge. In the case of an isolated rotor of narrow axial width, where interference from other blade rows does not exist , radial equilibrium method should be able to successfully predict the flow measured in a plane not too near.the impeller trailing edge. As will be seen later, radial equilibrium methods were able to successfully predict the flow in the experimental impeller measured about one chord downstream of the impeller central plane.

3.3.1 Radial equilibrium equation

Fig. 3.5 shows the possible nature of the flow through an isolated rotor. The following assumptions are made.

(i) the flow is axisymmetric and incompressible

(ii) at a great distance upstream and downstream from the blade row the streamlines lie on cylindrical surfaces

(iii) the radius of the stream surface in general will change after passing through the blade row

(iv) the radial shift of the streamlines takes place entirely within the blade row.

Considering stations 1 and 2 far upstream and far downstream where the flow is in radial equilibrium the equation of motion is reduced to

$$\frac{dp_1}{dr_1} = \frac{C_{\theta 1}}{r_1} \qquad (3.26)$$

and

$$\frac{dp_2}{dr_2} = \frac{C_{\theta 2}}{r_2} \qquad (3.27)$$

In rotating coordinates

$$p_1 + \frac{\rho}{2}(W_1^2 - \Omega^2 r_1^2) = p_2 + \frac{\rho}{2}(W_2^2 + \Omega^2 r_2^2) \qquad (3.28)$$

or

$$p_1 + \frac{\rho}{2}(C_{x1}^2 + C_{\theta 1}^2 - 2\Omega r_1 C_{\theta 1}) = p_2 + \frac{\rho}{2}(C_{x2}^2 + C_{\theta 2}^2 - 2\Omega r_2 C_{\theta 2}) \qquad (3.29)$$

The continuity equation gives

$$C_{x1} r_1 dr_1 = C_{x2} r_2 dr_2 \qquad (3.30)$$

If the upstream pattern is completely known, these equations can be solved if the outlet angle of the fluid from the blade is known as a function of r_2.

Then

$$C_{\theta 2} = \Omega r_2 - C_{x2} \tan \beta_2 \qquad (3.31)$$

By differentiating Eqn. 3.29 and substituting from Eqns. 3.26, 3.27 and 3.31 and after rearrangement

$$\frac{(\Omega r_2 - C_{x2} \tan \beta_2)^2}{r_2} + \tfrac{1}{2} \frac{d}{dr_1} \left[-\Omega^2 r_2^2 + \frac{C_{x2}^2}{\cos^2 \beta_2}\right]$$

$$= \left[\frac{C_{\theta 1}^2}{r_1} + \tfrac{1}{2} \frac{d}{dr_1} (C_{x1}^2 + C_{\theta 1}^2) - \Omega \frac{d}{dr_1} (r_1 C_{\theta 1})\right] \frac{dr_1}{dr_2}$$

The ratio $\frac{dr_1}{dr_2}$ is eliminated by substituting from Eqn. 3.30 giving with further rearrangement

$$\frac{d C_{x2}}{dr_2} + \left[\frac{\sin^2 \beta_2}{r_2} - \frac{d}{dr_2} (\text{Log}_e \cos \beta_2)\right] C_{x2} = \Omega[2 \cos \beta_2 \sin \beta_2 -$$

$$\frac{r_2}{r_1} \frac{1}{C_{x1}} \cos^2 \beta_2 \cdot \frac{d}{dr_1} (r_1 C_{\theta 1})] + \frac{r_2}{C_{x1} r_1} \left[\frac{C_{\theta 1}^2}{r_1} + \tfrac{1}{2} \frac{d}{dr_1} (C_{x1}^2 + C_{\theta 1}^2)\right] \cos^2 \beta_2$$

(3.32)

In the case of an isolated rotor where it may be assumed that there is no tangential velocity at inlet, the equation canbe reduced to

$$\frac{d C_{x2}}{dr_2} + \left[\frac{\sin^2 \beta_2}{r_2} - \frac{d}{dr_1} (\text{Log}_e \sin \beta_2)\right] C_{x2}$$

$$= \Omega [2 \cos \beta_2 \sin \beta_2] + \frac{r_2}{r_1} \cdot \frac{1}{C_{x1}} \left[\tfrac{1}{2} \frac{d}{dr_1} (C_{x1}^2)\right] \cos^2 \beta_2 \qquad (3.33)$$

This differential equation for C_{x2} is non linear because the right hand side contains functions of r_1 and r_2. The coefficient of C_{x2} is a known function

of r_2 and the right hand side of the equation is composed of known functions of r_1 and r_2. The exact solution requires simultaneous solving of equations 3.32 and 3.30. To obtain an approximate solution of equation 3.32, a linearization is made by equating $r_1 = r_2 = r$ as a first approximation. The right hand side then becomes a known function of r and the equation becomes a linear first order differential equation for C_{x2}. With C_{x2} determined and C_{x1} known the streamline shift, and therefore $\frac{r_2}{r_1}$ can be computed from the continuity equation. Eqn. 3.32 can now be resolved with the new value of $\frac{r_2}{r_1}$ to give a new distribution of C_{x2}. From this, a more correct value of $\frac{r_2}{r_1}$ can be estimated and used for a further iteration of Eqn. 3.32 if necessary.

This radial equilibrium equation was first derived by Bowen, Sabersky and Rannie [4]. They applied this for the flow analysis in an axial flow compressor stage of high solidity of hub tip radius ratio of 0.6. Good agreement was obtained outside the boundary layer regions. Hutton [39] applied this equation to analyse the flow in an isolated impeller of small hub tip radius ratio and low solidity. Reasonable agreement was obtained. However, in both the cases, the effect of secondary flows and axial velocity variation was not taken into consideration.

3.4 Effect of axial velocity variation

In the flow of an incompressible fluid through a two dimensional cascade, the axial velocity remains constant as the flow takes place between parallel planes normal to the blade span. If these bounding planes converge or diverge, due either to actual non parallelism of the physical bounding surfaces or boundary layer growth on otherwise parallel bounding surfaces,

there will be corresponding changes in the axial velocity as the flow passes through the cascade. In an impeller stage the same effect is caused by the varying distance between adjacent axisymmetric stream surfaces. The contraction of otherwise parallel walls due to say boundary layer growth can be simulated by a smear of line sources on these walls such that the resulting two dimensional "Rankine bodies" will follow the contour of the boundary layer displacement surface.

The line sources will lie along the cascade axis as shown in Fig. 3.6 and will induce equal and opposite velocities w_o upstream and downstream normal to the cascade axis. Within the region of the cascade, the induced velocities will still be normal to the cascade axis, but would vary in some manner from $-w_o$ upstream to $+w_o$ downstream.

Within the cascade region these induced velocities will have varying components v' and u' normal and parallel to blade chord. The component v' is largely responsible for modifying the usual tangency condition for the blade camber line. In a compressor cascade as in Fig. 3.6 this results in a lower bound circulation around the blade than in the absence of these induced velocities. One way of looking at it would be to say that the induced normal velocities introduce a curvature of the streamlines so that less of a blade bound circulation is necessary to make the flow conform to the blade camber line. A retardation of the axial velocity will have an opposite effect on a compressor cascade with an increase in blade circulation.

The velocities w_o are uniform all over the region upstream and downstream of the cascade and hence they modify the inlet and outlet velocity vectors W_1 and W_2 to give the resultant difference in their axial components. The effect of axial velocity change is thus seen to be a modification of the

blade circulation and distortion of the inlet and outlet velocities. As the induced velocities due to the blade circulation are symmetrical about the vector mean velocity W_m, the modified induced velocities due to the changed blade circulation will also be symmetrical about W_m. Let ABC in Fig. 3.7 represent the vertices of the composite velocity triangle in purely two dimensional flow through a compressor cascade, AB and AC being the inlet and outlet velocities W_1 and W_2. Due to circulation change alone the velocities W_1 and W_2 will become AD = W_1^* and AE = W_2^* making β_1^* and β_2^* with the axial direction. Due to the induced velocities w_o, W_1^* and W_2^* will be swung out to W_1' and W_2' making β_1' and β_2' with the axial direction. All changes being symmetrical, the vector mean velocity W_m remains unchanged throughout. Fig. 3.7 shows three situations,

(a) a two dimensional flow with quantities W_1, W_2, W_m, β_1, β_2, C_L etc.

(b) a two dimensional flow with reduced circulation with quantities W_1^*, W_2^*, W_m, β_1^*, β_2^*, C_L^* etc.

(c) a flow with reduced circulation and with axial velocity change, the corresponding quantities being W_1', W_2', W_m, β_1', β_2' and C_L' etc.

As w_o is normal to the cascade axis, the experimental circulation is proportional to DE and is thus equal to the circulation of (b) above. One effect of the axial velocity change is to alter the deviation. In Fig. 3.7 the deviation appears to be decreased (increased deflection), but depending on the percentage reduction in circulation, the magnitude of w_o and the cascade stagger it is apparent that the deviation might well have increased.

As reviewed in Chapter II, many workers have theoretically and experimentally investigated on this problem. Soundranayagam [43] has worked out a

simple method of calculating the effect of axial velocity change on another-wise two dimensional flow and vice versa. The essential approach is given in Appendix "C" and the same method was used to take into consideration the effect of axial velocity variation on outlet angle in this study.

3.5 Effect of secondary flows

Secondary flows occur when an annulus boundary layer, containing vorticity perpendicular to the streamline direction is deflected by a blade row. A component of vorticity is produced in the direction of stream. This vorticity will then give rise to radial and tangential secondary velocities. These secondary velocities change the outlet angle distribution. This vorticity is located in the channel between the blades. Besides this, a component of trailing vorticity also lies in the wakes of the blade. Smith [44] has shown that if the ratio of annulus boundary layer thickness to wake spacing is large, i.e. > 2, then the wake contribution increases and finally becomes equal and opposite to the secondary vorticity contribution. In the present study $\frac{d}{s \cos \beta_2}$ was of the order of about 0.4 (d being the boundary layer thickness); hence the effect of trailing vorticity was neglected.

3.5.1 Determination of Streamwise component of vorticity for flows in rotating passages.

Smith [31] derived an equation for the calculation of the streamwise component of vorticity for flows in rotating passages. Smith's equation for absolute secondary vorticity is

$$\left(\frac{{}^{w}v}{w}\right)_2 - \left(\frac{{}^{w}v}{w}\right)_1 = \int_1^2 \frac{2}{w^2 R} \left| \frac{\nabla I}{\rho} \right| \cos \gamma \, ds'' + \int_1^2 \frac{2\Omega}{w} \left| \frac{\nabla I}{\rho} \right| \cos \delta'' \, ds'' \qquad (3.34)$$

where w_v = absolute secondary vorticity

R = principal radius of curvature of the relative streamline

I = a quantity defined as $p + \frac{1}{2}\rho W^2 - \frac{1}{2}\rho U^2$

γ = angle between the direction of curvature of the relative streamline and $(\frac{\nabla I}{\rho}) \wedge \vec{W}$

s" = distance along a streamline or arbitrary line

δ" = angle between $\vec{\Omega}$ and $\frac{\nabla I}{\rho}$

$\rightarrow$ vector quantity.

These are shown in Fig. 3.8.

To obtain the quantity $(\frac{w_v}{W})_2$ for an isolated rotor, the following assumptions were made.

(a) radial velocity is zero. $C_{x1} = C_{x2}$. It follows that streamline does not alter in radial position as between upstream and downstream of the disc and that $(\frac{\nabla I}{\rho})$ is same on either side of given radius.

(b) this velocity distribution is for a blade row with finite number and axial width (though it is strictly applicable to infinite number of blades and zero axial length). Implicit in this assumption is that $(\frac{\nabla I}{\rho})$ remains radial, although in fact, the secondary flows in the rotor passage twist the surface of constant I out of their original cylindrical shape.

With $(\frac{\nabla I}{\rho})$ radial in direction, the second term on the right hand side of equation 3.34 is zero, and the solution given by Smith for

$$(\frac{w_v}{W})_1 = \frac{d\,C_{x1}}{dr} \cdot \frac{\sin\beta_1 \cos\beta_1}{C_{x1}}$$

and for $$\int_1^2 \frac{2}{W^2 R} \frac{\nabla I}{\rho} \cos\gamma\, ds'' = \frac{2(\frac{d\,C_{x1}}{dr})}{C_{x1}} \int_1^2 \cos^2\beta\, d\beta$$

$$\therefore \left(\frac{w_v}{W}\right)_2 = \frac{d\,C_{x1}/dr}{C_{x1}} \left[2 \int_1^2 \cos^2 \beta \, d\beta + \frac{\sin 2\beta_1}{2}\right]$$

or

$$w_{v2} = \frac{d\,C_{x1}}{dr} \cdot \frac{1}{\cos \beta_2} \left[(\beta_2 - \beta_1) + \frac{\sin 2\beta_2}{2}\right] \qquad (3.35)$$

From this relative streamwise secondary vorticity

$$W_{v2} = \frac{d\,C_{x1}}{dr} \cdot \frac{1}{\cos \beta_2} \left[(\beta_2 - \beta_1) + \frac{\sin 2\beta_2}{2}\right] - 2\Omega \cos \beta_2 \qquad (3.36)$$

3.6 Calculation of change in outlet angle

With the relative streamwise secondary vorticity determined, the change in mean outlet angle may be calculated from the series solution developed by Hawthorne [33]. If the relative streamwise secondary vorticity at exit from the rotor is $W_{v2}(r)$ where r is the distance from the wall, then the mean change of outlet angle across the blade space at a distance r from the wall is given by when $0 < r < d$

$$\Delta \beta_2(r) = \frac{8 \cos \beta_2}{2\,C_{x1}} (\beta_2 - \beta_1) \sum_{n=1,3,5}$$

$$\frac{1}{n}\left[\frac{\cosh \frac{n\pi r}{S''}}{\sinh \frac{n\pi h_b}{S''}} \int_r^d W_{v2}(r) \sinh \frac{n\pi (h_b - r)}{S''} \, dr\right.$$

$$\left. - \frac{\cosh \frac{n\pi (h_b - r)}{S''}}{\sinh \frac{n\pi h_b}{S''}} \int_0^r W_{v2}(r) \sinh \frac{n\pi r}{S''} \, dr\right] \qquad (3.37)$$

where h_b = blade height

d = annulus boundary layer thickness

$S'' = s \cos \beta_2$ where s is the space.

Hawthorne has shown that series term with $n > 1$ are small and therefore may be neglected.

CHAPTER IV

TEST APPARATUS AND INSTRUMENTATION

4.1 Test apparatus

For conducting research on axial flow impellers, a test apparatus was designed and installed in the Mechanical Engineering Department of the University of Edinburgh. Fig. 4.1 shows the general layout of the apparatus.

In this apparatus, air is drawn from the room through a faired entry and after passing through the test impeller, is delivered into a large settling chamber. The flow is smoothed out in the settling chamber and passes through a venturimeter. A flow straightner follows the venturimeter and is followed in turn by a booster fan and silencer. The air leaves the test apparatus by an exit flare, which is combined with a damper to form a flow throttle.

The inlet fairing is made of glass fibre reinforced exposy resin. The studs which support the outer casing which is 24 inches internal diameter, are faired with wood to form streamline struts to permit minimum disturbance to the air flow. A circumferential perspex window is provided at the impeller station to permit visual observation. For easy access to the impeller blades a flange joint is provided after the impeller, and by removing the bolts, the outer casing along with inner casing can be slid into the settling chamber supported by the rubber tyred wheels which move in the guide channels. The settling chamber, which is 6 ft. in diameter and 6 ft. in length, is made of wood, both ends being provided with cross stiffners. The settling chamber is provided with Dufaylite $\frac{1}{2}$" core honeycomb and wire gauge for removing the swirl from the flows and smoothing out irregularities. From the settling chamber, the flow enters the venturimeter through an inlet flare of 28 inches

diameter, which is inside the settling chamber. The inlet diameter of the venturimeter is 24 inches and the throat diameter, 15.25 inches. The inlet taper angle is 21° and outlet, 13°. Between the venturimeter and booster fan housing a Dufaylite $\frac{1}{2}$ inch core honeycomb flow straightner is provided. The two speed booster fan is mounted in a special casing along with the silencer which is 3 feet long. At the end, a discharge flare is provided together with circular adjustable wooden baffle board which can be moved axially to act as a throttle at the end of the duct. This can be adjusted to give a variety of operating conditions.

For traversing the flow upstream and downstream of the impeller, the traversing plane was located three inches upstream and three inches downstream of the centreline plane of the impeller. Four static pressure plugs at the outer casing and four static pressure plugs at the hub wall around the circumference were located downstream of the impeller. The four plugs in each set were interconnected by a ring manifold to measure the mean static pressure. Similarly, four static pressure plugs were located in the outer casing wall at the impeller inlet. No static pressure plugs could be located in the hub wall at inlet due to the impeller bearings. The static pressure plugs were located at the same plane as the traverse plane.

4.1.1 Traverse carriage

For traversing the probe, a traverse carriage was provided which could be fixed at the plane of traverse by two screws. The probe could be held in position tightly in the traverse carriage to avoid vibration. With the traverse carriage, it was possible to provide radial and angular motion

to the probe. It was possible to read a radial movement of 0.1 inch, and angular movement of $\frac{1}{2}$ degree from the traverse carriage head. There was no provision in the traverse carriage for the movement of the probe in the pitch plane.

4.1.2 Test impeller drive

The test impeller is driven by a 20 H.P. variable speed D.C. motor. The motor is supported on air bearings. The minimum air pressure for the bearings is 80 lbs. per square inch, and is supplied by a reciprocating compressor through an air cleaner and water droplet remover. Provision is also made to add an oil mist to the air before it enters the bearings. The motor is supplied by a control unit that provides it with the D.C. and also keeps it at any set speed $\pm$ 2 r.p.m. in the range 200 to 2000 r.p.m. The control unit senses motor speed by a tacho generator mounted on the tail shaft, the tacho generator signal also being displayed on a meter on the control cabinet.

4.1.3 Speed measurement

For measuring purposes the speed is read off a four digit frequency meter activated by the signal from a photoelectric cell mounted behind a perforated disc on the drive shaft. The perforated disc is housed inside the inner inlet fairing.

4.1.4 Torque measurement

The test impeller drive motor also acts as a dynamometer. On one side of the motor, a torque arm is provided for hanging dead weights and a force transducer of the range 1 to 20 Newtons (1 Newton = 0.225 lbs. wt.)

was used on the other side of the motor to measure small differences between 0 and 1.8 lbs.

4.2 Flow measurement

In this apparatus, a venturimeter is provided to measure the flow rate. Various devices can be used for flow measurement. In axial flow fan test rigs, generally the inlet cone (as prescribed by B. S. Code 848, 1963) is a more common device. However, these test rigs are used only to ascertain the overall efficiency of the fan and not for extensive research work. In axial flow impellers, sometimes it has been observed that at low flow rates the separation with extensive recirculation regions occurs upstream and downstream of the impeller (as was observed in the present study). In these cases, the inlet cone will be affected by such phenomena. A well designed venturimeter gives a greater pressure differential for a given flow rate and also there is less experimental scatter in the calibration of a venturimeter. (For maximum flow, a pressure differential of 8.6 inches of water was obtained).

4.2.1 Calibration of Venturimeter

For accurate flow measurement it is necessary that every flow measuring device should be calibrated in the flow range in which it is likely to be used. Moreover, the venturimeter in the test rig is used in an entirely non-standard situation with a very short entry pipe leading direct from the settling chamber. In such a case, the recommendation of the standard codes with regard to discharge coefficients have little meaning. It was decided to calibrate the venturimeter by traversing the throat to

obtain the velocity distribution. Several methods such as the so called tangential method of B. S. Code 1042, of 1943, and the log linear method of Winternitz and Fischl [45] exist to simplify the traverse procedure so that acceptable accuracy can be obtained in the determination of the flow rate with only a few readings taken along a traverse. These methods have been tested against fully developed pipe flow profiles. In the present situation, the flow in the throat is far from fully developed and it was decided to obtain the flow rate from a series of detailed velocity traverses, the integration for flow rate determination being done graphically. The flow rate Q_T at the throat is given by

$$Q_T = \int_0^{R_T} C_x \, 2\pi r \, . \, dr$$

$$= 2\pi \int_0^{R_T} C_x \, r \, . \, dr \qquad (4.1)$$

where C_x is the velocity calculated at the radius r, and R_T is the radius of the throat. The product $(C_x.r)$ is plotted against r, the area under the curve being proportional to the flow rate.

4.2.2 Instrumentation

Generally pressures were measured by projection micromanometers.

For pitot traverses a three hole cylindrical probe of 0.25 inches outside diameter was used. For measuring total pressure, the probe was adjusted by balancing the pressure measured by the two side orifices. A thermometer was recessed into the wall of the settling chamber for measuring

temperature. For atmospheric pressure measurements, a barometer, which is installed in the laboratory was used.

4.2.3 Static pressure plugs

Four static pressure plugs were equispaced round the circumference at the inlet and the throat of the venturimeter. $\frac{1}{32}$ inch diameter static pressure holes were made in all the plugs. All the static pressure holes were four diameters long and then enlarged to twice the surface diameter, before communicating with $\frac{1}{4}$ inch internal diameter tubing. All the plugs were flushed from inside and free from burrs. Extreme care was taken in making and fixing the plugs. To obtain the mean value of static pressures, the four plugs at the inlet were connected by a ring manifold and also at the throat. The ends of the manifold were connected to the two sides of a manometer to get the difference of head.

4.2.4 Calibration procedure

At low Reynolds number (based on throat diameter), the calibration was done using the test impeller alone, and to prevent any interference in the flow meter the booster fan was removed. Calibration was done (a) at constant speed of the impeller and varying the flow rate with the help of the throttle and (b) by keeping the throttle fully opened and changing the flow by running the impeller at different speeds. Calibration was also done at stalled flows in the test impeller for two different speeds.

Before starting traversing the flow it was noticed that the flow was not perfectly axial, the swirl being about 1 to 2 degrees. The behaviour of the flow meter was checked on two diameters and was found to be the same.

Therefore it was decided to traverse only on one diameter. To prevent vibration of the probe, traverses were made from the wall to the centre of the flow meter only. Traverses were made in steps of 0.1 inch using the same traverse carriage as used for the test impeller.

Calibration at higher Reynold's number was done by running both the test impeller and the booster fan at full speed and the throttle valve fully opened. In this case a swirl of about 5 to 7 degrees was observed in the venturimeter.

For each traverse, the venturimeter pressure differential, velocity head at each point, temperature of the air, room temperature and barometer readings were recorded.

4.2.5 Flow computation

As mentioned in 4.2.1, the flow rate in the throat Q_T was obtained by graphical integration. The indicated flow Q_i was calculated from the venturimeter pressure differential.

$$Q_i = A_T \sqrt{\frac{2 \cdot g \, (\Delta h)}{1 - (\frac{A_T}{A_i})^2}} \qquad (4.2)$$

where A_T is the area of the throat and A_i is the area of inlet of the venturimeter and Δh is the differential head of the venturimeter.

(True flow measured by traverse instrument) = C_d (Indicated flow calculated from measured pressure differential).

$\therefore$ The coefficient of discharge $C_d = \frac{Q_T}{Q_i}$ 4.3

4.2.6 Results and discussion

Fig. 4.2 shows the calibration curve, where C_d is plotted against Reynold's number based on throat diameter. The maximum scatter is 0.6 percent up to a Reynold's number of 10.6×10^5. Beyond this Reynold's number there is a continuous drop in the value of C_d, and at Reynold's number of 17×10^5, this drop is 1.7 percent below the average value of C_d at Reynold's number of 10.6×10^5. This drop in the value of C_d beyond Reynold's number of 10.6×10^5 can be attributed to the fact that the calibration beyond this Reynold's number was performed by running the booster fan and test impeller together to get higher flows. It was noticed while doing this that the flow was not axial and swirl was present in the mainflow and boundary layer flow. Apart from this there can be a slight compressibility effect. Correction for compressibility effect was applied but it showed very little improvement in the C_d values. Though a honeycomb was provided between the venturimeter and the booster fan it did not quite prevent flow disturbances from being felt upstream and a slight rotation of the flow was present in the venturimeter. This may be due to the fact that the booster fan was located very near the venturimeter.

The coefficient of discharge when the test impeller was stalled is about 1.7 percent less than its average value at the same Reynold's number in the unstalled flow. This drop is attributed to the unsteadiness of the flow under these conditions, the volume of the settling chamber not being large enough to remove these oscillations. The effect of oscillations in reducing the overall discharge coefficient can be understood if it may be appreciated that the oscillations will cause an apparently larger venturimeter pressure differential than would be caused by the steady mean flow. For example, in

the extreme case of a zero mean flow the oscillations will cause a finite pressure differential to be registered when in fact the differential due to the mean flow should be zero.

4.3 Calibration of force transducer

A force transducer of range 1 to 20 Newton was used for measuring small increments of force during torque measurement. The transducer was fixed by four screws in the special housing provided for this on the dynamometer. The transducer was fed by a 5 KH_Z electric supply from an oscillator supplied by a stabilised 27 volts D.C. power supply. The output signal due to a load on the transducer was passed through a demodulating unit into digital voltmeter.

To calibrate the transducer, it was fixed on a plate and the plate was fixed to table with screws. A circular disc was screwed on the 2 mm. dia transmission spindle of the transducer. The load was applied in steps of 0.1 lb. up to 1.8 lbs. and at each interval the reading of digital voltmeter was noted. The same procedure was repeated for decreasing load.

Fig. 4.3 shows the calibration curve of the transducer. The graph has been plotted between load and the reading on the digital voltmeter. Negligible difference in readings between the increasing load and decreasing load was observed. The characteristic of the transducer in the range tested is essentially linear.

4.4 Balance of the Dynamometer motor

To check the balance of the dynamometer motor, it was uncoupled from the transmission shaft. The compressed air was supplied to the bearings and the motor was run at different speeds. The reading of digital voltmeter was

zero at all speeds and as such the motor was found to be fully balanced.

4.5 Bearing friction and windage torque

For calculating the true torque on the shaft it is essential that bearing friction and windage torque should be subtracted from the observed torque. To measure this, the impeller was removed from the shaft. The motor was started and its speed was gradually increased and the reading of the digital voltmeter was recorded. The same was repeated with decreasing speed of the motor. Fig. 4.4 shows the relation between the bearings frictional and windage torque and the speed. A smooth curve was drawn between the points.

4.6 Three dimensional probe

Hutton [39] in his paper, has suggested the use of three dimensional probes for the aerodynamic survey of the flow in the impeller. Design and calibration curves for various types of the three dimensional probes are given by Dean [46], Winternitz [47], Bryer and Walshe [48] and others. As pointed out by Winternitz [47], a probe should have qualities such as (a) be sufficiently small to avoid significant changes in the prevailing condition of flow, (b) be able to measure as nearly as possible at a point, (c) instrument characteristic should be unaffected by variation in test conditions, (d) be easy to introduce and seal, (e) have rapid response, (f) be sufficiently robust to avoid vibration and not to lose calibration and (g) should be able to measure maximum flow properties with a single probe.

It is very difficult for any single probe to have all the qualities as mentioned above, and hence, compromise has to be made. Winternitz and Ramsay

[49] have developed a cantilever pitot cylinder for three dimensional flow surveys. In this, besides the usual three orifices of an ordinary cantilever pitot cylinder, a fourth orifice is located at the tip, and with the calibration which correlates the pressure distribution on the instrument head with the pitch angle of the flow inclination, The essential requirement is that this dependence on flow direction should be a unique one. Also the fourth orifice at the tip does not invalidate the essential features of the conventional probe which are fully retained.

This type of probe satisfied many of the qualities as mentioned above and as such it was decided to use this type of probe. Winternitz and Ramsay have given calibration curves for different designs. The essential difference between various designs is the location of the tip orifice and the position of the other three orifices from the tip. For maximum range of operation, they have recommended a probe in which the inclination of the tip orifice from the probe axis should be 60° and the position of the other three orifices from the tip should be equal to the outside diameter of the probe.

Initially a probe was made with 0.25 inch outside diameter with the tip orifice at an angle of 60° from the probe axis and the other three orifices at a distance of equal to the diameter of the probe, the angle between the centre orifice and side orifices being 42°. This probe was calibrated in the calibration rig (explained in the next paragraph), but it showed considerable Reynold's number effect in all coefficients. In the second probe, all other designs were kept the same except that the angle between the centre orifice and the two side orifices was made 36°. This probe is shown in Fig. 4.5.

4.6.1 Calibration of the three dimensional probe

The rig used for calibration of the probe consisted of a blower tunnel with a free jet section of $5\frac{1}{8}$ inch diameter arranged so that the jet was truly horizontal. An arrangement was devised to support the probe in such a way that pitch motion was possible on the centreline of the jet. The probe was mounted in the traversing gear and fixed by screws on the specially devised stand for calibration. The probe was set perpendicular to the jet direction, making the pitch angle zero. The pressure leads were connected to inclined paraffin manometers.

The blower was started and the total pressure at the point of measurement was first measured with an N.P.L. type pitot static tube. The static pressure of the free jet was found to be zero. The probe was then yawed at the beginning of the series of measurements until the pressures at orifices 2 and 4 (Fig. 4.5) were the same and the yaw manometer was registering zero deflection. Subsequent probe motion was restricted to the pitch plane within the range of $\pm 30^{\circ}$ in steps of 5°. For each step readings of pressure at orifices 1, 2 and 3 were recorded. To verify the effect of Reynold's number, the experiment was repeated at four different velocities of 140, 112, 84 and 46 ft./sec. No tests were run at varying yaw angle as the probe was to be used to measure yaw by the null method always balancing the pressures between orifices 2 and 4.

4.6.2 Presentation of results

Since the pressure coefficients are to be used to determine flow inclination, total pressure and static pressure from the readings of the probe,

the relevant pressure differentials are in each case made dimensional less by reference to the value $(P_1 - P_2)$ obtained for zero yaw angle, the subscript referring to the orifice where each particular pressure is measured. The calibration results are plotted as a function of the pitch angle and the three coefficients derived from calibration are

$$\text{Coefficient of Pitch angle } C_P = \frac{P_1 - P_3}{P_1 - P_2} \qquad (4.4)$$

$$\text{Coefficient of Total pressure } C_T = \frac{P_0 - P_1}{P_1 - P_2} \qquad (4.5)$$

$$\text{Coefficient of Static pressure } C_S = \frac{P_1 - P}{P_1 - P_2} \qquad (4.6)$$

To ascertain the useful range of operation of the probe, there must be a unique dependence of C_P on probe geometry, since the coefficient of pitch angle is used to find the relevant values of coefficient of total pressure and coefficient of static pressure. Fig. 4.6 shows all three coefficients plotted against pitch angle in the range $\pm$ 30°.

4.6.3 Discussion of results

The calibration curves of C_P and C_T show unique curves for the range of velocities for which calibration was done. But no such unique curve could be obtained for C_S, and as such for estimating static pressure an interpolation between the curves has to be done. Similar characteristics for the coefficients of static pressure for such types of probes are also shown by Dean [46]. Winternitz and Ramsay have not shown calibration points in their plots, though calibration was done at different velocities. It was also noticed that yaw angle varied by about $\frac{1}{2}$° in the range calibrated.

This instrument can be used in the range for which it was calibrated i.e. $\pm 30^{o}$ of the pitch angle.

4.7 Hot wire probe

The usual pressure measuring instruments such as combination pitot pressure probes average out the flow conditions and give details of the flow phenomena. Furthermore, the errors inherent in the averaging processes make the use of such instruments unreliable in the estimation of small changes in say average total pressure between two stations as pointed out by Ushakov and Brusilovski [50]. The hot wire anemometer probe with its low thermal inertia responds to the details of the flow and is useful in obtaining a picture of flow conditions in the wake. A stationary hot wire downstream of the impeller would resolve the shape of the velocity variation in the blade wakes as they sweep past it. It was decided to use such a hot wire probe to explore the shape of the blade wakes both to get qualitative picture of flow conditions as well as to attempt an estimation of flow losses.

Fig. 4.7 shows hot wire probe. Two steel needles were used as two prongs and they were fixed in Araldite. The distance between the needles was kept about 2 mm. To prevent excessive vibration of the needles, their length was kept about 4 mm. Wollaston wire with a core diameter of 0.0002 ins. was used to form the hot wire element between the tips of the prongs. The wire is of platinum-irridium alloy coated with silver and its outer diameter was 0.005 ins. This wire was soft soldered to the prongs of the probe. After soldering, the soldered ends were covered with wax and the probe dipped in nitric acid. In this way, the etching away of the silver coating of the wire was uniform and took only a few minutes. It was washed in water and

the wax removed making it ready for use. The stem diameter of the probe was made identical to that of the combination pressure probe so that it could be held in the standard traverse gear.

A D.I.S.A. constant temperature anemometer was used in conjunction with the probe. The anemometer was set up following the procedure given in the D.I.S.A. handbook [51]. Once the bridge was balanced, the cold resistance of the wire was obtained. The working resistance was set at 6.8 ohms, which was 1.8 times the cold resistance of the wire.

The hot wire was calibrated in a free jet against a standard pitot static tube. Fig. 4.8 shows the calibration graph. At higher velocities, the sensitivity of the wire is very much decreased and the calibration curve tends to become flat. The frequency response of the wire was estimated by observing the response of the wire to a square wave input signal. The details of the procedure are given in D.I.S.A. handbook [51]. To produce the picture of the wave faithfully, the wire should have high frequency in comparison with the frequency of the wave which is to be measured. The usual value is about 8 to 10 times the frequency of the wave to be measured. In this case the blade frequency was 300 cycles per second. The frequency of the wire obtained from square wave test was about 8000 cycles per second. Therefore the wire was quite suitable.

4.8 Details of test impeller

A nine bladed .33 hub tip radius ratio impeller was used for the tests. Except for the above, no other information was available.

To know the geometry of the blading at different radii, a blade, identical to that of the test impeller was cast in plaster of paris, and was

cut at different radii. Full size photographs of the different blade sections were obtained. From these photographs, details of the blade chord, thickness, camber line and blade angles were computed. From these, the basic lift coefficients, no lift angles and design angle of attack were computed using Glauert's thin aerofoil theory. The joint at the hub section was very thick and almost oval in cross-section with no pronounced camber. The cross-section of the blade at this point seemed to be determined mainly by mechanical considerations. No measurements of blade shape were made at this position. Fig. 4.9 gives approximate shape of the blade sections at different radii. Appendix "D" gives other details for the blade sections as measured and calculated.

4.9 Booster fan

A two speed booster fan is provided to investigate the behaviour of the test impeller at high flow coefficients. The lower speed of the fan is 1440 r.p.m. and the higher speed 2900 r.p.m. There was no arrangement to run the booster fan at any other speed except these two. With the booster fan it was possible to test the impeller up to maximum flow coefficient of $\bar{\emptyset} = 0.420$.

CHAPTER V

TEST PROCEDURE AND EXPERIMENTAL RESULTS

5.1 Test procedure

The performance characteristics were obtained by running the impeller at a constant speed of 2000 r.p.m. and varying the flow by the throttle valve. At each selected flow, the radial distribution of flow conditions were surveyed at 15 positions. Pressures P_1, P_2 and P_3 at orifices 1, 2 and 3 of the three dimensional probe (Fig. 4.5) were recorded after balancing the pressures at orifices 2 and 4. The yaw angle was recorded from the graduated head at the top of the traverse gear. Static pressures at inlet and outlet casing walls and at outlet hub wall were recorded. For flow rate determination, the static pressure difference between the venturi inlet and throat was recorded.

For the determination of torque known weights were placed on the torque arm until near balance was obtained and to this the load recorded by the transducer was added. For the calculation of the net torque bearing friction and windage torque was subtracted from the gross torque.

Barometric pressure, together with air and room temperatures were noted throughout the test. All readings were reduced to standard temperature and pressure (60°F and 30" Hg.). All pressures were measured relative to atmosphere.

From the readings of the pressures at orifices 1, 2 and 3 of the probe, the coefficient of pitch angle $(\frac{P_1 - P_3}{P_1 - P_2})$ was calculated. Once the coefficient of the pitch angle was known, the pitch angle, the coefficient of total pressure $(\frac{P_0 - P_1}{P_1 - P_2})$ and the coefficient of static pressure $(\frac{P_1 - P}{P_1 - P_2})$ were read off the calibration chart of Fig. 4.6. From these values, the true

value of total pressure and static pressure were calculated for each measuring station.

5.1.1 Use of the hot wire probe

The hot wire probe was positioned in the same plane as the combination probe, the probe being held in the same traverse gear, enabling the probe tip to be moved to any selected radial position. The wire axis was placed in such a way so that it was parallel to the rotor speed vector at that point, the wire thus measuring the axial velocity component of the flow. It is convenient to measure the axial component of flow since this component is identical in both the absolute and relative velocity triangles in the study of blade relative flow phenomena.

For photographing the wakes, the turbulence output terminal of the anemometer was connected to an oscilloscope. An oscilloscope camera was used in conjunction with polaroid film of speed A.S.A. 3000. At the time of taking the photographs, the oscilloscope was set on single sweep. When each sweep was exposed, the film was taken out and developed for ten seconds by the polaroid method.

5.2 Data accuracy

The primary method for ascertaining the reliability of the measured data is through the comparison of the integrated flows at the impeller inlet and outlet measuring stations with the values measured with the venturimeter and also to compare the calculated aerodynamic torque with the measured mechanical torque. These comparisons are shown in Fig. 5.1. The integrated flows at inlet are within $\pm$ 2.5% of the venturi flow; similarly at outlet

within ± 2% of the venturi flow. Flow comparisons are well within the values as generally experienced in single stage tests [Ref. 22]. The difference between the measured mechanical torque and the calculated aerodynamic torque is less than 2.5% except in one case where it is 3.1%. In the stalled region of flow no comparison was possible, as on both sides of the impeller, reverse flow took place and it is difficult to get reliable values of integrated flows at inlet and outlet.

5.3 Evaluation of results

The method for the evaluation of the various results is given in Appendix "E". However, it is necessary here to explain the way in which mean head rise coefficient was evaluated.

The head of the machine at a given capacity is calculated as the weighted average of the different head values produced by the various cylindrical sections through the impeller. When the head is not uniform at all radial sections, but the through flow velocity is the same upstream and downstream at all sections, the total head can be averaged as

$$\overline{\Delta H} = \frac{2\pi}{Q_v} \int_{r_h}^{r_t} r\, C_x\, (H_2 - H_1)\, dr \qquad (5.1)$$

where r_h and r_t are the hub and tip radii.

However, in three dimensional flow, when the through flow velocity is not constant from upstream to downstream and also not uniform at all radii, the total head can be averaged as

$$\overline{\Delta H} = \frac{2\pi}{Q_v} \int_{r_h}^{r_t} r\, (H_2\, C_{x2} - H_1\, C_{x1})\, dr \qquad (5.2)$$

Thus the mean head rise coefficient was obtained as

$$\overline{\psi} = \frac{\overline{\Delta H} \cdot 2g}{U_t^2}$$

The same procedure was applied for stalled flows.

5.4 Presentation of results

The experiments were performed at a number of flow coefficients in the unstalled and stalled flow regions. Separate graphs are plotted wherever this was considered necessary.

5.4.1 Overall performance

The overall performance of the impeller is shown in Figs. 5.2 and 5.3. The maximum flow point on the curve was obtained when the throttle valve was fully opened and the test impeller was running at 2000 r.p.m. with the booster fan at its maximum speed of 2900 r.p.m. The minimum flow condition was obtained at a flow coefficient down to which readings began to be affected by instrument error such as meniscus effects in the manometer.

In Fig. 5.2 the mean total head rise coefficient $\overline{\psi}$ and the mean efficiency $\overline{\eta}$ are shown as a function of mean inlet flow coefficient $\bar{\phi}$. The $\overline{\psi}$ curve shows a discontinuity as $\bar{\phi}$ was reduced below 0.259. Between $\bar{\phi} = 0.259$ and $\bar{\phi} = 0.210$, no flow rate could be established, the flow shifted from $\bar{\phi} = 0.259$ to $\bar{\phi} = 0.210$. When the flow shifted from $\bar{\phi} = 0.259$ to $\bar{\phi} = 0.210$, the impeller suddenly stalled as noticed by the change in noise. Fig. 5.3 shows the variation of the outer wall static pressure rise coefficients with $\bar{\phi}$. When the flow was throttled to the minimum possible flow and then unthrottled, stable flow was established only at a much higher flow

and thus a hysteresis loop was formed. When unthrottling the flow was possible from $\bar{\phi}$ = 0.210 to 0.250 and then it shifted to $\bar{\phi}$ = 0.262.

5.5 Presentation of results for unstalled flow

5.5.1 Axial velocity

Fig. 5.4 shows axial velocity upstream of the impeller. The axial velocity upstream was fairly uniform in the middle of the annulus but varied slightly in other regions. In the boundary layer regions it dropped considerably, specially at the tip, where the drop was quite steep. At $\bar{\phi}$ = 0.420, the drop in axial velocity in the tip region was steeper than at the other two flow coefficients. Fig. 5.5 shows axial velocity downstream of the impeller. Downstream axial velocity was not uniform at any flow rate. The axial velocity increased from the hub towards the tip at all flow rates. It began to drop considerably as the vicinity of the tip was reached, the drop being quite rapid in the boundary layer region. The increase in axial velocity with radius was greatest at the lowest flow coefficient, i.e. at $\bar{\phi}$ = 0.259.

5.5.2 Tangential velocity

Upstream of the impeller, tangential velocities were very small. Downstream, tangential velocity is shown in Fig. 5.6. The trend of tangential velocity at $\bar{\phi}$ = 0.420 and $\bar{\phi}$ = 0.358 was the same. At these flow coefficients there was a continuous increase in tangential velocity from hub to tip except for a slight drop just near the tip and at a hub tip radius ratio of 0.45. At $\bar{\phi}$ = 0.259 it increased continuously from hub to tip. In the tip region, the

increase was sudden with very little drop at the very tip. The rate of increase in the middle region was quite small and was the same at all flow rates.

5.5.3 Radial velocity

Any radial velocity upstream of the impeller was too small to be measured. Downstream of the impeller the radial velocities were quite small except near the hub and tip. In Fig. 5.7 radial velocities in the main part of the annulus are zero at $\bar{\phi} = 0.259$ and near zero at $\bar{\phi} = 0.420$. However, they are larger at the intermediate flow rate of $\bar{\phi} = 0.358$.

5.5.4 Total head

Fig. 5.8 shows total head upstream of the impeller. Except in the hub and the tip boundary layer region it is uniform and slightly less than zero. Fig. 5.9 shows total head downstream of the impeller. At $\bar{\phi} = 0.420$ and $\bar{\phi} = 0.358$ total head increased from hub towards the tip. It began to drop as the vicinity of tip was reached and the drop being quite rapid in the boundary layer region. At $\bar{\phi} = 0.420$ the total head was negative in the hub region. At $\bar{\phi} = 0.259$, total head increased from the hub to a radius ratio of 0.9 and then increased suddenly, remaining constant just at the tip. Fig. 5.10 shows the rise in total head across the impeller.

5.5.5 Static head

Fig. 5.11 shows static head upstream of the impeller. The reading from the pressure tap in the outer casing is also included in Fig. 5.11. Fig. 5.12 shows the variation of static head downstream of the impeller. It also

includes readings made at the hub and the casing walls. In both cases the probe records higher values in the tip region.

5.5.6 Absolute Flow direction

A small amount of swirl was present upstream of the impeller at all flow coefficients. The absolute angles of the flow downstream of the impeller are shown in Fig. 5.13. At $\bar{\phi}$ = 0.420 this angle was fairly constant in the middle region of the flow. It decreased from a radius ratio of 0.6 to 0.4 and then it slightly increased near the hub. It also slightly increased near the tip. At $\bar{\phi}$ = 0.358 it remained fairly constant for a considerable part of the annulus. It increased in the hub and tip region and its increase was steeper than that at $\bar{\phi}$ = 0.420. At $\bar{\phi}$ = 0.259 at no radius ratio it was constant. It increased very sharply in the hub region and became negative. In the tip region also its rise was steeper than at the two other flow coefficients.

5.5.7 Deflection of the relative flow

Fig. 5.14 shows the deflection of the flow through the impeller. The deflection was a minimum at the maximum flow and it increased with the reduction of flow. At all flow coefficients there was no diffusion of the flow near the hub.

5.6 Presentation of results for stalled flow

5.6.1 Axial velocity

Fig. 5.15 shows the axial velocity upstream of the impeller. When

the impeller stalled at $\bar{\phi}$ = 0.210, reverse flow set in on the suction side near the tip of the impeller. The portion of the annulus affected by the reverse flow increased with the reduction of flow. At a flow coefficient of $\bar{\phi}$ = 0.065 about 25 percent of the annulus height from the tip was affected by the reverse flow and therefore the region of uniform velocity decreased. Fig. 5.16 shows axial velocity downstream of the impeller. Recirculation downstream of the impeller occurred even when the fan was unstalled [Fig. 5.5]. The region of recirculation increased with decreasing flow until at $\bar{\phi}$ = 0.065 it extended to about 60% of the annulus height from the hub.

5.6.2 Tangential velocity

Fig. 5.17 shows tangential velocity upstream of the impeller. With reverse flow on the suction side the tangential velocity increased sharply towards the outer radius. As the flow was reduced, the magnitude of the tangential velocity increased throughout the annulus. Fig. 5.18 shows tangential velocity downstream of the impeller. In all cases it increased from hub to tip. In the boundary layer region near the tip it dropped slightly. The tangential velocity curves for different flow coefficients are overlapping each other. This is associated with the fact that in the stalled flow region, the $\bar{\psi}$ - $\bar{\phi}$ curves do not increase or decrease steadily. $\bar{\psi}$ drops at one flow coefficient, recovers slightly at a lower flow coefficient and drops again as the flow coefficient is reduced.

5.6.3 Radial velocity

Figs. 5.19 and 5.20 show the variation of radial velocity upstream and downstream of the impeller. Radial velocities are present over the

whole annulus both upstream and downstream at all flow coefficients.

5.6.4 Total head

Fig. 5.21 shows total head upstream of the impeller. In the region of reverse flow it was positive and increased sharply as the flow was reduced. It falls slightly in the tip boundary layer region. Fig. 5.22 shows total head downstream of the impeller. It increased from hub to tip and the rate of increase was more at outer radii. Fig. 5.23 shows rise in total head across the impeller. The rise in total head decreased sharply in the boundary layer region and it became even negative. It recovered slightly just near the tip.

5.6.5 Static head

Fig. 5.24 shows static head upstream of the impeller. The static head increased sharply towards the tip becoming positive at very low flow coefficients. Fig. 5.25 shows static head downstream of the impeller. There was a gradual increase from hub to tip. In these cases also probe recorded higher values in the tip region.

5.7 Presentation of experimental results (hot wire probe)

The blade wakes are expected to diffuse with the free stream flow as they move downstream and the picture cannot be clear as just near the trailing edge of the blade. Fessler and Hartmann [52] compared the wakes behind a subsonic compressor by placing a hot wire probe at a distance of 0.25, 0.60 and 2.25 inches from the trailing edge of the rotor blades. Very little difference was noticed between the quality of the wakes for the two positions

0.25 ins. and 0.60 ins. of the probe. But the wakes that were obtained by placing the probe at 2.25 inches behind the rotor trailing edge, were quite different. It was noticed that the blade wakes were diffused and that the vertical scale had to be doubled for comparing these pictures with those taken closer to the blade trailing edge.

In the present study the probe was placed at an axial distance of 3 inches from the centre line . Therefore in each photograph, the wakes have started diffusing with the main flow. Also the wakes are not identical at a given flow condition and from this it seems that all the blades were not manufactured to the same finish and also that the setting of the blades was not quite the same. Better wake pictures could have been obtained if it would have been possible to locate the hot wire probe very close to the trailing edges of the blades. But besides obtaining the blade wake pictures, the interest was also to measure the R.M.S. value of the mean velocity to obtain and compare the losses obtained by pitot tube. Also at the survey plane which is about one chord downstream, the static pressure in the tangential direction becomes uniform.

However, from these wake photographs at different flow coefficients and at different radius ratios, the working of the blade elements can be studied.

5.7.1 Hot wire measurements of the blade wakes

The pictures of the wakes were obtained at flow coefficients of $\bar{\phi}$ = 0.420, 0.282, 0.259 and 0.210, and were taken for hub tip radius ratios of 0.983, 0.933, 0.8, 0.7, 0.6, 0.5 and 0.4. These are given in Fig. 5.26. In these photographs, where there are three wakes, the scales were 1 millisecond

per centimetre and 0.2 volts per centimetre. At the hub tip radius ratio where clear wakes were observed generally three wakes were photographed at larger scale. The highest trace represents the loss free region and the downward deflection represents a decreased mass flow. The left hand side of the downward going trace represents the suction.surface boundary of the passing blade wake and the right hand side going upward represents the pressure surface boundary of the wakes. The traces at a given hub tip radius ratio for different flow coefficients are compared briefly below. The use of the wake traces to obtain the estimates of the blade losses is discussed in detail in Chapter VI.

Hub tip radius ratio of 0.983

At $\bar{\phi}$ = 0.420, though the wakes are not very clear, they can be distinguished from other flow losses which are always present near the tip. With the reduction of flow, the size of the wakes increased, and other flow losses also increased. At $\bar{\phi}$ = 0.210, the flow was completely disturbed and the blade wakes were submerged in the overall tip loss region as the blade tip stalled.

Hub tip radius ratio of 0.933

At $\bar{\phi}$ = 0.420, the blade wakes are clear, but other flow losses are also present. At reduced flow the size of the wakes increased and other losses also increased. At $\bar{\phi}$ = 0.210, the flow was completely disturbed and the blade wakes were submerged in the overall tip loss region as the tips of the blades stalled.

Hub tip radius ratio of 0.8

At $\bar{\phi}$ = 0.420, the wakes are clear except for some minor flow irregularities. When the flow was reduced, the size of the wakes increased.

At $\bar{\phi}$ = 0.259, the wakes are quite clear. When the flow was further reduced to $\bar{\phi}$ = 0.210, the impeller was stalled near the tip, $\bar{\psi}$ dropped and loss regions appeared in the flow outside the immediate regions of the wakes and this smudges the clear out wakes when the blade tip is not stalled.

Hub tip radius ratio of 0.7

At $\bar{\phi}$ = 0.420, the wakes are not very clear, but as the flow was reduced, the blade wakes become quite large and no other flow losses are noticeable. At $\bar{\phi}$ = 0.210, the whole flow was disturbed due to the stalling of the blade at the tip.

Hub tip radius ratio of 0.6

At $\bar{\phi}$ = 0.420, the wakes are not very clear, When flow was reduced, the size of the wakes increased, but some other losses also appeared. At $\bar{\phi}$ = 0.210, other losses have not increased due to the stalling of the blades at the tip as at other radius ratios described above.

Hub tip radius ratio of 0.5

At $\bar{\phi}$ = 0.420, the wakes are clearer than at radius ratios of 0.5 and 0.6. When the flow was reduced all the wakes were disturbed and other flow losses increased.considerably. At $\bar{\phi}$ = 0.210, it seems the losses are not increased more than what they were at $\bar{\phi}$ = 0.259, rather it seems they are slightly decreased.

Hub tip radius ratio of 0.4

At no flow coefficients the wakes can be separated from other losses. It seems that at all flow coefficients very high losses are present and this blade section did not work satisfactorily at any flow coefficient.

5.8 General discussion of the experimental results.

The mean head rise produced by the impeller increased continuously

as the flow was reduced from $\bar{\phi}$ = 0.420 and a maximum value of 0.351 was obtained at $\bar{\phi}$ = 0.259. When flow was further reduced, it shifted to $\bar{\phi}$ = 0.210 and the mean head rise coefficient dropped off to a value approximately 64 percent of the maximum value. At this mean flow coefficient the impeller was stalled. With further reduction of flow there was not any appreciable recovery of mean head rise coefficient and after a flow coefficient of $\bar{\phi}$ = 0.093, it dropped off steeply.

The maximum mean efficiency of 81.4 percent was attained at $\bar{\phi}$ = 0.259. With a further reduction of flow, the mean efficiency also dropped to a value approximately 64 percent of the maximum value and with further reduction of flow it continued to drop steeply. The higher efficiency range of the impeller was from $\bar{\phi}$ = 0.360 to $\bar{\phi}$ = 0.259. The maximum efficiency was attained just before the impeller was about to stall. Generally, just before stall aerofoils work at their minimum loss incidence angles. Immediately prior to stall, the boundary layer on the upper surface of the blade is about to separate and this condition is associated with very low skin friction due to the low boundary layer velocity gradient at the wall. At stall, the boundary layer separates with a sudden increase in the eddy or form losses causing a drop in the efficiency. In this particular case, the mean head rise coefficient dropped to a value of 64 percent of the maximum value and the efficiency dropped by the same amount, suggesting a drop in head coefficient was due to the sudden increase in loss rather than sudden drop in the lift of the blade at separation. Unlike with isolated aerofoils, the loss of lift at stall in a cascade of blade is relatively gradual specially in cases of large stagger.

Fig. 5.3 shows that when the flow was throttled and when it was unthrottled, a hysteresis loop was formed. This phenomena seems to be common.for axial flow impellers as reported by Hutton [39] and Miller, Crouse and Sandercock [20]. A possible explanation for this phenomena in the impeller can be inferred from the behaviour of isolated aerofoils. When an aerofoil works at its maximum lift coefficient, the point near the stall, there is bound to be separation of the flow from the surface other than at the trailing edge, and stall almost always implies, therefore separation from the front half of the aerofoils. Thwaites [5] has stated that the state of the boundary layer on the aerofoil largely determines the stalling characteristics since on it depend the points of separation and the formation of the separation bubbles. The position of separation and the pressure within the bubble are the principal agencies in determining the characteristics of the flow as a whole. There are two possibilities, separation of (a) the laminar boundary layer near the nose and (b) a turbulent layer near the trailing edge. The former is usually found on thin aerofoils and the latter on thicker aerofoils. Thwaites [5] defines thick aerofoil as where the maximum section thickness is greater than 12 percent of the chord.

For thick aerofoils, as the lift is increased, the separation point first appears near the trailing edge and then moves forward as the lift increased further as a consequence of the increased positive pressure gradients over the rear of the aerofoil. A free boundary or vortex sheet springing from the separation point encloses a bubble of air in which a turbulent circulating motion is set up by the shear layer along the bubble boundary and by the turbulent mixing at the rear end. On thin aerofoils, an important

feature of the flow is the occurence of separation of the laminar boundary layer near the leading edge as soon as a pronounced minimum of pressure is formed there. For moderate incidences, reattachment as a turbulent boundary layer occurs, some distance downstream, a bubble thus being formed. Long and short bubbles under these circumstances are approximately classified. If the Reynold's number based on momentum thickness is greater than 500, a short bubble will be formed. The length of the short bubble is from a half percent to one percent of the chord. The bubble causes very little deviation from the pressure distribution given by the first invisid approximation. As the lift increases, the pressure decreases in the bubble and this is counteracted by increased curvature which in turn implies a decrease in the size of the bubble. At some critical angle of attack, the short bubble suddenly bursts forming a long bubble with marked loss of lift. The long bubble is about 2 to 3 percent of the chord on formation at low angle of attack but grows rapidly with increasing incidence until the separated layer fails to reattach. In the course of this lengthening of the bubble, the gradient of the lift curve steadily decreases and maximum lift is usually attained when the bubble extends beyond the trailing edge.

Isolated aerofoils show a hysteresis behaviour at stall. When, after the stall, the incidence angle is decreased, there is no reattachment after the separation near the leading edge and decrease of the incidence at first has little effect on the separated region covering the whole surface, but with further decrease of incidence the flow suddenly reverts to a short bubble configuration. Thwaites [5] has pointed out that it is quite impossible to predict the difference in the two values of the incidence for which the bubble

bursts and reforms. It seems the same phenomena cause a similar behaviour in the impeller, which is evident from Fig. 5.3 as when the flow was unthrottled, there was no reattachment of the flow at the flow coefficient at which it separated. However, as pointed out earlier, there will be no sudden drop of the lift as in the case of isolated aerofoils.

From the experimental results it is clear that the behaviour of the impeller was completely changed at $\bar{\phi}$ = 0.210. Even in the unstalled region of flow the impeller has shown strong three dimensional behaviour. Three dimensional effects increased as the flow was decreased. The distribution of axial velocity downstream of the impeller was not uniform at any flow rate. At $\bar{\phi}$ = 0.259, the axial velocity became zero and then negative near the hub and this phenomena increased with further reduction of flow. At $\bar{\phi}$ = 0.069, about 60 percent of the annulus height from the hub was affected due to this. Due to radial equilibrium requirements, if the given flow is to adhere to the hub at downstream of the impeller, it should have some definite value for the ratio of tangential velocity to axial velocity at the hub. If this value i.e. the absolute flow angle downstream increases from the critical value, the flow separates from the hub and a dead air bubble is formed at the hub and the critical hub radius is more than the existing one. If the flow is reduced further, the size of the dead air bubble increases. In the dead air bubble eddies are formed. It has been shown later that when the flow was analysed by radial equilibrium equation at $\bar{\phi}$ = 0.259, it was zero near the hub. It shows that for this flow coefficient the value of critical hub ratio was more than 0.33. Barna [53] has given a graph plotted between critical hub tip ratio and absolute flow angle at outlet. This gives a critical angle of 10 degrees for a hub tip radius ratio of 0.33. However,

from Fig. 5.13 it will be seen that in the test impeller the critical angle at which flow reversal starts, at the hub, is much higher than 10 degrees. In fact, Barna's graph is applicable for free vortex design.

The inlet axial velocity was nearly uniform in a large part of the annulus from $\bar{\phi}$ = 0.420 to $\bar{\phi}$ = 0.259. At $\bar{\phi}$ = 0.210 and below the inlet velocity was not uniform as at the outer radius reverse flow set in and thus the axial velocity varied from maximum to zero and then became negative. About 25 percent of the annulus height was affected by reverse flow at the outer radius on the suction side. Betz [54] has suggested that when flow separates from a blade then the pressure produced in the cross section at this point usually falls below that produced by the other blades. The energy supplied by the rotor is now deficient at this section, and the deficiency must be compensated for by the kinetic energy $\frac{\rho C_{x1}^2}{2}$ of the fluid passing the blade. The flow velocity C_{x1} is reduced at such sections but if this velocity is small, the kinetic energy $\frac{\rho C_{x1}^2}{2}$ may not be sufficient to replace the missing energy supply and reverse flow occurs at the section. From this the flow about the neighbouring blades is severely disturbed so that separation occurs on those blades as well. Betz [54] has also suggested that reverse flow occurs at a definite value of a "loading factor" defined as $\frac{\bar{\psi}}{\bar{\phi}^2}$. Betz has given this value as between 3 and 5 for an axial flow fan. In the test impeller, reversal of the flow at the inlet tip region is clearly seen at $\bar{\phi}$ = 0.210. There are reasons as will be shown later, tc believe that reversal of the flow in this region did in fact start at $\bar{\phi}$ = 0.259 though the region of reversal did not extend to the inlet traverse plane. The loading factor at both $\bar{\phi}$ = 0.259 and 0.210 turns

out to be about 5 confirming the values suggested by Betz.

In the unstalled region of flow, the radial velocities measured at the outlet traverse plane were very small, and the maximum velocities were 4, 9 and 17 percents of the maximum axial velocities at $\bar{\phi}$ = 0.420, 0.358 and 0.259 respectively. However, all these maximum velocities were either near the tip or near the hub. At $\bar{\phi}$ = 0.259, the radial velocity in the greater part of the annulus was zero, which shows that the flow had settled down at the measuring plane and radial equilibrium reached. This was also confirmed by Fig. 5.27, where the calculated values of static pressure from $\frac{dp_2}{dr_2} = \frac{\rho (C_{\theta 2})^2}{r_2}$ have been plotted. Good agreement has been achieved except near the tip, which is partly due to the over-estimation of static pressure near the tip. At $\bar{\phi}$ = 0.259, the hub is affected by reverse flow and therefore there is recirculation of fluid. Due to this the probe has measured the strength and direction of the radial velocity of the reverse flow and it suggests that the outer boundary of the reverse flow is up to a hub tip radius ratio of 0.5. At $\bar{\phi}$ = 0.420 and $\bar{\phi}$ = 0.358, just near the hub the direction of the radial velocity shows that the flow is trying to move towards the hub. It seems that due to the very thick blade sections near the hub, there is a blockage effect. Due to the blockage effect, flow would be moved radially outwards in the impeller and then would tend to move back towards the hub downstream of the impeller. In the stalled flow region radial equilibrium was not reached at the measuring plane due to the severe distortion of the axial flow by the recirculating regions at the hub and the tip, and the radial velocities were quite high.

Fig. 5.19 shows the radial velocity variation at inlet. In the region

which is not affected by the reverse flow, the flow tried to shift towards the tip and just near the hub, the radial velocity is zero. At the outlet the radial velocities were present throughout the annulus as can be seen from Fig. 5.20. The magnitude and direction change from positive to negative were different for different flow coefficients, but the trend at all the flow coefficients was the same. The magnitude of the radial velocities increased.with the reduction of flow. In the reverse flow region, the radial velocities of the reverse flow have been measured. The general nature of the flow when the impeller is stalled can be imagined as given in Fig. 5.28.

Fig. 5.8 shows the variation of total head at inlet. The total head at inlet should be zero but it shows a very small negative head. This is due to instrument error. One possible explanation is that the instrument was calibrated in a rig where the turbulence was high and of a different nature than the flow at the impeller traverse plane when the impeller was unstalled. The instrument error would be similar, but of different magnitudes, at the inlet and outlet traverse planes so that the effect of the error would be cancelled or much reduced when inlet and outlet readings are subtracted to give the total head rise. This applies to the variation of total head rise plotted in Fig. 5.10. From 5.9 it can be seen that at $\bar{\phi} = 0.259$, just near the tip, the total head increased suddenly. Correspondingly tangential velocity and absolute flow direction also increased. If the corresponding values of these parameters are examined for stalled flows at the tip, then there is similarity between the two. From this it seems that the flow separation at the tip at inlet is imminent or has already begun and a very small recirculation eddy has formed which does not necessarily

extend up to the probe measuring plane. At the same flow coefficient the impeller attained maximum mean efficiency and that this confirms the idea that the losses are low just before or as separation is just starting. Once separation is well established the form losses increase rapidly and efficiency falls as happened at $\bar{\phi} = 0.210$.

As can be seen from Figs. 5.21 and 5.22 that there is a sharp increase in head at the tip at inlet as well as at outlet of the impeller in the stalled flow region. At inlet, it rises to a positive value, what happens is that when recirculation starts at the inlet, fluid that enters at a lower radius is pumped out again into the inlet region at a greater radius with a higher total head. This same fluid enters the impeller again at the original lower radius but this time with a lower total head as it gives up some of its energy to the neighbouring throughput streamlines by mixing. The energy of the recirculating eddy remains a constant as it yields any pumping work done on it to the neighbouring throughput streamlines by mixing. Thus the throughput streamlines near the tip enter the impeller with a total head higher than normal and end up in the downstream tip region with an enhanced total head rise. The sudden increase in total head at the downstream tip region is thus a sign that reversal and recirculation of the flow has started at inlet. At $\bar{\phi} = 0.420$ the total head rise near the hub is negative. For a given blade angle according to head flow relationship of Eqn. 3.3 there will be a definite value of local flow coefficient ϕ_2 up to which the section will generate positive head. The flow coefficient for zero head rise will be $\phi_2 = \frac{1}{\tan \beta_{2b}}$. For radius ratio of 0.4 this value comes to 1.2. For two dimensional flow when the deviation of the fluid is taken into consideration the value of ϕ_2 for zero head comes to 0.95. Due to secondary flows there is a lot of underturning at the hub and the actual value of ϕ_2 for zero head

could be less than this. At $\bar{\phi}$ = 0.420, the value of ϕ_2 at radius ratio of 0.4 was 0.861, and zero head rise must have been reached at a mean flow coefficient somewhat lower than this. From the rise in total head it can be seen that the maximum work is being done at the outer radius.

In Fig. 5.12 plots of static head at outlet of the impeller also include readings made at the hub and the casing wall. In the unstalled flow region, the approximate value of the static head can be obtained by joining the reading at the hub and the casing wall by a straight line. This confirms the common industrial practice of linear extrapolanation between readings made at the hub and the casing walls. However, when the impeller is stalled the linear extrapolation approximation is not quite justified as can be seen from Fig. 5.25. At unstalled and stalled flows cylindrical type probe records higher values of static pressure near the tip as can be seen from Figs. 5.11, 5.12, 5.24 and 5.25. Such behaviour for cylindrical probes has also been pointed out by Khane [17] and Horlock [21].

If Fig. 5.14 be examined, it will be seen that even in the unstalled region of flow there was no diffusion of flow near the hub. As stated earlier the hub section was very thick and oval in shape without any appreciable camber and due to this there was considerable interference and blockage of the flow. Due to this there was no diffusion of the flow as in compressor cascades the thickness of the blades makes the outlet angle greater than what it would be if the thickness was zero.

Fig. 5.29 shows the relative outlet angle of flow in the unstalled region. It can be seen from the figure that in the middle region where the space shord ratio is between 1 and 1.7, the outlet angle was nearly constant.

But beyond a space chord ratio of 1.7 there was considerable variation in outlet angle for different flow coeffi cients. Near the hub though the space chord ratio was less than unity, the outlet angle was not constant. At $\bar{\phi}$ = 0.259, the outlet angle near the hub increased sharply as the axial velocity there tends to be zero. At stalled flows outlet angle is not constant at any radius ratio for different flow coefficients as can be seen from Fig. 5.30.

To know the behaviour of different blade elements at different flow coefficients, the hot wire traces of blade wakes can give useful information. From examining the blade wakes at different flow coefficients it can be seen that the hub region did not work satisfactorily at any flow coefficient. The flow was disturbed at all flow coefficients. This may be due to the very thick section near the hub and due to this there will be blockage in the flow. At $\bar{\phi}$ = 0.259 and 0.210 reverse flow also affected the picture. Similarly very near the tip the blade section did not work well, but it worked better than the hub section as at $\bar{\phi}$ = 0.420 the blade wakes can be distinguished from the other flow disturbances which are caused by the tip clearance flow. At $\bar{\phi}$ = 0.210 when the blade was stalled at the tip, the whole flow was so much disturbed and mixed that it was impossible to distinguish the wakes from other flow disturbances. In fact this process started at $\bar{\phi}$ = 0.259 and there is further evidence that flow reversal and recirculation at the tip started at $\bar{\phi}$ = 0.259, when the mean efficiency was maximum. At $\bar{\phi}$ = 0.420, clear wakes could not be obtained at radius ratios of 0.7 and 0.6. Pitot tube measurements have not shown any unusual phenomena at these radius ratios and it seems difficult to explain why good wakes were not obtained at these radius ratios. At $\bar{\phi}$ = 0.259, the tip

clearance flow has affected the flow at a radius ratio of 0.933 and reverse flow has affected the flowat a radius ratio of 0.5. At all other radius ratios, good wake pictures were obtained. When the flow was stalled, that is at $\bar{\phi}$ = 0.210 it is interesting to notice that the separation of the flow took place at the tip disturbing a large part of the annulus up to a hub tip radius ratio of 0.7. However, it seems that the blade element at a radius ratio of 0.6 was working satisfactorily and at radius ratios of 0.5 it has shown some improvement in comparison to $\bar{\phi}$ = 0.259. The reason for this seems to be that due to reverse flow at the tip, the flow was shifted towards the hub and the incidence angle was reduced at this section.

CHAPTER VI

LOSS ESTIMATION

6.1 General description of losses

As pointed out in Chapter III, the head rise coefficient $\psi = \eta_H \mu$

where $\eta_H = 1 - \frac{\bar{w} \times g}{U (C_{\theta 2} - C_{\theta 1})}$

In the case where $C_{\theta 1} = 0$

$$\eta_H = 1 - \frac{\bar{w} \times g}{U C_{\theta 2}} \qquad (6.1)$$

Therefore to predict the head rise coefficient it is essential that the total head loss should be known.

Losses in a turbomachine may be classified according to their physical causes, or their location. Generally these are skin friction losses, form drag, secondary flow losses, recirculation losses, annulus losses on the casing and the hub and the losses within the blade row.

The major part of the loss is connected with the formation of boundary layers which are the result of viscous flow. The boundary layers, mostly turbulent, begin to form on the inside walls of the intake ducts and on the blade surfaces. The turning of the annulus wall boundary layer through the blade passages creates trailing and passage vorticities. The boundary layers on the blades are shed as wakes. These vorticities and wakes represent regions of high loss.

Due to the effects of the variation of circulation along the blade length, the blade tip clearance and the relative motion of the rotor blade and annulus walls create vortices and further losses are created. Losses caused

by the separation of the boundary layers off the annulus wall are considered serious. These occur as a result of the interaction of the wall and blade boundary layer in the corner bounded by the end wall and the suction surface of the blade. Also off design loadings increase the loss due to separation associated with strong adverse pressure gradients on blade suction surfaces.

Howell [23] was the first who arbitrarily divided the losses in a turbomachine into (a) profile loss (in blade cascade), (b) annulus loss (on casing and hub wall) and (c) secondary loss (miscellaneous).

6.2 Profile loss

This can generally be obtained from experimental cascade data through correlations made by Howell [23], Carter [55] and others using British C_4 circular arc blades. Howell's data for the total pressure loss is expressed in terms of the difference between incidence and the so called nominal incidence. Carter's correlation is based on the difference between incidence and optimum incidence, where the latter is the incidence for maximum lift drag ratio. Loss estimation can also be based on Lieblein's [24] low speed relationship between the equivalent diffusion ratio and the wake momentum thickness at any flow condition. This relationship which is for two dimensional incompressible flow was derived from boundary layer theory assuming mean values for the form factor and momentum thickness of the wake or boundary layer in the integration of the momentum equation. It was also assumed that the blade peak suction surface velocity occurred close to the leading edge so that the initial boundary layer at the start of the diffusion is small, and that the boundary layer of the suction surface contributes the major portion of the wake. Lieblein's equation for the calculation of

equivalent diffusion can only be used for British C_4 and N.A.C.A. 65 (A_{10}) blades. Klapproth [56] has shown that Lieblein's equation may be modified to account for change in the axial velocity ratio. Balje [27] showed that using cascade criteria such as aerodynamic blade loading coefficient (ratio of the actual tangential force per unit blade height to the ideal tangential force per unit blade height) and the blade surface diffusion ratio, generalized relations for the loss in cascades of axial flow machines can be formulated. With the help of experimental and theoretical considerations, he derived a relation between the equivalent diffusion ratio and wake momentum thickness. Then an equation for the profile loss based on Lieblein's approach was derived. In this equation, the value of the form factor of the wake is the same as that suggested by Lieblein and it is assumed that it does not change with flow coefficient. As far as determination of profile loss is concerned, the method suggested by Balje does not have any special advantage over Lieblein's method. However, Balje has correlated profile loss to other losses as will be discussed later.

6.3 Secondary losses

In a cascade (designed for constant circulation at all spanwise positions) trailing vortices of opposite direction occur at the end of the inner and outer diameters. At the tip where the circulation drops off at the outer portions of the blade because of tip clearance, the trailing vortex in actuality consists of a sheet which however is supposed to roll up into a discrete vortex. In addition to these vortices, secondary vortices occur, which are caused by the boundary layers at the inner and outer channel walls.

The direction of these vortices will be opposite to each other. These vortex filaments induce secondary velocities in the discharge side of the cascade.

The kinetic energy of the induced velocity represents a loss and Vavra [25] has shown that for a two dimensional cascade, this loss is proportional to C_L^2. He has further shown that the secondary vortices are influenced by the conditions at the blade tips and the flow is much more complex, empirical relations being frequently used to take account of three dimensional effects.along the blade height. Howell [23] has given a single empirical equation to take into account the losses due to secondary flows which also includes tip clearance loss. Vavra [25] has given two different equations for secondary loss, one takes into account secondary flows and the other tip clearance flow effects. Empirical relations also exist to give the drag coefficient due to fluid friction on the annulus wall. Howell [23] gives this drag coefficient as $C_{DS} = .02 \frac{s}{h_b}$ i.e. C_{DS} will increase if there are fewer blades, but Vavra [25] has suggested that this is contrary to the experimental results and has suggested the expression $C_{DS} = 0.018 \frac{c}{h_b}$ i.e. based on chord length. This takes account of the fact that the frictional losses on the walls depend to a greater extent on the interference effects between the walls and the profile boundary layer than on the wall boundary layer alone.

These drag coefficients as given by Howell or Vavra are energy averaged over the blade height. In order that these coefficients may be used for a particular blade element, new coefficients referred to these elements must be calculated. Also it has to be decided what percentage of blade height

is affected by these losses and what should be the nature of distribution of these losses in the affected region, i.e. should the distribution be linear or parabolic etc. Betz [54] has suggested that due to tip clearance circulation falls off to zero at the tip and the extent of the blade height in which there is noticeable fall in circulation depends upon the tip clearance and a distance $S'' = s \cos \beta_2$. He has given graphs for various values of the ratio of blade tip clearance to S", from which the blade height affected by the tip clearance can be calculated. Secondary flow and annulus wall drag effects may be assumed to affect a blade height equal to the boundary layer thickness. A linear distribution of losses has sometimes been assumed as suggested by Schlichting and Das [57]. Balje [27] has given one expression for the tip clearance loss and another for the end wall loss which includes secondary flow and annulus drag effects. These loss coefficients are defined in such a manner that they are additive to the profile loss at different radii.

6.4 Limitations of semi empirical methods of loss estimation

The semi empirical methods just described have been developed for and depend on correlation aimed at predicting losses in axial compressors. They relate to standard blade forms and to values of space chord ratios and staggers that apply to compressor practice. They are an uncertain guide to losses at the higher space chord ratios and staggers that are met within low pressure impellers such as the one in the present study.

6.5 Loss estimation by hot wire measurements in the blade wakes

It was thought that the experimental measurement of loss should be quite

independent of total pressure measurements behind the impeller. In this way there is no possibility of the loss coefficient derived from total pressure measurements being used in turn in a "pseudo self validating" procedure to adjust the calculated total pressure rise in the impeller to correspond to the actual measured total pressure rise. It was decided to derive the loss from hot wire anemometer measurements made downstream of the impeller.

Fessler and Hartman [52] obtained hot wire traces of the wakes at the exit of the rotor of a subsonic compressor over the top half of the annulus. The losses calculated from these blade wakes were approximately the same as those obtained by total pressure measurements in the compressor. Fujie [26] obtained wake traces behind an axial flow fan and compared the drag coefficients calculated from these with those given by Howell [23], Vavra [25] and Betz. He has proposed his own empirical rules for drag coefficients for secondary flows, annulus and, tip clearance.

In calculating the losses from the wake traces, Fessler and Hartman [52] assumed that the highest trace of the wake represented the ideal value of the axial velocity and that this was equivalent to the reading of the D.C. voltage recorded by an anemometer. However, the anemometer D.C. voltmeter reading corresponds to the average velocity. Further to calculate the mean loss it is also necessary to plot the ratio of relative total pressure to ideal relative total pressure against distance in the tangential direction. For this purpose, the wakes should be quite clear. It is quite possible to do this in the middle region of the blades but near the hub and the tip where the blade wakes are mixed with other losses, it is difficult to plot the ratio

of relative total pressure to ideal relative total pressure against distance in the tangential direction. Also this is quite a lengthy process. For their calculation they assumed that the static pressure is uniform in the tangential direction. Such an assumption is not valid because they measured their wakes very close to the blade trailing edges.

The basis for loss estimation is discussed in what follows. A method is proposed for the rapid determination of the loss from hot wire measurements. The method depends on the direct measurement of the R.M.S. value of the wake wave form by the anemometer thus abreviating the lengthy procedure of analysing the actual wave form.

6.6 Calculation of losses in cascades

The mean loss in total pressure $\bar{q}$ is defined as the decrement in relative total pressure between the inlet to the cascade and a station well downstream of the cascade where the wakes have smoothed out and all flow conditions are uniform. In Fig. 6.1 it is assumed that the traverse plane is one chord downstream where the static pressure p_2 and the outlet angle β_2 are constant. In going from the traverse plane to the smoothed out flow downstream there is a change in p_2 and β_2 due to mixing out of the wakes.

The static pressure and angle downstream are denoted by p_3 and β_3.

If the momentum theorem is applied in the axial direction, then

$$(p_2 - p_3)\, s = (W_3 \cos \beta_3)^2 \rho\, s - \int_0^s \rho (W_2 \cos \beta_2)^2 \, dy$$

or

$$(p_2 - p_3) = \rho (W_3 \cos \beta_3)^2 - \rho \int_0^1 (W_2 \cos \beta_2)^2 \, d\frac{y}{s} \qquad (6.2)$$

The momentum theorem applied in tangential direction gives

$$(W_3 \cos \beta_3) \rho s W_3 \sin \beta_3 = \int_0^s W_2 \cos \beta_2 \rho \, dy \, W_2 \sin \beta_2$$

$$\text{or} \quad W_3^2 \cos \beta_3 \sin \beta_3 = \int_0^1 W_2^2 \cos \beta_2 \sin \beta_2 \, d\frac{y}{s} \qquad (6.3)$$

and from the continuity equation

$$W_3 \cos \beta_3 = \int_0^1 W_2 \cos \beta_2 \, d\frac{y}{s} \qquad (6.4)$$

squaring Eqn. 6.4 and dividing by Eqn. 6.3

$$\tan \beta_3 = \frac{\int_0^1 W_2^2 \cos \beta_2 \sin \beta_2 \, d\frac{y}{s}}{\left[\int_0^1 W_2 \cos \beta_2 \, d\frac{y}{s}\right]^2}$$

or

$$\tan \beta_3 = \tan \beta_2 \frac{\int_0^1 W_2^2 \, d\frac{y}{s}}{\left[\int_0^1 W_2 \, d\frac{y}{s}\right]^2} \qquad (6.5)$$

Now the mean total pressure loss in the cascade is

$$\bar{q} = P_{01} - P_{03} \qquad (6.6)$$

$$= P_{01} - \tfrac{1}{2} \rho W_3^2 - p_3$$

Substituting from Eqn. 6.4

$$\bar{q} = P_{01} - \tfrac{1}{2} \rho \left[\sec \beta_3 \int_0^1 W_2 \cos \beta_2 \, d\frac{y}{s}\right]^2 - p_3$$

Substituting from Eqn. 6.2 for p_3

$$\bar{q} = P_{01} - \tfrac{1}{2}\rho\left[\sec\beta_3 \int_0^1 W_2 \cos\beta_2 \, d\frac{y}{s}\right]^2 - p_2 + \rho(W_3 \cos\beta_3)^2$$

$$- \rho\int_0^1 (W_2 \cos\beta_2)^2 \, d\frac{y}{s}$$

Substituting for $W_3 \cos\beta_3$ from Eqn. 6.4

$$\bar{q} = P_{01} - \tfrac{1}{2}\rho\left[\sec\beta_3 \int_0^1 W_2 \cos\beta_2 \, d\frac{y}{s}\right]^2 - p_2 + \rho\left[\int_0^1 W_2 \cos\beta_2 \, d\frac{y}{s}\right]^2$$

$$-\rho\int_0^1 (W_2 \cos\beta_2)^2 \, d\frac{y}{s}$$

$$= P_{01} - \tfrac{1}{2}\rho\sec^2\beta_3 \cos^2\beta_2 \left[\int_0^1 W_2 \, d\frac{y}{s}\right]^2 - p_2 + \rho\cos^2\beta_2$$

$$\left[\int_0^1 W_2 \, d\frac{y}{s}\right]^2 - \rho\cos^2\beta_2 \int_0^1 W_2^2 \, d\frac{y}{s}$$

$$\bar{q} = P_{01} - p_2 - \tfrac{1}{2}\rho\cos^2\beta_2 [\sec^2\beta_3 - 2]\left[\int_0^1 W_2 \, d\frac{y}{s}\right]^2$$

$$- \rho\cos^2\beta_2 \int_0^1 W_2^2 \, d\frac{y}{s} \qquad (6.7)$$

Let $\int_0^1 W_2 \, d\frac{y}{s} = \bar{W}_2$

We can assume here that $\beta_2 \simeq \beta_3$. The difference between β_2 and β_3 is quite small and assuming that they are equal, this will simplify the calculations without introducing significant error in the magnitude of $\bar{q}$.

Then eqn. 6.7 is

$$\bar{q} = P_{01} - p_2 - \tfrac{1}{2}\bar{W}_2^2 + \rho\cos^2\beta_2 \overline{W_2}^2 - \rho\cos^2\beta_2 \overline{W_2^2} \qquad (6.8)$$

Also let $W_2 = \overline{W_2} + \Delta W_2$ (6.9)

as $\overline{W_2}$ is mean of W_2 over blade space

$$W_2^2 = \overline{W_2}^2 + 2\overline{W_2}\,\Delta W_2 + (\Delta W_2)^2$$

Also $\overline{W_2^2} = \overline{W_2}^2 + \overline{(\Delta W_2)^2}$ as $\overline{\Delta W} = 0$ by definition (6.10)

$$\therefore \bar{q} = P_{01} - p_2 - \tfrac{1}{2}\rho\,\overline{W_2}^2 + \rho\cos^2\beta_2\,\overline{W_2}^2 - \rho\cos^2\beta_2\,\overline{(\Delta W_2^2)}$$

$$= P_{01} - p_2 - \tfrac{1}{2}\rho\,\overline{W_2}^2 - \rho\cos^2\beta_2\,\overline{(\Delta W_2)^2}$$

substituting from Eqn. 6.10 for $\overline{W_2}^2$

$$\bar{q} = P_{01} - p_2 - \tfrac{1}{2}\rho\,\overline{W_2^2} + \tfrac{1}{2}\rho\,\overline{(\Delta W_2)^2} - \rho\cos^2\beta_2\,\overline{(\Delta W_2)^2}$$

or

$$\bar{q} = P_{01} - \overline{P_{02}} + \tfrac{1}{2}\rho\,\overline{(\Delta W)^2}\,[1 - 2\cos^2\beta_2] \qquad (6.11)$$

where $\overline{P_{02}} = \frac{1}{s}\int_0^s P_{02}\,dy$ i.e. the space averaged total pressure at the traverse plane. $P_{01} - \overline{P_{02}}$ is the space averaged total pressure loss $= \bar{q}_t$

$$\therefore \bar{q} = \bar{q}_t + \tfrac{1}{2}\rho\,\overline{(\Delta W)^2}\,[1 - 2\cos^2\beta_2] \qquad (6.12)$$

This equation gives the loss of total pressure at the point where the wakes have smoothed out using the readings taken at the traverse plane.

From the velocity triangle of Fig. 6.1, the loss can also be written as

$$\bar{q} = P_{01} - [p_3 + \tfrac{1}{2}\rho\,C_3^2 - \rho\,U_3\,C_{\theta 3}] \qquad (6.13)$$

Now $C_3^2 = C_{x3}^2 + C_{\theta 3}^2$

$$= C_{x3}^2 + [U_3 - C_{x3} \tan \beta_3]^2$$

$$= C_{x3}^2 + U_3^2 + C_{x3}^2 \tan^2 \beta_3 - 2U_3 C_{x3} \tan \beta_3$$

Also $U_3 C_{\theta 3} = U_3(U_3 - C_{x3} \tan \beta_3)$

$$= U_3^2 - U_3 C_{x3} \tan \beta_3$$

$$\therefore \tfrac{1}{2} \rho [C_3^2 - 2 U_3 C_{\theta 3}] = \tfrac{1}{2} \rho [C_{x3}^2 (1 + \tan^2 \beta_3) - U_3^2]$$

$$= \tfrac{1}{2}[C_{x3}^2 \sec^2 \beta_3 - U_3^2]\rho = \tfrac{1}{2} \rho [W_3^2 - U_3^2]$$

If P_{01} is assumed to be zero as in the case of an isolated rotor then

$$\bar{q} = - [p_3 + \tfrac{1}{2} \rho W_3^2 - \tfrac{1}{2} \rho U_3^2]$$

$U_3 = U_2$, if there is no radial shift of streamlines after the traverse plane.

$$\therefore \bar{q} = - [p_3 + \tfrac{1}{2} \rho W_3^2 - \tfrac{1}{2} \rho U_2^2]$$

$$\bar{q} = - [P_{03} - \tfrac{1}{2} \rho U_2^2] \qquad (6.14)$$

P_{03} being the relative total pressure far down stream.

It is now required to express P_{03} is terms of quantities measured at the outlet traverse plane.

Substituting from Eqn. 6.11

$$\bar{q} = - [\overline{P_{02}} - \tfrac{1}{2} \rho \overline{(\Delta W_2)^2} (1 - 2 \cos^2 \beta_2) - \tfrac{1}{2} \rho U_2^2] \qquad (6.15)$$

$$= - [p_2 + \tfrac{1}{2} \rho \overline{W_2^2}] + \tfrac{1}{2} \rho U_2^2 + \tfrac{1}{2} \rho \overline{(\Delta W_2)^2} (1 - 2 \cos^2 \beta_2)$$

$$\text{or } \bar{q} = - p_2 - \tfrac{1}{2}\rho \sec^2 \beta_2 \overline{C_{x2}^2} + \tfrac{1}{2}\rho \overline{U_2^2} + \tfrac{1}{2}\rho \overline{(\Delta W_2)^2} (1 - 2\cos^2 \beta_2) \qquad (6.16)$$

Now

$$\frac{\bar{q}}{\frac{1}{2}\rho \overline{C_{x2}}^2} = \left(\frac{U_2}{\overline{C_{x2}}} \right)^2 - \frac{p_2}{\frac{1}{2}\rho \overline{C_{x2}}^2} - \sec^2 \beta_2 \frac{\overline{C_{x2}^2}}{\overline{C_{x2}}^2} + \frac{\overline{(\Delta W_2)^2}}{\overline{C_{x2}}^2} (1 - 2\cos^2 \beta_2) \qquad (6.17)$$

Let $C_{x2} = \overline{C_{x2}} + \Delta C_{x2}$

$$C_{x2}^2 = \overline{C_{x2}}^2 + 2\,\overline{C_{x2}}\,\Delta C_{x2} + (\Delta C_{x2})^2$$

$$\frac{C_{x2}^2}{\overline{C_{x2}}^2} = 1 + 2\frac{\Delta C_{x2}}{\overline{C_{x2}}} + \frac{(\Delta C_{x2})^2}{\overline{C_{x2}}^2}$$

Also $$\frac{\overline{C_{x2}^2}}{\overline{C_{x2}}^2} = 1 + \frac{\overline{(\Delta C_{x2})^2}}{\overline{C_{x2}}^2}$$

Average of $\Delta C_{x2} = \overline{\Delta C_{x2}} = 0$. This follows by definition

$$\therefore \frac{\bar{q}}{\frac{1}{2}\rho \overline{C_{x2}}^2} = \left(\frac{U_2}{\overline{C_{x2}}} \right)^2 - \frac{p_2}{\frac{1}{2}\rho \overline{C_{x2}}^2} - \sec^2 \beta_2 - \sec^2 \beta_2 \frac{\overline{(\Delta C_{x2})^2}}{\overline{C_{x2}}^2}$$

$$+ \frac{\overline{(\Delta W_2)^2}}{\overline{C_{x2}}^2} (1 - 2\cos^2 \beta_2) \qquad (6.18)$$

The pressure p_2 is constant along the traverse plane as the latter is situated about one chord downstream of the blades. If it is assumed that there is at least one streamline at the traverse plane which has not suffered

an increase of entropy, and therefore having maximum relative velocity W_{2M}, p_2 can be determined

$$p_2 = \tfrac{1}{2}\rho U_2^2 - \tfrac{1}{2}\rho W_{2M}^2 \qquad (6.19)$$

$$\therefore \quad \frac{p_2}{\tfrac{1}{2}\rho \overline{C_{x2}}^2} = \frac{U_2^2}{\overline{C_{x2}}^2} - \left(\frac{W_{2M}}{\overline{C_{x2}}}\right)^2 \qquad (6.20)$$

Substituting from Eqn. 6.20 into the Eqn. 6.18

$$\frac{\bar{q}}{\tfrac{1}{2}\rho \overline{C_{x2}}^2} = \left(\frac{W_{2M}}{\overline{C_{x2}}}\right)^2 - \sec^2\beta_2 - \sec^2\beta_2 \frac{\overline{(\Delta C_{x2})^2}}{\overline{C_{x2}}^2} + \frac{\overline{(\Delta W_2)^2}}{\overline{C_{x2}}^2}(1 - 2\cos^2\beta_2)$$

$$= \left(\frac{C_{x2M}}{\overline{C_{x2}}}\right)^2 \sec^2\beta_2 - \sec^2\beta_2 - \sec^2\beta_2 \frac{\overline{(\Delta C_{x2})^2}}{\overline{C_{x2}}^2} + \frac{\overline{(\Delta W_2)^2}}{\overline{C_{x2}}^2} \sec^2\beta_2$$

$$(1 - 2\cos^2\beta_2) \qquad (6.21)$$

Also $C_{x2M} = \overline{C_{x2}} + \Delta C_{x2M}$

$$(C_{x2M})^2 = \overline{C_{x2}}^2 + (\Delta C_{x2M})^2 + 2\,\overline{C_{x2}}\,(\Delta C_{x2M})$$

$$\frac{(C_{x2M})^2}{\overline{C_{x2}}^2} = 1 + \left[\frac{\Delta C_{x2M}}{\overline{C_{x2}}}\right]^2 + 2\left[\frac{\Delta C_{x2M}}{\overline{C_{x2}}}\right] \qquad (6.22)$$

$$\therefore \frac{\bar{q}}{\tfrac{1}{2}\rho \overline{C_{x2}}^2} = \left(\frac{\Delta C_{x2M}}{\overline{C_{x2}}}\right)^2 \sec^2\beta_2 + 2\,\frac{\Delta C_{x2M}}{\overline{C_{x2}}} \sec^2\beta_2 \qquad \text{(contd.)}$$

$$- \frac{\overline{(\Delta C_{x2})^2}}{\overline{C_{x2}^2}} \sec^2 \beta_2 + \frac{\overline{(\Delta C_{x2})^2}}{\overline{C_{x2}}^2} \sec^2 \beta_2 (1 - 2 \cos^2 \beta_2)$$

or

$$\frac{\bar{q}}{\frac{1}{2}\rho \overline{C_{x2}}^2} = \sec^2 \beta_2 \left[\left(\frac{\Delta C_{x2M}}{\overline{C_{x2}}} \right)^2 + 2 \left(\frac{\Delta C_{x2M}}{\overline{C_{x2}}} \right) - 2 \cos^2 \beta_2 \frac{\overline{(\Delta C_{x2})^2}}{\overline{C_{x2}}^2} \right] \qquad (6.23)$$

If a hot wire anemometer be used to measure the instantaneous variation of C_{x2}, all the quantities in Eqn. 6.23 can be found. With a hot wire probe situated at a radius r and with the impeller rotating at Ω, the blade to blade distance s is given by

$$s = r \Omega t \qquad (6.24)$$

$$ds = r \Omega dt$$

$$\therefore \frac{1}{s} \int x \, ds = \frac{1}{r\Omega t} \int x \, r \Omega \, dt = \frac{1}{t} \int x \, dt \qquad (6.25)$$

$\therefore$ space average $\equiv$ time average as measured by the anemometer.

If (ΔC_{x2M}) can be measured directly from an oscilloscope trace, then from Eqn. 6.23 it will be possible to calculate the loss. $\overline{(\Delta C_{x2})}^2$ is obtained from the R.M.S. reading as given by the anemometer. If (ΔC_{x2M}) cannot be measured directly, an estimate of it can be made in terms of $[\overline{(\Delta C_{x2})^2}]^{\frac{1}{2}}$, i.e. in terms of the R.M.S. of C_{x2}, if suitable shape of the wake form may be assumed.

6.7 Estimation of (ΔC_{x2M}) for different wave forms

Examination of the hot wire traces of the wakes showed that in some cases the wakes were more or less clearly separated while in others there

was no clearly defined region which could be said not to belong to the wakes. For purposes of calculation, simplified modes of the wake shape are postulated, one a saw tooth type of profile, the second a more clearly separated wake and the third a sine wave wake form. All these are shown in Fig. 6.2.

For a saw tooth type wake form from Fig. 6.2

$$\Delta C_{x2} = \left(a - \frac{2a}{b} x\right) \tag{6.26}$$

$$(\Delta C_{x2})^2 = a^2 + \frac{4a^2 x^2}{b^2} - 4a^2$$

$$\overline{(\Delta C_{x2})^2} = \frac{1}{b} \int_0^b \left(a^2 + \frac{4a^2 x^2}{b^2} - \frac{4a^2 x}{b}\right) dx$$

$$= \frac{1}{b} \left[a^2 b + \frac{4a^2 b^3}{3b^2} - \frac{4}{2} \frac{a^2 b^2}{b}\right]$$

$$= a^2 + \frac{4}{3} a^2 - 2a^2$$

$$= \frac{a^2}{3}$$

$$\therefore a = \sqrt{3} \left[\overline{(\Delta C_{x2})}\right]^{\frac{1}{2}} \tag{6.27}$$

This result is independent of the magnitude b

$$\therefore (\Delta C_{x2M}) = \sqrt{3} \quad [\text{R.M.S. of } \Delta C_{x2}] \tag{6.28}$$

For well separated wakes from Fig. 6.2

$$\overline{C_{x2}} (d + b + e) = C_{x2M} (d + b + e) - \frac{1}{2} (b + e) \tag{6.29}$$

$$\overline{C_{x2}} = C_{x2M} - \frac{1}{2} \left(\frac{b + e}{b + e + d}\right)$$

$$= \overline{C_{x2}} + \Delta C_{x2M} - \frac{1}{2} \left(\frac{b + e}{b + e + d}\right)$$

$$\therefore \Delta C_{x2M} = \frac{\ell}{2}\left(\frac{b + e}{b + e + d}\right) \qquad (6.30)$$

As derived in the previous case

$$[\Delta C_{x2}]^2 = (\Delta C_{x2M})^2 - (\Delta C_{x2M})\left(\frac{b + e}{b + e + d}\right)\ell + \frac{\ell^2}{3}\frac{(b + e)}{(b + e + d)} \qquad (6.31)$$

From Eqn. 6.30 and 6.31

$$\overline{(\Delta C_{x2})^2} = \frac{\ell^2}{4}\left(\frac{b + e}{b + e + d}\right)^2 - \frac{\ell^2}{2}\left(\frac{b + e}{b + e + d}\right)^2 + \frac{\ell^2}{3}\left(\frac{b + e}{b + e + d}\right) \qquad (6.32)$$

By examining the traces of the wakes it was noticed that the value of d in relation to (b + e) varies approximately 0.5 to 1.5. However, the value of 1.5 is in rare cases. By assuming a suitable value of d in relation to (b + e), the value of ΔC_{x2M} can be calculated.

Let the value of d be assumed = 0.5 (b + e)

Then from Eqns. 6.30 and 6.32

$$\overline{(\Delta C_{x2})^2} = 0.999\,(\Delta C_{x2M})^2$$

or

$$\Delta C_{x2M} \simeq \left[(\Delta \overline{C}_{x2})^2\right]^{\frac{1}{2}}$$

For sine wave form

$$(\Delta C_{x2M}) = \sqrt{2}\ [\text{R.M.S. of } \Delta C_{x2}] \qquad (6.33)$$

Therefore for saw tooth type wake form

$$\frac{\bar{q}}{\frac{1}{2}\rho\,\overline{C}_{x2}^{\,2}} = \sec^2\beta_2\left[3\left(\frac{\text{R.M.S. of } \Delta C_{x2}}{\overline{C}_{x2}}\right)^2 + 2\sqrt{3}\left(\frac{\text{R.M.S. of } \Delta C_{x2}}{\overline{C}_{x2}}\right) - 2\cos^2\beta_2\left(\frac{\text{R.M.S. of } \Delta C_{x2}}{\overline{C}_{x2}}\right)^2\right] \qquad (6.34)$$

For separated wakes when d = 0.5 (b + e)

$$\frac{\bar{q}}{\frac{1}{2}\rho \overline{C_{x2}}^2} = \sec^2 \beta_2 \left[\left(\frac{\text{R.M.S. of } \Delta C_{x2}}{\overline{C_{x2}}}\right)^2 + 2\left(\frac{\text{R.M.S. of } \Delta C_{x2}}{\overline{C_{x2}}}\right)^2 - 2\cos^2 \beta_2 \left(\frac{\text{R.M.S. of } \Delta C_{x2}}{\overline{C_{x2}}}\right)^2\right] \quad (6.35)$$

For sine wave wake form

$$\frac{\bar{q}}{\frac{1}{2}\rho \overline{C_{x2}}^2} = \sec^2 \beta_2 \left[2\left(\frac{\text{R.M.S. of } \Delta C_{x2}}{\overline{C_{x2}}}\right)^2 + 2\sqrt{2}\left(\frac{\text{R.M.S. of } \Delta C_{x2}}{\overline{C_{x2}}}\right)^2 - 2\cos^2 \beta_2 \left(\frac{\text{R.M.S. of } \Delta C_{x2}}{\overline{C_{x2}}}\right)^2\right] \quad (6.36)$$

The percentage R.M.S. value of C_{x2} appearing in the above equations is obtained from the anemometer voltmeter readings using the relation

$$\left(\frac{\text{R.M.S. of } \Delta C_{x2}}{\overline{C_{x2}}}\right) = V_{RMS}\left(\frac{4V}{V^2 - V_o^2}\right) \text{ from Ref. [51]}$$

where V_{RMS} = Readings of R.M.S. Voltmeter

V = Mean velocity voltage on D.C. voltmeter of bridge

V_o = zero velocity voltage on D.C. voltmeter.

6.8 Calculation of losses and discussion of results

At a flow coefficient of $\bar{\phi}$ = 0.259, the wake traces were photographed at different radii. These wakes are shown in Fig. 5.26. From these wakes it was observed that at radius ratios of 0.983, 0.933 and 0.4 they approximated to sine wave form and thus the loss was calculated by Eqn. 6.36. At other radius ratios the wakes were separate and the loss was calculated from

Eqn. 6.35. The results are plotted in Fig. 6.3 in the form of relative total head loss coefficient = $\frac{\bar{\omega} \times 2g}{W_1^2}$. Results obtained from pitot tube measurements are also plotted. The method for obtaining loss coefficients by pitot tube is given in Appendix "E".

For a flow coefficient of $\bar{\phi}$ = 0.420 wakes are given in Fig. 5.26. From these wakes it was observed that at a radius ratio of 0.983, the wake form showed a separated wake and at a radius ratio of 0.4 it approximated to a sine wave form. Therefore at these two radius ratios, losses were calculated by equations 6.35 and 6.36 respectively. At other radius ratios the wake form could be approximated to the saw tooth type and thus losses were calculated by Eqn. 6.34. The results are plotted in Fig. 6.4. Here also the agreement with the losses obtained from pitot tube measurement is good.

For a flow coefficient of $\bar{\phi}$ = 0.358 wake traces were not obtained but the readings of V_{RMS} and V were recorded at different radii. For the calculation of losses it was assumed that the wake form at radius ratios of 0.983 and 0.4 corresponded to a sine wave, at a radius ratio of 0.933 it corresponded to a saw tooth form and at all other radii it corresponded to well separated wakes. Losses were calculated with the respective equations and are plotted in Fig. 6.4. There is good agreement with the results.obtained with the pitot tube except near the outer radius. There seems to be error in the loss computation by the pitot tube as the loss coefficient near the tip is less than at radius ratio of 0.933. It could be due to a wrong estimation of the outlet angle.

From this it can be concluded that good estimation of losses can be made by hot wire anemometer readings even in the absence of photographs of

of the wakes by assuming suitable wake forms. However, photographs of the wake form will help in a better estimation of the wake form and thus losses.

CHAPTER VII

PERFORMANCE CALCULATIONS

7.1 Calculation of two dimensional outlet angles

In the case of impellers whose blade section at different radii are of standard form, i.e. circular arc, or N.A.C.A. 65 (A_{10}) series, and the solidity such that cascade data can be applied, then a two dimensional outlet angle can be predicted from the semi empirical rules as given by various workers and compiled by Horlock [21].

For the impeller under test, these methods could not be applied with sufficient accuracy as the shape of the profile did not correspond to the standard forms and the space-chord ratio at the outer radius was beyond the range covered by cascade data. Also it is known that at high space-chord ratio, the outlet angle does not remain constant with incidence angle. It was decided to use potential flow solutions to obtain the two dimensional outlet angles of the blade cascades at different radii in the impeller. Many methods of solution exist, most of them adapted for use in high speed digital computers. One such method is the computer programme written by Bailly, Houlton and Muregesan [58] and stored at the National Engineering Laboratory, East Kilbride, Glasgow. This programme was used to obtain the outlet flow angles shown in Fig. 7.1. The angle of incidence varies as the flow coefficient $\bar{\phi}$ varies and the results of Fig. 7.1 are given for three values of $\bar{\phi}$. It will be seen that there is considerable variation of outlet angle with incidence as the space shord ratio increases with increasing radius.

7.2 Performance calculations using two dimensional methods

In Chapter III performance prediction in the form of work-flow coef-

ficients was discussed. In Fig. 7.2 (a to f) performance curves are drawn for the impeller using various theories as discussed in Chapter III. These include

1. predictions based on the simple Euler theory,
2. predictions on the basis of constant deviation. The deviation angle was calculated from Constant's rule ($\delta = 0.26\theta \sqrt{\frac{s}{c}}$ where θ is the camber angle),
3. predictions on the basis of variable deviation by Eqn. 3.8 ($\psi = 2(1 - B) - 2 \phi_2 A_3$). This has been done only in a limited range as the variation of β_2 with β_1 was known for only a limited range,
4. predictions based on the slip theory as given by Numachi [40].

These results are plotted for radius ratios of 0.933, 0.8, 0.7, 0.6, 0.5 and 0.4. The results are plotted as $\psi - \phi_2$ curves for a particular radius ratio, where $\psi = \frac{\Delta H.2g}{U^2}$ based on the head rise and blade speed for that radius ratio and $\phi_2 = \frac{C_{x2}}{U}$, based on outlet axial velocity and blade speed for the same radius ratio.

7.3 Discussion of results

7.3.1 Constant deviation

From Fig. 7.1 it is clear that deviation is not constant at the high space chord ratio. However, for comparison, the head flow variation calculated on the basis of constant deviation from Constant's rule is plotted in Fig. 7.2 (a to f). Except at the smallest radius ratio they pass through the region

of the experimental results. The gradient of the predicted curve is higher than the gradient of the experimental results at the higher radius ratios. It should not be assumed that the prediction is fairly satisfactory because the predicted curve passes through the experimental results at some point. The predicted curve has to be multiplied by the efficiencies to make the comparison more valid which in most of the cases would make the predicted head coefficients too low.

7.3.2 Variable deviation

The performance from variable deviation was calculated from Eqn. 3.8 ($\psi = 2(1 - B) - 2 \phi_2 A_3$) and the values of A_3 and B from Eqn. 3.6, when F is constant and equal to B, using the computed two dimensional outlet angles given in Fig. 7.1. The slopes of the work flow coefficient curves are more in agreement with the experimental results than the predictions on the basis of constant deviation. Therefore when efficiency will be taken into consideration they will give better agreement.

7.3.3 Numachi Slip theory

It has been shown earlier, that the Numachi slip theory is not based on total head rise. Its use in predicting the total head rise is unjustified. In the discussion of ref. [39], Numachi used it to predict the head coefficients obtained experimentally by Hutton [39] and got apparently good agreement. Numachi's equation is plotted for comparison in Fig. 7.2 (a to f) from which it can be seen that the claim that it predicts the experimental head coefficients is unjustified.

7.4 Flow analysis by three dimensional theories

As the two dimensional theories failed to predict the performance it was necessary to investigate if simple invisid three dimensional analysis would be able to predict the performance satisfactorily. The radial equilibrium equation 3.33 as derived in Chapter III was used to analyse the flow. For this analysis it was assumed that the inlet velocity was uniform. The air outlet angles were obtained from Fig. 7.1. The equation was solved by a numerical iteration. At each stage of iteration the condition of continuity from Eqn. 3.30 in its integral form was satisfied between station (1) and (2)

i.e. $$\int_{r_h}^{r_t} C_{x1}\, r\, dr_1 = \int_{r_h}^{r_t} C_{x2}\, r_2\, dr_2 \qquad (7.1)$$

In Fig. 7.3, the outlet axial velocity as obtained by the analysis is plotted along with the experimental values at three flow coefficients. The agreement is good in the middle region, but only fair towards the hub and the tip. It was therefore necessary to consider the effect of secondary flows.

7.5 Change in outlet angle due to secondary flows

As mentioned in Chapter III due to non-uniform inlet velocity, secondary flows are developed and due to this there is a change in the outlet angle. Therefore it was necessary to calculate this change in the outlet angle.

7.5.1 Calculation of non-uniform inlet axial velocity

Due to boundary layer growth at the outer wall and at the hub, the inlet velocity is less in these regions than in the regions outside the boundary layer. However, the measured inlet velocity was not uniform even

outside the boundary layer regions. This is due to the proximity of the measuring station to the impeller. Upstream of this the flow will be uniform outside the boundary layers. The inlet flow was taken to be uniform outside the boundary layer regions which were taken to be 0.8 inches thick both at the hub and at the outer casing. The thickness was taken to remain constant at all flow rates.

In the boundary layer region at the hub and the tip, measured axial velocity was taken. Outside the boundary layer region uniform velocity was calculated by equating the flow in the three regions to the measured flow, i.e.

$$2\pi \int_{r_h}^{r_h + d} C_{x1}\, r\, dr + 2\pi \int_{r_h + d}^{r_t - d} C_{x1}\, r\, dr + 2\pi \int_{r_t - d}^{r_t} C_{x1}\, r\, dr = Q_v \qquad (7.2)$$

where d is the boundary layer thickness and Q_v is the flow measured by the venturimeter.

7.5.2 Calculation of the change in the outlet angle

Once the inlet velocity profile was decided, the relative streamwise secondary vorticity was calculated by Eqn. 3.36. The change in outlet angle was calculated by Eqn. 3.37. Eqn. 3.37 as given by Hawthorne [33] is applicable to rectangular passage. It has been used in the present study and by Horlock [32] for sector shape passage.

The outlet angle after taking into account the change due to secondary flows, the two dimensional angles as obtained by potential flow solution and the experimentally obtained angles uncorrected for axial velocity ratio are shown in Figs. 7.4 to 7.6. From these figures it can be seen that in the

tip region at all the three flow coefficients the agreement between the calculated and experimentally measured angles is good. In the tip region relative streamwise secondary vorticity is in the stream direction. In this region there is considerable underturning due to the component of relative streamwise vorticity from the wall boundary layer at inlet to the blades. On the inner wall near the hub, no agreement could be reached. Here also the direction of relative streamwise vorticity is in the stream direction. At $\bar{\phi}$ = 0.420 the two dimensional outlet angle is more than the inlet angle and due to this after correction, the theory has shown overturning while the experiment has shown underturning. At $\bar{\phi}$ = 0.358 and $\bar{\phi}$ = 0.259 also there is no agreement but the trend is the same between the experimental results and the theory. One of the reasons for this non agreement could be that the derivation of Eqn.3.36 depends on the assumption of zero radial velocity, but in actual practice at all coefficients, radial velocity was present and specially at $\bar{\phi}$ = 0.259 axial velocity at outlet was tending towards zero and became negative. The experimental values of outlet angles are uncorrected for axial velocity ratio. Better agreement will be obtained after the correction as the axial velocity ratio at the hub is much less than unity.

7.6 Calculation of the complete flow pattern

The following procedure for the calculation of the complete flow pattern was adopted.

(i) For this calculation inlet axial velocity was taken to be non uniform in the boundary layers and uniform outside the boundary layers. The same values of axial velocities as calculated in 7.5.1 were used.

(ii) In the boundary layer regions two dimensional angles corrected

for secondary flows as given in Figs. 7.4 to 7.6 were used, and outside the boundary layers two dimensional angles as given in Fig. 7.1 were used.

(iii) Radial equilibrium Eqn. 3.33 was used for the calculation of the outlet axial velocities at the three flow coefficients of $\bar{\phi}$ = 0.420, 0.358 and 0.259. The results are plotted in Figs. 7.7 to 7.9.

(iv) From this outlet axial velocity, the axial velocity ratio was obtained and the change in outlet angle due to the axial velocity ratio was obtained by the method given by Soundranayagam [43] and discussed in Chapter III.

(v) The flow through the impeller was again calculated by the radial equilibrium equation 3.33 using the outlet angles as obtained in stage (iv) above.

The outlet axial velocity profile thus calculated is shown in Figs. 7.7 to 7.9 for three flow coefficients. For comparison, the velocity obtained by experiment is also plotted. At $\bar{\phi}$ = 0.420, the agreement between the experimental values and the calculated values without taking into consideration the effect of axial velocity ratio is good except near the hub and the tip. When the effect of axial velocity ratio was taken into consideration, the agreement became better in the middle region, but it slightly deteriorated in the boundary layer regions both at the hub and the tip. This is due to the fact that when axial velocity was calculated according to step (iii) above, the outlet axial velocity was more than the inlet axial velocity near to hub and due to this axial velocity ratio was greater than unity. When the change in outlet angle was calculated due to the axial velocity ratio it was further reduced and became less than even the two dimensional angle, which is unrealistic and this affected the calculated result. At $\bar{\phi}$ = 0.358 the agreement between the experimental value and the calculated result without taking into consideration the effect of the axial velocity ratio is good except near the hub. When the

effect of axial velocity ratio was taken into consideration, the agreement improved near the hub and in the middle region, but it slightly deteriorated near the tip but as a whole there was improvement. At $\bar{\emptyset} = 0.259$ also the agreement was much improved when the effect of axial velocity ratio was taken into consideration.

7.7 Calculation of the head flow coefficient

From the calculated outlet axial velocity and with the knowledge of relative outlet angle, the tangential velocity $C_{\theta 2}$ was calculated at different radius ratios and for different flow coefficients. From this the value of the work coefficient was obtained. To obtain the head rise coefficient, the value of the work coefficient was multiplied by the blade element efficiency as plotted in Fig. 7.10. The values of head rise coefficients so obtained are plotted in Fig. 7.2 (a to f) for different radius ratios against $\emptyset_2$, based on outlet axial velocity.

The integrated mean head rise coefficient for the impeller was obtained in the same manner as described in Chapter V, by integrating from hub to tip. The results are plotted in Fig. 7.11.

From Fig. 7.2 (a to g) it can be seen that the agreement between the experimental values and calculated values of local head rise coefficient is good for all flows except at radius ratio of 0.933, it may be considered only fair at high flows.

For integrated mean head rise coefficient, the agreement for the majority of flow conditions can be considered good. At maximum flow, the agreement is only fair. The calculated value of mean head rise coefficient is about 20 percent higher than the experimental value at $\bar{\emptyset} = 0.420$.

CHAPTER VIII

GENERAL DISCUSSIONS AND CONCLUSIONS

8.1 General discussion

The agreement between the experimentally obtained and theoretically predicted head flow characteristics at different radii as well as that between the experimental and theoretical overall head characteristics can be considered good. However, wherever there is a difference it could be due to two factors, namely (a) between the experimentally obtained outlet angles and the angles used for flow analysis and (b) incorrect estimation of losses at any particular radius ratio for a particular flow coefficient.

For accurate analysis and performance prediction it is necessary that the experimentally obtained and theoretically predicted angles should be the same. When radial equilibrium solutions were obtained from Eqn. 3.33 using experimentally obtained angles, the agreement between theory and experiment was very good as can be seen in Fig. 8.1. From this figure it can also be seen that at $\bar{\phi} = 0.259$, the radial equilibrium equation is able to predict the separation of the flow from the hub as discussed in Chapter V.

To obtain the correct outlet angle, the effect of secondary flows and the effect of axial velocity ratio was taken into consideration. For the calculation of relative streamwise secondary vorticity, the boundary layer thickness at inlet and outlet of the impeller, at the hub and the tip and at all flow coefficients was assumed to be the same i.e. 0.8 inches which was the experimentally measured value at a single flow coefficient. It is known that the thickness of the boundary layer is not the same at the hub and at the tip and also it varies with the flow coefficient as pointed out by Gregory-Smith [59]. Also, wherever there is a large gradient of velocity it is difficult

to measure the actual thickness of the boundary layer specially with pitot cylinder type of probe. The representative value of 0.8 inches for the boundary layer thickness at hub and casing was taken as a constant for convenience. The variation of the boundary layer thickness from this value was not large and it was not expected that significant error would have resulted from this assumption. In this analysis emphasis was placed on allowing for the change in outlet angle through the tip and hub boundary layers only. Small changes in angles would also occur outside the boundary layer in the main stream region. In addition there is the trailing vorticity shed from the blades which have been neglected for reasons given in Chapter III. The disagreement between the experimental and calculated outlet angles can be attributed in part to the neglect of these factors. There is also the important point that the theoretical two dimensional angles were calculated on the basis of inviscid flow which does not allow for the profile boundary layer growth. The calculated two dimensional angles cannot be expected to be exact specially at the larger space to chord ratios.

The effect of axial velocity ratio on outlet angle was also taken into consideration. According to the method of Soundranayagam [43] which has been used here, both the inlet and outlet angles change with axial velocity but θ_m, the angle of attack remains constant. It means that graphs have to be plotted showing the variation of inlet and outlet angles for various axial velocity ratios, so that new outlet angle can be estimated which corresponds to a slightly different inlet angle. This is a very long procedure and therefore for this analysis the inlet angle was assumed to be constant, the change in outlet angle due to a slight change in the inlet angle being negligibly small. Also for calculating basic lift coefficient certain constants were obtained from

Mellor's [60] chart. Strictly speaking these constants are to be used for N.A.C.A. 65 series thickness distributions, while the same constants have been used in the present case where the thickness distribution was quite different from the N.A.C.A. 65 series. Mellor suggested that such use was allowable where outlet angle and lift coefficient calculations were involved, without detailed calculation of the pressure distribution along the aerofoil. This might have also affected the final value in the change in outlet angles due to axial velocity ratio.

However, with all these shortcomings when the combined effect of the angle variation was taken into consideration, the axial velocity profiles improved considerably in comparison with those calculated using the theoretical two dimensional angles. Furthermore, flow losses were not taken into account in using the radial equilibrium equation (Eq. 3.33) to calculate the outlet axial velocity distribution. It was not possible to make an accurate estimation of the losses beforehand from the usual loss correlations, though the losses were later measured as described in Chapter VI and taken into account for estimating the head rise. It was decided to neglect the losses in calculating the outlet axial velocity distribution. It seems that the flow calculation is not very sensitive to the neglect of the losses if the correct outlet angles are known as can be seen from Fig. 8.1.

The second factor in any non agreement between the experimental and predicted head flow relationship can be the incorrect estimation of the relative total head loss coefficient. This estimation was done experimentally. Estimation of loss by subtracting the measured outlet total head rise from the calculated ideal total head rise would inevitably lead by a circular argument to perfect agreement between the predicted head rise and the measured total

head. For the sake of comparison, the losses calculated from the hot wire measurements are plotted alongside the losses determined from the total pressure measurements as above in Figs. 6.3 and 6.4. The agreement in the middle region of the blade span is good with not too much of a divergence in the hub and tip regions. The most likely source of the non agreement is the assumption made about the shape of the wake wave form. Better agreement could be obtained by adjusting the numerical constants to correspond more to the actual shape of the wave forms observed on the oscilloscope in the hub and tip regions. Another source of non agreement could be the assumption made that there is at least one streamline which has not suffered an increase in entropy. It appears that this assumption was justified in the mid blade region, but introduced error in the hub and tip regions where the greatly increased losses make this assumption questionable.

This method has given reasonable values of blade efficiency at different flow coefficients as plotted in Fig. 7.10. It showsthat at $\bar{\phi} = 0.259$, the flow coefficient just before the stalling of the impeller, all the blade elements have high efficiency and variation is small. At $\bar{\phi} = 0.420$, the maximum efficiency of any blade element is only 76 percent and the efficiency varies from zero at radius ratio of 0.4 to zero at the tip. However, at all flow coefficients, the efficiency at the tip was zero, which may be due to error in the loss measurements.

As can be seen from the experimental results the behaviour of the impeller completely changed when the flow was reduced from $\bar{\phi} = 0.259$. The question arises whether it is possible to analyse the flow and predict the performance below $\bar{\phi} = 0.259$? For this it is necessary to know (1) the profile inlet velocity, (2) the correct outlet angle, and (3) the correct estimation

of losses. As known from experiment in this region, the fluid started flowing out at the outer radius at inlet, the inlet axial velocity varying from maximum to zero and then becoming negative. Thus to assume a uniform velocity throughout the annulus or a variation of velocity in the boundary layer region would be very far from real conditions. Two dimensional outlet angles could have been obtained from potential flow solutions, but due to reverse flow at the inner radius at outlet, there was no comperison between the actual angles and the two dimensional angles. Also for correct analysis it is necessary to take into consideration the effect of secondary flows. In this region it was not possible to do the same as the inlet velocity profile could not be estimated to any accuracy. For estimation of losses by hot wire the value of the outlet angle and axial velocity should be known. Due to reverse flow at the inner radius, the axial velocity is negative and thus an unrealistic value of loss would have been obtained. Therefore it seems that it is not possible to predict the performance in this region to any accuracy.

In Fig. 8.2 the effect of axial velocity ratio on outlet angle at different radii is plotted. It can be seen from the figure that for a particular axial velocity ratio, the change in outlet angle is the same at all radii. From this it seems that for this particular impeller the change in outlet angle due to axial velocity ratio is independent of stagger, space chord ratio and blage geometry and is only a function of the axial velocity ratio. However, before generalising this, further experiments will be necessary on different types of impellers.

8.2 Conclusions

From this study the following conclusions can be drawn.

1. The concept of a constant slip factor is unfounded. The slip

factor is not a constant just because the deviation may be constant. The Wislicenus formula for the slip factor is valid only when the deviation is zero, when in any case the slip factor would be unity by definition.

2. Following from the above the slip factor approach and the deviation approach to the two dimensional performance prediction have been completely reconciled and the two approaches are in no way contradictory. They are both essentially the same in that they each take into consideration the deviation of the flow from the blade.

3. The use of the Numachi slip equation to predict the total head rise has no justification as it has been shown to depend on the rise in static head.

4. For an impeller of small hub tip radius ratio and whose space chord ratio is more than 1.5 at the outer radius, it is possible to analyse the flow correctly with the help of the radial equilibrium equation, when the effect of secondary flows and axial velocity ratio are taken into consideration, together with two dimensional outlet angles calculated on the basis of inviscid potential flow.

5. Reasonable values of relative total pressure loss coefficient can be estimated by simple calculation from hot wire anemometer readings of wake R.M.S. voltage if suitable assumptions about the wake wave form can be.made.

6. The use of Betz's loading factor has been confirmed in connection with flow reversal at the tip.

7. Flow reversal at the hub when the mean flow coefficient is reduced can be successfully predicted by radial equilibrium equation.

8. It is possible to design a low pressure rise impeller of small hub tip radius ratios and moderately large space chord ratio at the tip in the

same way as conventional compressors are designed, provided correct estimation of the outlet angle can be made at different flow coefficients, as at large pitch chord ratio the outlet angle is not constant with the incidence angle.

REFERENCES

1. Wislicenus, G.F. "Fluid Mechanics of Turbomachinery", Vol. I, Dover Publications, Inc., New York, 1965, pages 142, 246.

2. Weinig, F.S. "Theory of two dimensional flow through cascades", Section B, Chapter I, High speed aerodynamics and jet propulsion, Volume X, Aerodynamics of turbines and compressors. Editor W.R. Hawthorne, Oxford University Press, London, 1964.

3. Cohen, H. and White, E.M. "The theoretical determinations of the three dimensional flow in an axial compressor, with special reference to constant reaction blading". A.R.C. Rep. 6842, 1943.

4. Bowen, J.T., Sabersky, R.H. and Rannie, W.D. "Investigation of axial flow compressors". Trans. A.S.M.E., Vol. 73, 1951, pp 1-15.

5. Thwaites, B., "Incompressible Aerodynamics, Fluid Motion Memoirs", Oxford University Press, 1960, pages 200, 490, 492.

6. Ruden, P. "Investigation of single stage axial flow fans". N.A.C.A., T.M., 1062, 1944.

7. Marble, F.E., "The flow of a perfect fluid through an axial turbomachine with prescribed blade loading". J. Aero. Sci., Vol. 15, 1948, pp 473-485

8. Bragg, S.L. and Hawthorne, W.R. "Some exact solutions of the flow through annular cascade actuator discs". J. Aero. Sci. Vol. 17, 1950, pp 243-249.

9. Horlock, J.H. "Some actuator disc theories for the flow of air through axial turbomachines". A.R.C., R and M., 3030, 1952.

10. Horlock, J.H. "Experimental and theoretical investigations of the flow of air through two single stage compressors". A.R.C., R and M, 3031, 1955.

11. Hawthorne, W.R. and Horlock, J.H. "Actuator disc theory of the incompressible flow in axial compressors". Proc. Inst. Mech. Engrs., London, Vol. 176, 1962, pp 789-814.

12. Horlock, J.H. and Deverson, E.C. "An experiment to determine the position of an equivalent actuator disc replacing a blade row of a turbomachine". A.R.C., C.P., 426, 1959.

13. Lewis, R.I. Discussion of Ref. (11).

14. Wu, C.H. "A general theory of three dimensional flow in subsonic and supersonic turbomachines of axial, radial, and mixed flow types". N.A.C.A., T.N., 2604, 1952.

15. Marsh, H. "The through flow analysis of axial flow compressors". University of Cambridge, Department of Engineering report, CUED/A - Turbo/TR11, 1970.

16. Marsh, H. "A digital computer program for the throughflow fluid mechanics in an arbitrary turbomachine using a matrix method" A.R.C., R. & M., 3509, 1968.

17. Khane, A. "Investigation of Axial flow fan and compressor rotors designed for three dimensional flow". N.A.C.A., T.N., 1652, 1948.

18. Mikhail, S. "Three dimensional flow in axial pumps and fans". Proc. Inst. Mech. Engrs., London, Vol. 172, 1958, pp 973-986.

19. Barna, P.S. "The off design behaviour of ducted axial flow fans". Auburn University, Auburn, Alabama, Engineering experiment Station, Bulletin 44, 1964.

20. Miller, M.J., Crouse, J.E., and Sandercock, D.M. "Summary of experimental investigation of three axial flow pump rotors tested in water". Trans. A.S.M.E. Ser. A. J. Eng. for Power, Vol. 89, 1967, pp 589-599.

21. Horlock, J.H. "Axial flow compressors" Butterworths Scientific Publications, London, 1958, pages 58, 61, 73, 159.

22. Miller, M.J., Sandercock, D.M. "Blade element performance of axial flow pump rotor with blade tip diffusion factor of 0.66". N.A.S.A., T.N. D - 3602, 1966.

23. Howell, A.R. "Fluid dynamics of axial compressors" Proc. Inst. Mech. Engrs.,, London, Vol. 153, 1945. pp 441-452.

24. Lieblein, S. "Loss and stall analysis of compressor cascade". Trans. A.S.M.E., Ser. D, J. Basic Eng., Vol. 81, 1959, pp 387-400.

25. Vavra, M.H. "Aero-Thermodynamics and Flow in turbomachines". John Wiley & Sons, Inc., New York, 1960. pp 378, 380.

26. Fujie, K. "A study of the flow through the rotors of an axial compressor". A proposition of formulae of drag coefficients. Bulletin of J.S.M.E., Vol. 5, 1962. pp 292-301.

27. Balje, O.E. "Axial cascade technology and application to flow path design". Part I, Axial cascade technology, Trans. A.S.M.E., Ser. A, J. of Eng. for Power, Vol. 90, 1968. pp 309-340.

28. Laxminarayana, B. and Horlock, J.H. "Review. Secondary flows and losses in cascades and axial flow turbomachines". Int J. Mech. Sci, Pergamon Press Ltd., Vol. 5, 1963, pp 287-307.

29. Squire, H.B. and Winter, K.G. "Secondary flow in a cascade of aerofoils in a non uniform stream". J. Aero. Sci., Vol. 18, 1951, pp 271-277.

30. Hawthorne, W.R. "Secondary circulation in fluid flow". Proc. Royal Society, Ser. A, Vol. 206, 1951. pp 374-387.

31. Smith, A.G. "On the generation of the streamwise component of vorticity for flows in rotating passages". Aero Quart., Vol. 8, 1957, pp 369-383.

32. Horlock, J.H. "Annulus wall boundary layers in axial flow compressor stage". Trans. A.S.M.E., Ser. D., J. of Basic Eng., Vol. 85, 1963, pp 55-65.

33. Hawthorne, W.R. "Some formulae for the calculation of secondary flow in cascades" A.R.C., 17519, 1955.

34. Pollard, D. and Horlock, J.H. "A theoretical investigation of the effect of change in axial velocity on the potential flow through a cascade of aerofoils". A.R.C., C.P., 619, 1962.

35. Mani, R. and Acosta, A.J. "Quasi two dimensional flows through cascade" Trans. A.S.M.E., Ser. A, J. of Eng. for Power, Vol. 90, 1968, pp 119-128.

36. Pollard, D. and Gostelow, J.P. "Some experiments at low speed on compressor cascades". Trans. A.S.M.E., J. for Power, Vol. 89, 1967, pp 427-436.

37. Shaalan, M.R.A. Discussion of Ref. (38).

38. Horlock, J.H. "Some recent research in turbomachinery". Proc. Inst. Mech. Engrs., London, Vol. 182, Part I, 1967-68, pp 571-594.

39. Hutton, S.P. "Three dimensional motion in axial flow impellers". Proc. Inst. Mech. Engrs. London, Vol. 170, 1956, pp 863-873, and 884-908.

40. Numachi, F. Discussion of Ref. [39]

41. Turner, R.C. "Notes on ducted fan design". A.R.C., C.P., 895, 1966.

42. Bannie, W.D. "The axial compressor stage" Section F, High speed aerodynamics and jet propulsion, Vol. X, Aerodynamics of turbines and compressors. Editor W.R. Hawthorne, Oxford University Press, London, 1964.

43. Soundranayagam, S. "The effect of axial velocity variation of aerofoil cascades". To be published.

44. Smith, S.L., Discussion of Ref. [32].

45. Winternitz, F.A.L. and Fischl, C.F. "A simplified integration technique for pipe flow measurements". Water Power, Vol. 9, 1957, pp 225-234.

46. Dean, R.C. Jr. "Aerodynamic measurements" Gas turbine laboratory, Mass. Inst. of Technol. The Mass Inst of Technol. Press, Cambridge, 1953.

47. Winternitz, F.A.L. "Probe measurements in three dimensional flow. A comparative survey of different types of instruments". Aircraft Engineering, Vol. 28, 1956, pp 273-278.

48. Bryer, D.W. and Walshe, D.E. "Pressure probes selected for three dimensional flow measurements". A.R.C., R and M., 3037, 1958.

49. Winternitz, F.A.L. and Ramsay, W.J. "A cantilever Pitot cylinder for three dimensional flow surveys". N.E.L., report 77, 1963.

50. Ushakov, K.A. and Brusilovski, V. "Investigation into the annular cascade of the rotating impeller of the axial fan". Promyshlennaya Aerodinamika Sb No. 10, 1958, pp 43-60, D.S.I.R., RTS 1080.

51. D.I.S.A. Constant temperature Anemometer Instruction manual, 1965, D.I.S.A. Elecktronik A/S Herler. Denmark.

52. Fessler, T.E. and Hartmann, M.J. "Preliminary Survey of Compressor rotor blade wakes and other flow phenomena with a hot wire anemometer". N.A.C.A., R.M.E 56A 13, 1956.

53. Barna, P.S. "Preliminary aerodynamic design considerations of axial flow fans" Auburn University, Auburn, Alabama, Engineering Experimentation Station, Bulletin 50, 1965.

54. Betz, A. "Introduction to the theory of flow machines", Pergamon Press London, 1966, pages 150, 265.

55. Carter, A.D.S. "The low speed performance of related aerofoils in cascades". A.R.C., C.P., 29, 1950.

56. Klapproth, J.F. Discussion of Ref. [24].

57. Schlichting, H. and Das, A. "Recent research on cascade flow problems". Trans. A.S.M.E., Ser. D, J. Basic Eng. Vol. 88, 1966, pp 221-220.

58. Railly, J.W., Houlton, J.M. and Murugesan, K. "A solution to the direct problem of flow in an arbitrary mixed flow turbomachine". N.E.L. report No. 413, 1969.

59. Gregory-Smith, D.G. "An investigation of annulus wall boundary layers in axial flow turbomachines". University of Cambridge, Department of Engineering report CUED/A/Turbo/TR4, 1969.

60. Mellor, G.L., "An analysis of axial compressor cascade aerodynamics". Part I and Part II. Trans. A.S.M.E., Ser. D. J. Basic Eng., Vol. 81, pp 362-386, Also Vol. 84, 1962, pp 619-621.

LIST OF ABBREVIATIONS

A.R.C.	Aeronautical Research Council of Great Britain.
A.S.M.E.	American Society of Mechanical Engineers.
C.P.	Current Paper.
N.A.C.A.	National Advisory Council for Aeronautics, U.S.A.
N.A.S.A.	National Aeronautics and Space Administration, U.S.A.
N.E.L.	National Engineering Laboratory, East Kilbride, Glasgow.
R. & M.	Report and Memoranda.
T.M.	Technical Memorandum.
J.S.M.E.	Japan Society of Mechanical Engineers.

APPENDIX "A"

Derivation of Numachi's slip equation

As shown in Chapter III

$$\Delta H = \frac{C_{\theta 2} \cdot U}{g} \qquad (3.1)$$

$$\psi = \frac{\frac{\Delta H}{U^2}}{2g} = \frac{2\, C_{\theta 2}}{U} = 2(1 - \phi_2 \tan \beta_2)$$

$$\psi = 2(1 - \phi_2 \tan \beta_2) \qquad (3.2)$$

$$\psi_E = 2(1 - \phi_2 \tan \beta_{2b}) \qquad (3.3)$$

$$\therefore C_H = \frac{\psi}{\psi_E}$$

Static head rise

$$\Delta h = \frac{1}{2g} [W_1^2 - W_2^2] \qquad (A.1)$$

$$= \frac{1}{2g} [C_{x1}^2 + U^2 - \{ C_{x2}^2 + (U - C_{\theta 2})^2 \}]$$

$$= \frac{1}{2g} [C_{x1}^2 + U^2 - \{ C_{x2}^2 + U^2 + C_{\theta 2}^2 - 2\, U\, C_{\theta 2} \}]$$

$$= \frac{1}{2g} (2\, U\, C_{\theta 2} - C_{\theta 2}^2), \text{ assuming } C_{x1} = C_{x2}$$

$$= \frac{U\, C_{\theta 2}}{g} - \frac{C_{\theta 2}^2}{2g}$$

$$= \frac{1}{g} [U - \frac{C_{\theta 2}}{2}]\ C_{\theta 2}$$

or

$$\frac{\Delta h}{\frac{U^2}{2g}} = \psi_{ES} = 2[1 - \frac{C_{\theta 2}}{2U}] \frac{C_{\theta 2}}{U} \qquad (A.2)$$

But $C_{\theta 2} = U - C_{x2} \tan \beta_{2b}$

$$\frac{C_{\theta 2}}{U} = 1 - \phi_2 \tan \beta_{2b} \qquad (A.3)$$

$$\therefore \psi_{ES} = 2[1 - \tfrac{1}{2}(1 - \phi_2 \tan \beta_{2b})] (1 - \phi_2 \tan \beta_{2b})$$

But due to slip actual $C_{\theta 2} = C_H$ (ideal $C_{\theta 2}$)

$$\therefore \psi_S = 2.C_H[1 - \frac{C_H}{2} (1 - \phi_2 \tan \beta_{2b})] [1 - \phi_2 \tan \beta_{2b}] \qquad (A.4)$$

Also from Eqn. A.1

$$\psi_{ES} = \frac{\Delta h}{\frac{U^2}{2g}} = [\frac{W_1^2 - W_2^2}{U^2}] = \frac{C_{x1}^2 + U^2 - C_{x2}^2 + C_{x2}^2 \tan^2 \beta_{2b}}{U^2}$$

For two dimensional flow $C_{x1} = C_{x2}$

$$\therefore \psi_{ES} = 1 - \phi_2^2 \tan^2 \beta_{2b}$$

$$\therefore \phi_2 \tan \beta_{2b} = \sqrt{1 - \psi_{ES}} \qquad (A.5)$$

Substituting for $\phi_2 \tan \beta_{2b}$ in Eqn. A.4

$$\psi_S = 2 C_H [1 - \frac{C_H}{2} (1 - \sqrt{1 - \psi_{ES}})] [1 - \sqrt{1 - \psi_{ES}}] \qquad (A.8)$$

APPENDIX "B"

Total head rise efficiency for a blade element

Work output = Efficiency x work input.

$$\text{Blade Element efficiency} = \frac{\text{work output}}{\text{work input}}$$

$$= \frac{\text{work input - losses}}{\text{work input}}$$

$$= \frac{\dfrac{C_{\theta 2}\, U}{g} - \bar{w}}{\dfrac{C_{\theta 2}\, U}{g}}$$

$$\eta_H = 1 - \frac{g \times \bar{w}}{C_{\theta 2} \cdot U} \qquad \text{(B.1)}$$

where $\bar{w}$ is the mean loss of total head and η_H total head rise efficiency for a blade element.

APPENDIX "C"

Calculation of the effect of axial velocity variation

C.1 Velocities induced in the cascade due to axial velocity change

A blade cascade is a device to deflect a uniform inlet flow to give another uniform flow at exit. In Fig. C.1, if a vortex sheet of constant circulation Γ_1 is superimposed on a uniform mainstream of velocity W_m, induced velocities of strength $\frac{\Gamma_1}{2}$ are set up parallel to the sheet upstream and downstream. These have the effect of changing W_m to uniform velocities W_1 upstream and W_2 downstream. If the vortex sheet is separated into individual vortices of strength $\Gamma = \Gamma_1 s$ where s is the space between them and the latter are replaced by aerofoils with circulation Γ, then the overall strength of the vortex sheet is unaltered and is now simulated by a blade cascade, with a vector mean velocity W_m. The lift of each aerofoil can be expressed by

$$L = \rho W_m \Gamma = C_L \cdot \tfrac{1}{2} \rho W_m^2 c$$

$$\therefore \Gamma = \frac{W_m c C_L}{2} \qquad (C.1)$$

Therefore the induced velocities $\frac{\Gamma}{2s}$ of Fig. C.1 are equal to $\frac{W_m c C_L}{4s}$. If the complete velocity triangles for inlet and outlet flow are drawn as shown in Fig. C.1, it is seen that the flow angles may be expressed as

$$\tan \beta_1 = \frac{W_m \sin \beta_m + \frac{W_m c C_L}{4s}}{W_m \cos \beta_m}$$

$$= \tan \beta_m + \frac{c C_L}{4s \cos \beta_m} \qquad (C.2)$$

and
$$\tan \beta_2 = \tan \beta_m - \frac{c\, C_L}{4s \cos \beta_m} \qquad (C.3)$$

C.2 The change in circulation due to change in axial velocity

C.2.1 The effect of camber on the lift coefficient

The camber line of an aerofoil blade is given as a distribution of ordinates y_c for varying values of x, the distance along the chord.

$$\frac{y_c}{c} = y\left(\frac{x}{c}\right) \qquad (C.4)$$

The blade camber is meaningfully described by

$$C_b \equiv 2 \int_0^{\pi} \frac{dy_c}{dx} \cos \theta \, d\theta \qquad (C.5)$$

where θ is given by $\frac{x}{c} = \frac{1}{2}(1 - \cos \theta)$

The camber line itself can be written

$$\frac{y_c}{c} = C_b \, f_c \left(\frac{x}{c}\right) \qquad (C.6)$$

where f_c is some function of $\frac{x}{c}$. C_b will be recognised as the ideal lift coefficient for the isolated aerofoil as given by the Glauert thin aerofoil theory and is a known constant once the shape of the camber line is specified. For symmetrically cambered isolated aerofoils, the lift coefficient varies linearly with C_b. A statement of this nature cannot be made beforehand for cascade aerofoils. Soundranayagam [43] has shown that for any given angle of attack, the variation of C_L with C_b is linear to a very good approximation. He has further suggested that this linear relationship holds for all aerofoil

cascades even if they do not have symmetrical camber lines. Therefore the lift coefficient of a cascade blade at a given angle of attack can be written as

$$C_L = C_L \text{ of zero cambered blade} + C_L \text{ due to camber} \qquad (C.7)$$

The second term on the right hand side of the Eqn. C.7 is a linear function of C_b. The first term on the right hand side of Eqn. C.7 would be given by the well known Weinig flat plate cascade results [2] with a modification for the blade thickness effect and is called C_L basic

$$C_L = C_L \text{ basic} + C_L \text{ due to camber} \qquad (C.8)$$

C.2.2 The tangency condition

In a two dimensional cascade, the blades are replaceable by infinitely long vortex and source sink lines lying parallel to the blade span and distributed along the chord. This array of singularities, when superimposed on a uniform stream W_m, gives the resultant two dimensional flow. Let u and v be the induced velocities parallel and normal to the chord, at a point on the central aerofoil, due to the entire singularity distribution. The slope of the camber line at a point on the aerofoil must lie equal to the ratio of the total vertical velocity to the total horizontal velocity at that point.

$$\therefore \frac{W_m \sin \theta_m + v}{W_m \cos \theta_m + u} = \frac{dy_c}{dx} \qquad (C.9)$$

The induced velocities v' and u' associated with the axial velocity change are due to the smear of sources (and/or sinks) on the side walls which would lie normal to the span. So with axial velocity change we have a uniform stream W_m, a system of infinitely long vortex and source sink lines lying

along the span and located at the blade positions periodically in the pitch direction, and a system of groups of infinitely long line sources normal to the span lying along the cascade axis and periodic in the span-wise direction one span length apart. The tangency condition at centre span can now be written

$$\frac{W_m \sin \theta_m + v + v'}{W_m \cos \theta_m + u + u'} = \frac{dy_c}{dx} \qquad (C.10)$$

i.e.

$$\frac{W_m \sin \theta_m + v}{W_m \cos \theta_m + u} = \frac{dy_c}{dx}\left(1 + \frac{u'}{W_m \cos \theta_m + u}\right) - \frac{v'}{W_m \cos \theta_m + u}$$

For small blade camber and small velocity change, the product $\left(\frac{dy_c}{dx}\right)$ $[u'/(W_m \cos \theta_m + u)]$ can be neglected. The quantity u in the denominator of the last term is also dropped to enable a manageable solution to be obtained. The tangency condition now becomes

$$\frac{W_m \sin \theta_m + v}{W_m \cos \theta_m + u} = \frac{dy_c}{dx} - \frac{v'}{W_m \cos \theta_m} \qquad (C.11)$$

which is the same as for two dimensional flow with a reduced camber line slope. The effective camber line is say $Y_c = Y(x)$ where

$$\frac{dY_c}{dx} = \frac{dY_c}{dx} - \frac{v'}{W_m \cos \theta_m} \qquad (C.12)$$

without axial velocity change

$$\frac{W_m \sin \theta_m + v}{W_m \cos \theta_m + u} = \frac{dy_c}{dx} = C_b f_c'\left(\frac{x}{c}\right) \qquad (C.13)$$

where the prime stands for differentiation with respect to $\left(\frac{x}{c}\right)$

With axial velocity change

$$\frac{W_m \sin \theta_m + v}{W_m \cos \theta_m + u} = \frac{dY_c}{dx} = C_b^* F_c' \left(\frac{x}{c}\right)$$

where $$C_b^* = 2 \int_0^{\pi} \left(\frac{dy_c}{dx} - \frac{v'}{W_m \cos \theta_m}\right) \cos \theta \, d\theta$$

$$= 2 \int_0^{\pi} \frac{dy_c}{dx} \cos \theta \, d\theta - 2 \int_0^{\pi} \frac{v'}{W_m \cos \theta_m} \cos \theta \, d\theta$$

$$= C_b - C_{b1} \qquad (C.14)$$

where C_{b1} is the modification to C_b due to axial velocity change. The effective camber is C_b^*.

C.2.3 The calculation of C_{b1} and C_b

C_{b1} can be calculated once the variation of v' from the blade leading edge to the trailing edge is known. This will depend on the way in which the axial velocity varies, which depends in turn on the way in which passage dimensions vary. It may be assumed that the axial velocity changes uniformly from the cascade edge to the trailing edge.

The induced velocity w_o can be written

$$w_o = W_m \cos(\lambda + \theta_m)\left(\frac{k - 1}{k + 1}\right) \qquad (C.15)$$

where λ is the stagger angle and k is the axial velocity ratio $\left(\frac{C_{x2}}{C_{x1}}\right)$. The induced velocity v' normal to the chord varies linearly as in the bottom of Fig. 3.6

$$C_{b1} = 2 \int_0^{\pi} \frac{v'}{W_m \cos \theta_m} \cdot \cos \theta \, d\theta$$

$$= 2\int_0^{\pi} \frac{w_o \sin\lambda - 2 w_o \sin\lambda \frac{x}{c}}{W_m \cos\theta_m} \cos\theta \, d\theta$$

$$= \frac{2 w_o \sin}{W_m \cos\theta_m} \int_0^{\pi} (1 - \frac{2x}{c}) \cos\theta \, d\theta$$

$$= \frac{2 \sin\lambda \; W_m \cos(\lambda + \theta_m)(\frac{k-1}{k+1})}{W_m \cos\theta_m} \int_0^{\pi} (1 - 2\frac{x}{c}) \cos\theta \, d\theta$$

$$= \frac{2 \sin\lambda \cos(\lambda + \theta_m)(\frac{k-1}{k+1})}{\cos\theta_m} \int_0^{\pi} \cos^2\theta \, d\theta$$

where $\frac{x}{c}$ has been written in terms of θ.

This gives

$$C_{b1} = \frac{\pi \sin\lambda \cos(\lambda + \theta_m)}{\cos\theta_m} [\frac{k-1}{k+1}] \qquad (C.16)$$

which is a function of the stagger, angle of attack and axial velocity ratio. It is independent of the shape of the blade. For a given set of cascade parameters and axial velocity ratio, the two dimensional camber C_b can now be modified to give the effective camber C_b^*. C_{b1} changes sign depending on whether k is greater than or less than unity.

$$C_b^* = C_b - |C_{b1}| \qquad k > 1$$

$$C_b^* = C_b + |C_{b1}| \qquad k < 1$$

C.2.4 Calculation of the effective circulation

For a given cascade of arbitrarily cambered aerofoils, the two

dimensional circulation is proportional to the length BC of Fig. 3.7 and the reduced or effective circulation is proportional to DE. The ratio of the effective circulation to the two dimensional circulation will thus be equal to the ratio of the effective lift coefficient to the two dimensional lift coefficient, the effective lift coefficient is given by

$$C_L' = C_L^{*} = 2 \frac{s}{c} \frac{2}{k+1} \left[\tan \beta_1' - k \tan \beta_2'\right] \cos \beta_m \qquad (C.17)$$

The first step is to determine the basic lift coefficient of a non cambered blade ($C_b = 0$) of the same thickness ratio placed in cascade at the appropriate stagger and space chord ratio. Referring to the paper by Mellor [60], it is possible to write the lift coefficient of such a non cambered blade as

$$C_L \text{ basic} = 2 \pi A_\alpha \sin \theta_m + 2 \pi A_t \frac{t}{c} \qquad (C.18)$$

where $\frac{t}{c}$ is the thickness ratio.

A_a is the same as the Weinig flat plate cascade influence coefficient. A_t is the coefficient that allows for blade thickness effects. The effect of distributing finite thickness on a thin camber line is to deflect the flow away from the axial direction. Mellor [60] has computed a chart giving A_t as a function of stagger and space chord ratio for the thickness distribution of N.A.C.A. 65 series compressor blades. The same value of A_t applies with good accuracy for the thickness distribution of all aerofoil shapes for the purpose of calculating the overall lift coefficient. The detailed shape of the thickness distribution is important only for detailed surface velocity calculations.

Knowing the geometry of the blade camber,line, the parameter C_b can be calculated. C_{b1} can be found from Eqn. C.16 for a given axial velocity

ratio. Hence the effective camber C_b^* from Eqn. C.14.

Assuming that the two dimensional lift coefficient is known, Eqn. C.8 gives

$$C_L \text{ due to camber (2d)} = C_L - C_L \text{ basic}$$

As the effective camber changes due to axial velocity change, C_L basic remains the same but the C_L due to camber changes linearly with C_b.

$$\therefore \text{ effective } C_L = C_L^* = C_L \text{ basic} + C_L \text{ due to camber (2d)} \times \frac{C_b^*}{C_b}$$

$$= C_L \text{ basic} + C_L \text{ due to camber} \qquad (C.19)$$

C.3 Method of application

C.3.1 Calculation of experimental lift coefficient

The usual formula for calculating the lift coefficient is

$$C_L = 2 \frac{s}{c} (\tan \beta_1 - \tan \beta_2) \cos \beta_m \qquad (C.20)$$

In an actual experimental flow with acceleration of axial velocity use of this formula would give

$$C_L' = 2 \frac{s}{c} (\tan \beta_1' - \tan \beta_2') \cos [\text{arc tan } \tfrac{1}{2}(\tan \beta_1' - \tan \beta_2'] \qquad (C.21)$$

which would yield a wrong estimate of the actual experimental lift as the formula assumes the circulation to be proportional to GF of Fig. 3.7 instead of the actual experimental value of DE. Cos β_m' would, however, be a little less than cos β_m as β_m' based on β_1' and β_2' as above would be greater than the real vector mean angle.

The change in axial velocity is described by the axial velocity ratio k where

$$k = \frac{\text{outlet axial velocity}}{\text{inlet axial velocity}}$$

$$= \frac{W_2' \cos \beta_2'}{W_1' \cos \beta_1'}$$

$$= \frac{W_2 \cos \beta_2 + {}^{w}_{o}}{W_1 \cos \beta_1 - {}^{w}_{o}} \qquad (C.22)$$

Remembering $W_1 \cos \beta_1 = W_2 \cos \beta_2 = W_m \cos \beta_m$, this gives

$${}^{w}_{o} = W_m \cos \beta_m \left(\frac{k - 1}{k + 1}\right) \qquad (C.23)$$

The angles β_1^* and β_2^* are now given by

$$\tan \beta_1^* = \frac{2}{k + 1} \tan \beta_1' \qquad (C.24)$$

$$\tan \beta_2^* = \frac{2}{k + 1} \tan \beta_2' \qquad (C.25)$$

and the true vector mean angle β_m is given by

$$\tan \beta_m = \frac{1}{k + 1} [\tan \beta_1' + k \tan \beta_2'] \qquad (C.26)$$

The experimental lift coefficient due to the experimental circulation DE Fig. 3.7 is given by

$$C_L' = C_L^* = 2 \frac{s}{c} \cdot \frac{2}{k + 1} [\tan \beta_1' - k \tan \beta_2'] \cos \beta_m$$ as given previously by Eqn. C.17. β_m being given by Eqn. C.26.

C.3.2 Calculation of angle change

There are two possible cases to be evaluated. The first is given known initial two dimensional conditions to determine what the corresponding conditions would be if there was a change in the axial velocity. The

other starts with a flow of known axial velocity ratio and calculates what the corresponding two dimensional flow would be. In the first case vector mean angle is calculated and from that θ_m, the angle of attack and C_L basic is determined from Eqn. C.19 and the effective lift coefficient C_L^* by Eqn. C.17 for the given value of k.

β_1^* and β_2^* are calculated from

$$\tan \beta_1^* = \tan \beta_m + \frac{c\, C_L^*}{4s \cos \beta_m} \qquad (C.27)$$

$$\tan \beta_2^* = \tan \beta_m - \frac{c\, C_L^*}{4s \cos \beta_m} \qquad (C.28)$$

which corresponds to Eqns. C.2 and C.3.

The actual flow angles are now calculated from Eqns. C.24 and C.25. The two flows do not have the same inlet angle but the same angle of attack θ_m of the unchanging vector mean velocity.

In the second case when a flow with axial velocity change is known, β_m is calculated using Eqn. C.26 and the experimental lift coefficient C_L' ($= C_L^*$) calculated using Eqn. C.17. C_L basic is determined and C_{b1} calculated, and the two dimensional lift coefficient is given by

$$C_L = C_L \text{ basic} + (C_L^* - C_L \text{ basic}) \frac{C_b}{C_b - C_{b1}}$$

The two dimensional flow angles β_1 and β_2 are calculated from Eqns. C.2 and C.3. Again the angle of attack θ_m has remained unchanged.

APPENDIX "D" - Details of the impeller

TABLE D.1

Hub-Tip radius ratio	0.33	0.4	0.5	0.6	0.7	0.8	0.933	1.00
Radius (inches)	4	4.8	6.00	7.2	8.4	9.6	11.2	12.0
Chord length (inches)	3.180	4.250	4.328	4.125	3.969	3.766	3.531	3.422
Space-Chord ratio	0.877	0.77	1.00	1.22	1.630	1.763	2.19	2.45
Stagger angle* (degrees)	50.45	47.55	48.99	50.45	52.10	54.10	56.99	58.00
Camber angle (degrees)	-	26	40	35	35	39	39	38
Blade inlet angle (degrees)	-	65.05	77.49	73.45	77.10	83.10	85.99	86.50
Blade outlet angle (degrees)	-	39.05	37.49	38.45	42.10	44.10	46.99	48.50
Design lift coeff.	-	0.2880	0.4105	0.3969	0.3540	0.3330	0.3607	0.3133
No lift angle (degrees)	-	-2.9	-2.9	-3.4	-3.3	-3.33	-3.25	-3.68
Design angle of attack** (degrees)	-	0	0.25	0	0.1	0	0.5	0.08
Maximum thickness (% chord)	-	17.08	12.13	11.51	10.95	10.22	9.24	8.59

The mean tip clearance was 0.9 percent of the blade height.

* Angles measured from axial direction as explained in Fig. D.1

** The so called optimum angle of attack for an isolated blade of this shape to give non infinite velocities at the leading edge when thickness effects are neglected.

From Glauert's thin aerofoil theory

$$\text{Design lift coefficient} = 2 \int_0^{\pi} \frac{dy}{dx} \cos\theta \, d\theta \qquad \text{(D.1)}$$

$$\text{No lift angle} = \frac{1}{\pi} \int_0^{\pi} \frac{dy}{dx} (1 - \cos\theta) \, d\theta \qquad \text{(D.2)}$$

$$\text{Design angle of attack} = \frac{1}{\pi} \int_0^{\pi} \frac{dy}{dx} \, d\theta \qquad \text{(D.3)}$$

Measurements at 18 points on the camber line were taken and the slope of the camber line $\frac{dy}{dx}$ was obtained at each point.

The above equations were solved by graphical integration for each camber line.

APPENDIX "E"

EVALUATION OF RESULTS

After obtaining pitch angle β_p, total pressure P_o and static pressure p from the calibration chart of Fig. 4.6 and measuring yaw angle α from the divided traverse head, the other results were evaluated as follows.

(1) **Velocities**

$$P_o = p + \tfrac{1}{2}\rho C^2 \qquad (E.1)$$

$$\therefore \quad C = \sqrt{\frac{2(P_o - p)}{\rho}} = \sqrt{\frac{2\,p_v}{\rho}}$$

where p_v = dynamic pressure

$$p_v = \gamma_w h_w$$

$$\therefore \quad C = \sqrt{\frac{2\gamma_w h_w}{\rho}}$$

$$C = \sqrt{2g.\frac{\gamma_w h_w}{\gamma_a}} \qquad (E.2)$$

where γ_w = specific weight of water

γ_a = specific weight of air

h_w = dynamic head in ft. of water.

ρ = density of air

From this, other velocities were calculated as follows:-

Axial velocity, $C_x = C.\cos\beta_p \cos\alpha$ (E.3)

Tangential velocity, $C_\theta = C.\cos\beta_p \sin\alpha$ (E.4)

Radial velocity, $C_r = C.\sin\beta_p \sin\alpha$ (E.5)

Mean inlet axial velocity, $\overline{C_{x1}} = \dfrac{Q_v}{60 \cdot (r_t^2 - r_h^2).\pi}$ (E.6)

(2) Blade speed

$$\text{At any radius, } U = \frac{2\pi N r}{60} \qquad \text{(E.7)}$$

$$\text{At tip, } \qquad U_t = \frac{2\pi N r_t}{60} \qquad \text{(E.8)}$$

(3) Flow coefficients

$$\text{Flow coefficient based on inlet axial velocity, } \phi_1 = \frac{C_{x1}}{U} \qquad \text{(E.9)}$$

$$\text{Flow coefficient based on outlet axial velocity, } \phi_2 = \frac{C_{x2}}{U} \qquad \text{(E.10)}$$

$$\text{Mean flow coefficient, } \phi = \frac{\overline{C_{x1}}}{U_t} \qquad \text{(E.11)}$$

(4) Head rise coefficient

$$\text{Head rise of a blade element, } \Delta H = H_2 - H_1 \qquad \text{(E.12)}$$

$$\text{Head rise coefficient of a blade element, } \psi = \frac{\Delta H . 2g}{U^2} \qquad \text{(E.13)}$$

$$\text{Weighted mean head rise, } \overline{\Delta H} = \frac{2\pi}{Q_v} \int_{r_h}^{r_t} r(H_2 C_{x2} - H_1 C_{x1})\, dr \qquad \text{(E.14)}$$

$$\text{Mean head rise coefficient, } \overline{\psi} = \frac{\overline{\Delta H} . 2g}{U_t^2} \qquad \text{(E.15)}$$

(5) Loss of total head from pitot tube

$$\text{Blade element ideal head rise, } \Delta H_i = \frac{U . C_{\theta 2}}{g} \qquad \text{(E.16)}$$

where $C_{\theta 2}$ calculated from experimental results and $C_{\theta 1}$ assume to be zero.

Actual head rise obtained by pitot tube = ΔH

$$\therefore \text{ Mean relative total head loss, } \overline{\omega} = \Delta H_i - \Delta H \qquad \text{(E.17)}$$

$$\therefore \text{ Relative mean total head loss coefficient } = \frac{\overline{\omega} . 2g}{W_1^2} \qquad \text{(E.18)}$$

(6) Torque calculation

Aerodynamic torque

$$T_a = 2\pi \int_{r_h}^{r_t} \rho \cdot C_{\theta 2} \cdot C_{x2} \cdot r^2 \cdot dr \qquad \text{(E.19)}$$

Mechanical torque (net)

T_m = [(Dead load on dynamometer + load calculated by transducer reading) x torque arm] - [Bearing friction torque] (E.20)

(7) Horse power

$$\text{Shaft horse power (S.h.p.)} = \frac{2\pi . N . T_m}{33,000} \qquad \text{(E.21)}$$

$$\text{Output Air horse power (A.h.p.)} = \frac{\gamma_a Q_v \overline{\Delta H}}{33,000} \qquad \text{(E.22)}$$

(8) Efficiency

$$\text{Overall mean efficiency, } \bar{\eta} = \frac{\text{A.h.p.}}{\text{S.h.p.}} \times 100 \qquad \text{(E.23)}$$

APPENDIX "F"

CONVERSION OF EXPERIMENTAL ANGLES FOR A.V.R. OF UNITY

Figs. F.1 and F.2 show the experimentally obtained relative inlet and outlet angles at different radius ratios converted to unity axial velocity ratio. For comparison, two dimensional angles have been plotted. It can be seen that after the correction for axial velocity ratio, the corrected angles can be joined by a smooth curve in the same manner as the two dimensional angles. Wherever there was large variation of axial velocity ratio from unity, the correction is also puite high as can be seen for radius ratio of 0.4. Therefore, whenever the two dimensional angles are to be compared with experimentally obtained angles, the experimentally obtained angles should be corrected for axial velocity ratio effect.

APPENDIX "G"

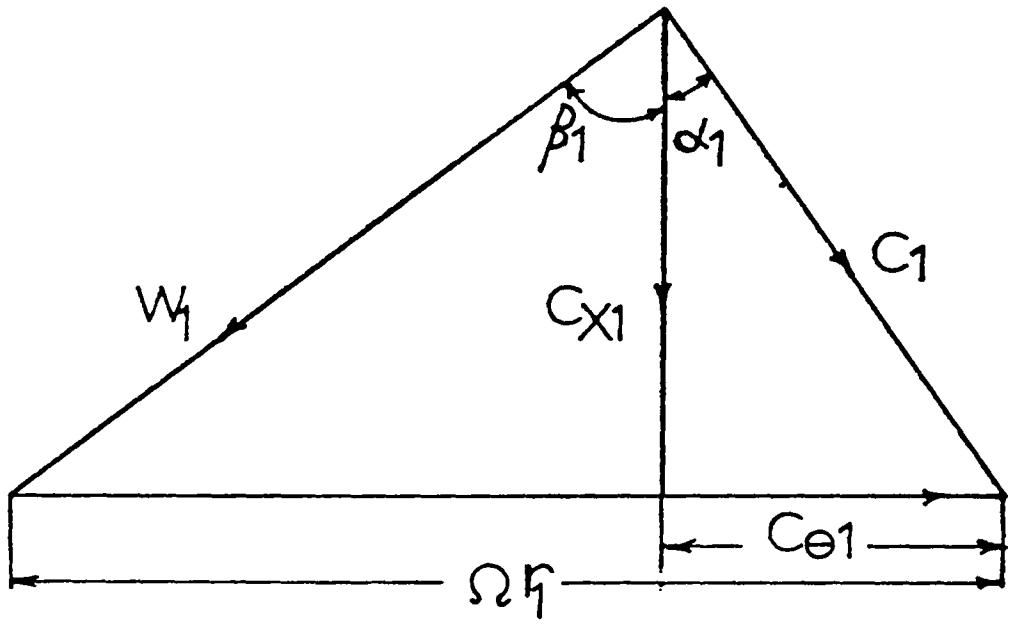

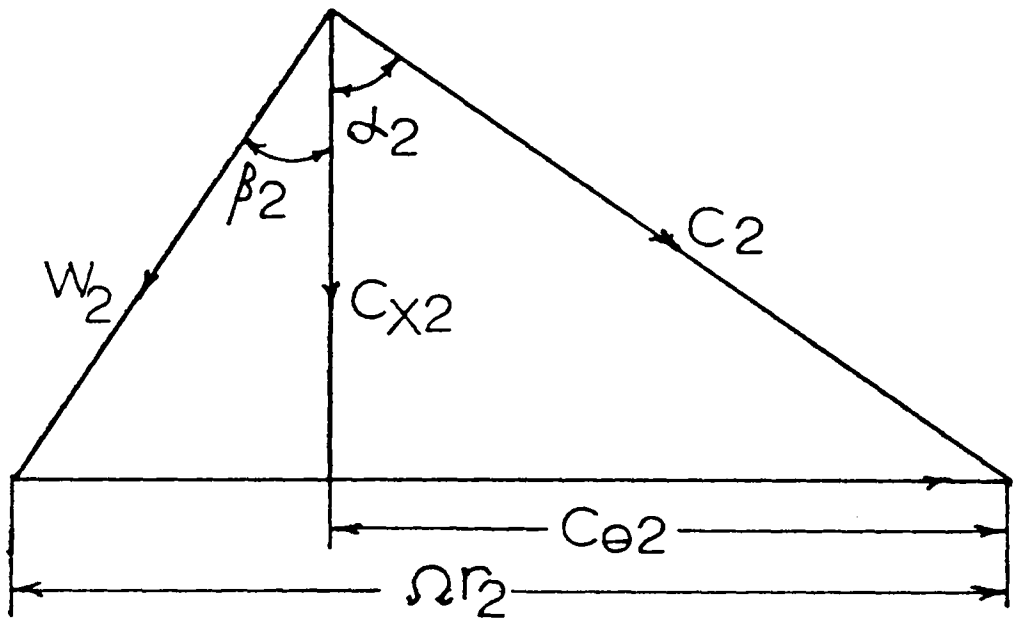

VELOCITY TRIANGLES FOR AN IMPELLER

Fig. 2.1

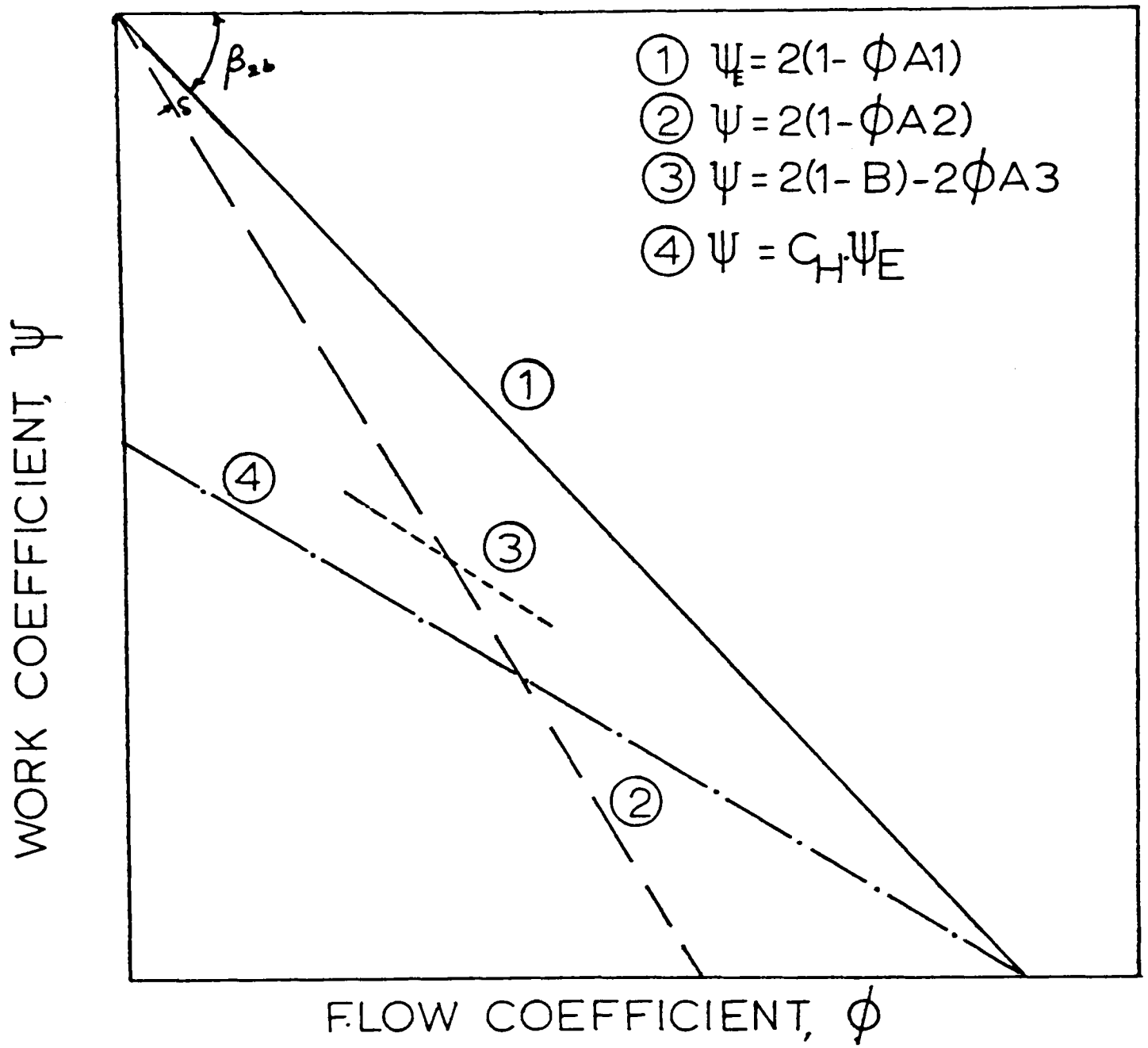
β_{2b}
① $\psi_E = 2(1-\phi A1)$
② $\psi = 2(1-\phi A2)$
③ $\psi = 2(1-B)-2\phi A3$
④ $\psi = C_H \cdot \psi_E$
①
④
③
②
WORK COEFFICIENT, ψ
FLOW COEFFICIENT, ϕ

Fig. 3.1

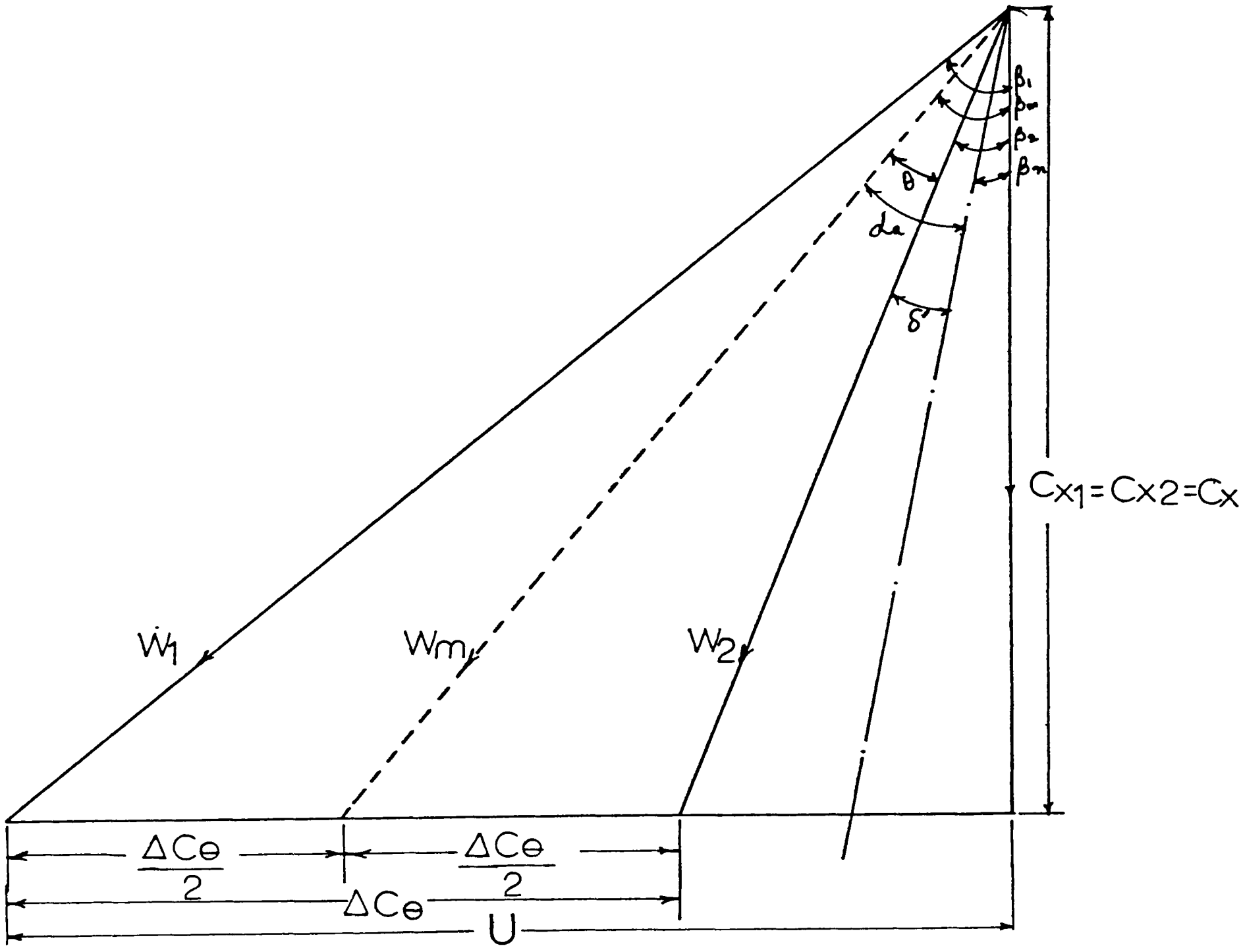

Fig. 3.2

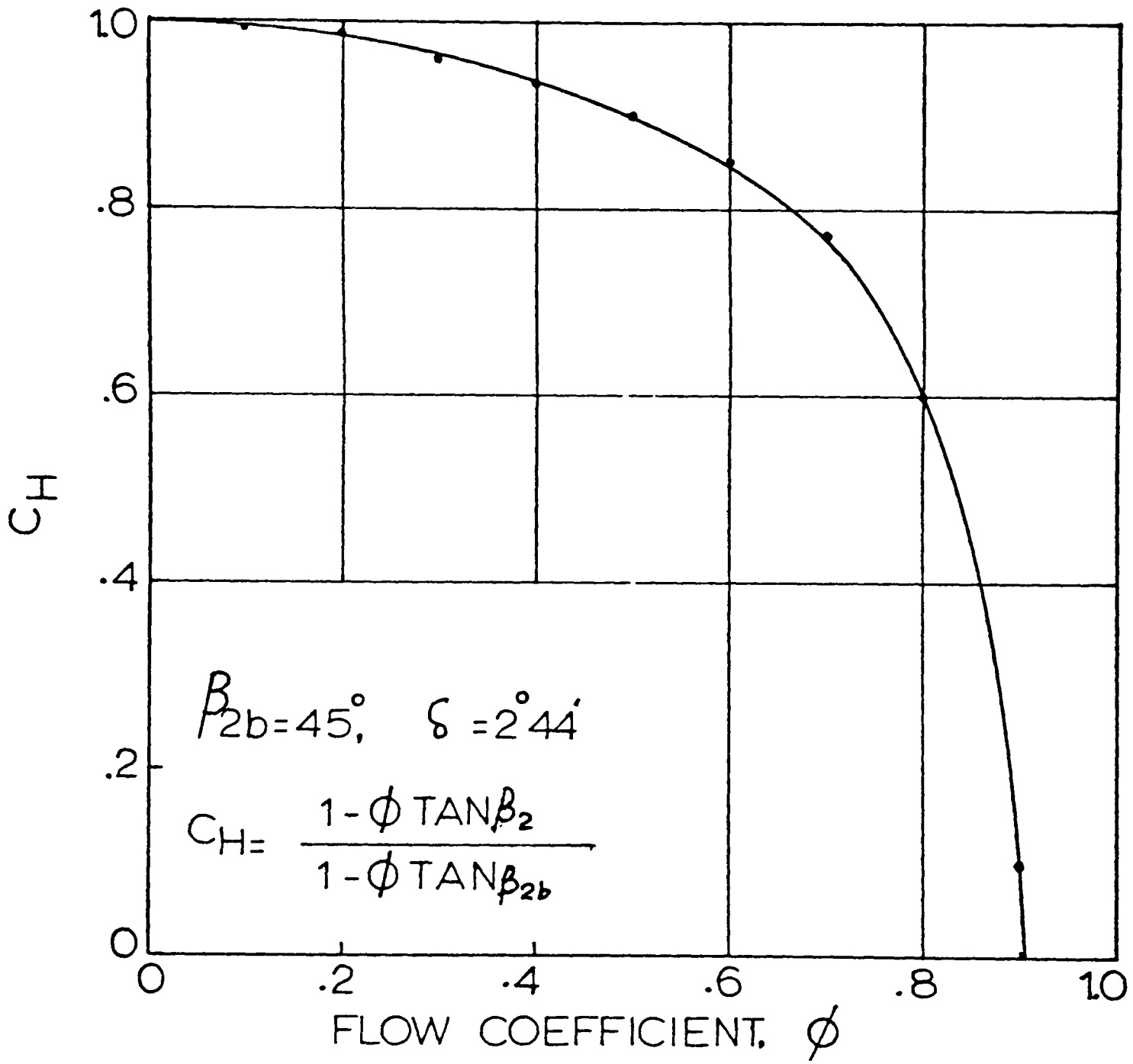

VARIABLE SLIP FACTOR

Fig. 3.3

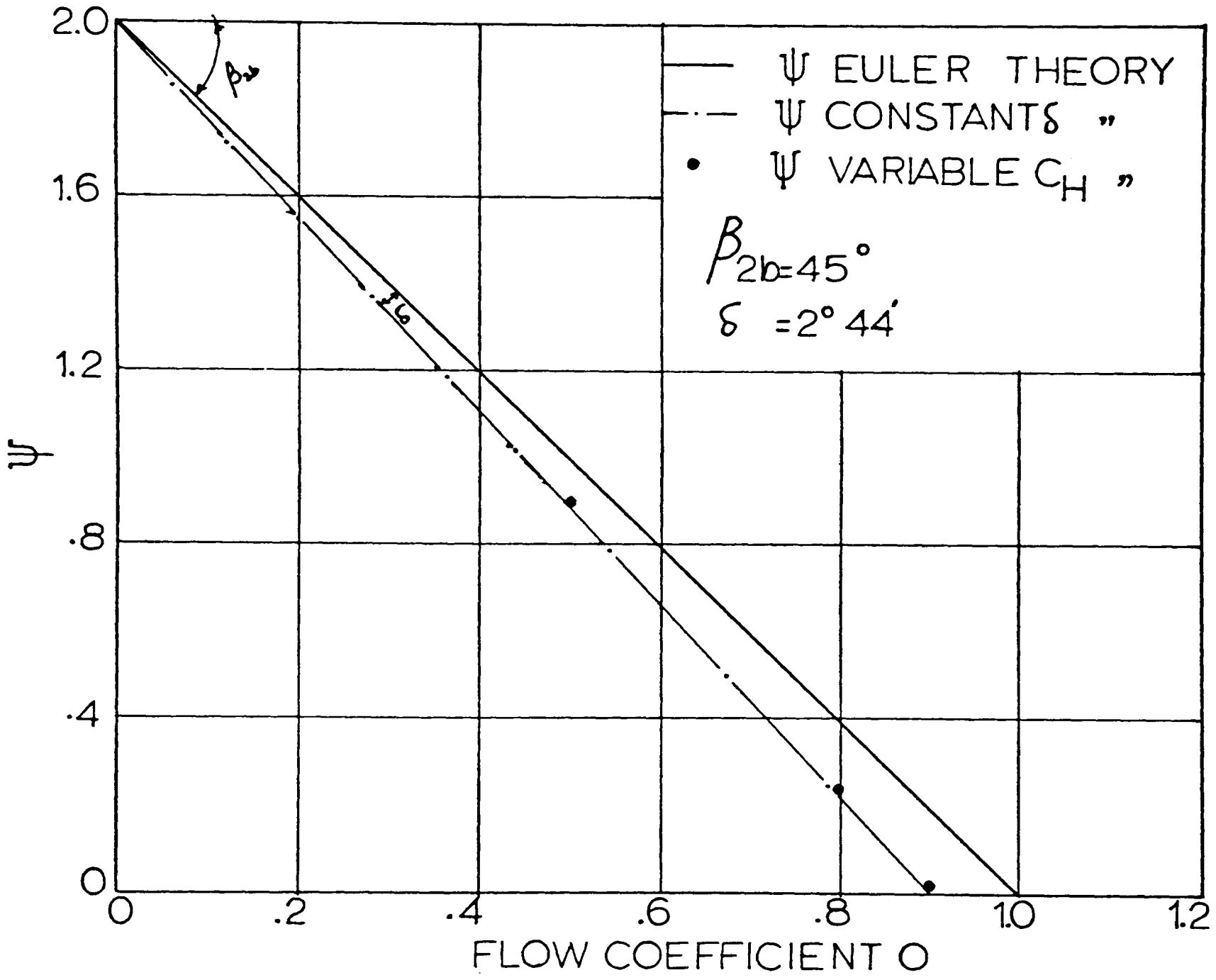

COMPARISON OF PERFORMANCE

Fig. 3.4

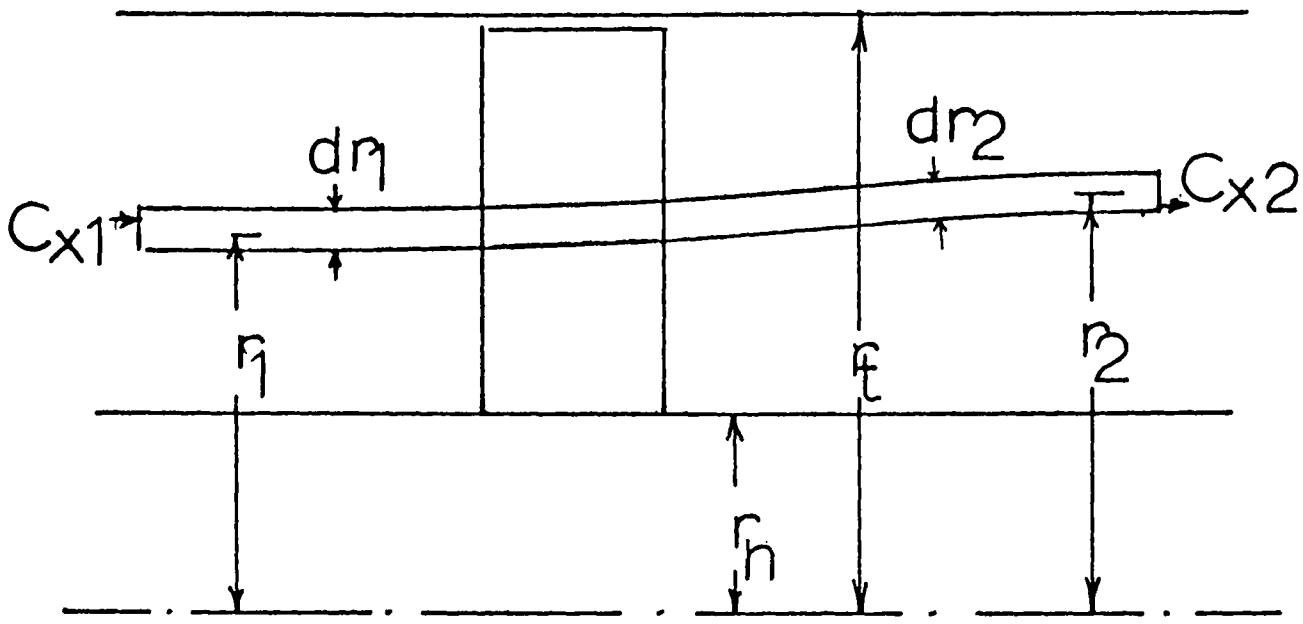

streamline shiftthrough bladesystem

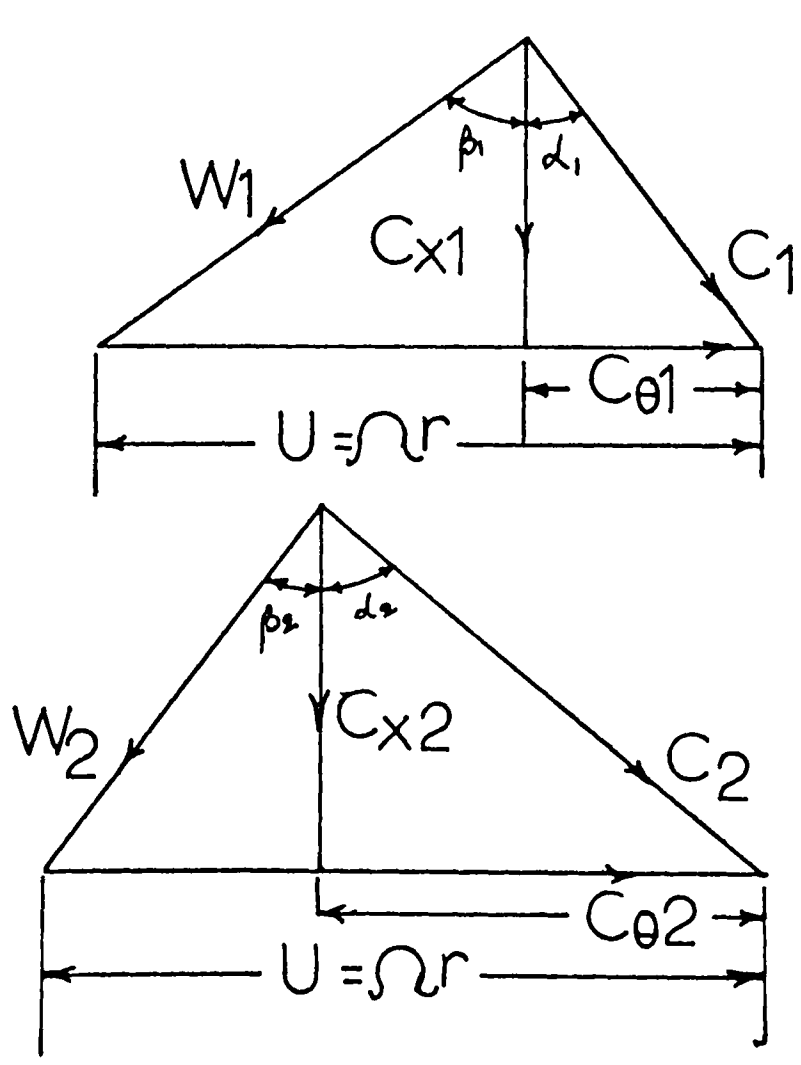

Fig. 3·5

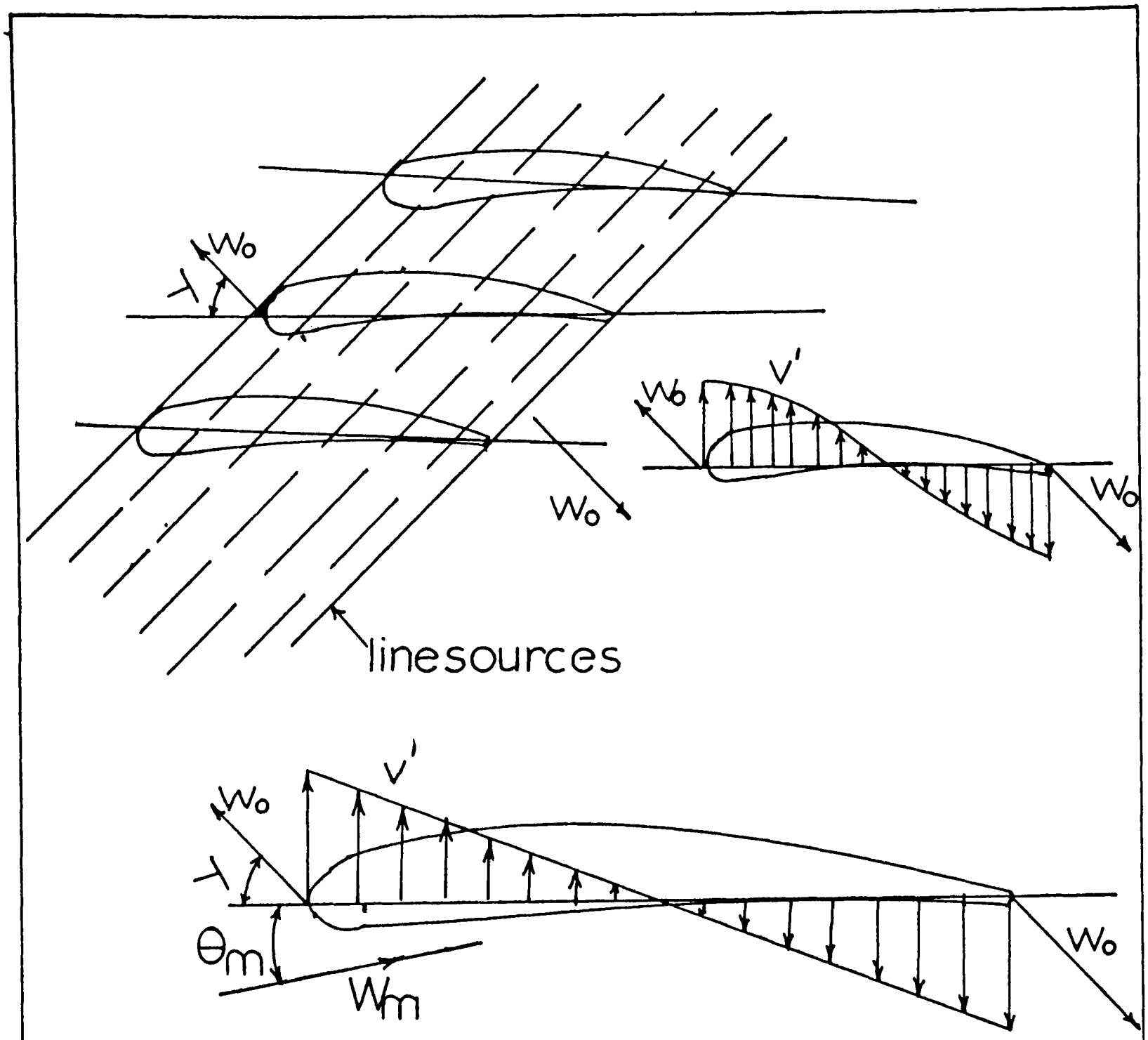

$$v' = w_o \sin\lambda - 2w_o \sin\lambda \frac{x}{c}$$

for linear variation of v'

LINE SOURCES AND INDUCED VELOCITIES

Fig. 3.6

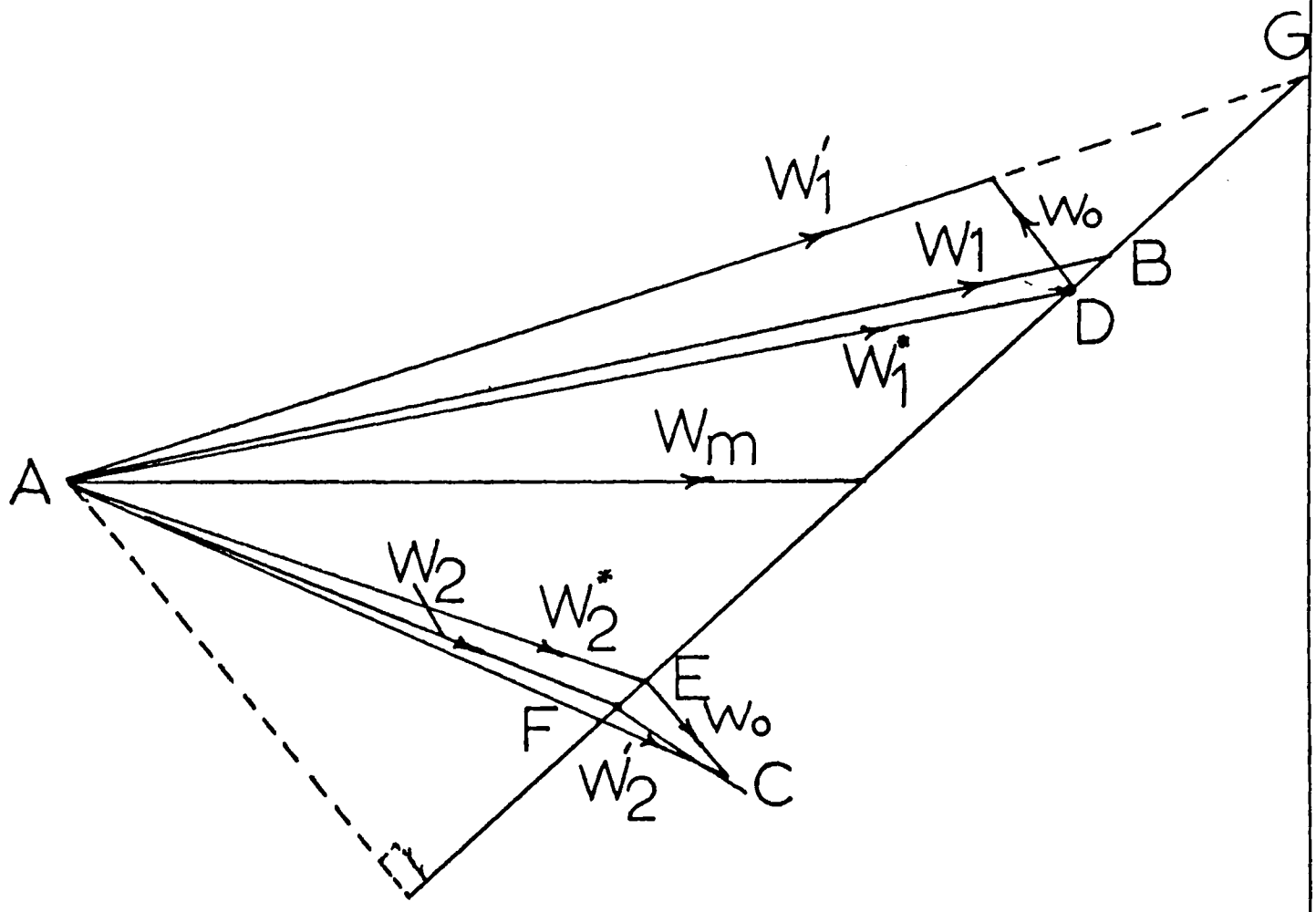

VELOCITY TRIANGLES, WITH CHANGE IN AXIAL VELOCITY

Fig.3.7

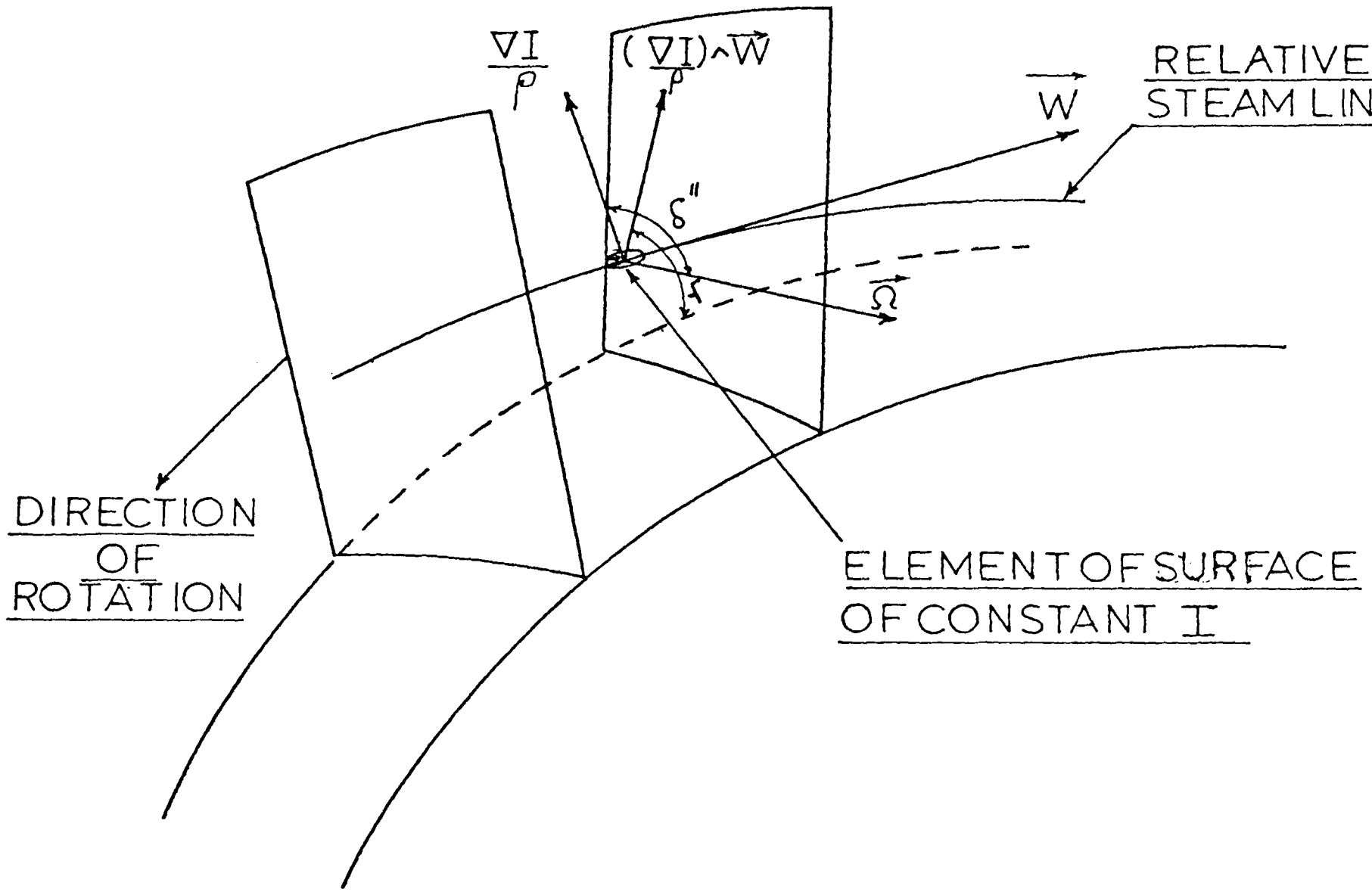

NOTATIONS FOR THE CALCULATION OF RELATIVE STREAMWISE SECONDARY VORTICITY

Fig. 3.8

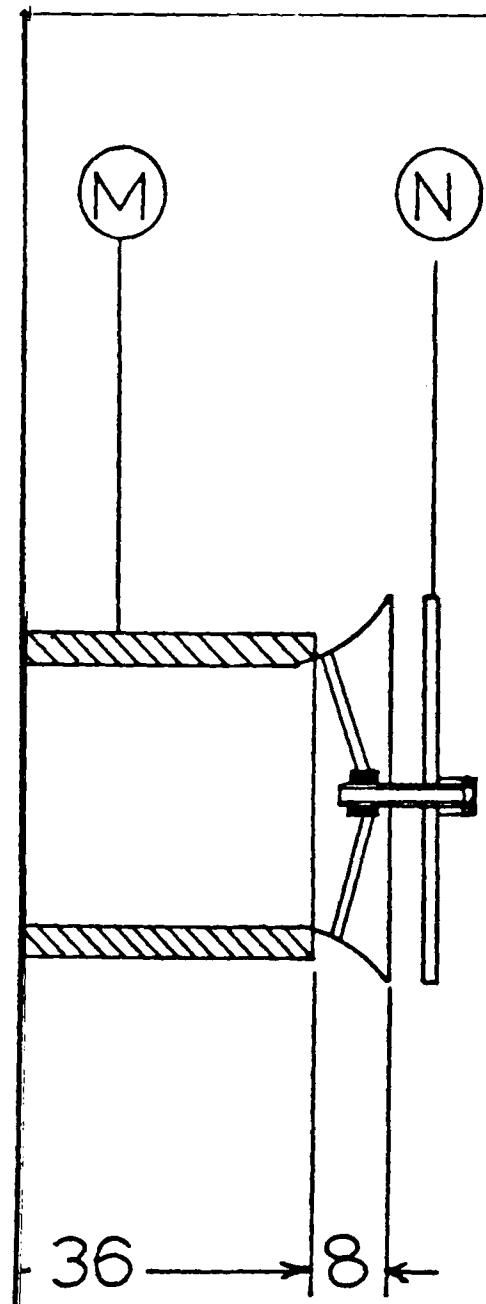

A Tachogenerator
B 20H.P Motor
C Transducer pad
D Air bearing
E Disc with 60 holes
F Test impeller
G Settling chamber
H Dufaylite honeycomb
I Flow straightener
J Venturimeter
K Dufaylite honeycomb
L Booster fan
M Silencer
N Throttle board
t Traversing plane
s Static pressureplugs

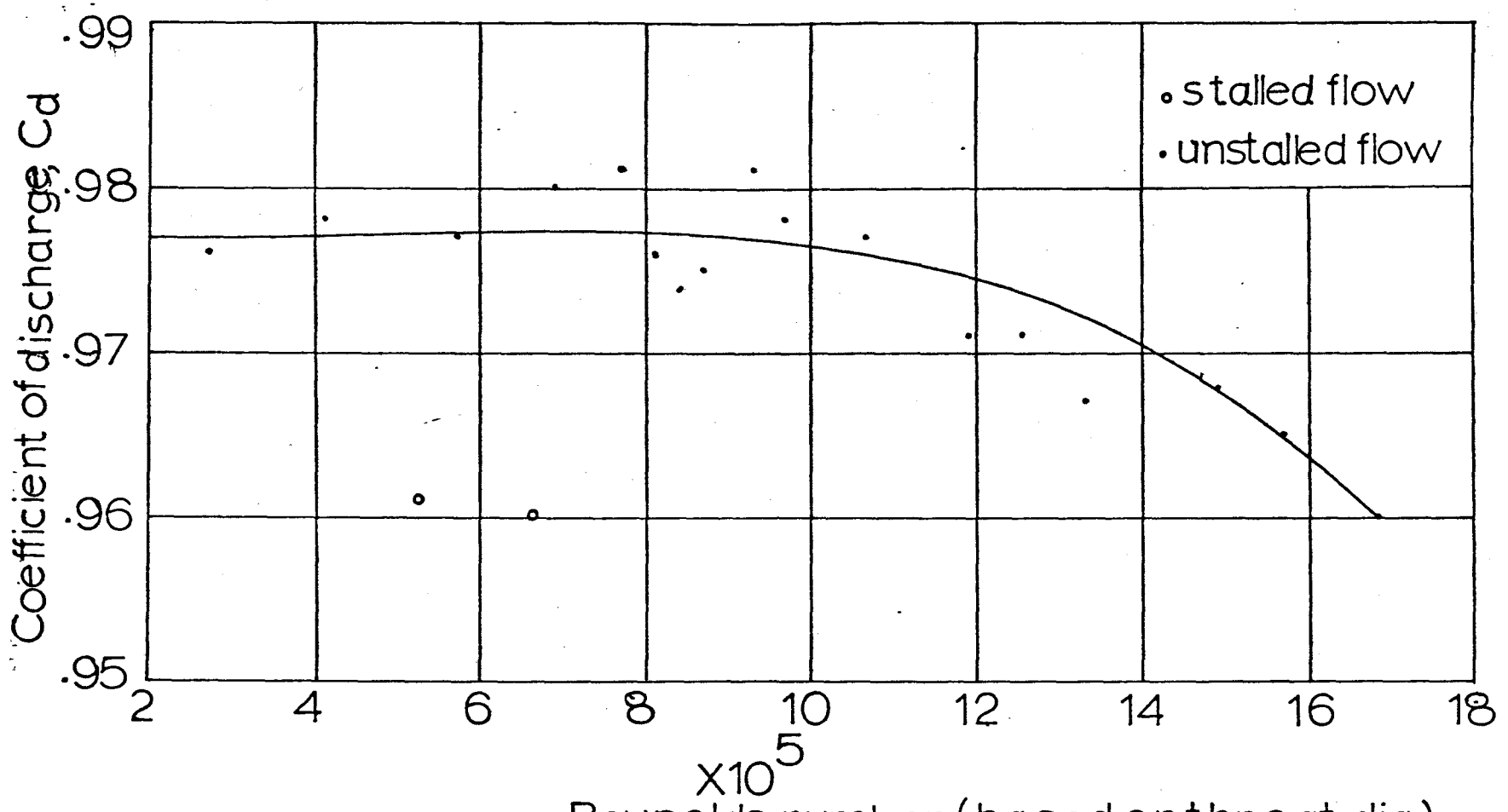

CALIBRATION CURVE OF VENTURIMETER

Fig. 4.2

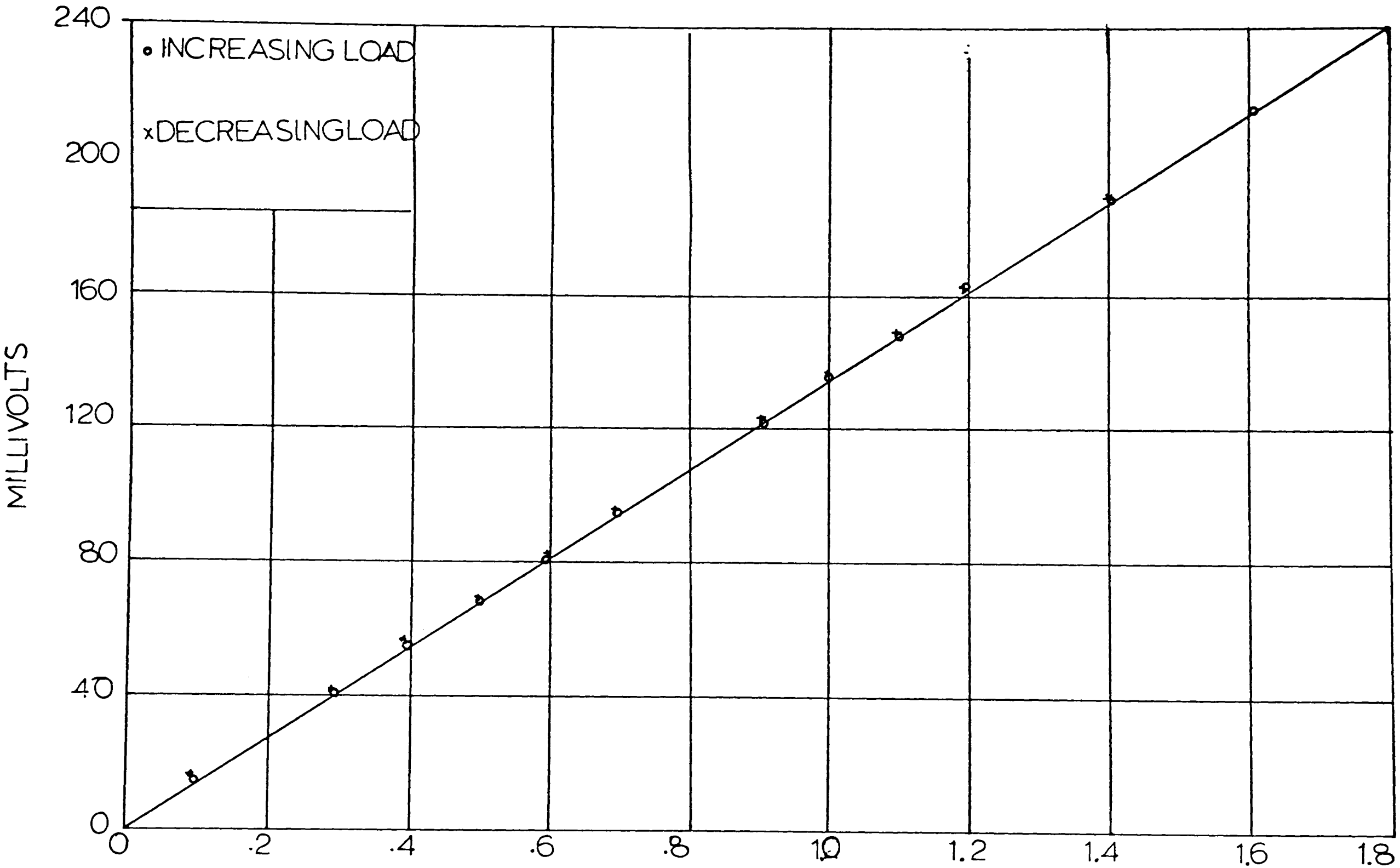

CALIBRATION CURVE OF TRANSDUCER

Fig. 4.3

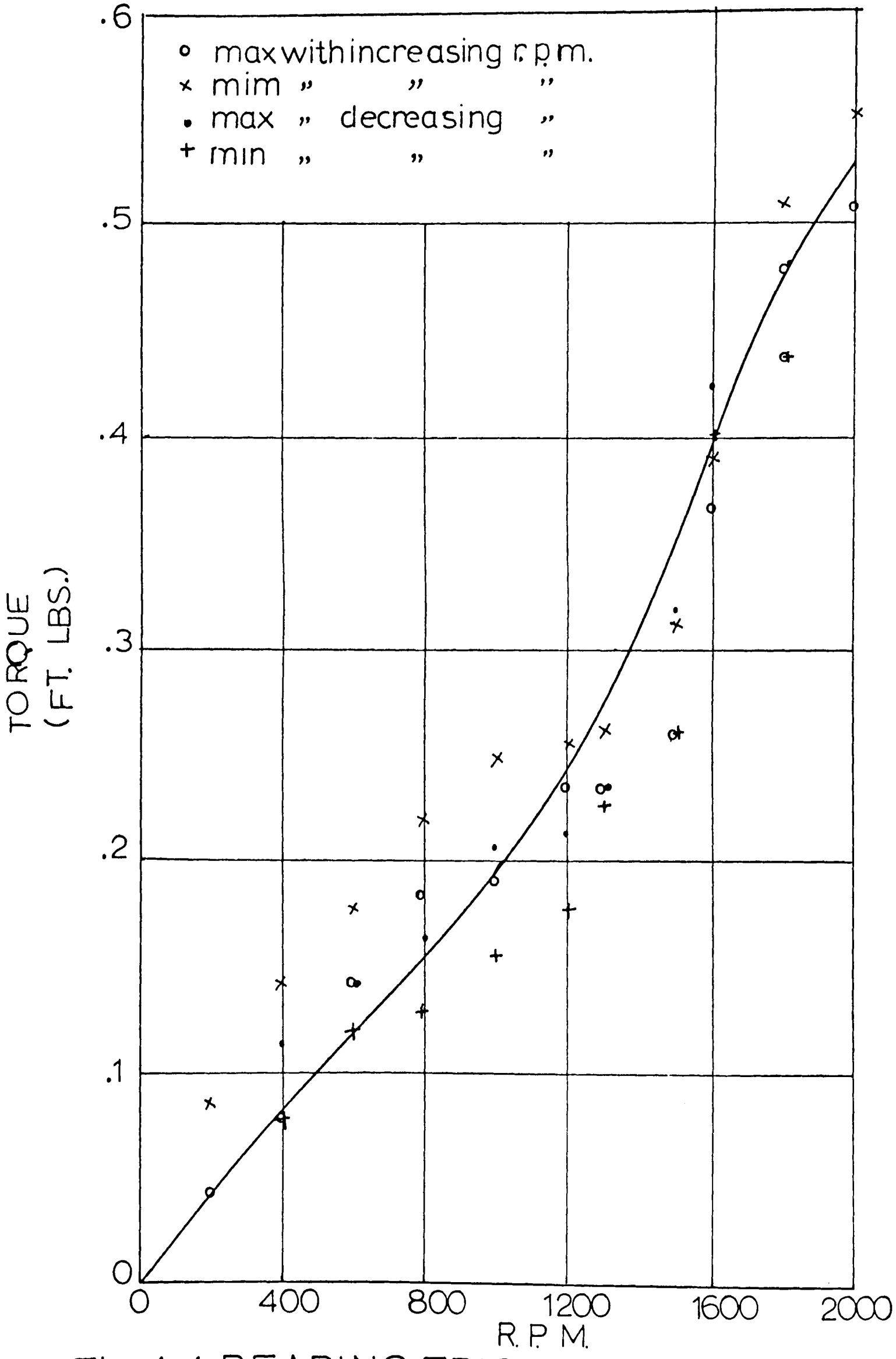

Fig. 4.4, BEARING FRICTION TORQUE

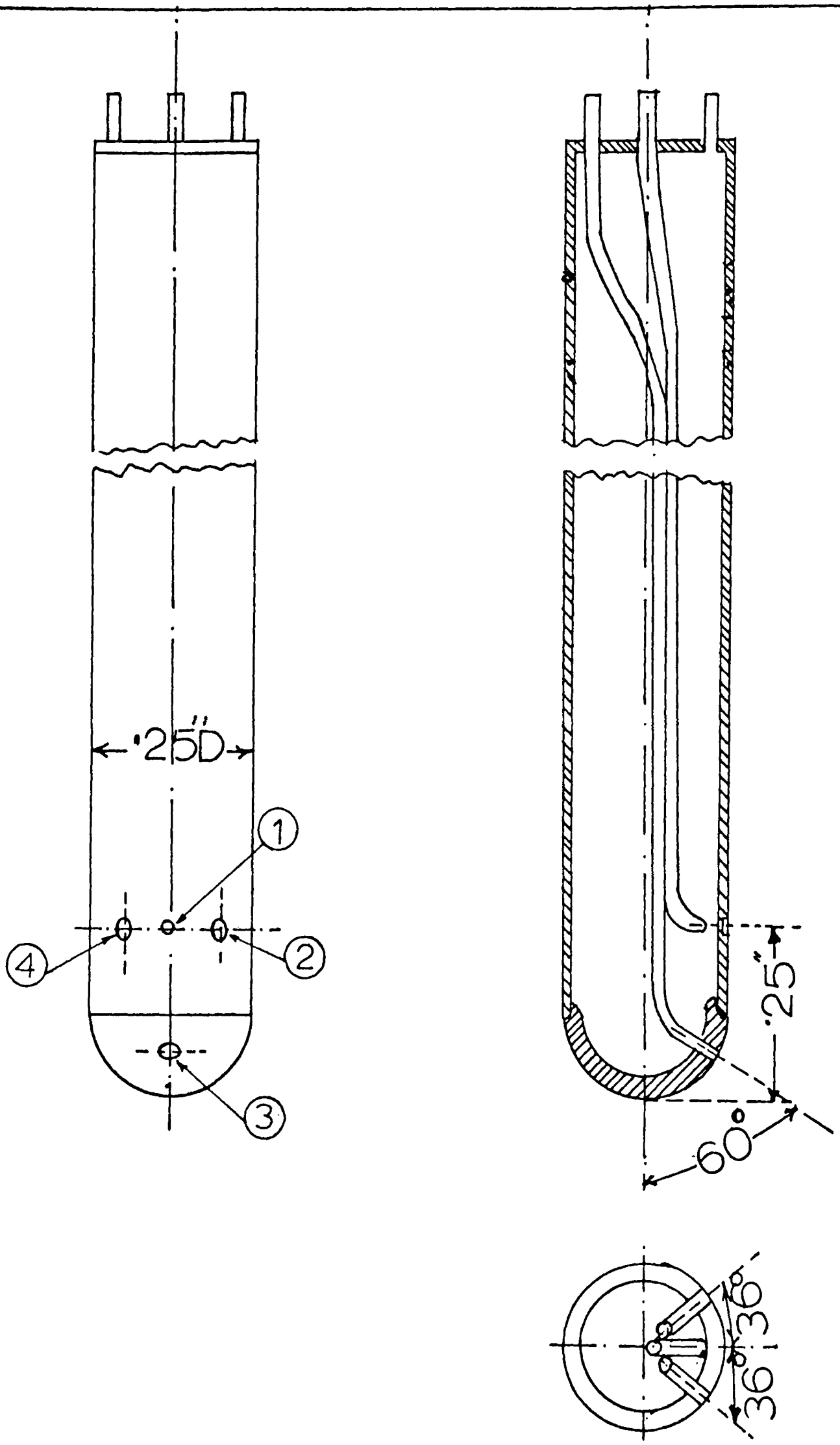

FOUR ORIFICE CANTILEVER PITOT CYLINDER

Fig. 4.5

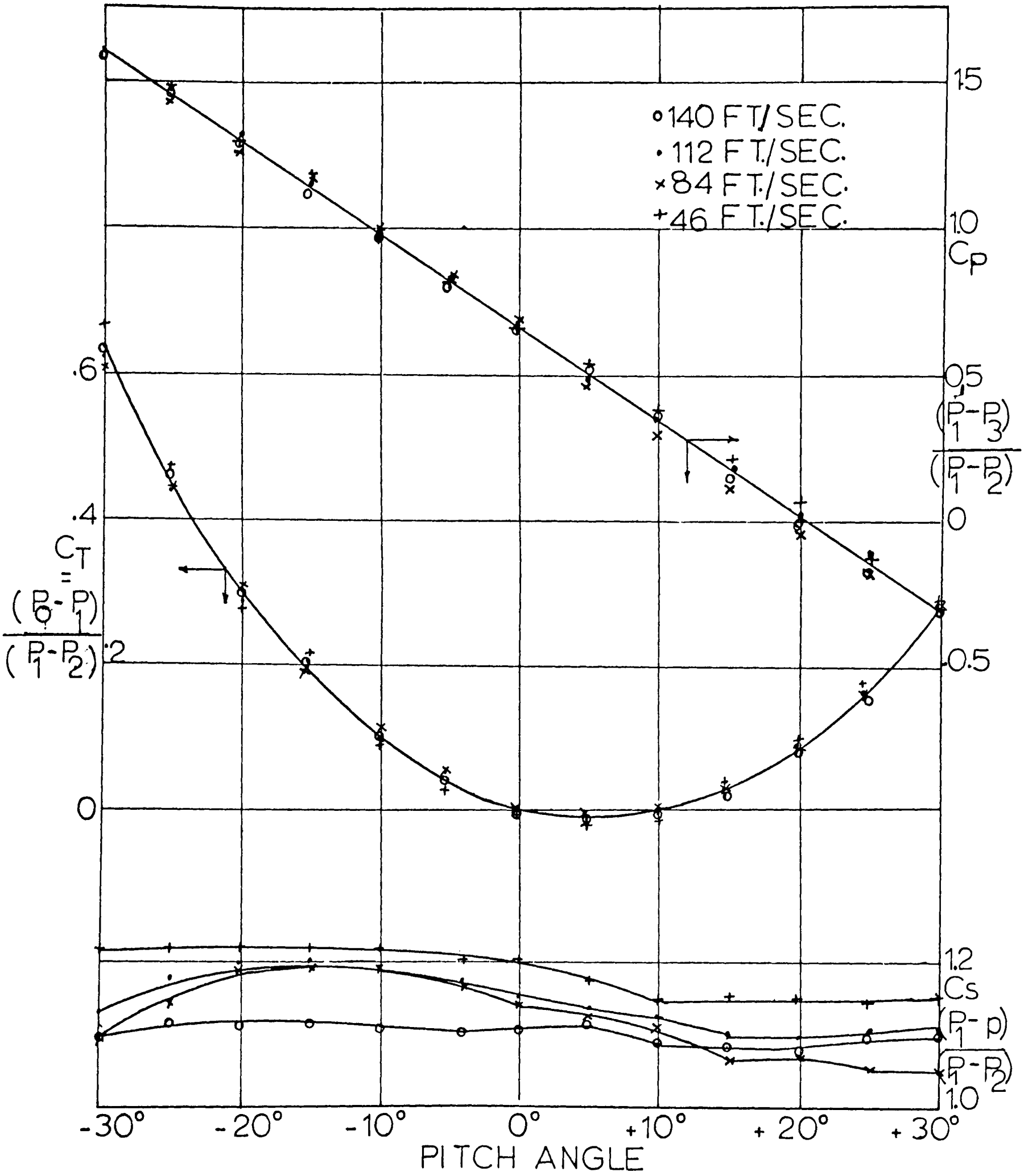

CALIBRATION CURVES OF 3D PROBE

Fig. 4.6

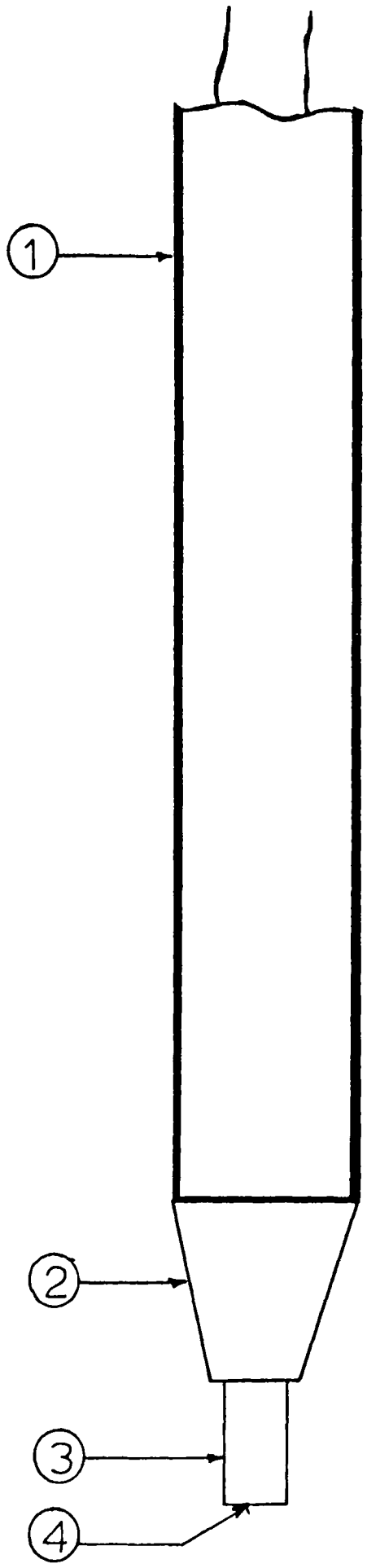

① STEM 0.25 IN. DIA.

② NEEDLE HOLDER (ARALDITE)

③ STEEL NEEDLES 4 mm. LONG

④ WOLLASTON WIRE
LENGTH = 2 mm
OUTSIDE DIA. = 0.005 IN.
CORE DIA. = 0.0002 IN.

HOT WIRE PROBE

Fig. 4.7

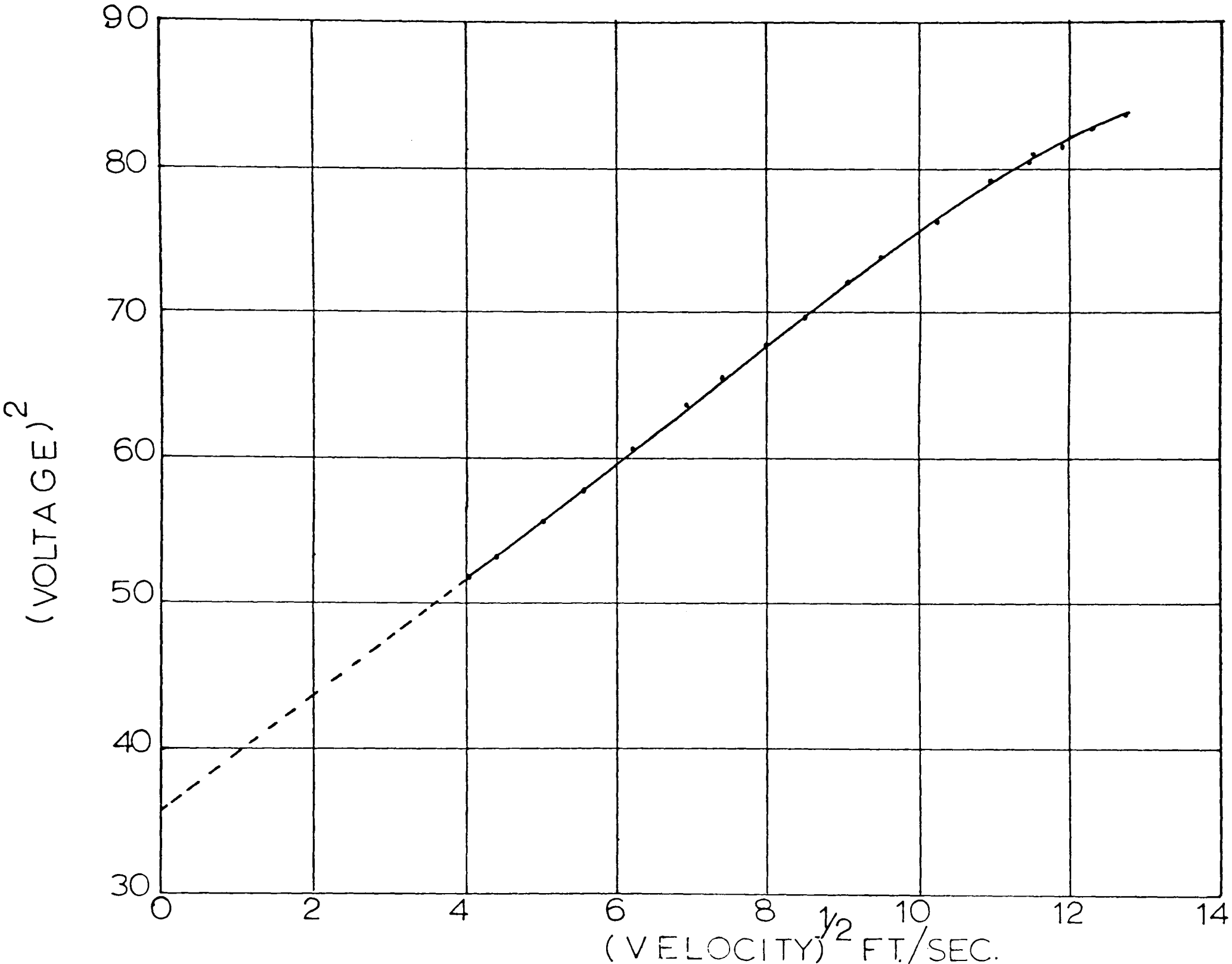

Fig.4.8. CALIBRATION CURVE OF HOTWIRE PROBE

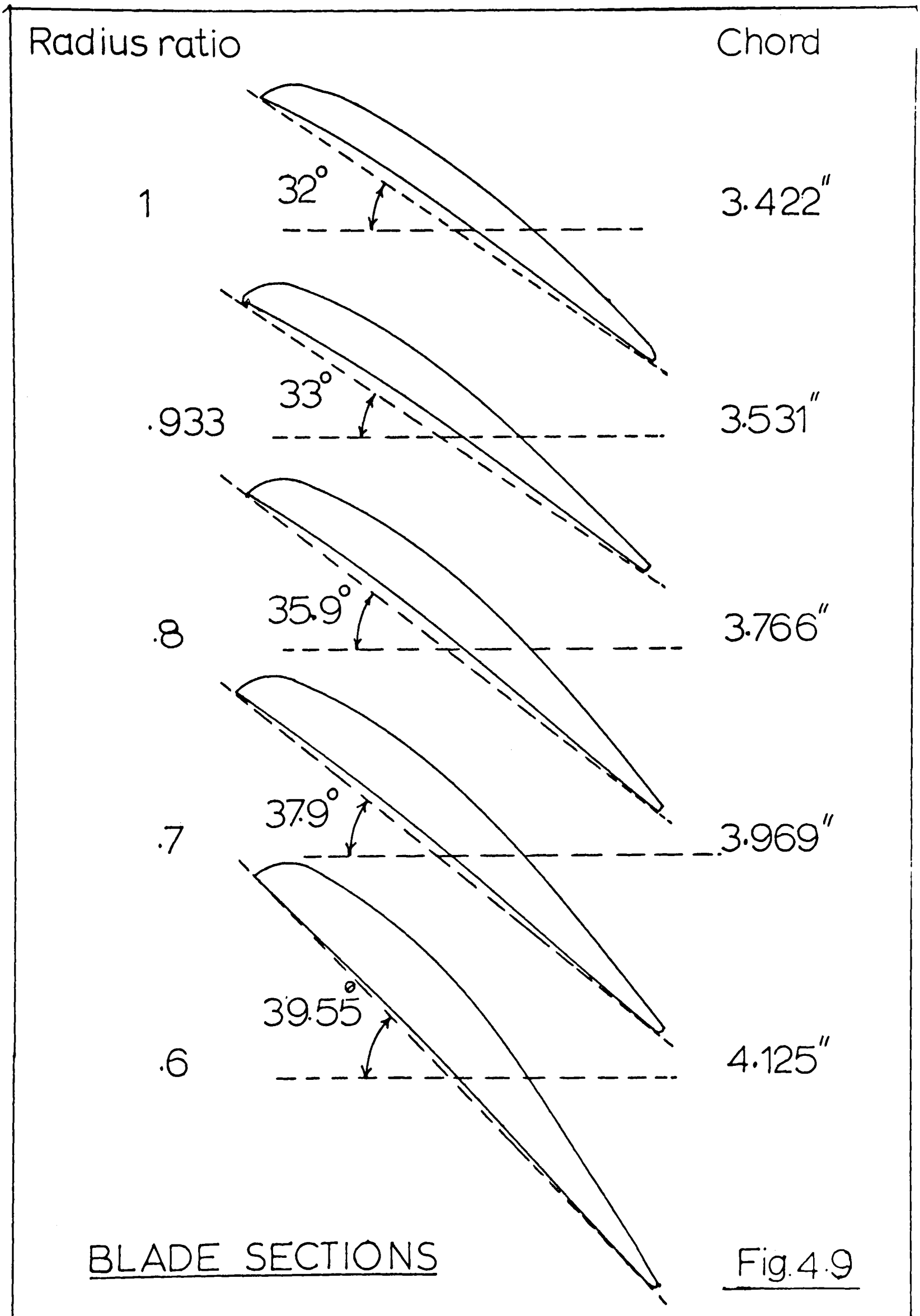

BLADE SECTIONS

Fig. 4.9

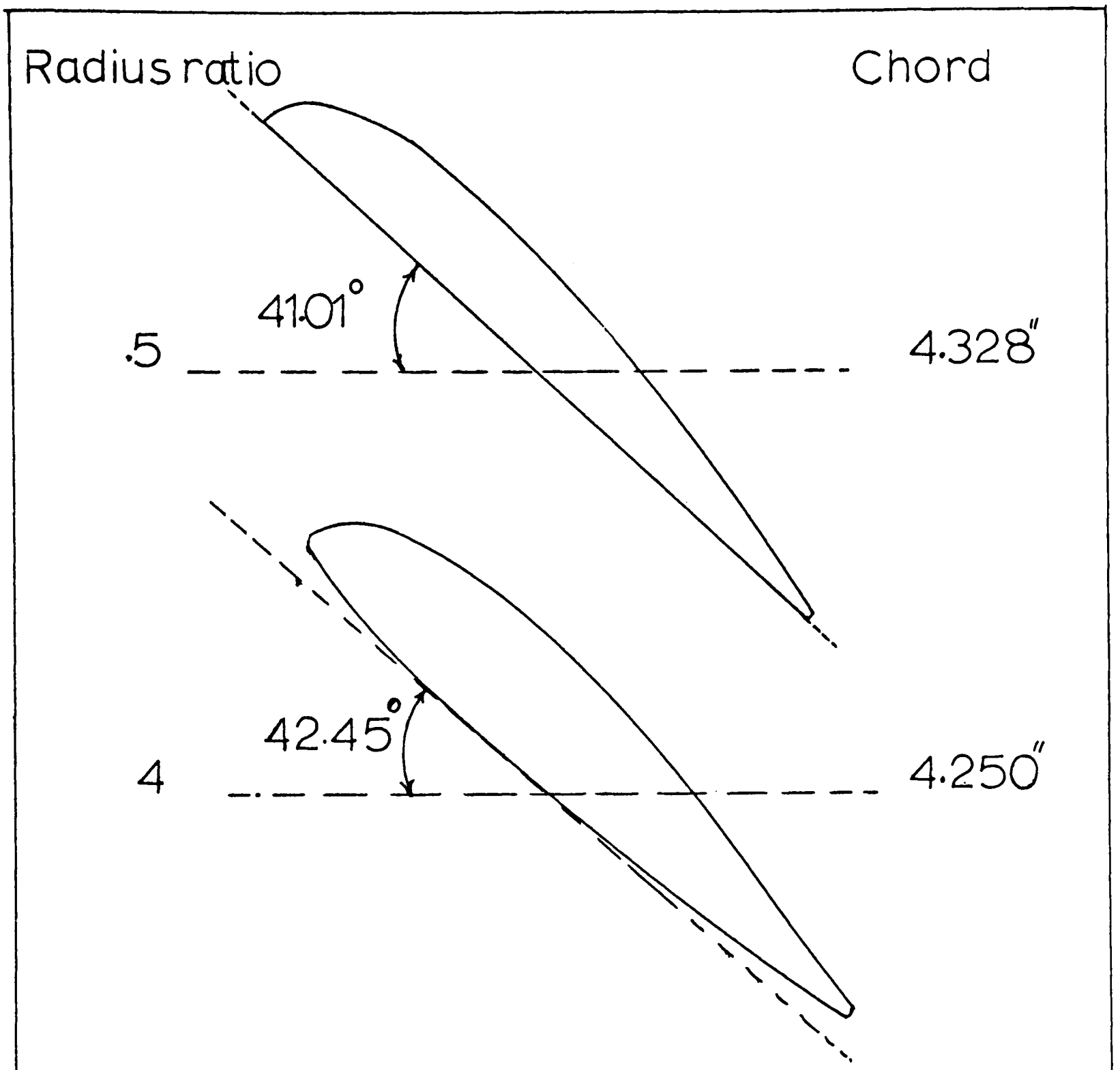

BLADE SECTIONS

Fig. 4.9 (CONCLUDED)

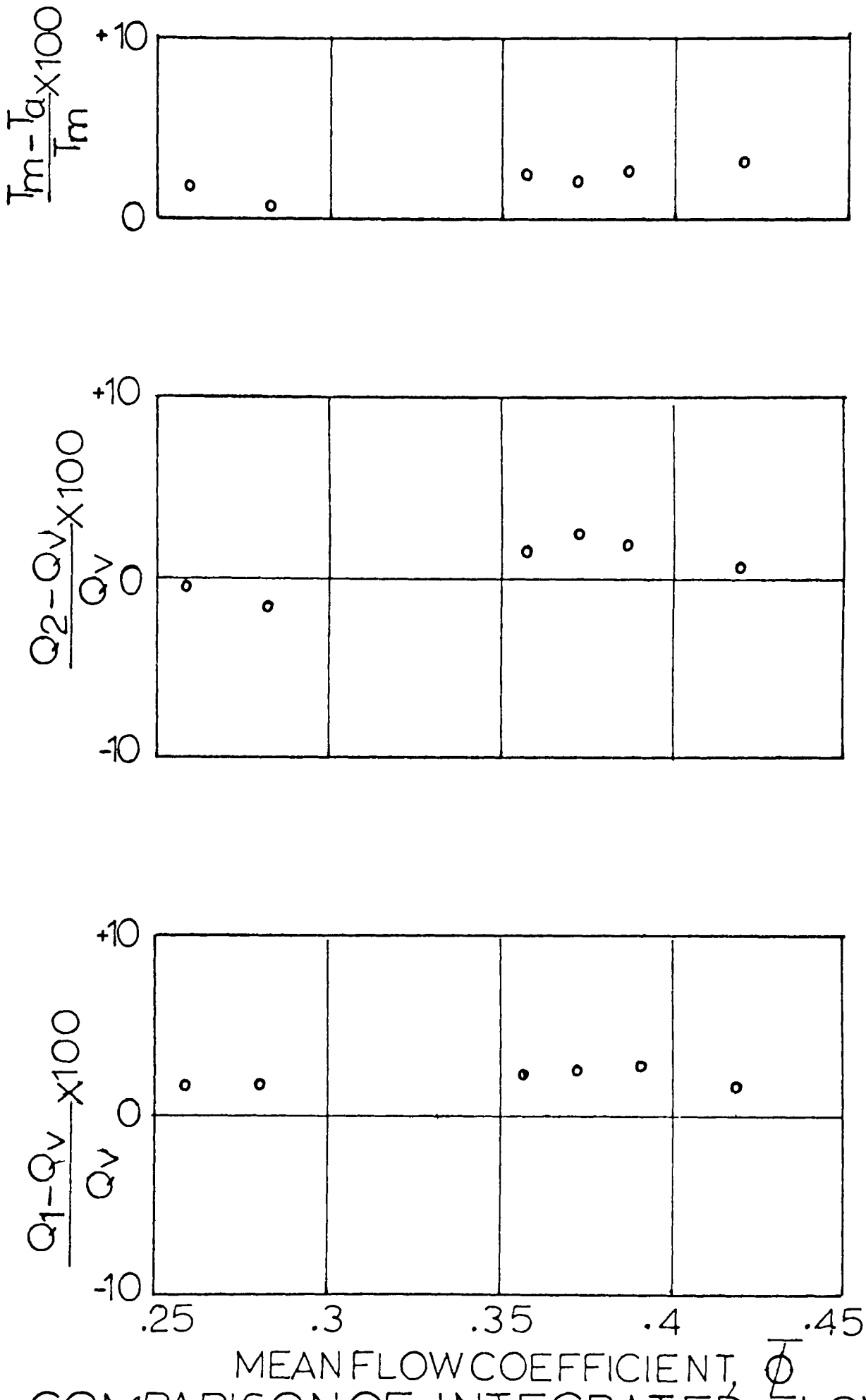

COMPARISON OF INTEGRATED FLOWS WITH THOSE MEASURED BY VENTURI METER AND COMPARISON OF MECH. AND AERODYANAMIC TORQUE

Fig. 5.1

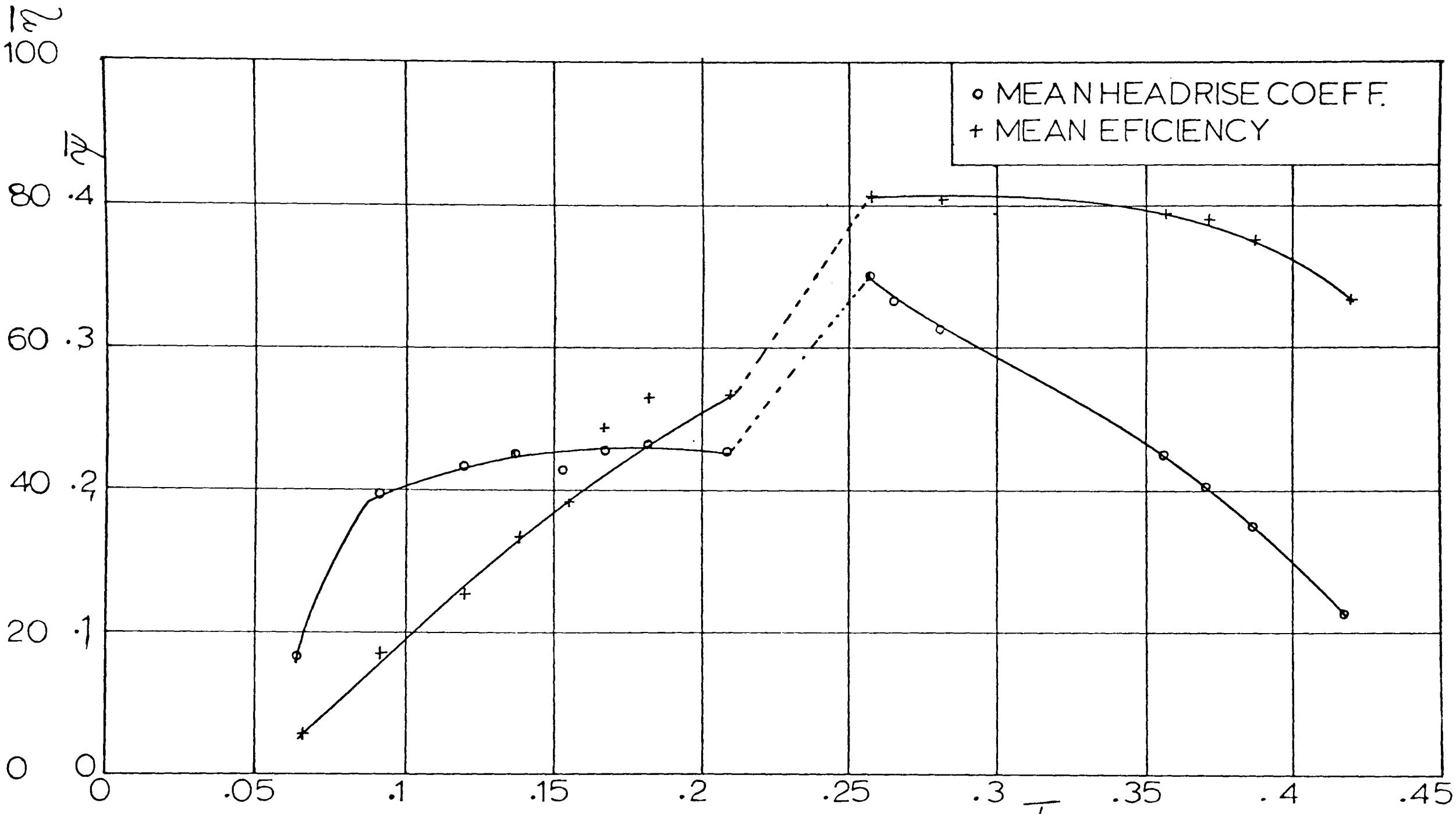

INTEGRATED TOATAL HEAD RISE COEFF. AND EFFICIENCY

Fig. 5.2

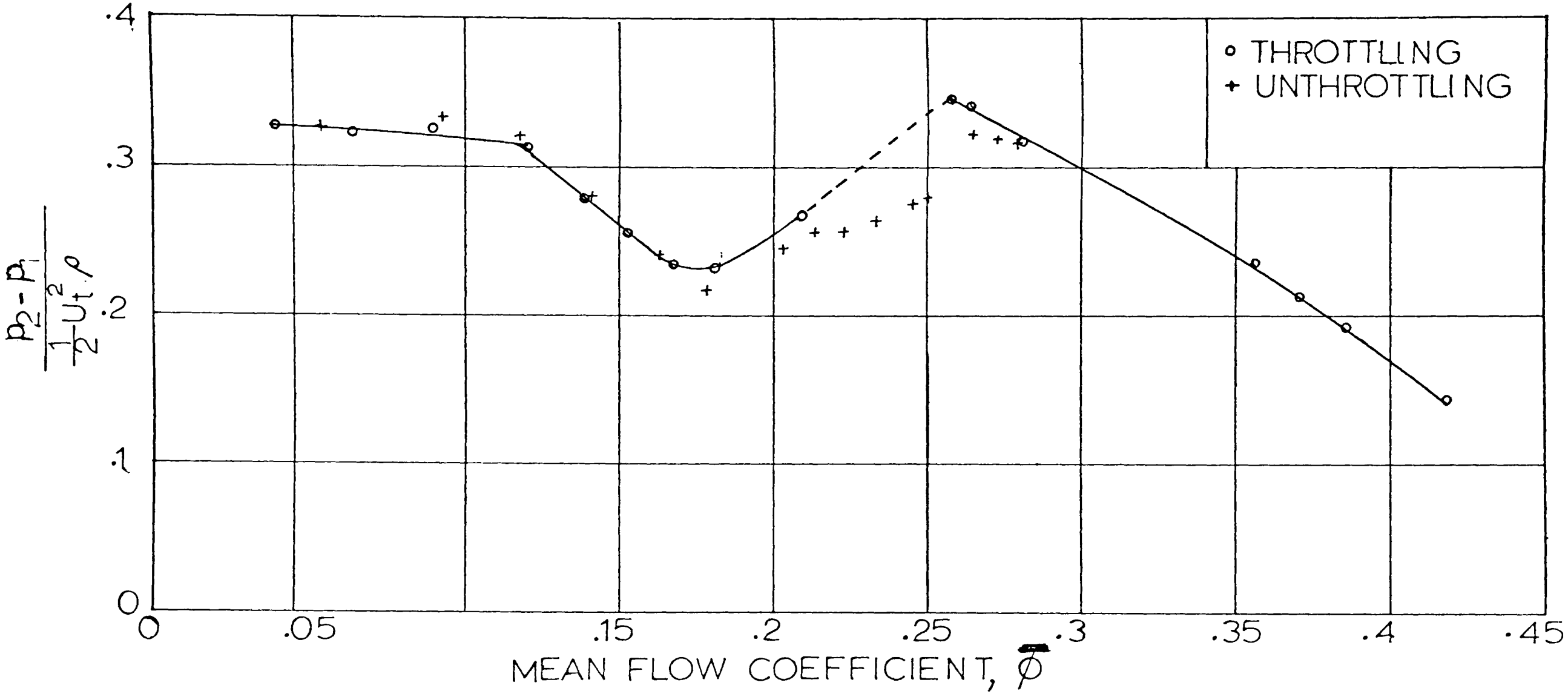

OUTER WALL STATIC PRESSURE RISE COEFFICIENT

Fig. 5.3

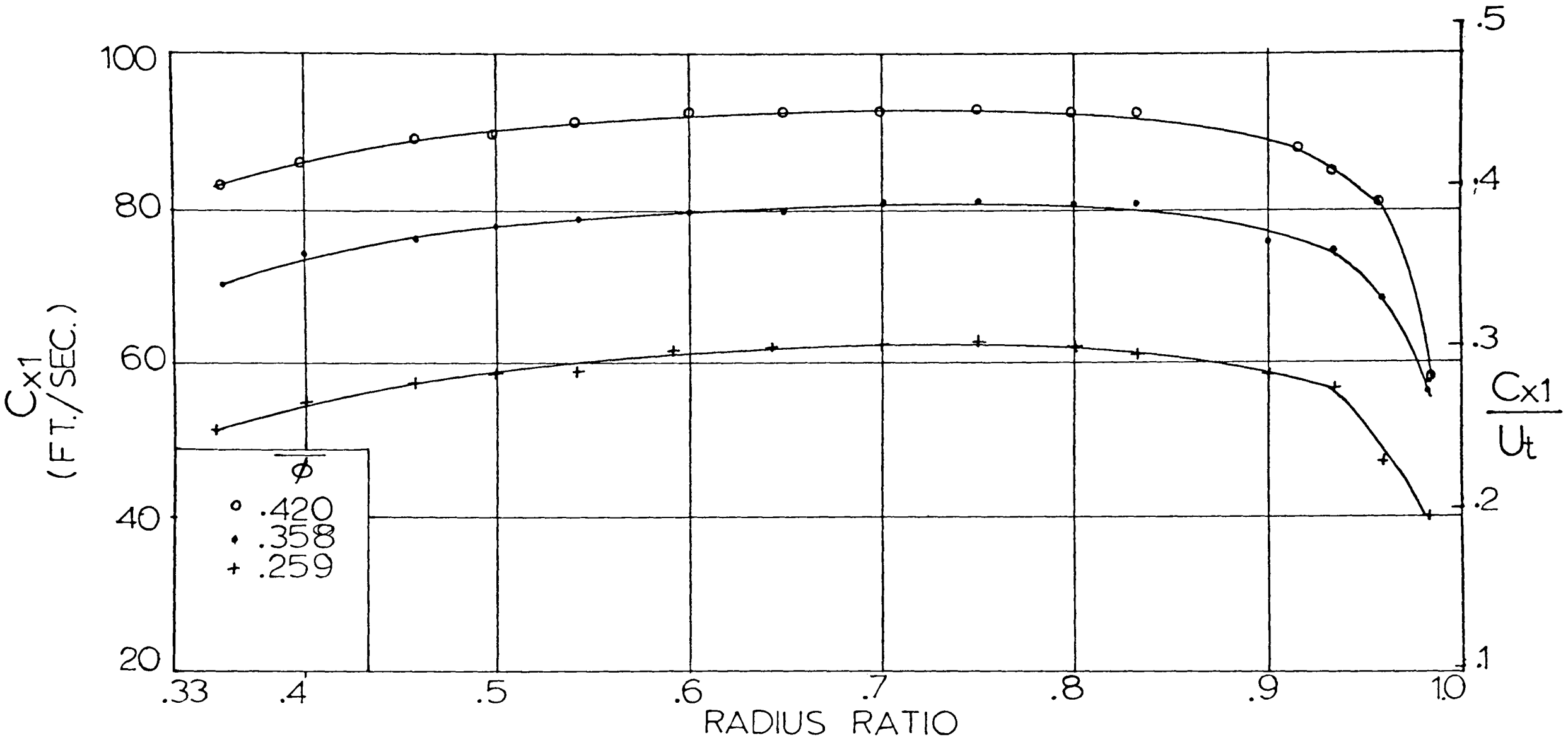

INLET AXIALVELOCITY

Fig.5.4

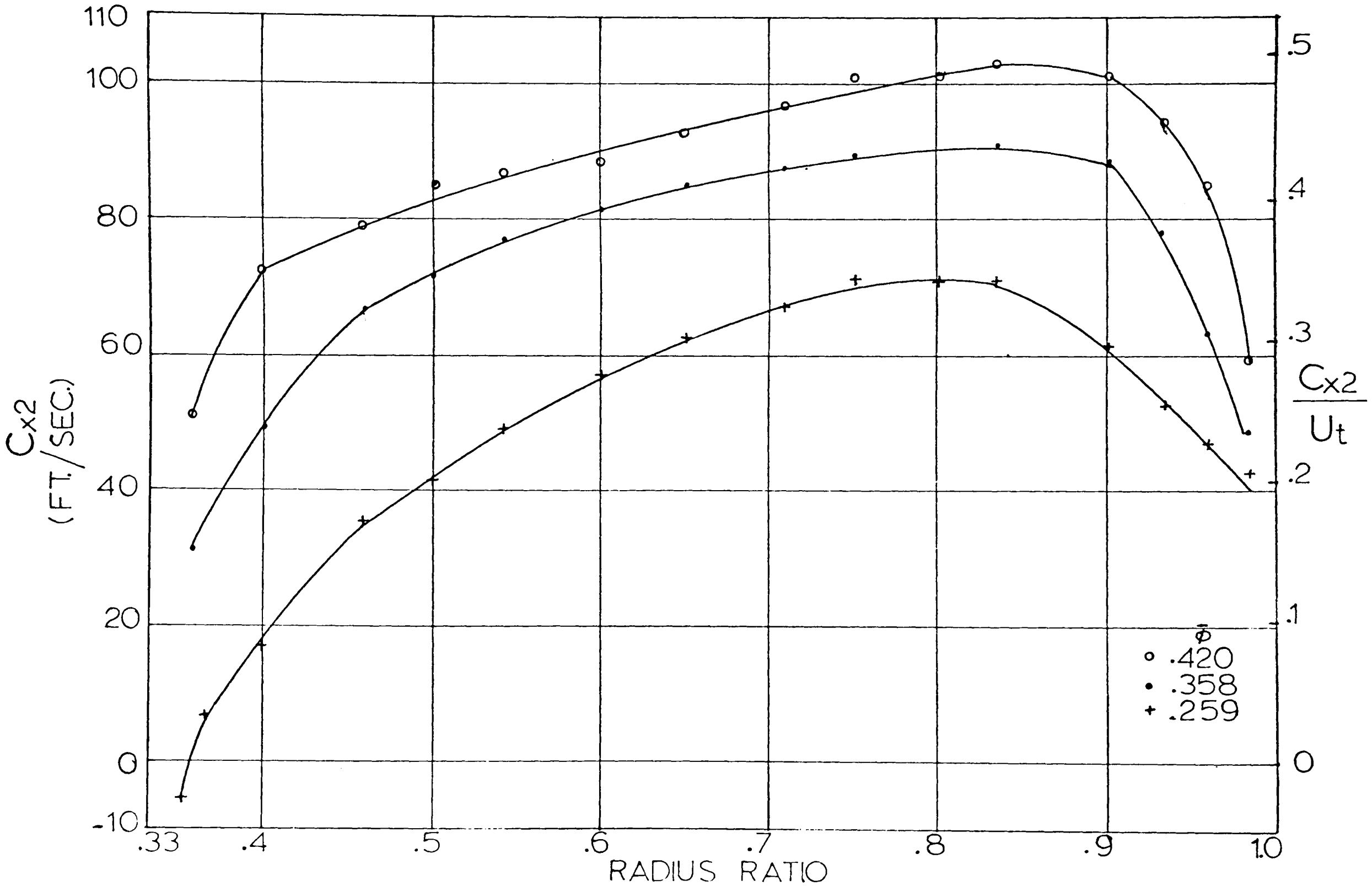

Fig.5.5 OUTLET AXIAL VELOCITY

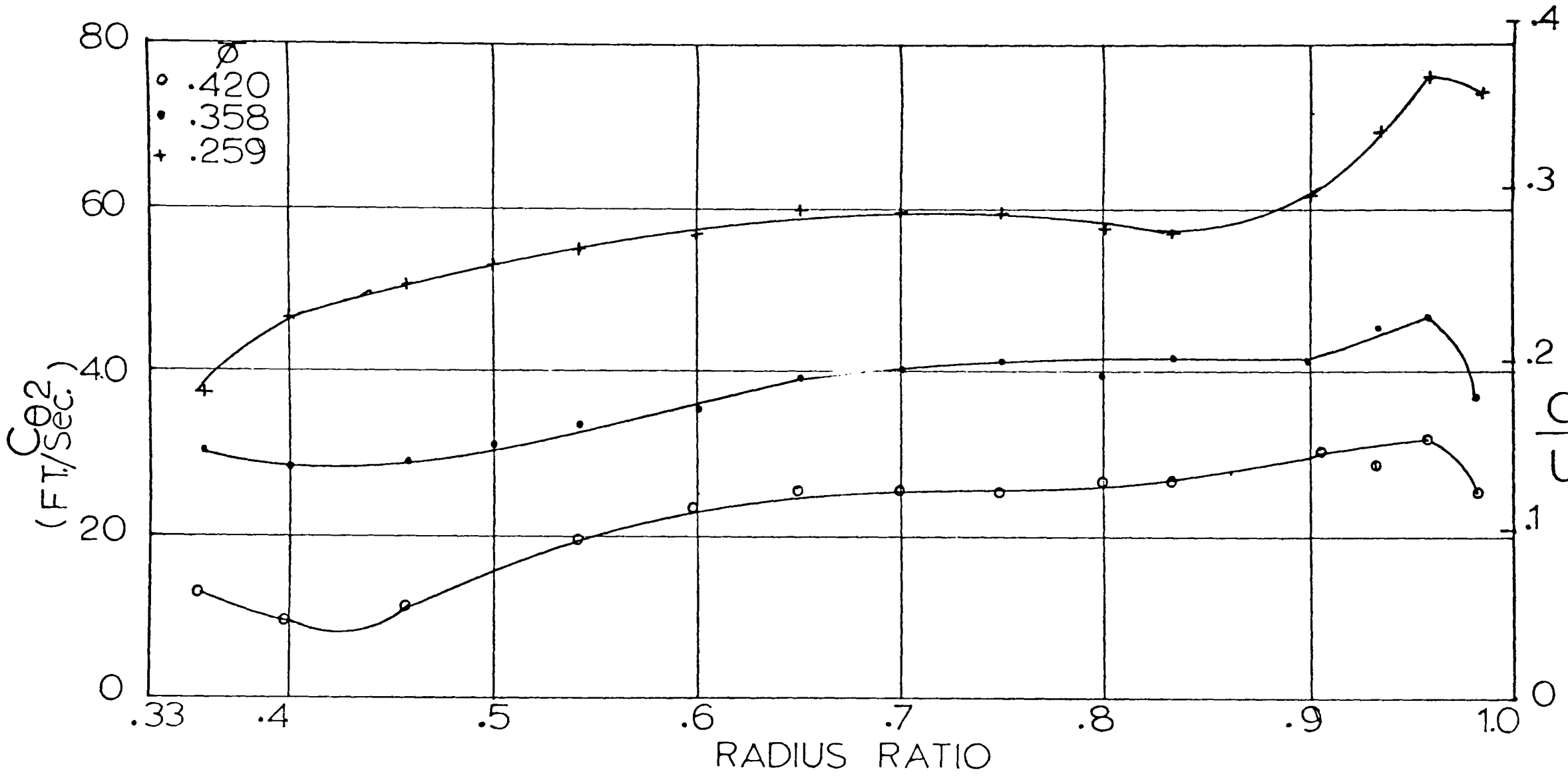

OUTLET TANGENTIAL VELOCITY

Fig.5.6

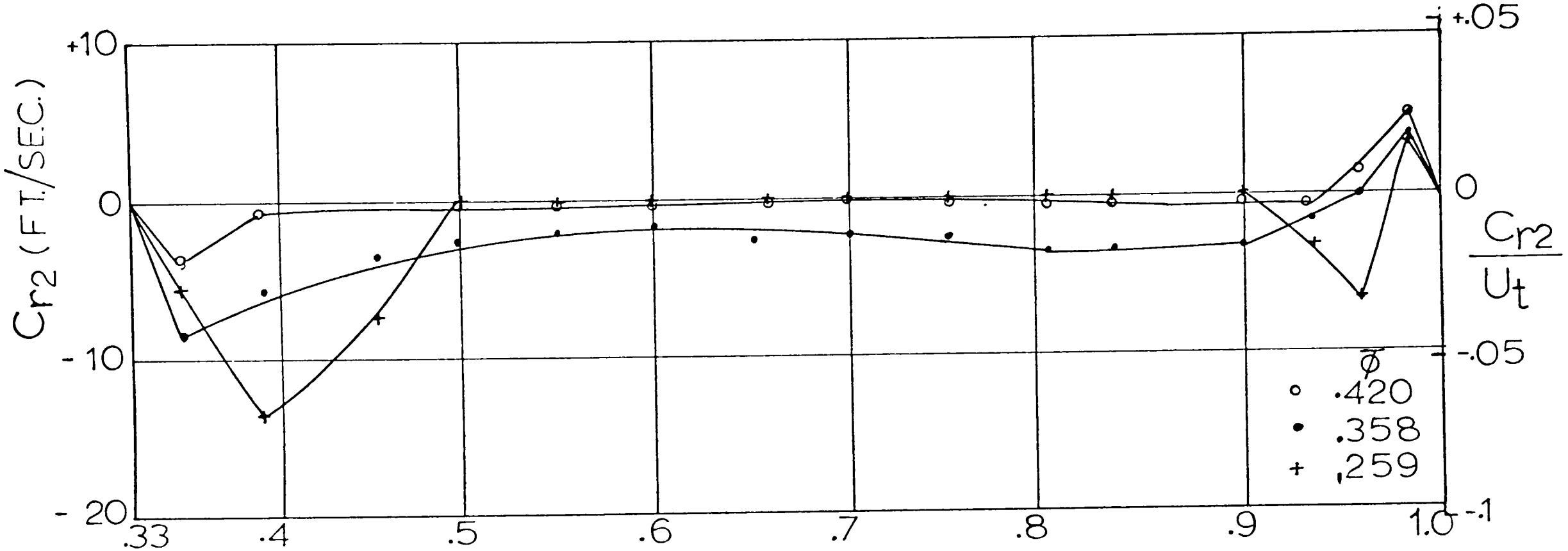

OUTLET RADIAL VELOCITY

Fig.5.7

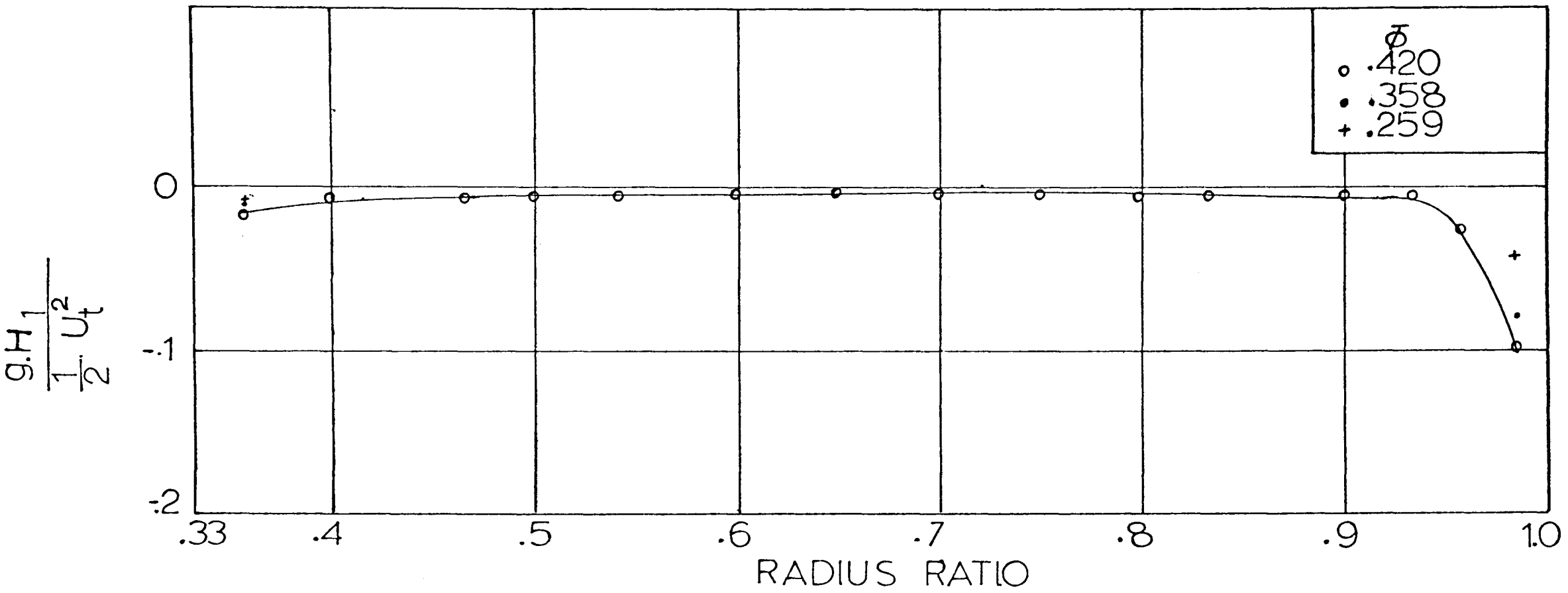

INLET TOTAL HEAD COEFFICIENT

Fig.5.8

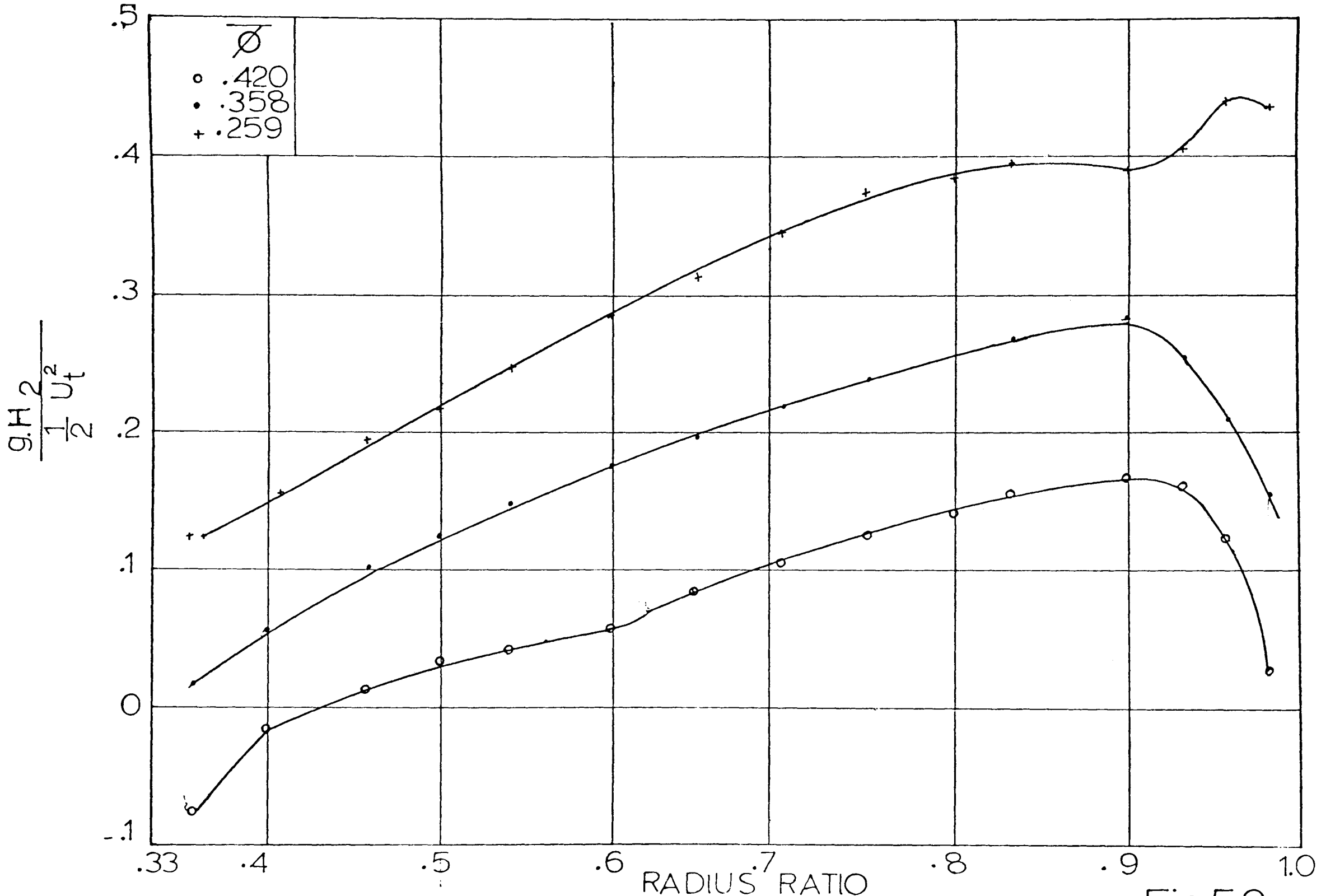

OUTLET TOTAL HEAD COEFFICIENT.

Fig.5.9

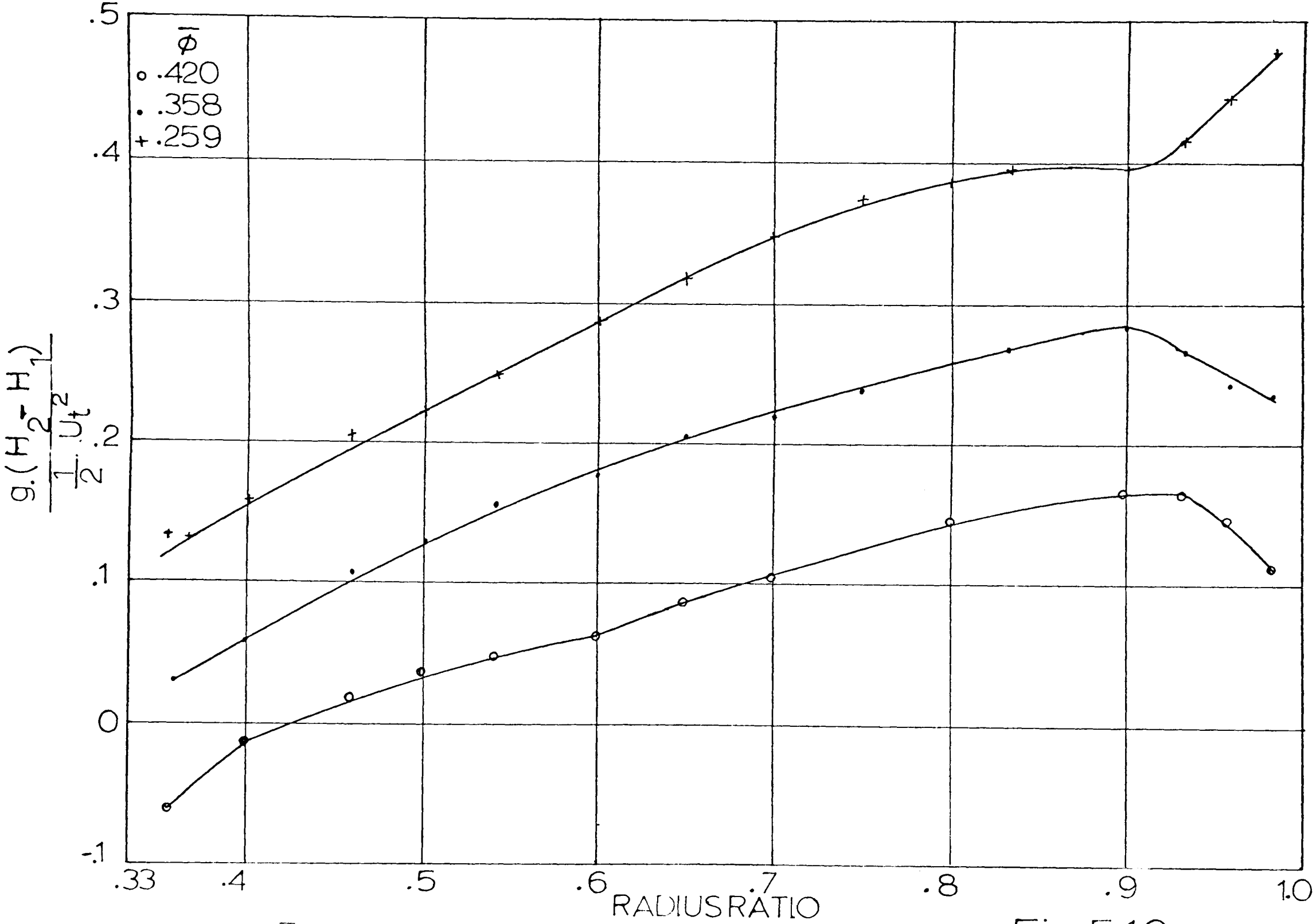

TOTAL HEAD RISE COEFFICIENT

Fig. 5.10

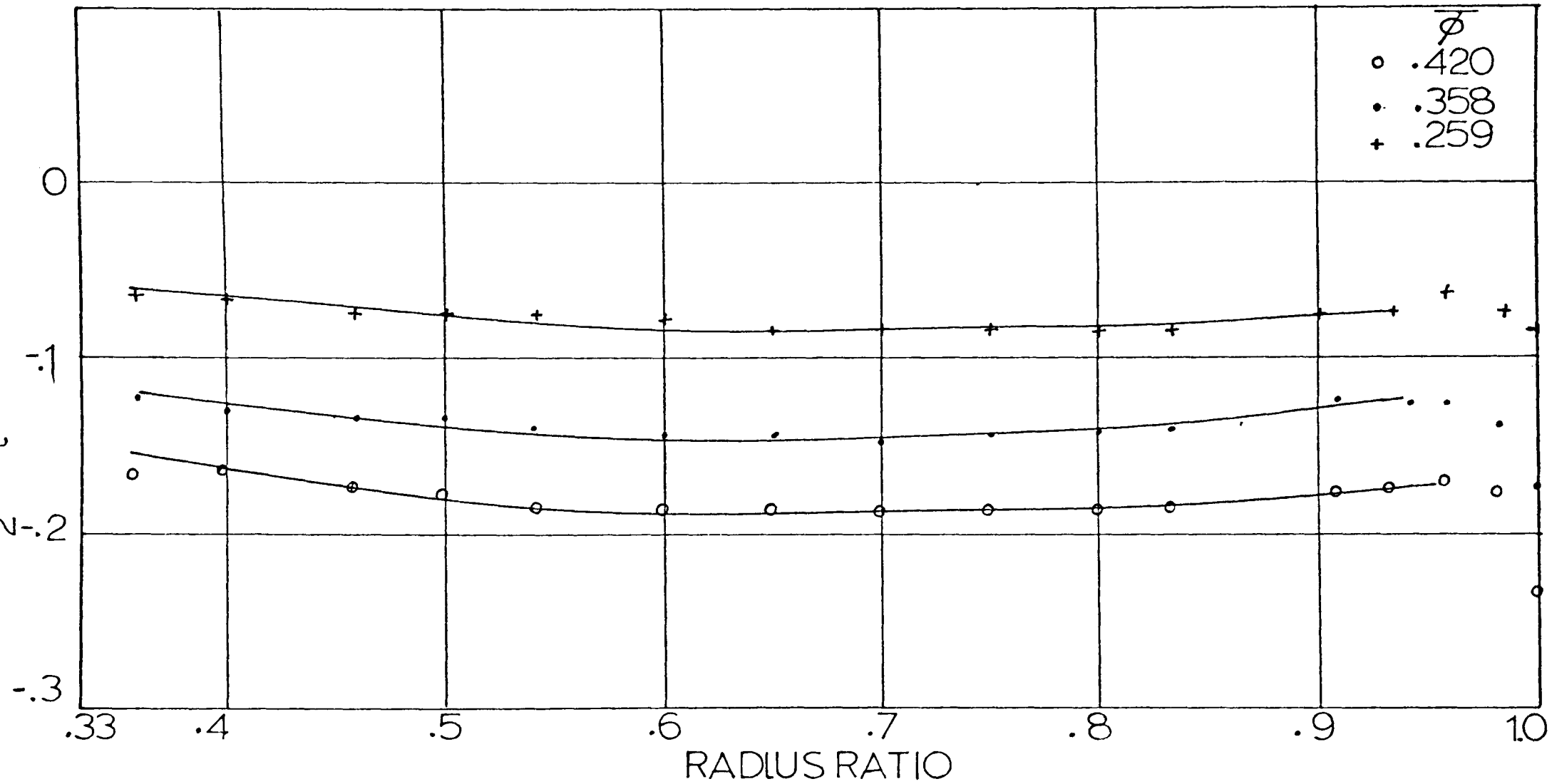

INLET STATIC HEAD COEFFICIENT

Fig. 5.11

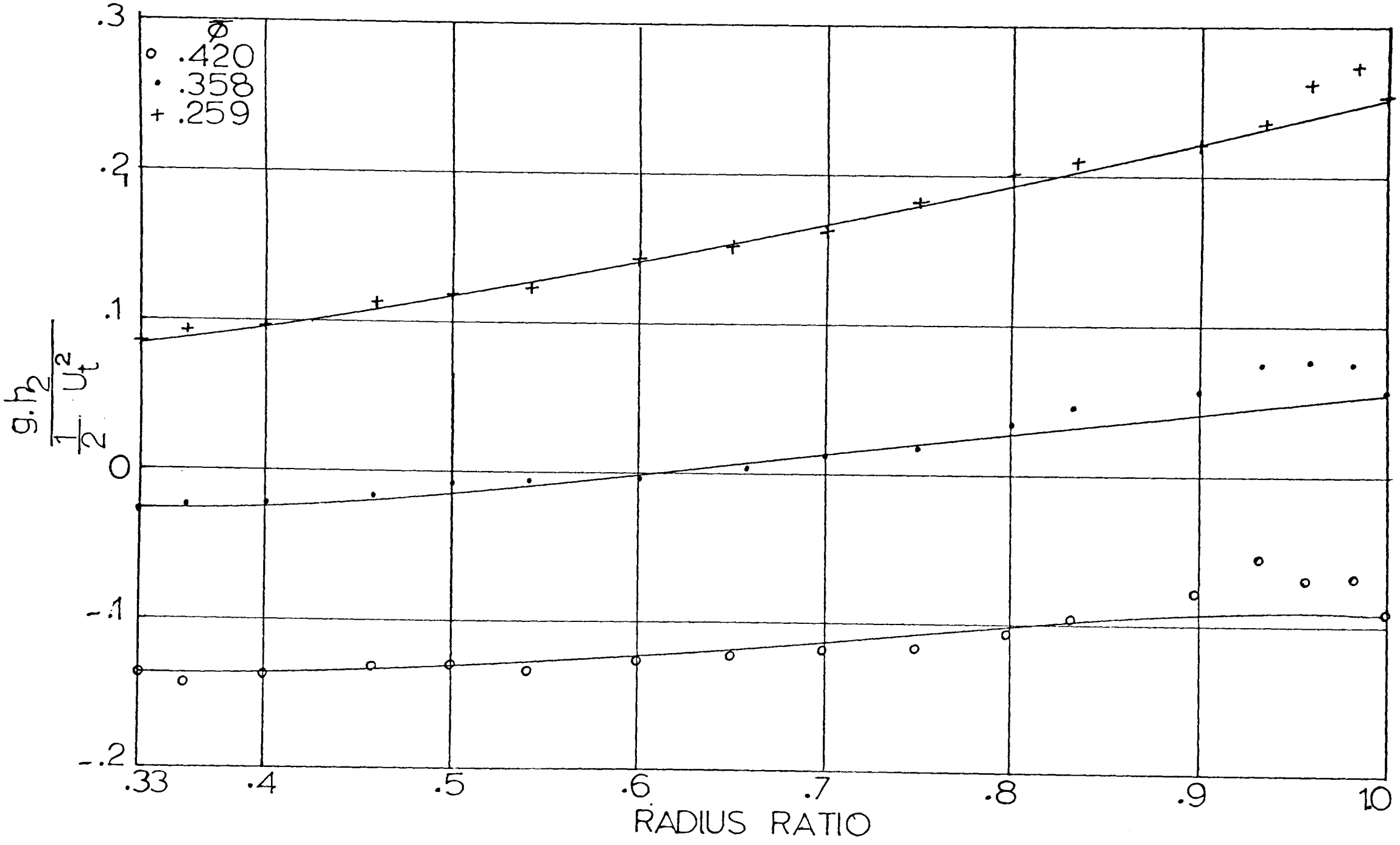

OUTLET STATIC HEAD COEFFICIENT

Fig. 5.12

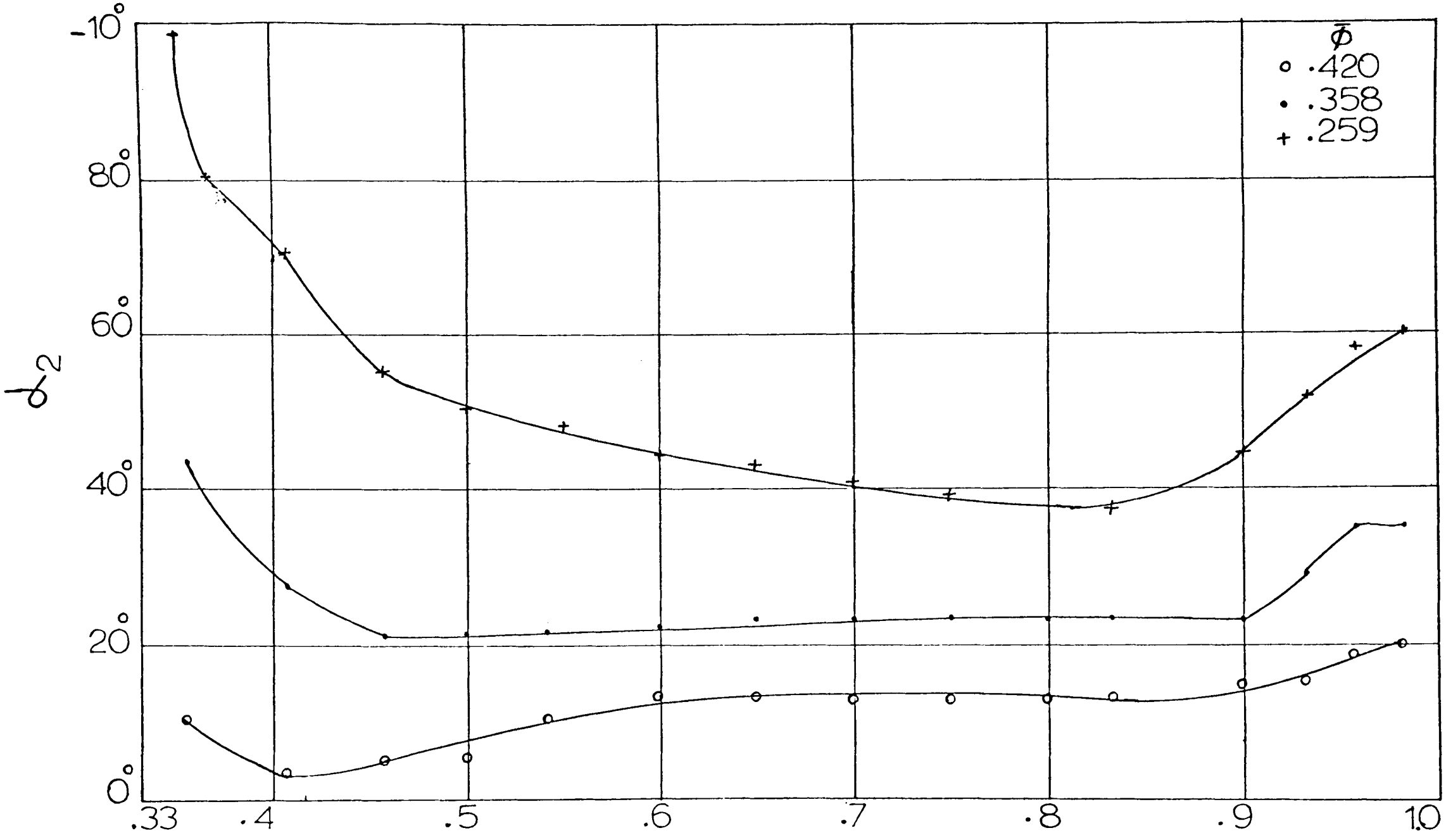

ABSOLUTE OUTLET FLOW ANGLE

Fig. 5.13

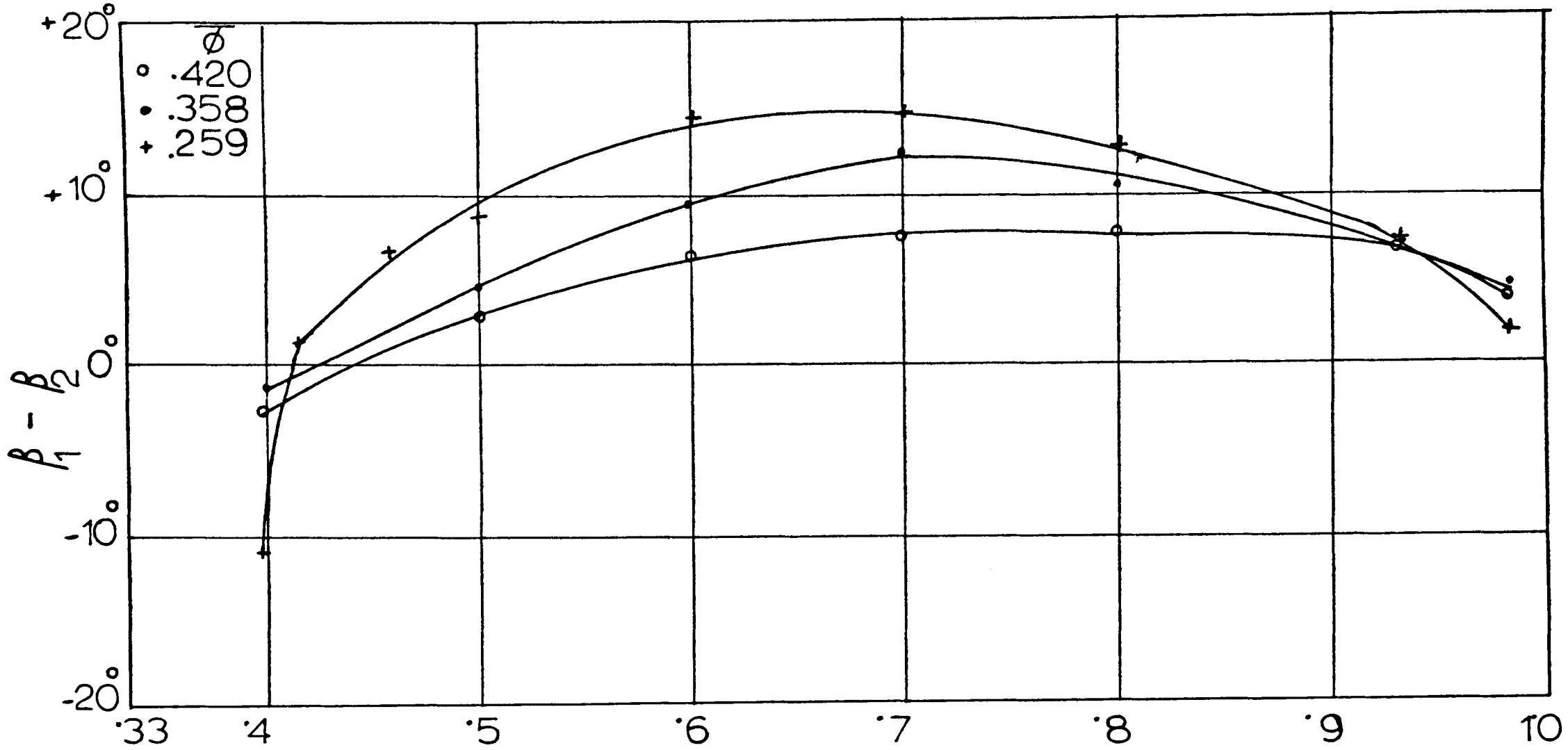

AIR TURNING ANGLES

Fig. 5.14

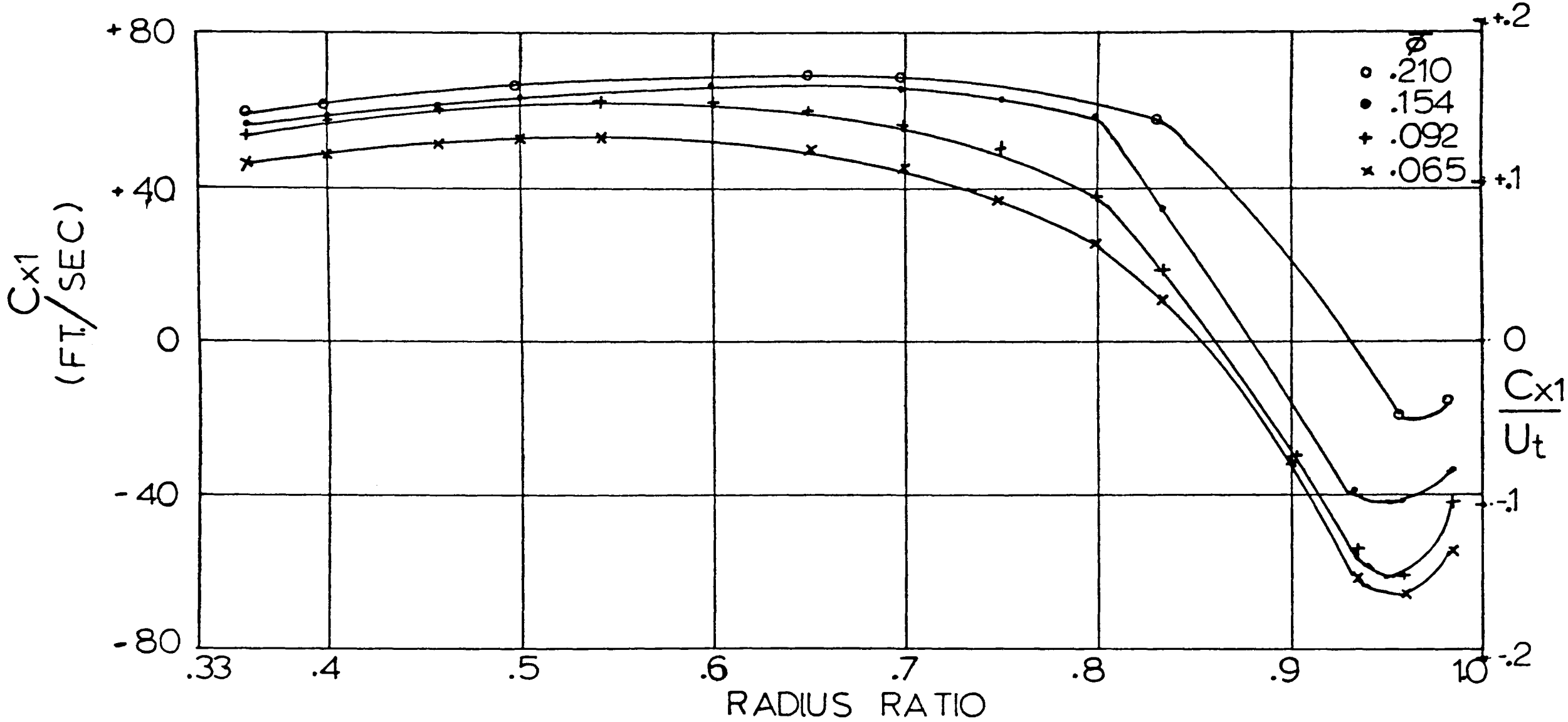

INLET AXIAL VELOCITY

Fig. 5.15

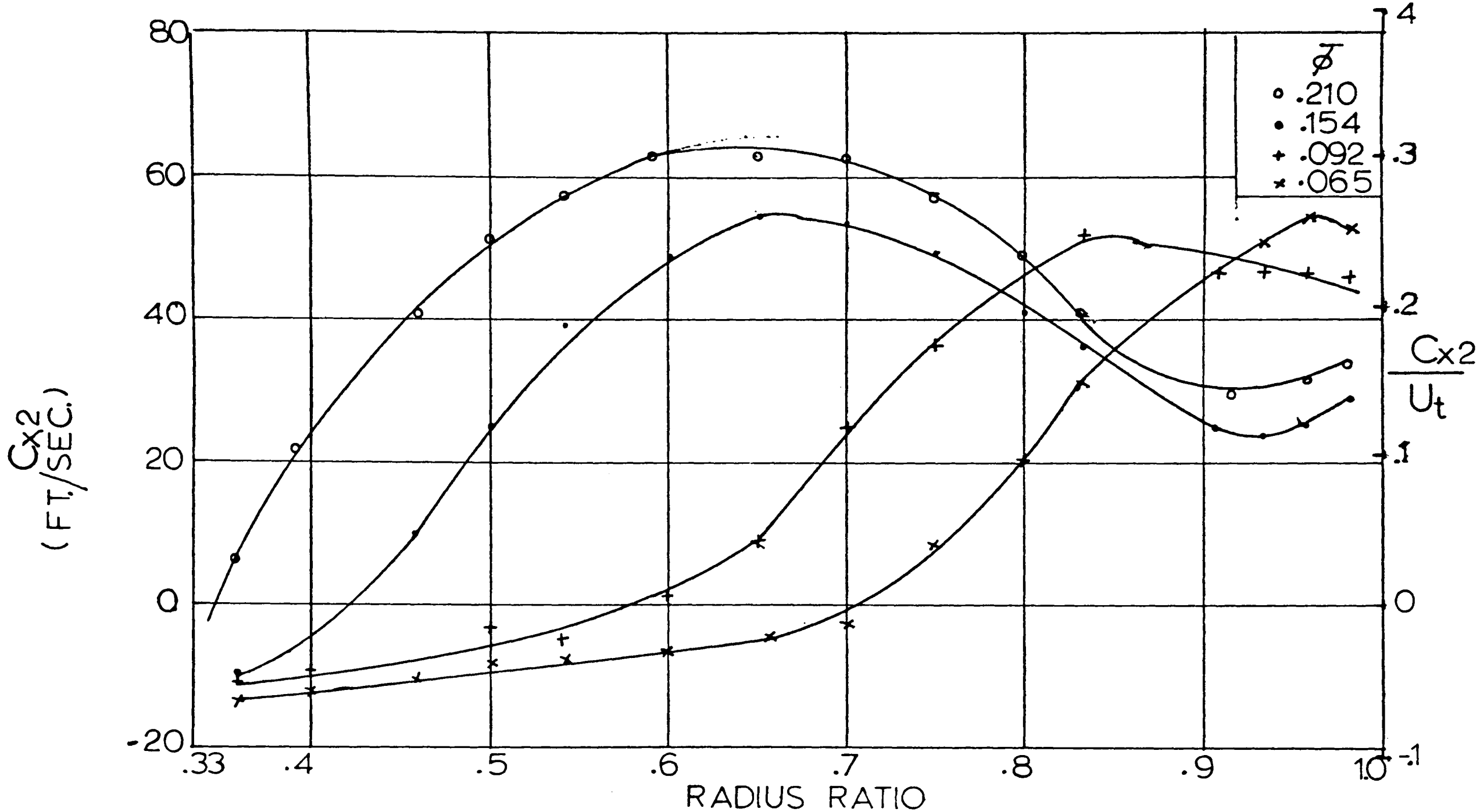

Fig. 5.16, OUTLET AXIAL VELOCITY

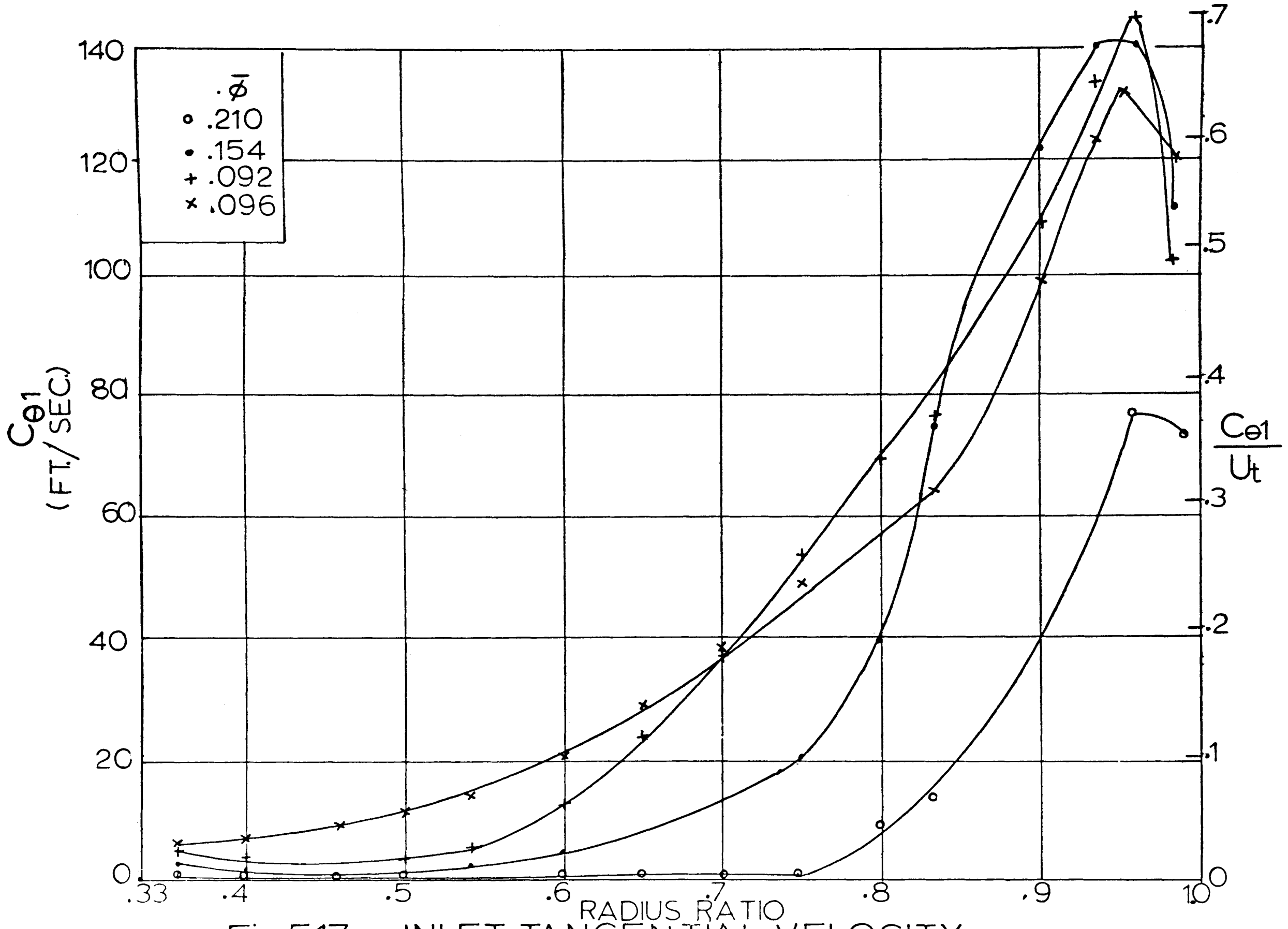

Fig. 5-17 INLET TANGENTIAL VELOCITY

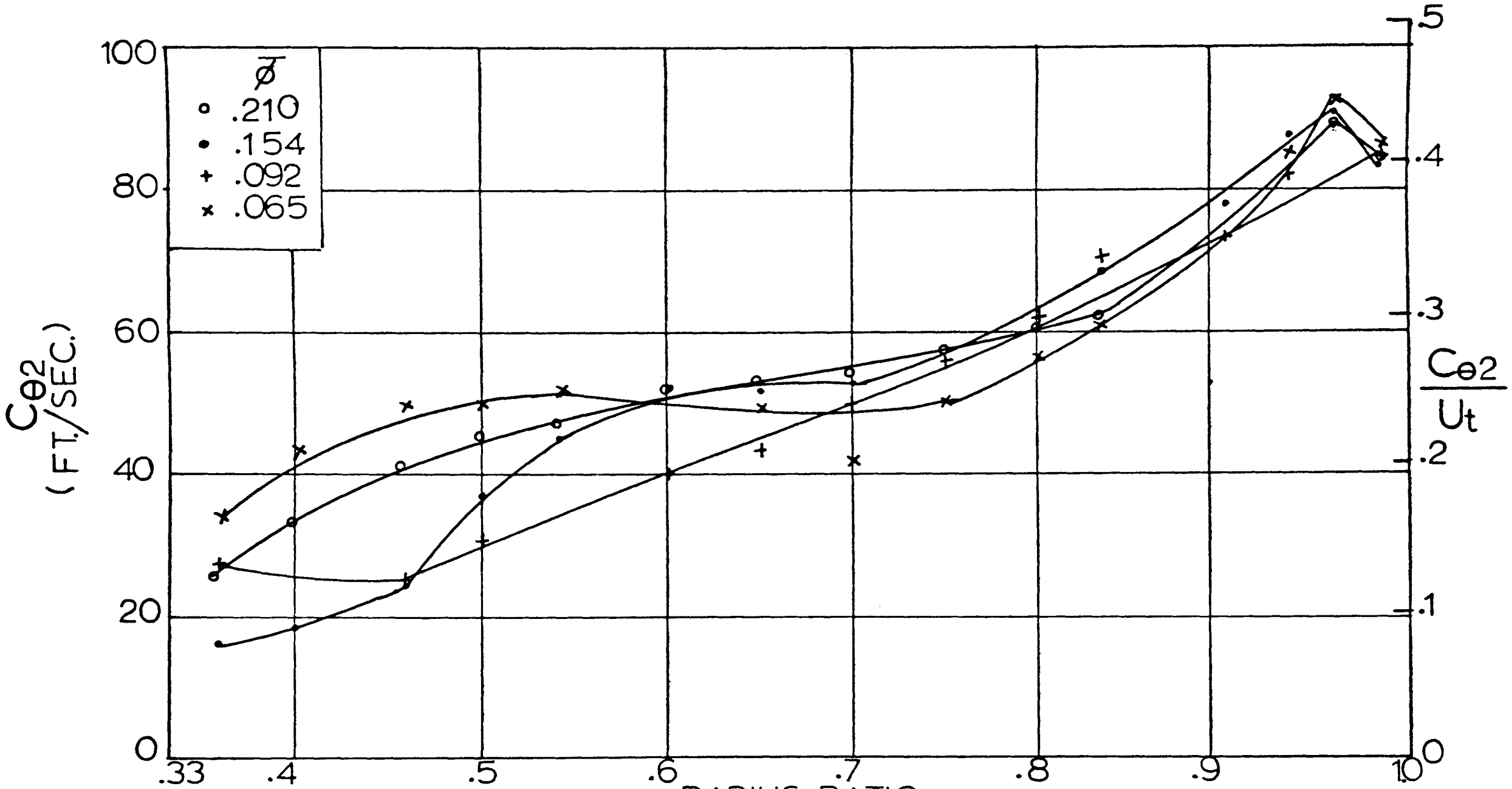

OUTLET TANGENTIAL VELOCITY

Fig. 5.18

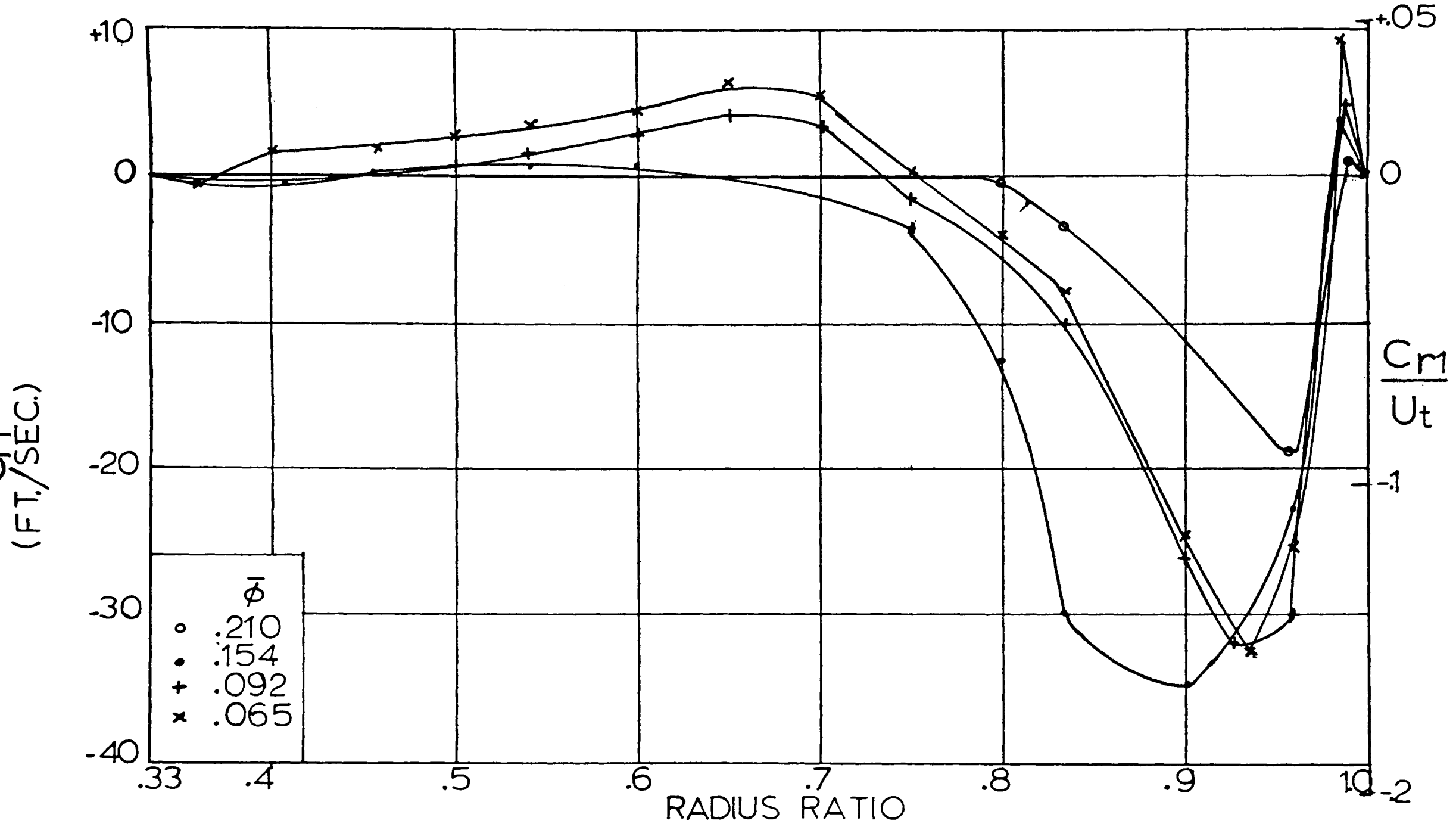

INLET RADIAL VELOCITY

Fig. 5.19

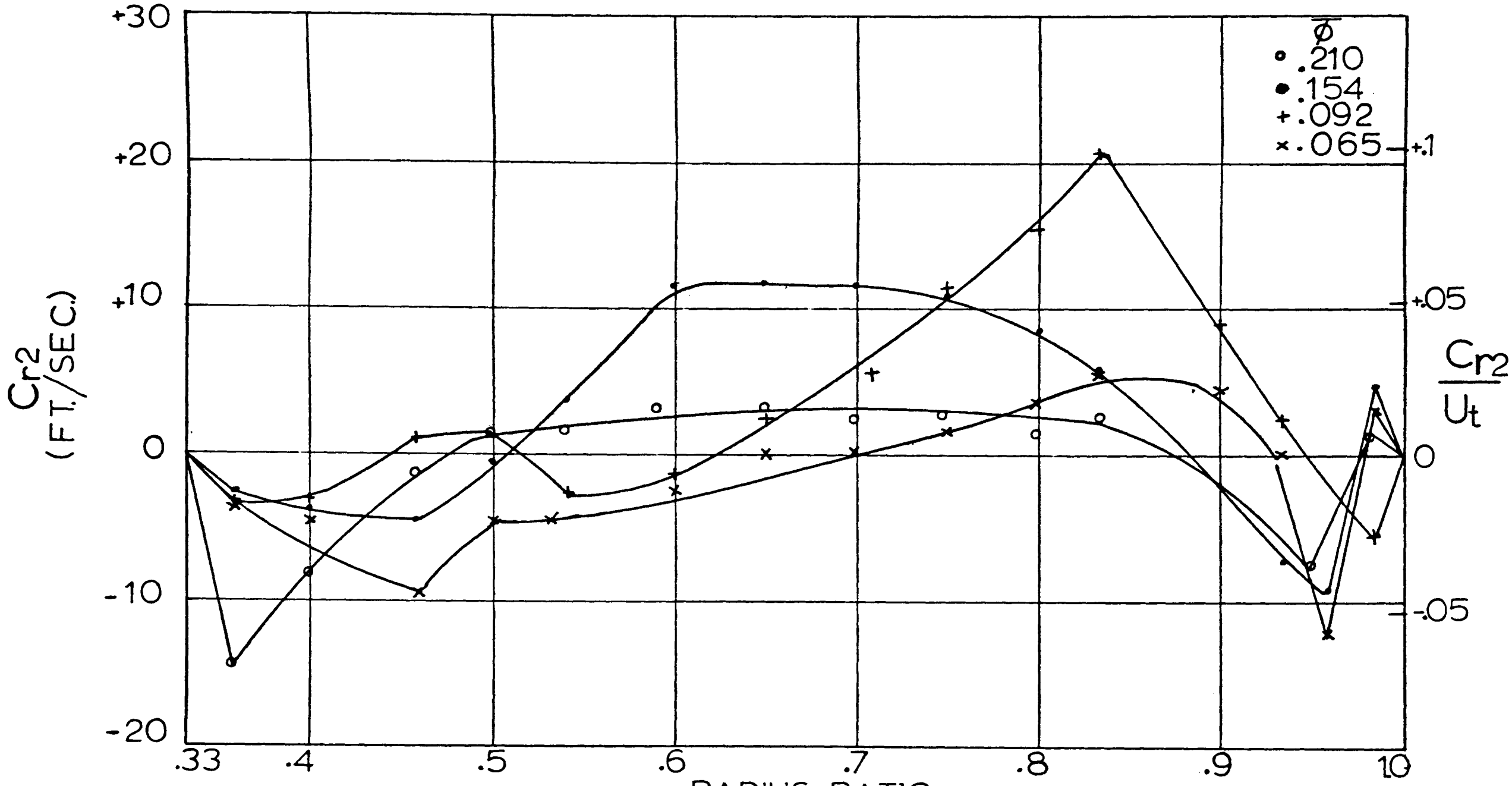

OUTLET RADIAL VELOCITY

Fig. 5.20

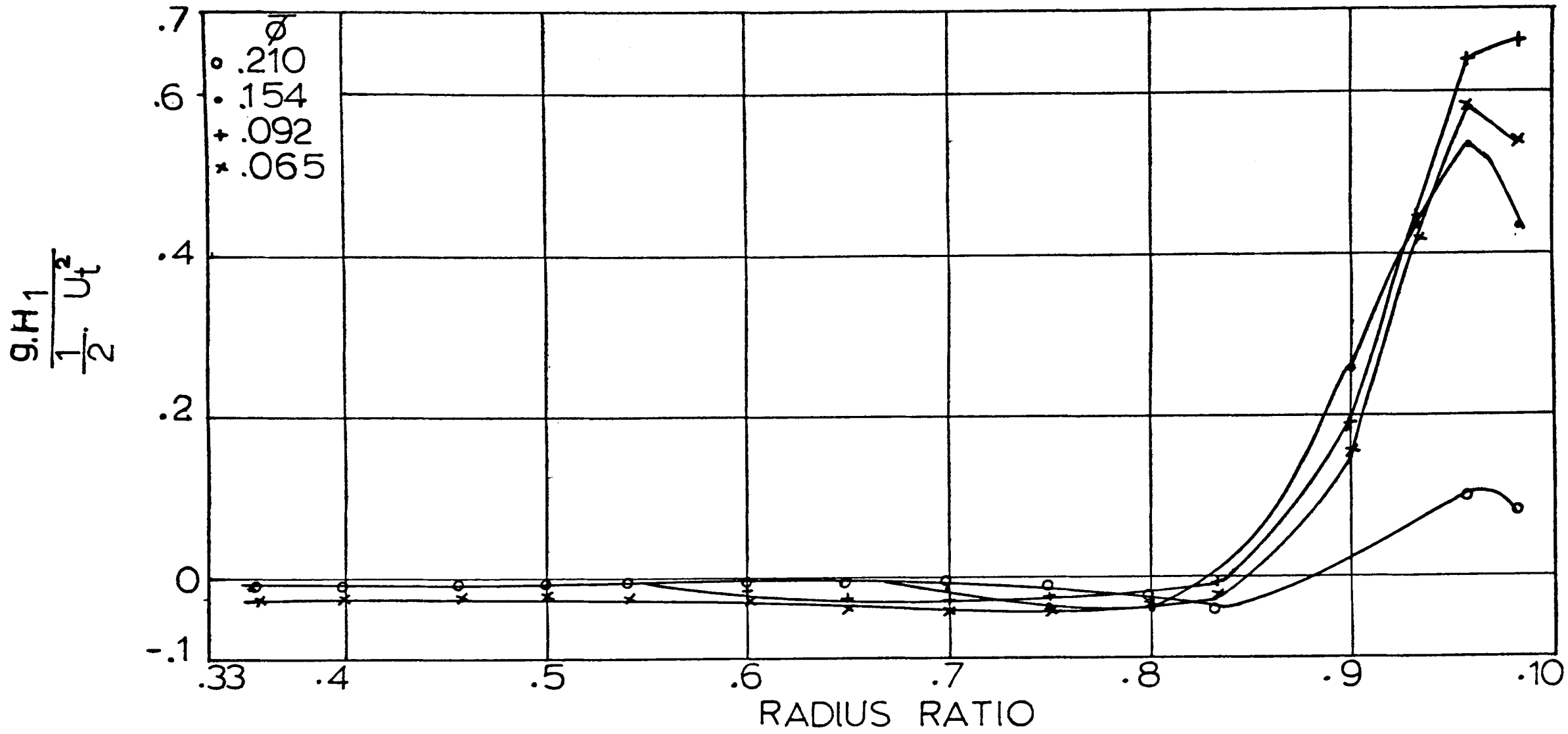

INLET TOTAL HEAD COEFFICIENT

Fig.5.21

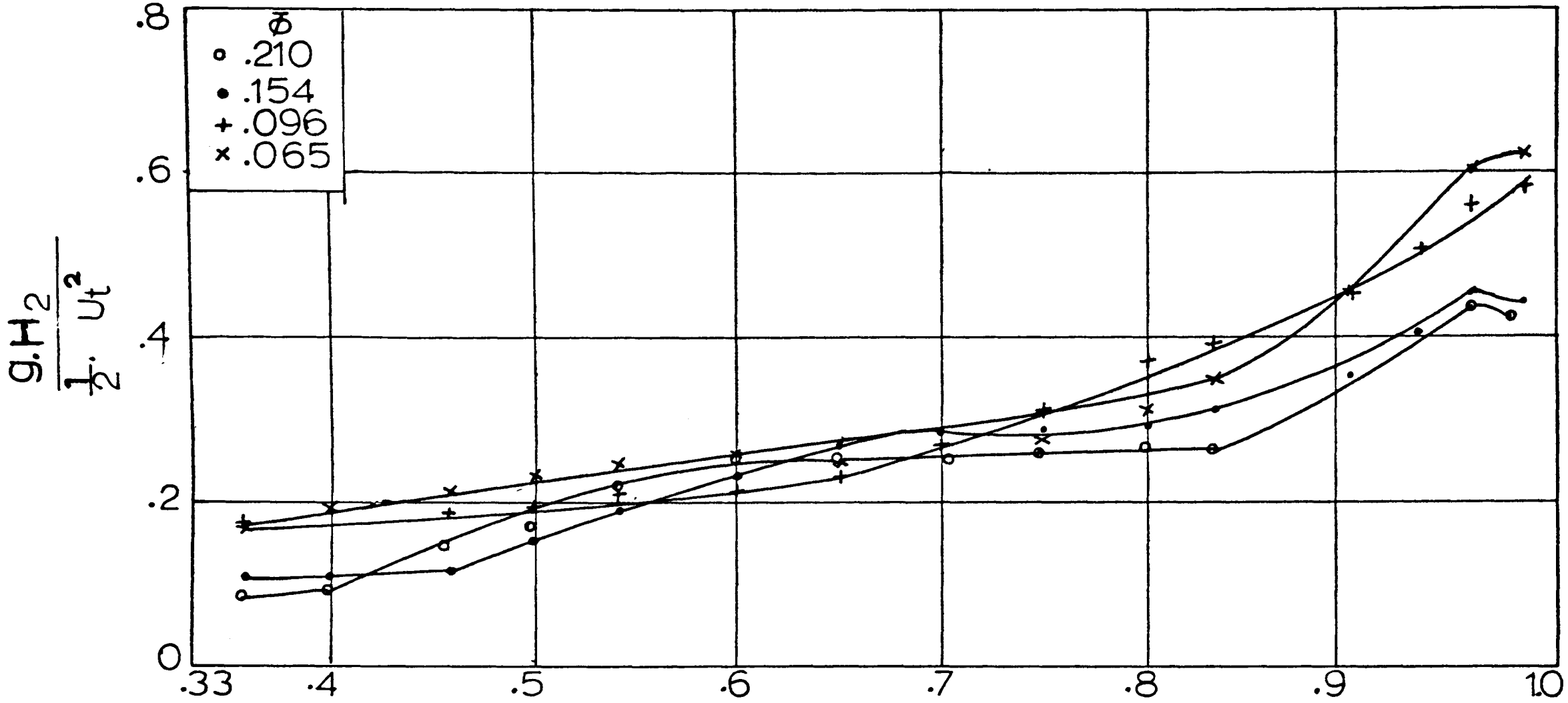

OUTLET TOTAL HEAD COEFFICIENT

Fig. 5.22

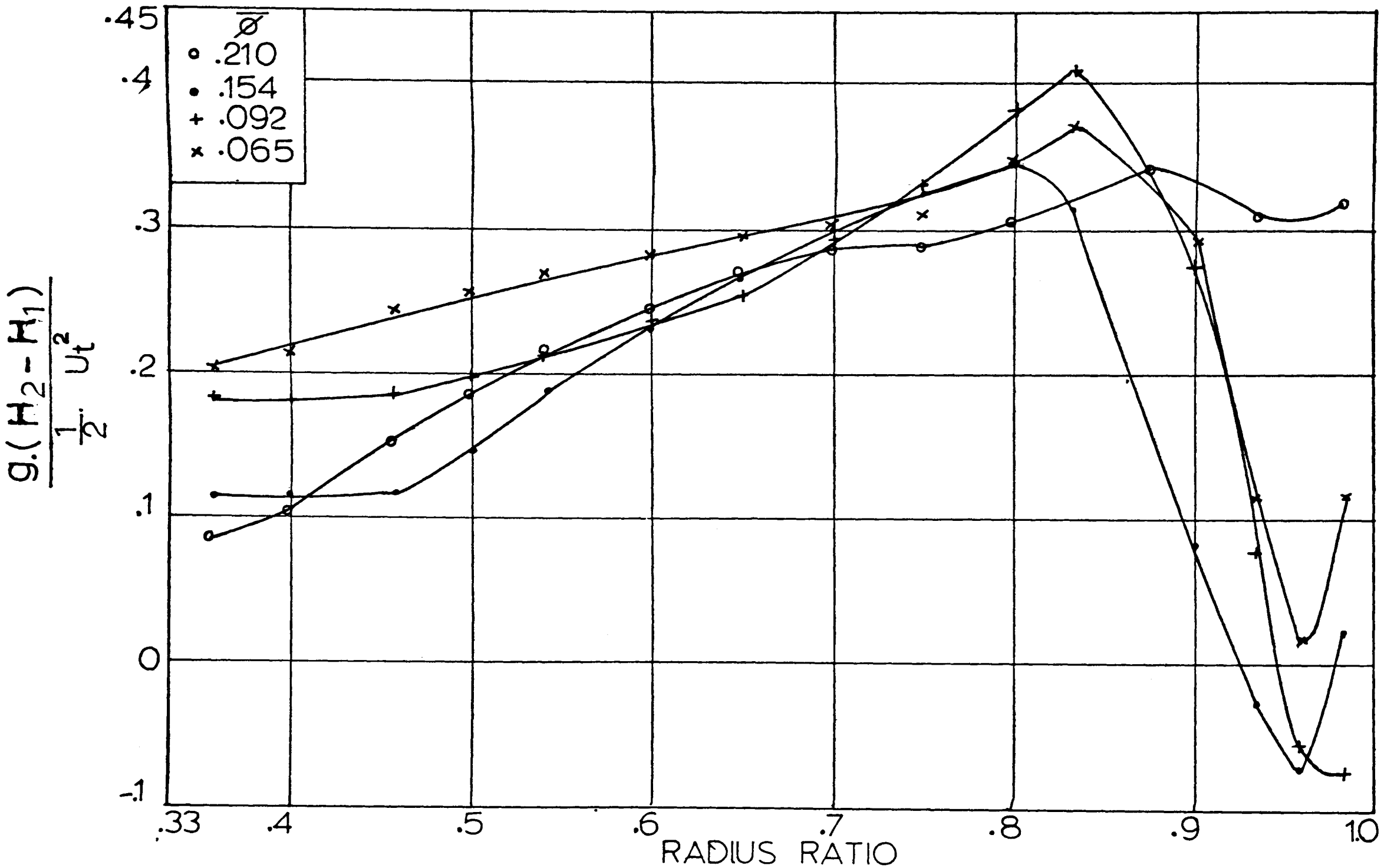

Fig 5.23, TOTAL HEAD RISE COEFFICIENT

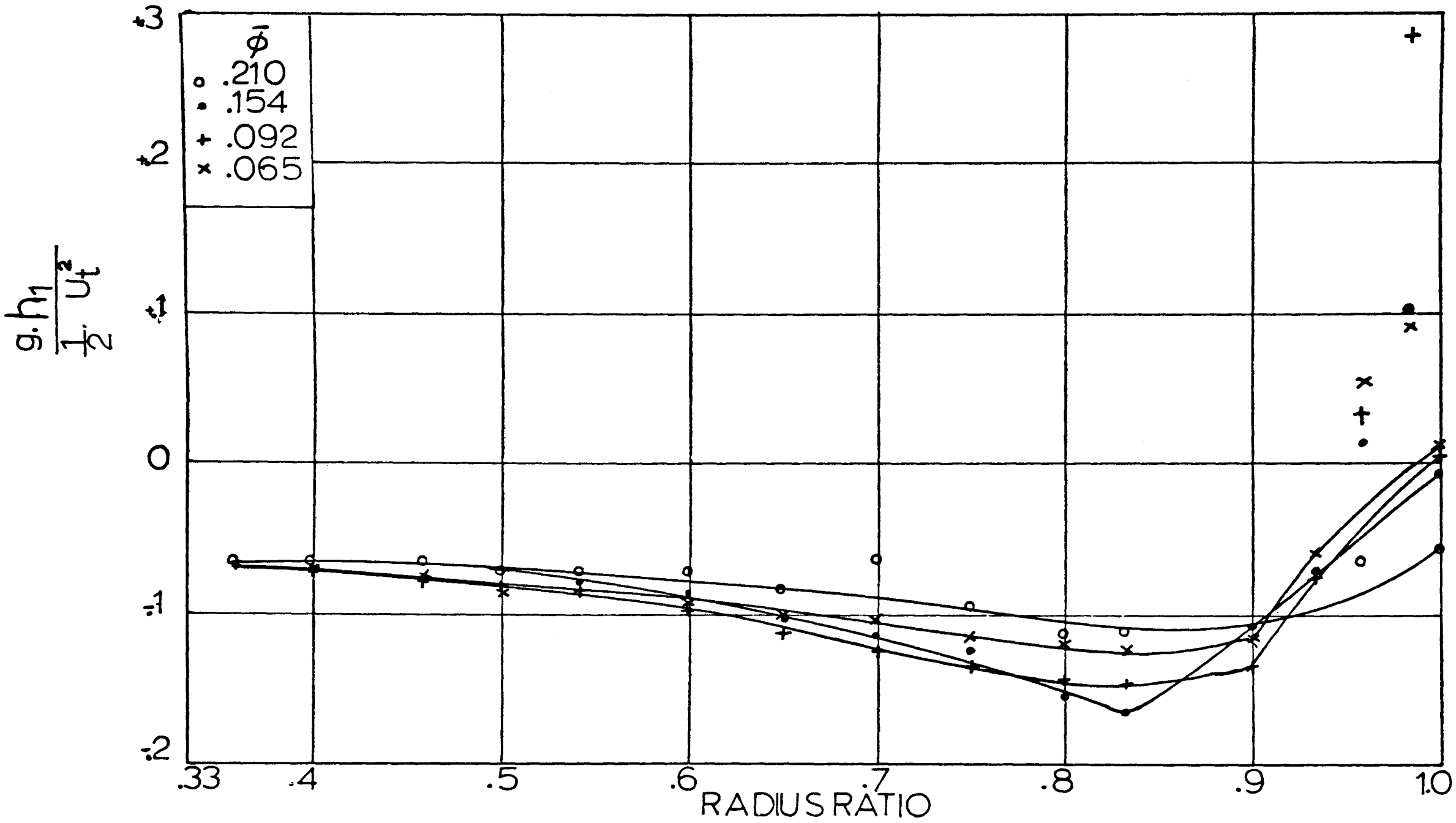

INLET STATIC HEAD COEFFICIENT

Fig 5.24

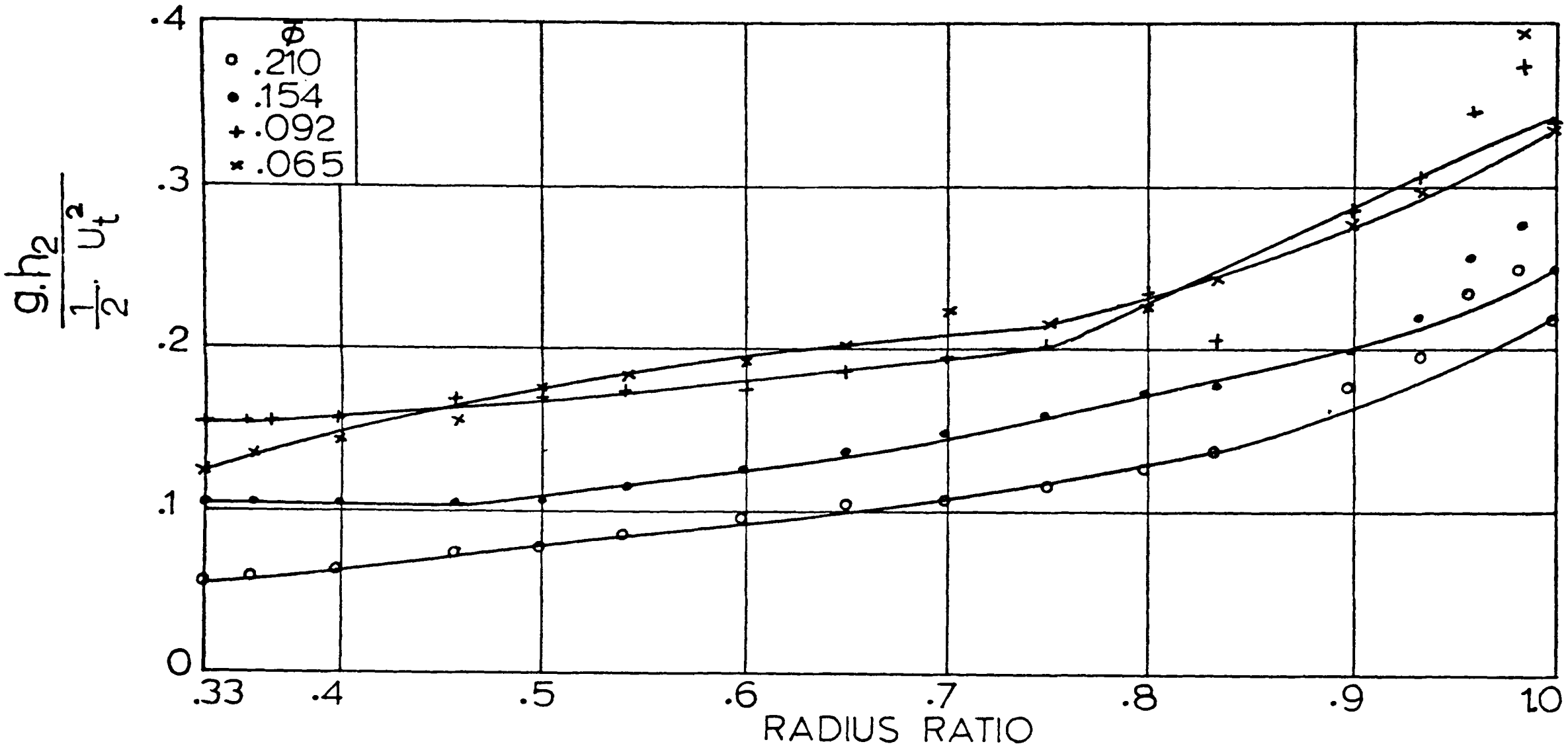

Fig. 5.25, OUTLET STATIC HEAD RISE COEFFICIENT

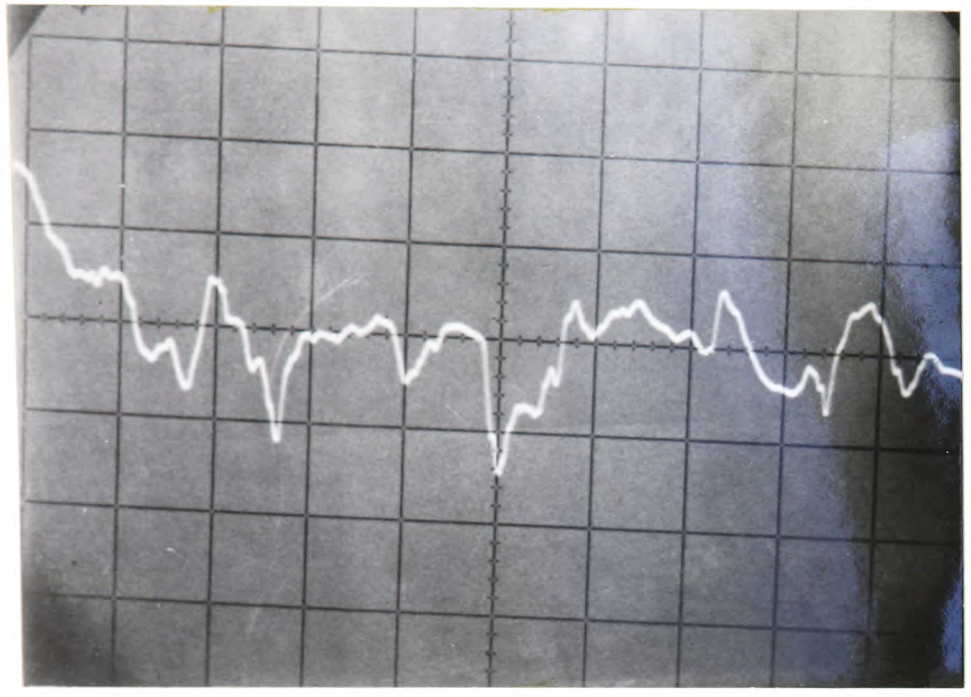

$\bar{\phi}$ = 0.420

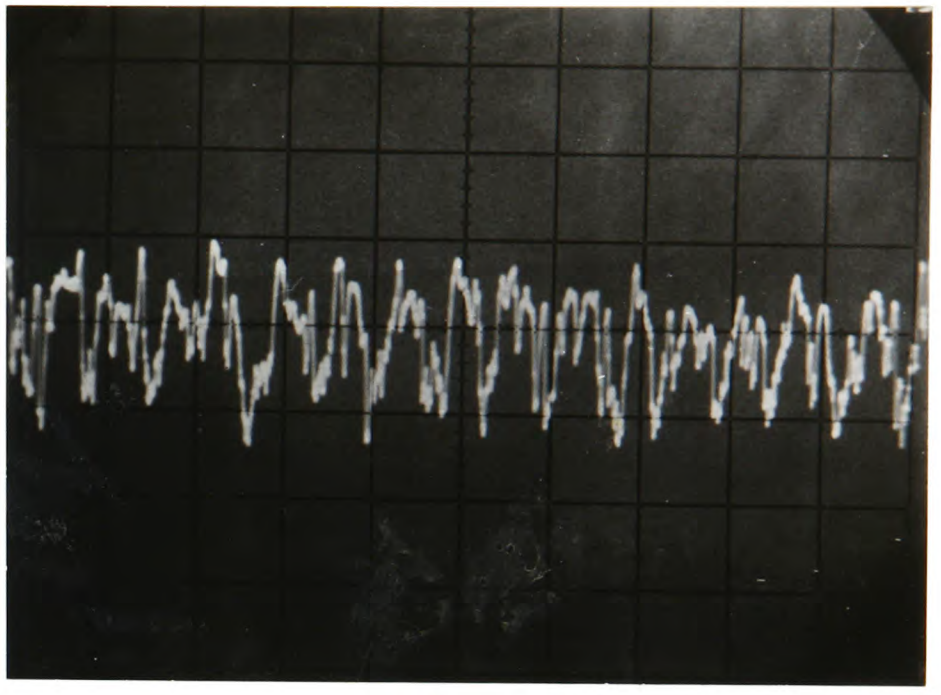

$\bar{\phi}$ = 0.282

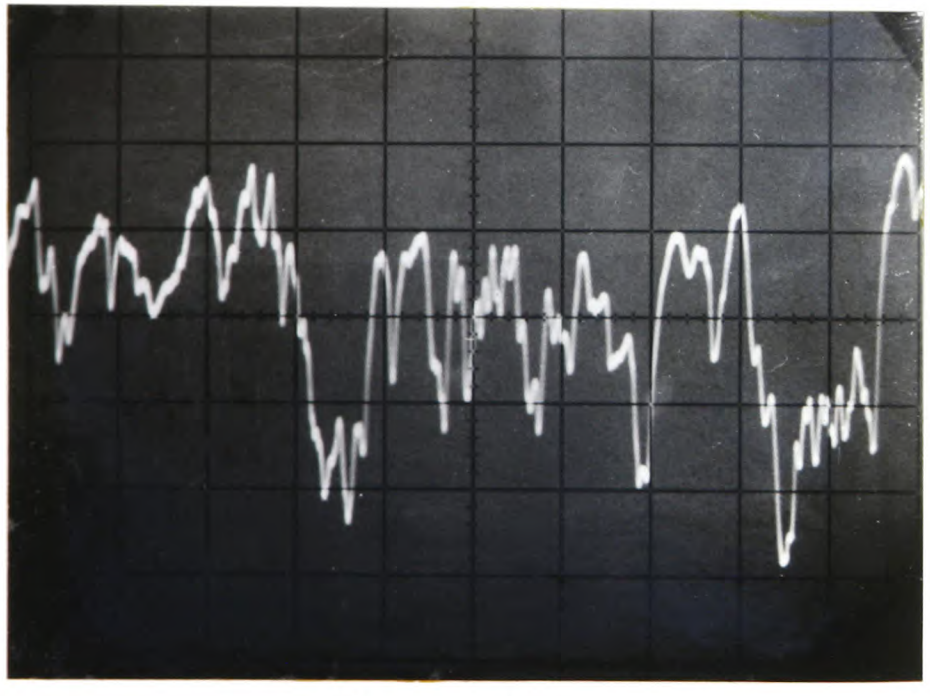

$\bar{\phi}$ = 0.259

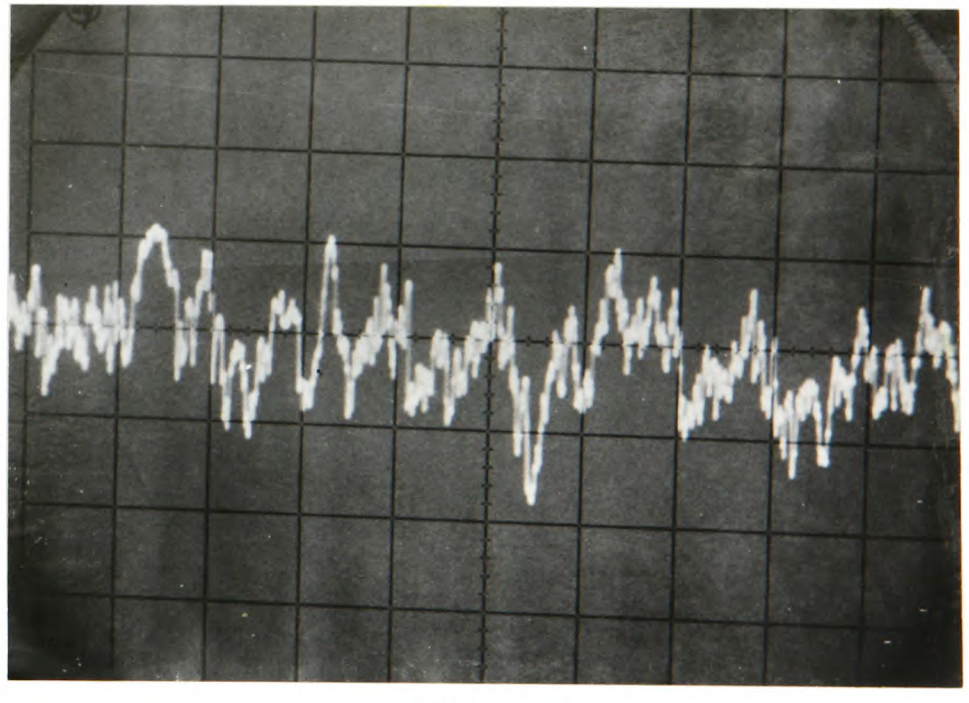

$\bar{\phi}$ = 0.210

FIG. 5.26. HOT WIRE TRACES OF IMPELLER OUTLET FLOW CONDITIONS AT HUB TIP RADIUS RATIO OF 0.983.

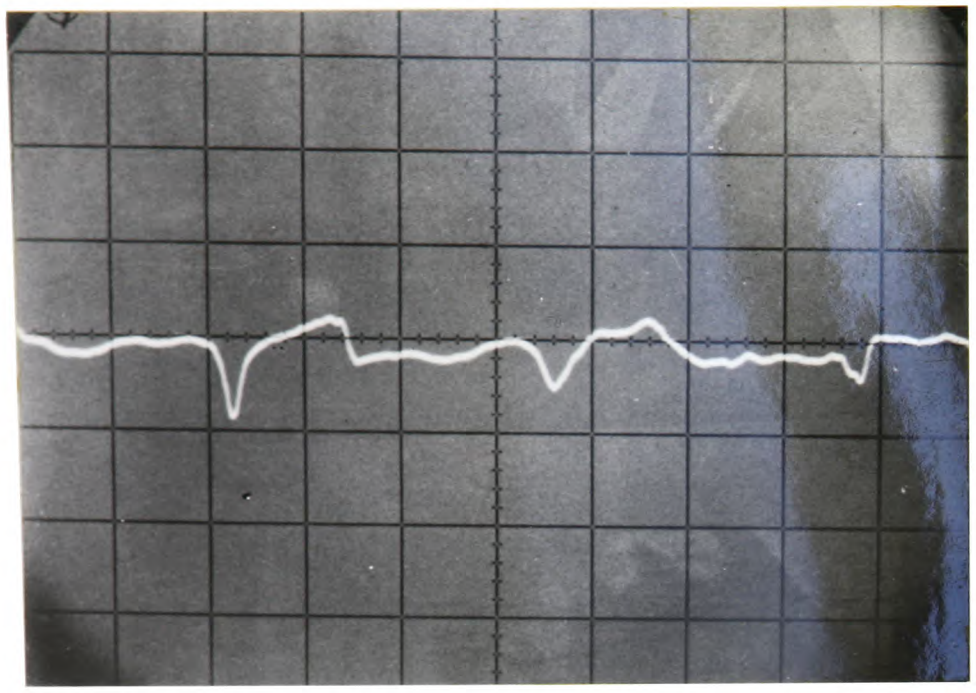

$\bar{\phi}$ = 0.420

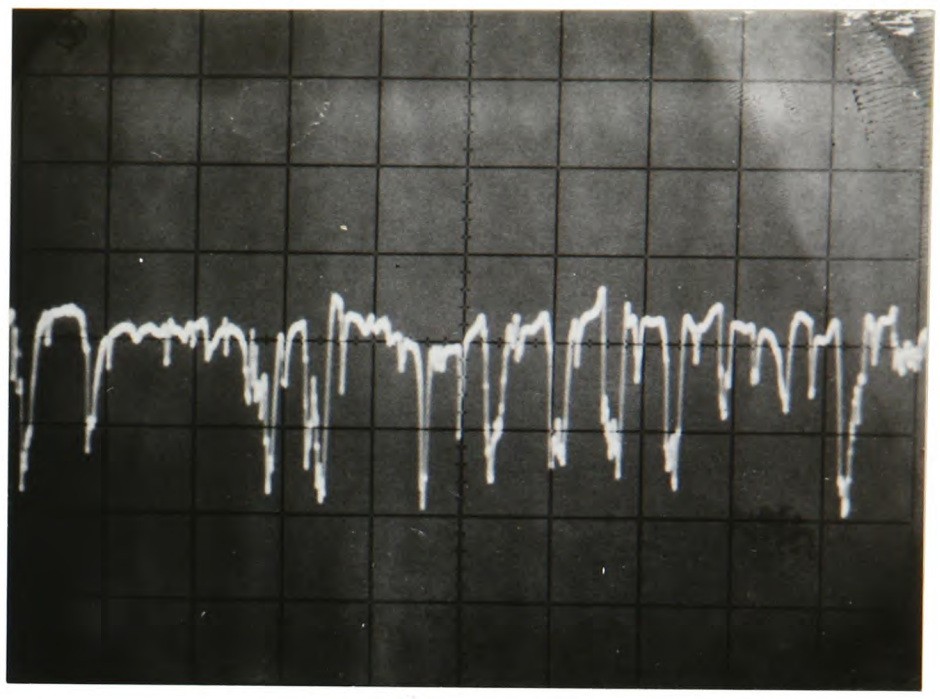

$\bar{\phi}$ = 0.282

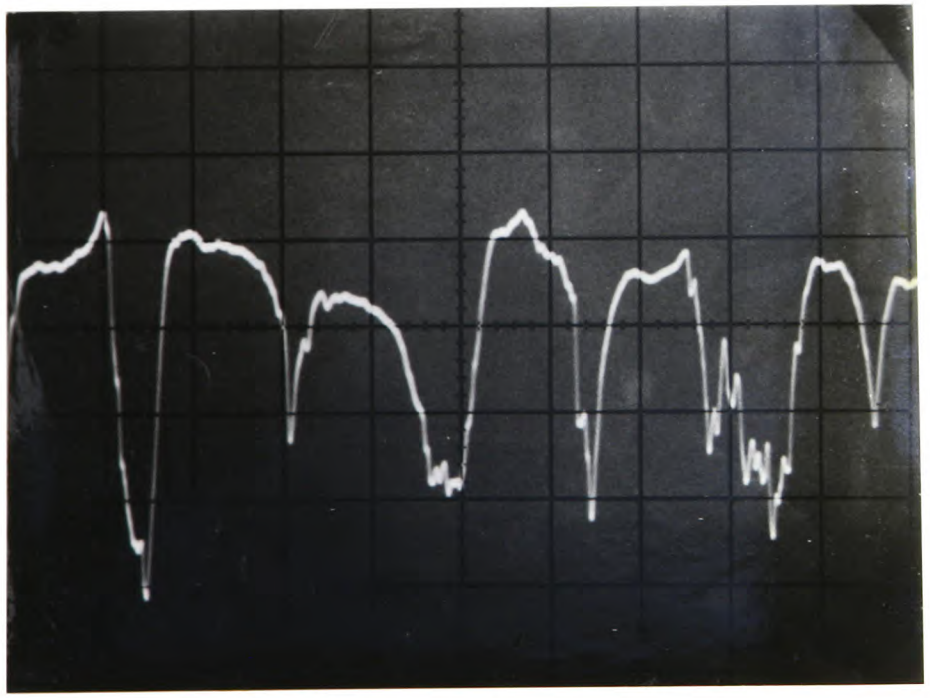

$\bar{\phi}$ = 0.259

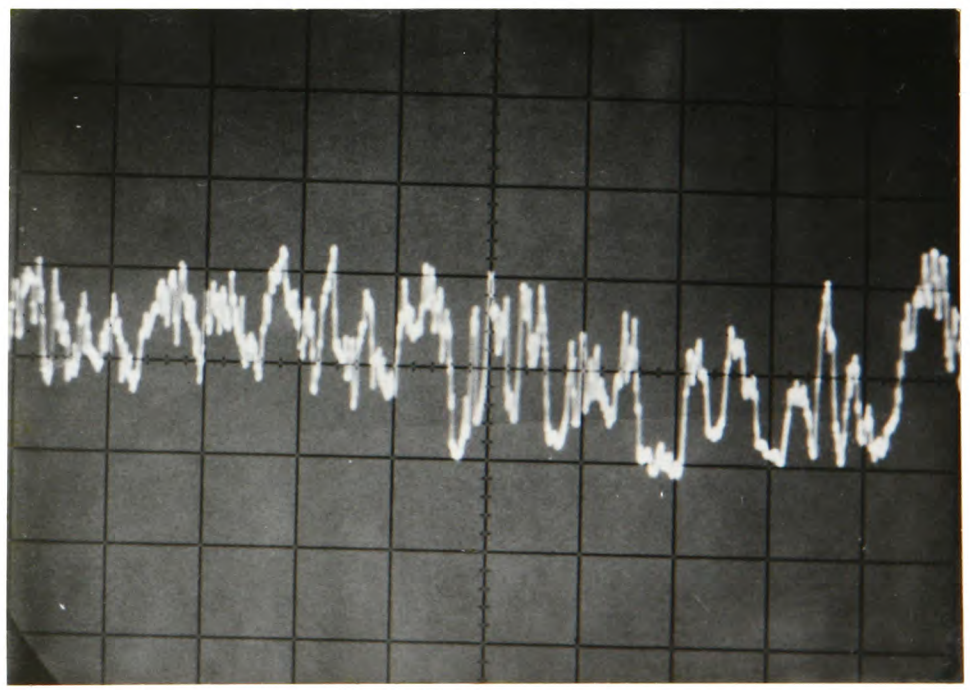

$\bar{\phi}$ = 0.210

FIG. 5.26 (contd.) HOT WIRE TRACES OF IMPELLER OUTLET FLOW CONDITIONS AT HUB TIP RADIUS RATIO OF 0.933.

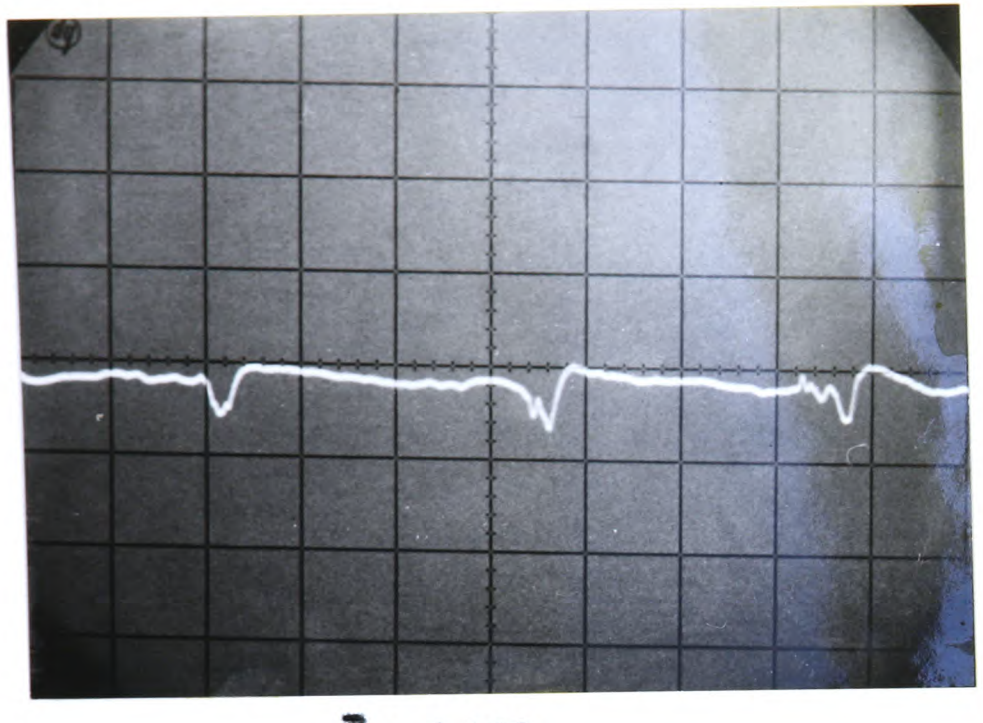

$\bar{\phi}$ = 0.420

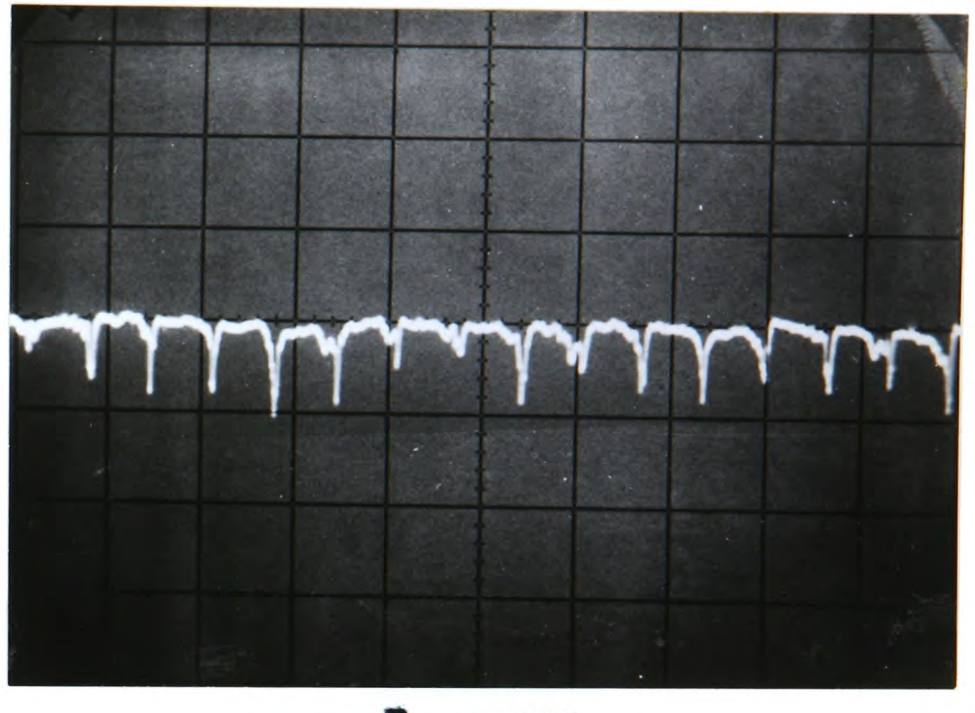

$\bar{\phi}$ = 0.282

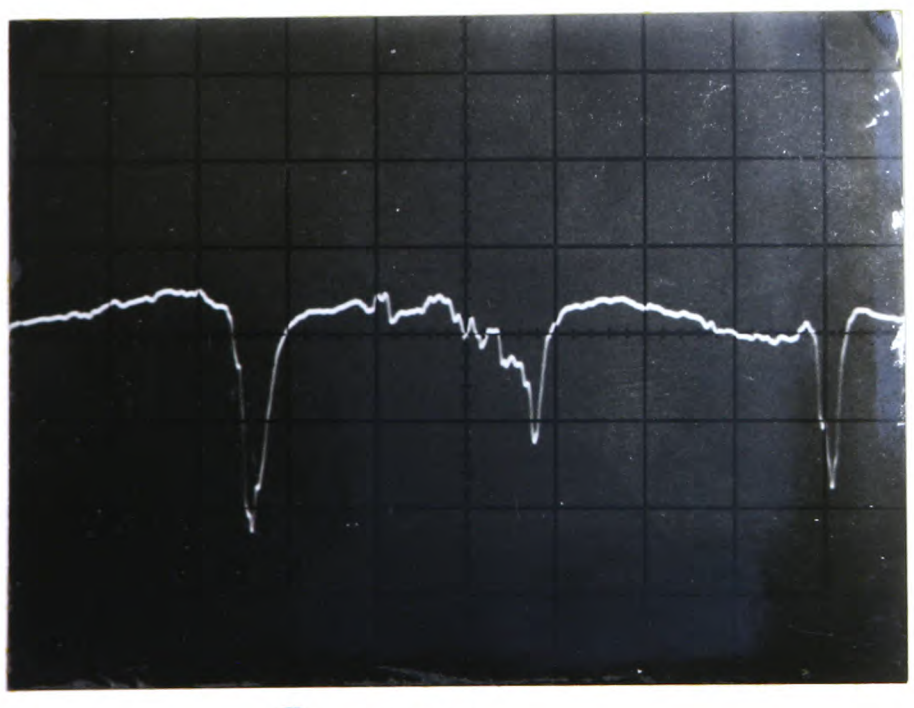

$\bar{\phi}$ = 0.259

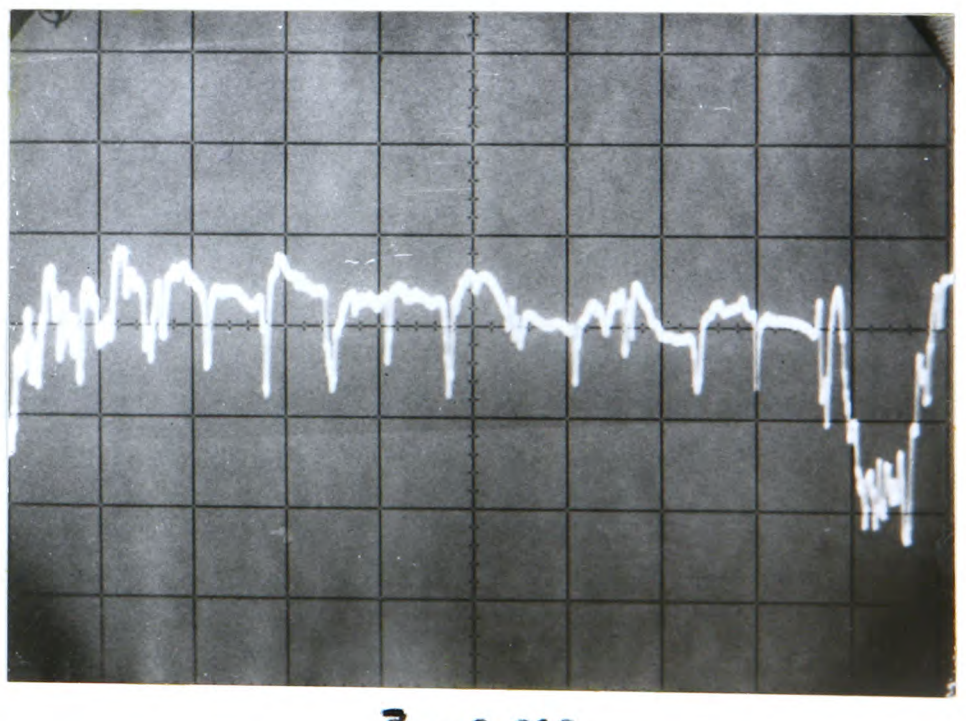

$\bar{\phi}$ = 0.210

FIG. 5.26 (contd.) HOT WIRE TRACES OF IMPELLER OUTLET FLOW CONDITIONS AT HUB TIP RADIUS RATIO OF 0.8

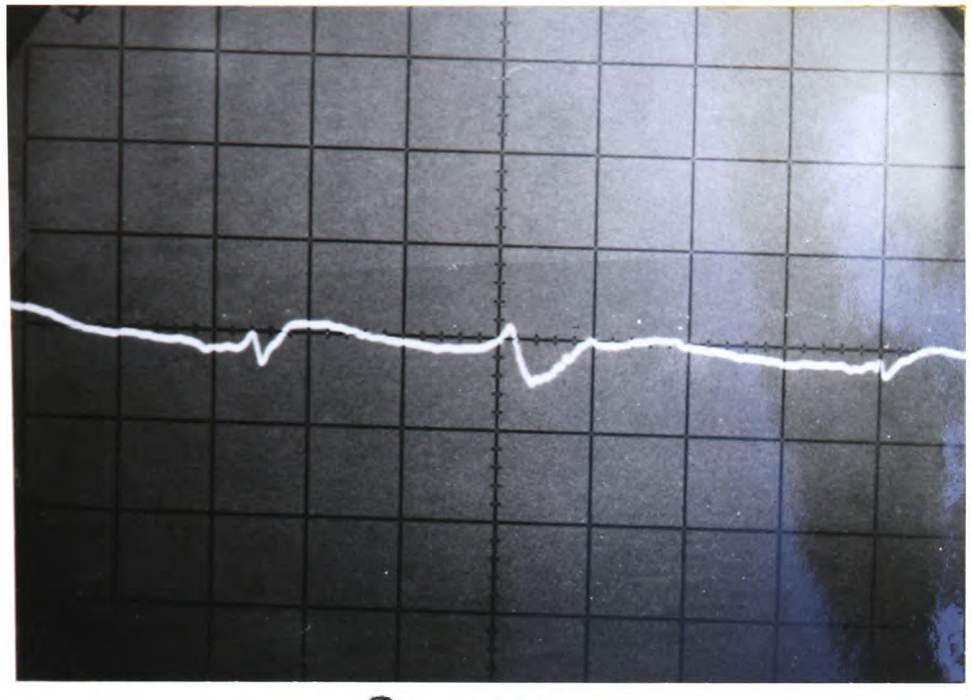

$\bar{\phi}$ = 0.420

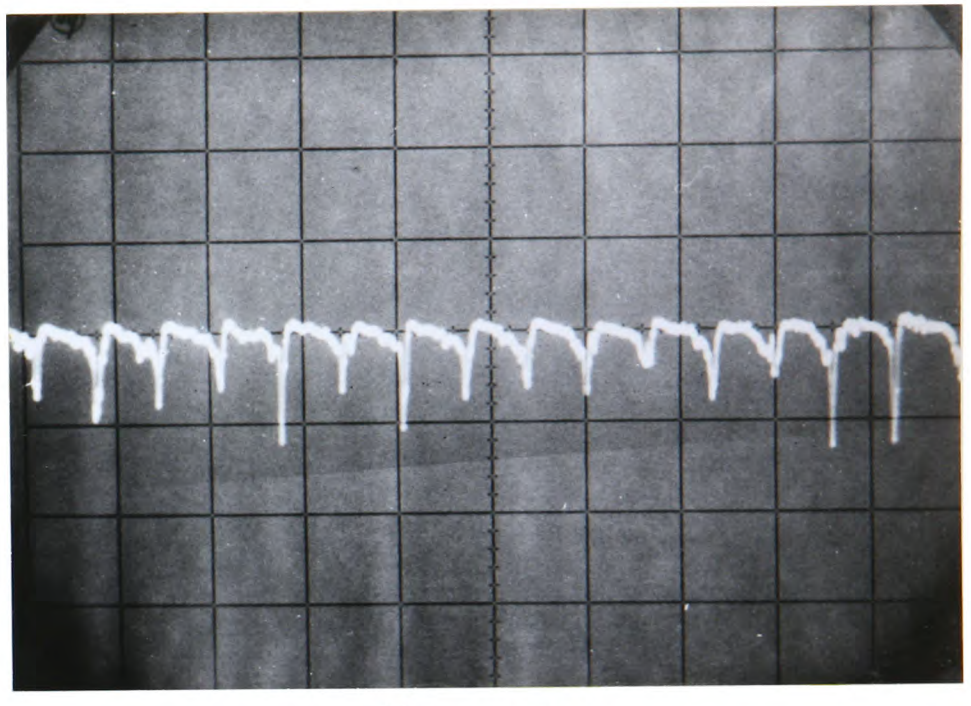

$\bar{\phi}$ = 0.282

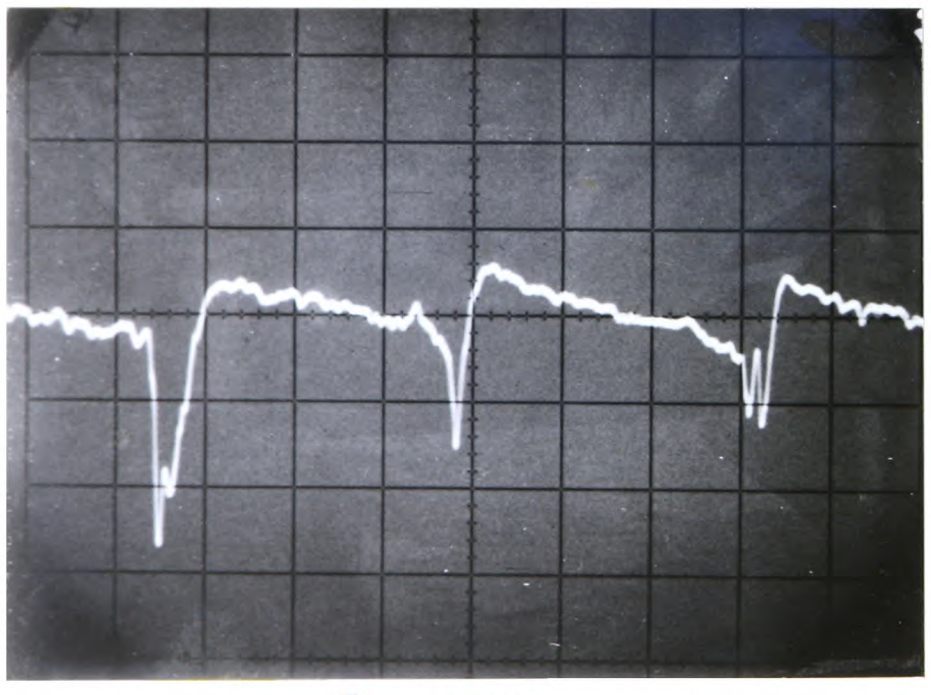

$\bar{\phi}$ = 0.259

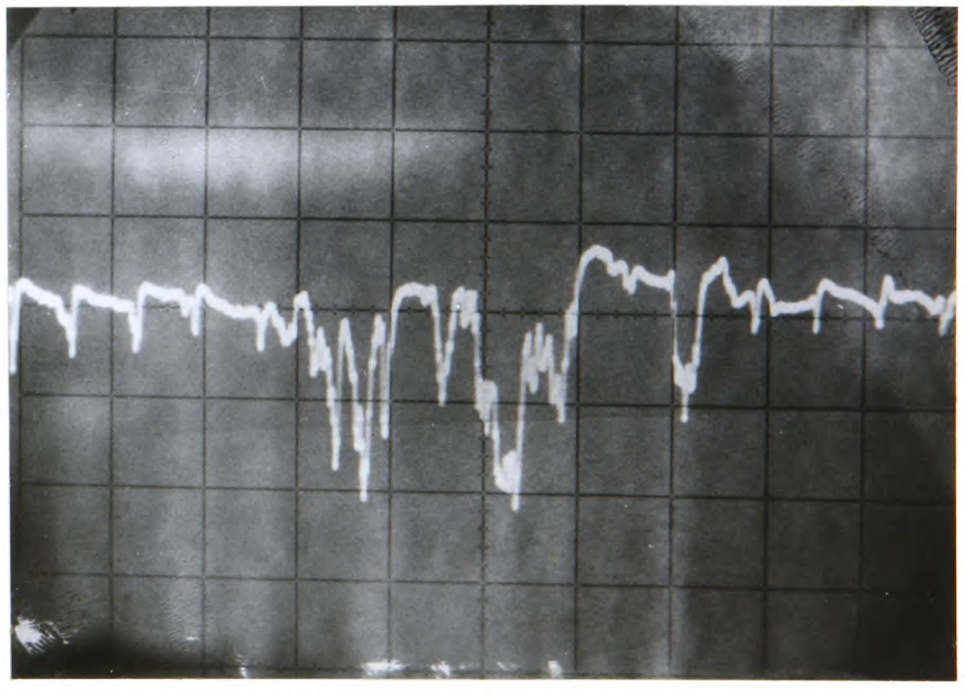

$\bar{\phi}$ = 0.210

FIG. 5.26 (contd.) HOT WIRE TRACES OF IMPELLER OUTLET FLOW CONDITIONS AT HUB TIP RADIUS RATIO OF 0.7

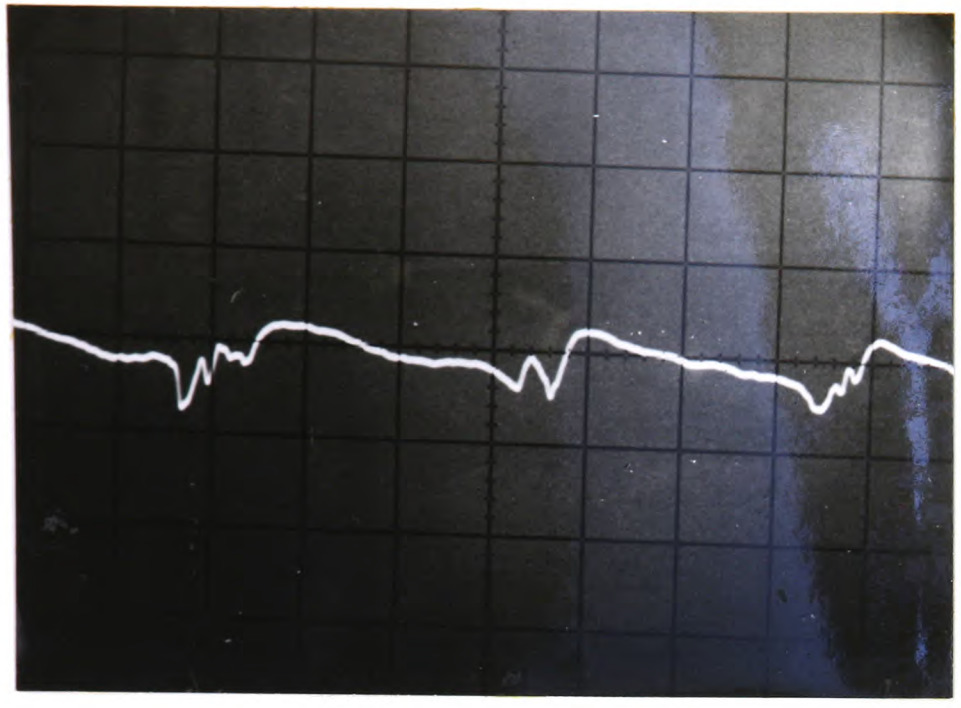

$\bar{\phi}$ = 0.420

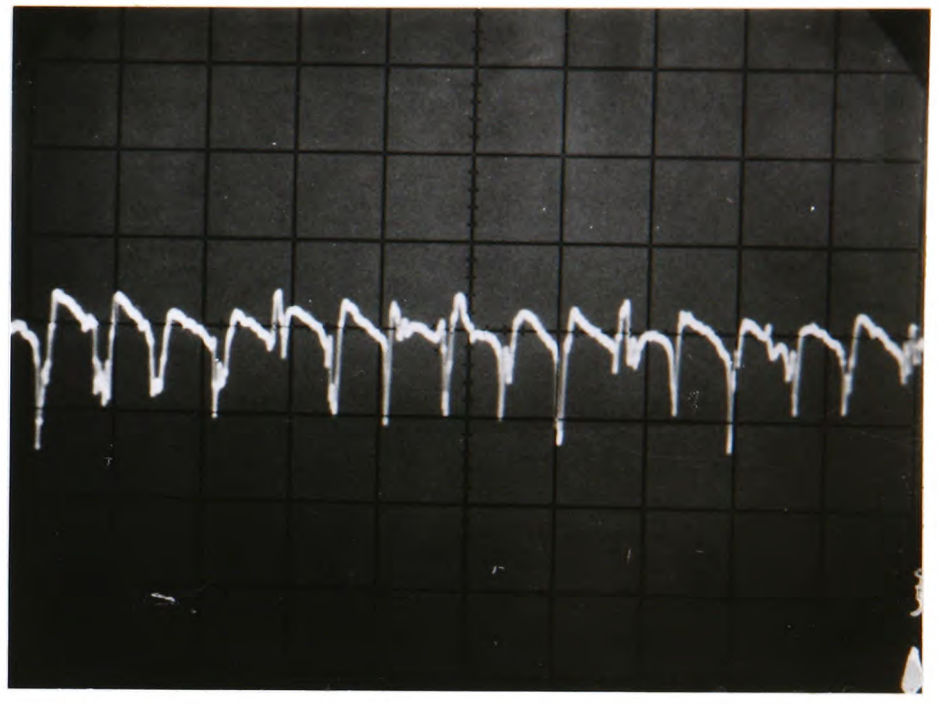

$\bar{\phi}$ = 0.282

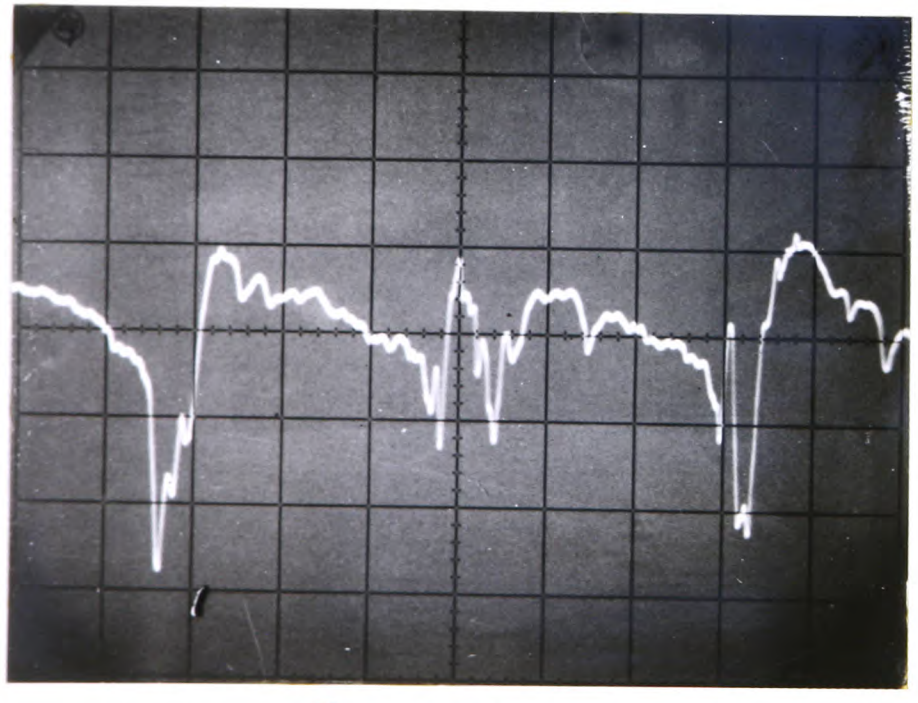

$\bar{\phi}$ = 0.259

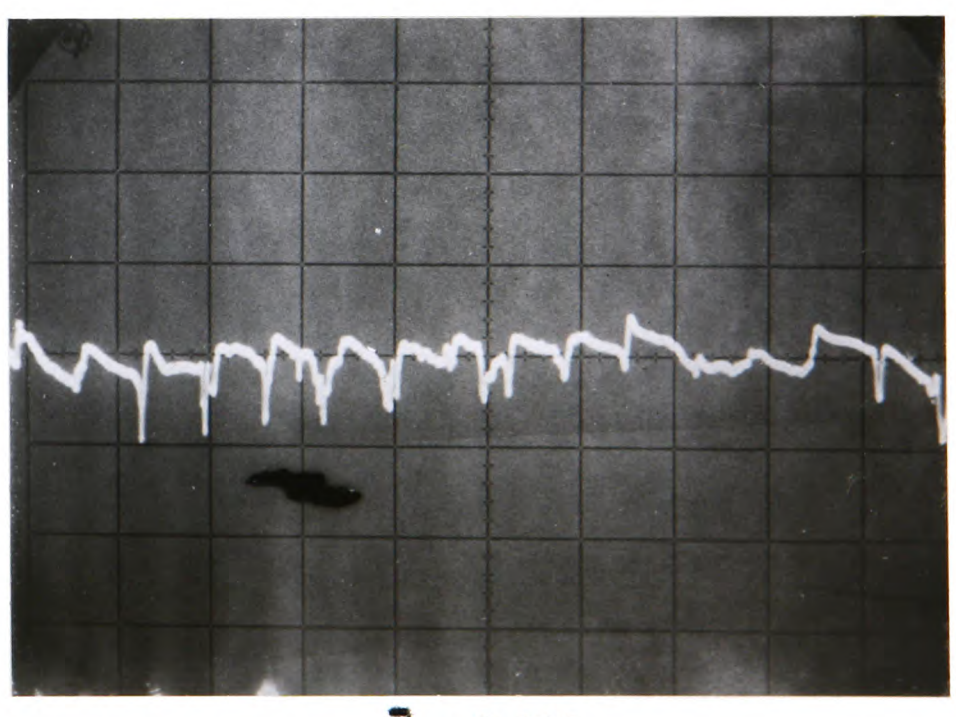

$\bar{\phi}$ = 0.210

FIG. 5.26 (contd.) HOT WIRE TRACES OF IMPELLER OUTLET FLOW CONDITIONS AT HUB TIP RADIUS RATIO OF 0.6

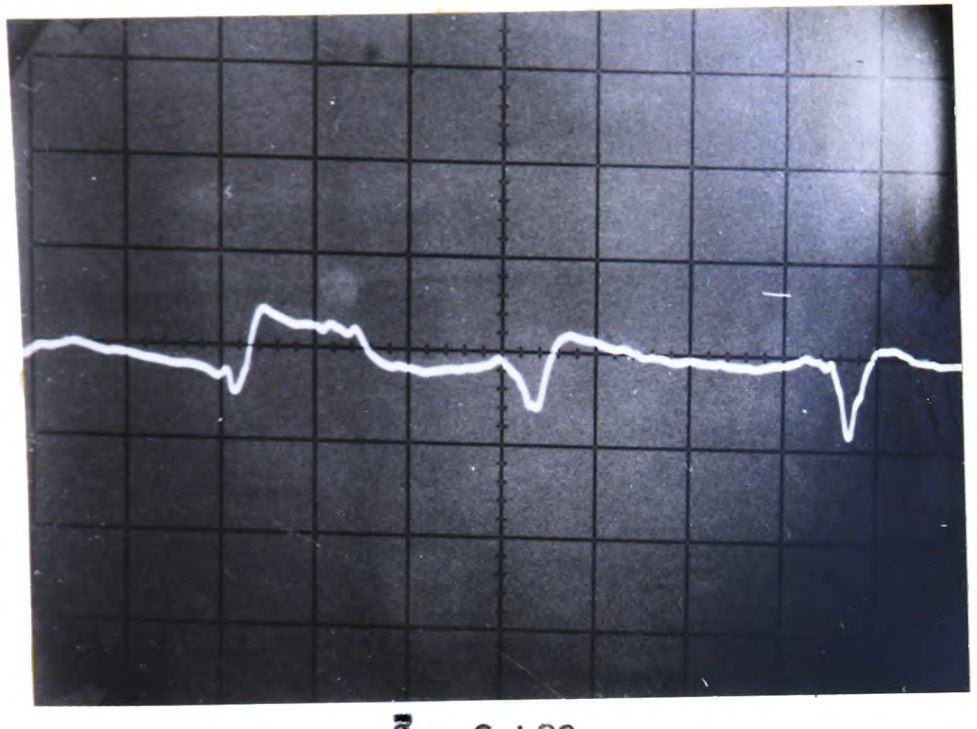

$\bar{\phi}$ = 0.420

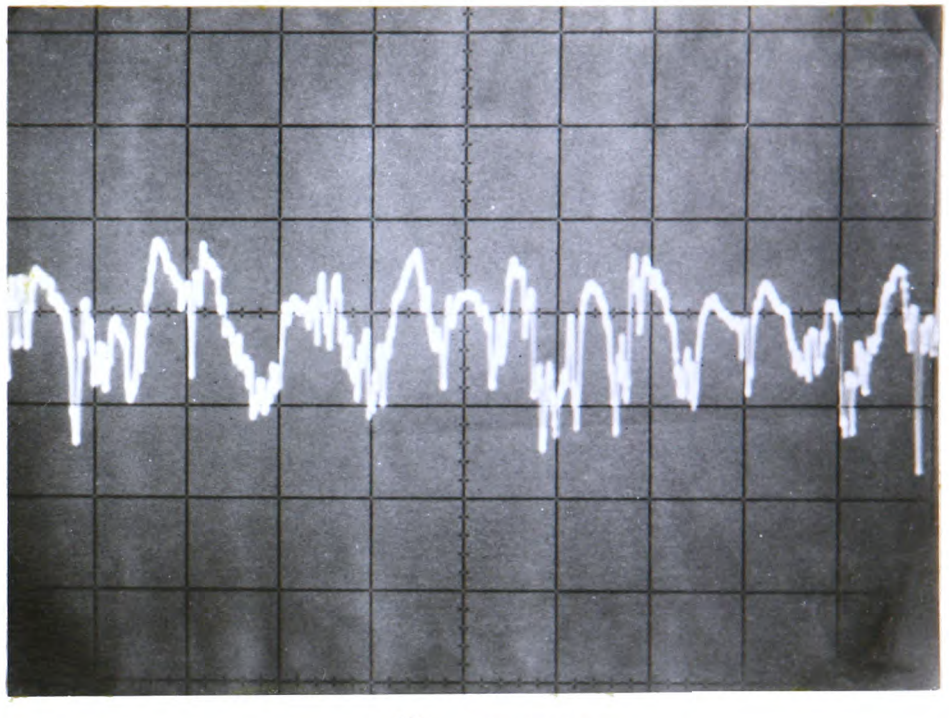

$\bar{\phi}$ = 0.282

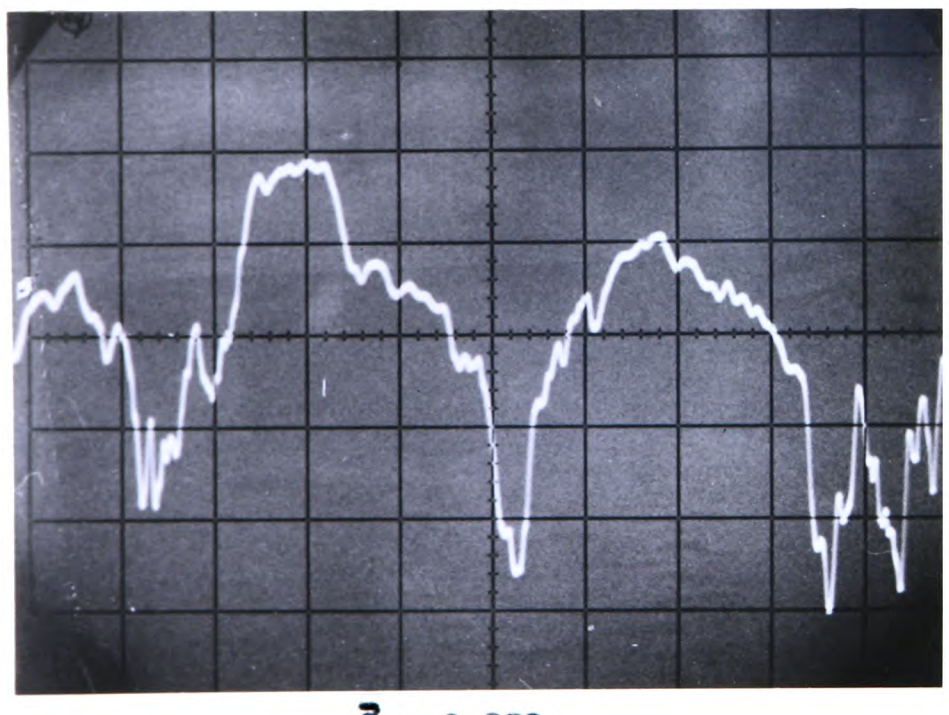

$\bar{\phi}$ = 0.259

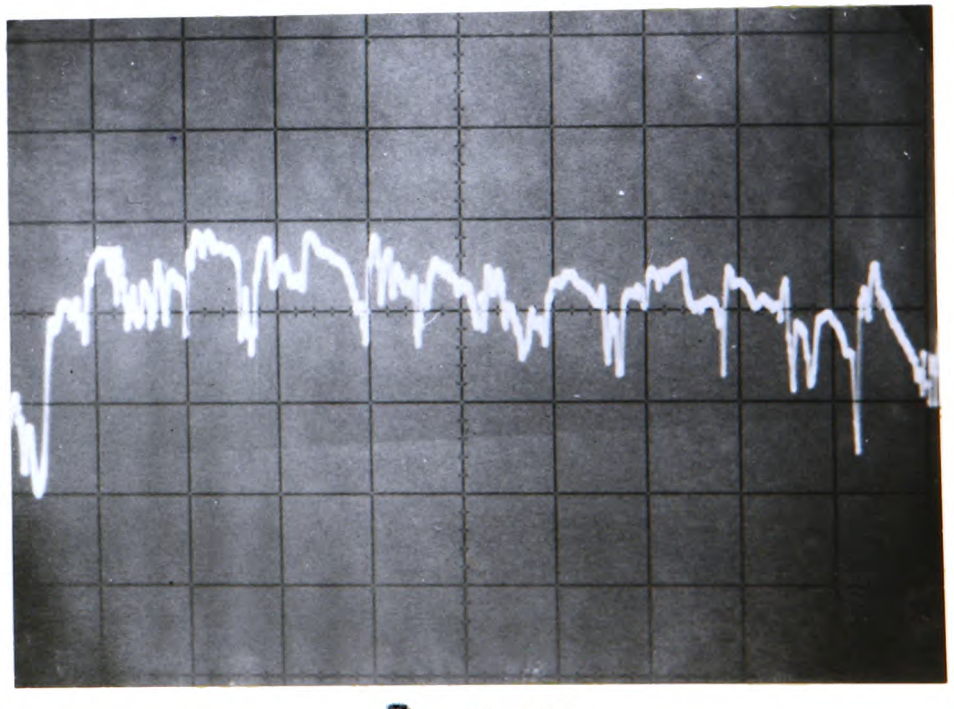

$\bar{\phi}$ = 0.210

FIG. 5.26 (contd.) HOT WIRE TRACES OF IMPELLER OUTLET FLOW CONDITIONS AT HUB TIP RADIUS RATIO OF 0.5

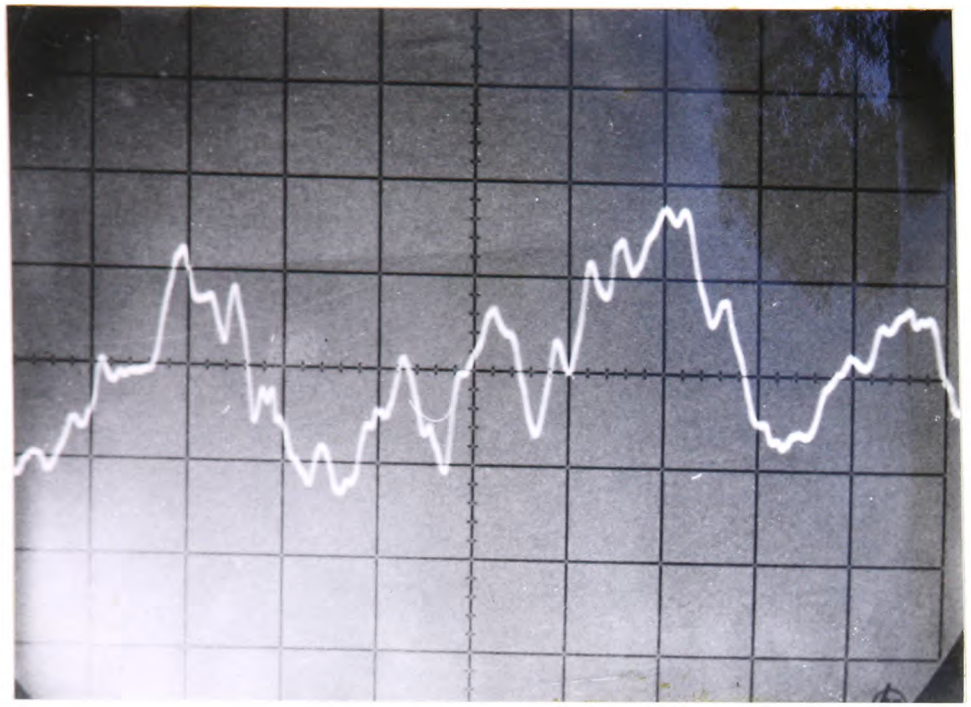

$\bar{\phi}$ = 0.420

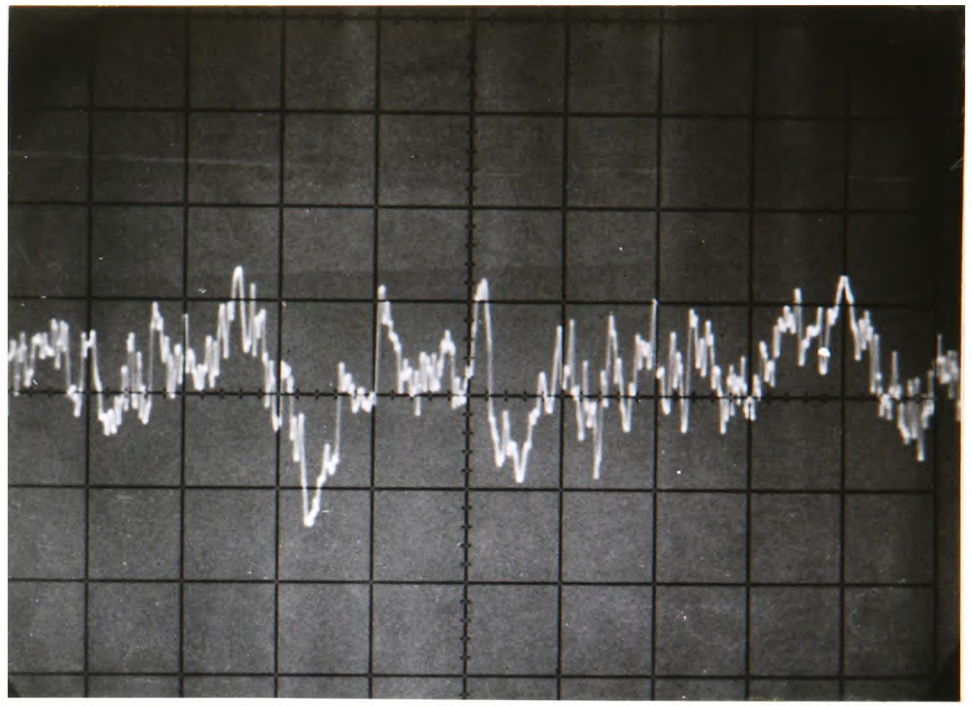

$\bar{\phi}$ = 0.282

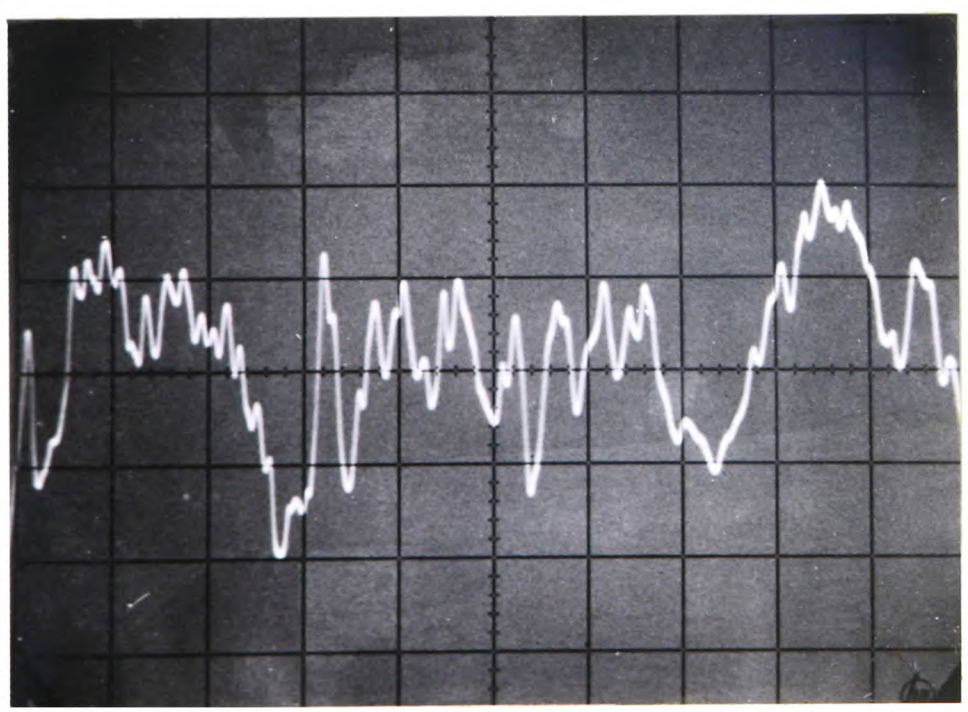

$\bar{\phi}$ = 0.259

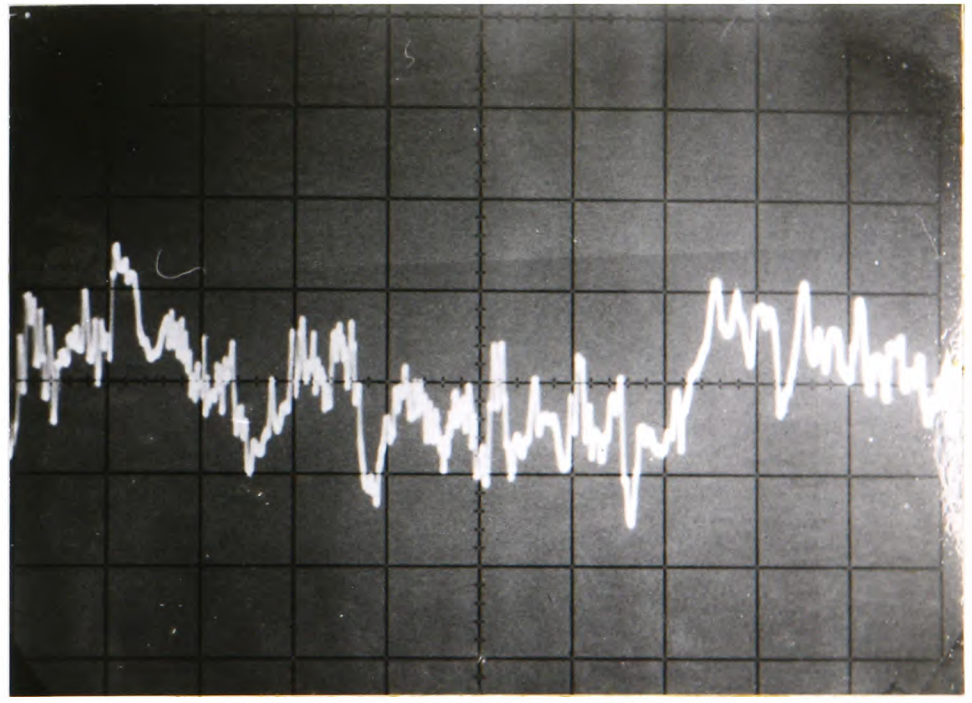

$\bar{\phi}$ = 0.210

FIG. 5.26 (concluded) HOT WIRE TRACES OF IMPELLER OUTLET FLOW CONDITIONS AT HUB TIP RADIUS RATIO OF 0.4

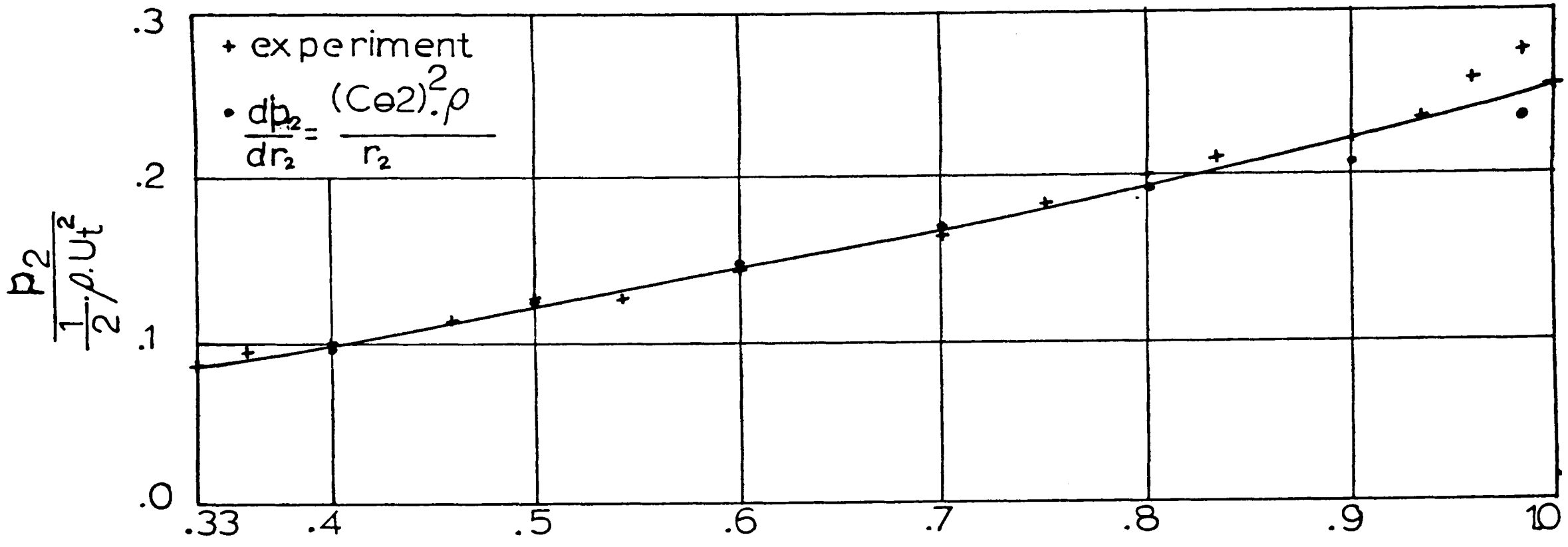

CHECKING OF RADIAL EQUILIBRIUM CONDITION AT $\bar{\phi}$=.259

Fig. 5.27

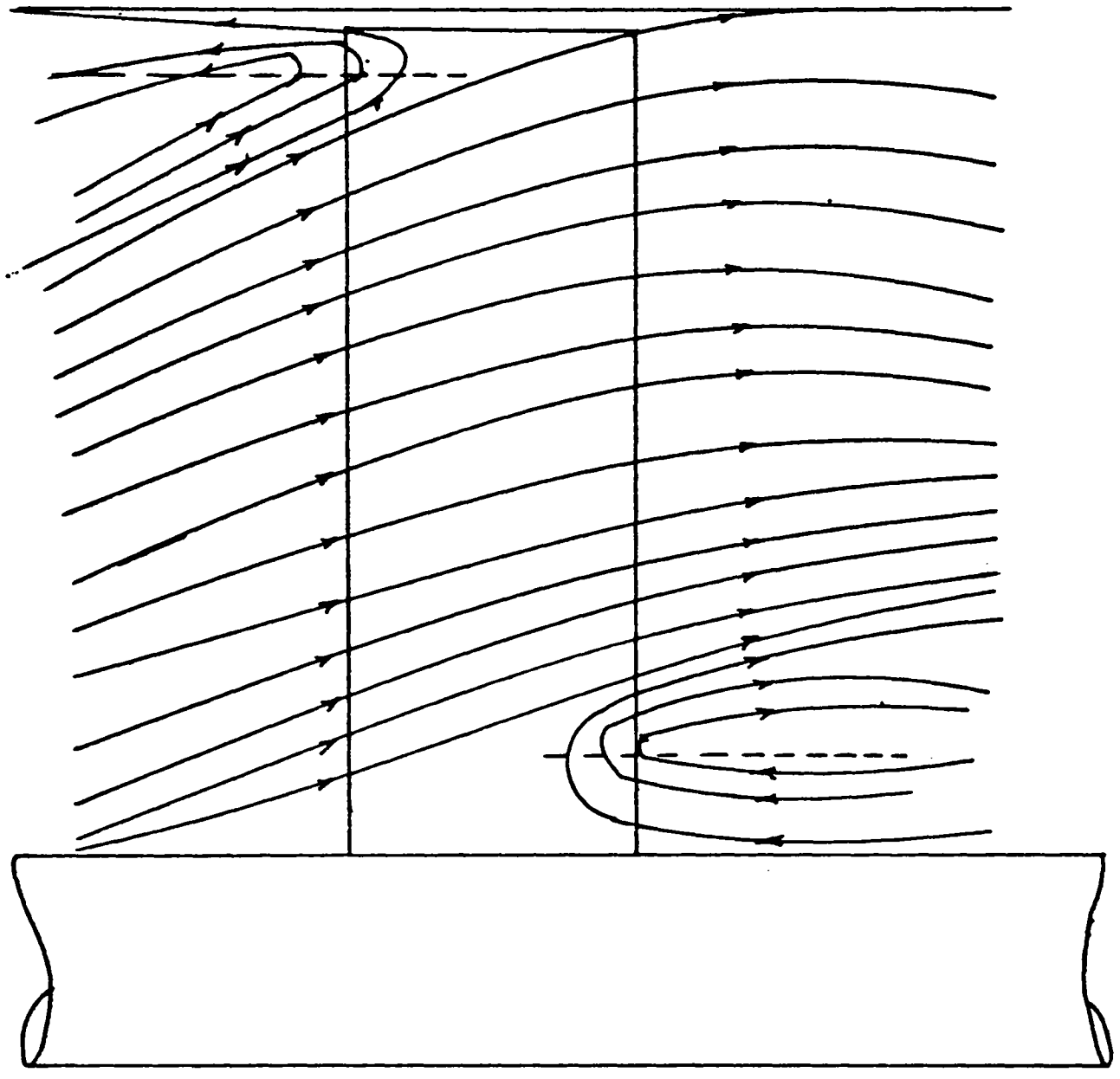

NATURE OF FLOW INTHE STALLED IMPELLER

Fig. 5.28

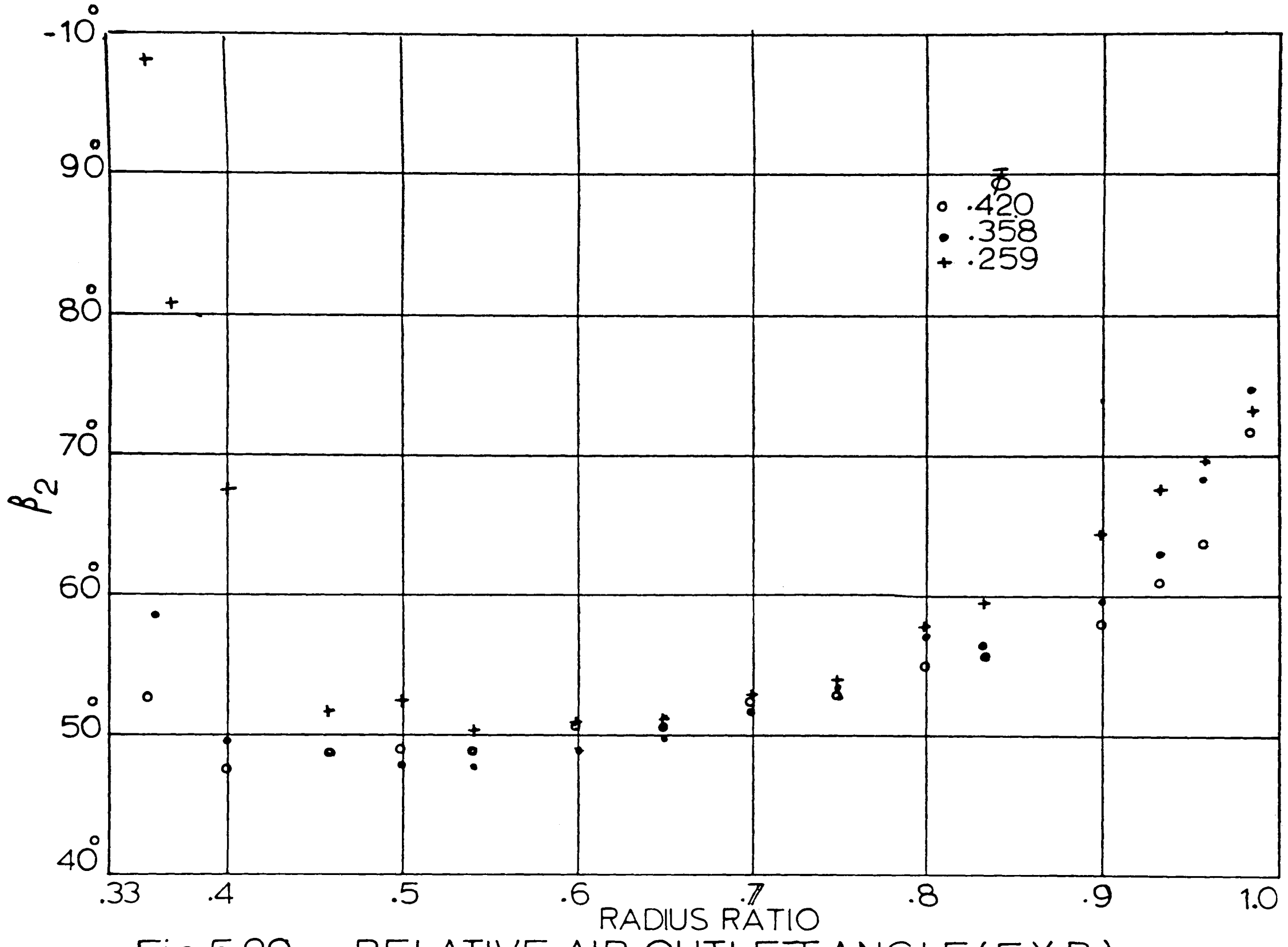

Fig 5.29 RELATIVE AIR OUTLET ANGLE (EXP.)

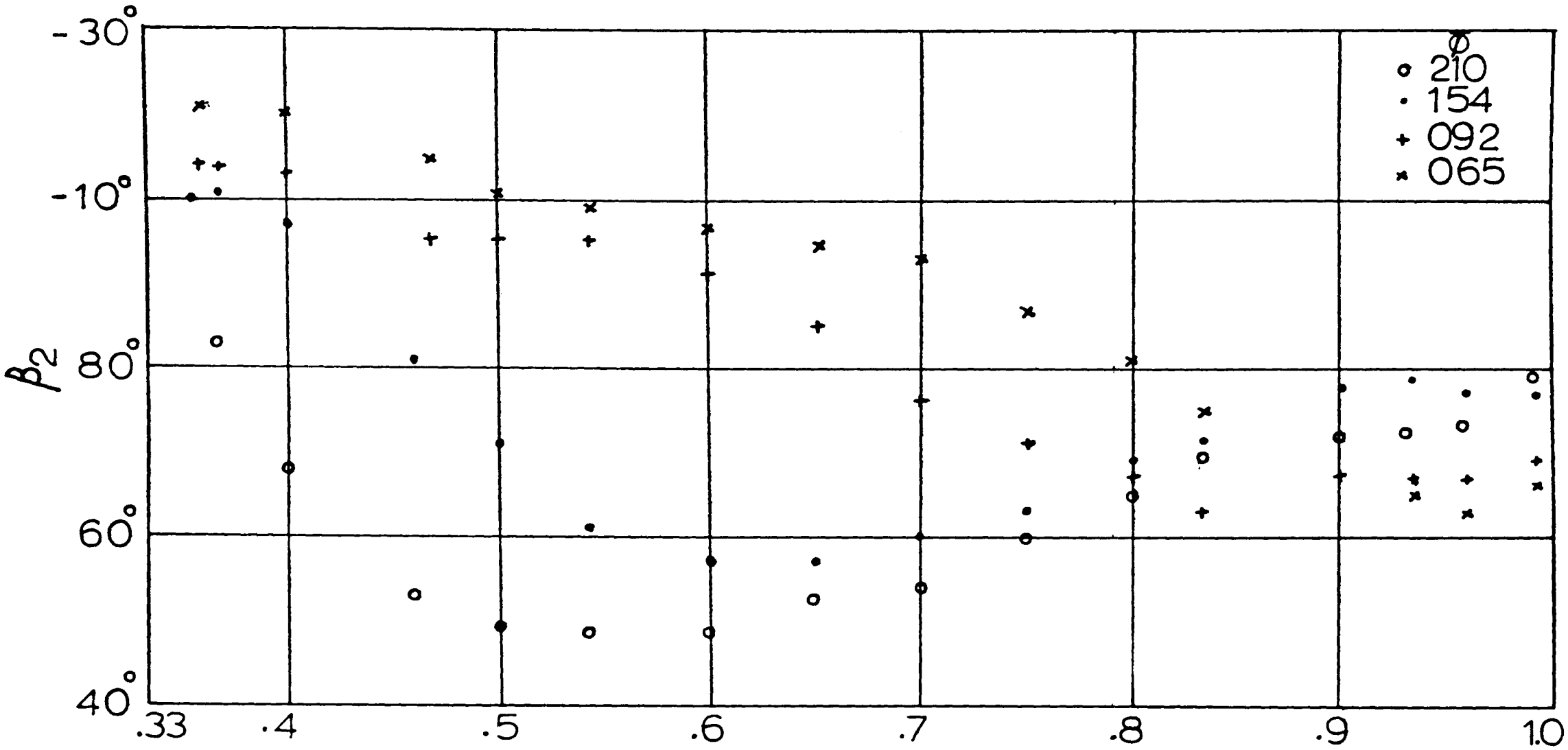

RELATIVE AIR OUTLET ANGLES (EXP.)

Fig. 5.30

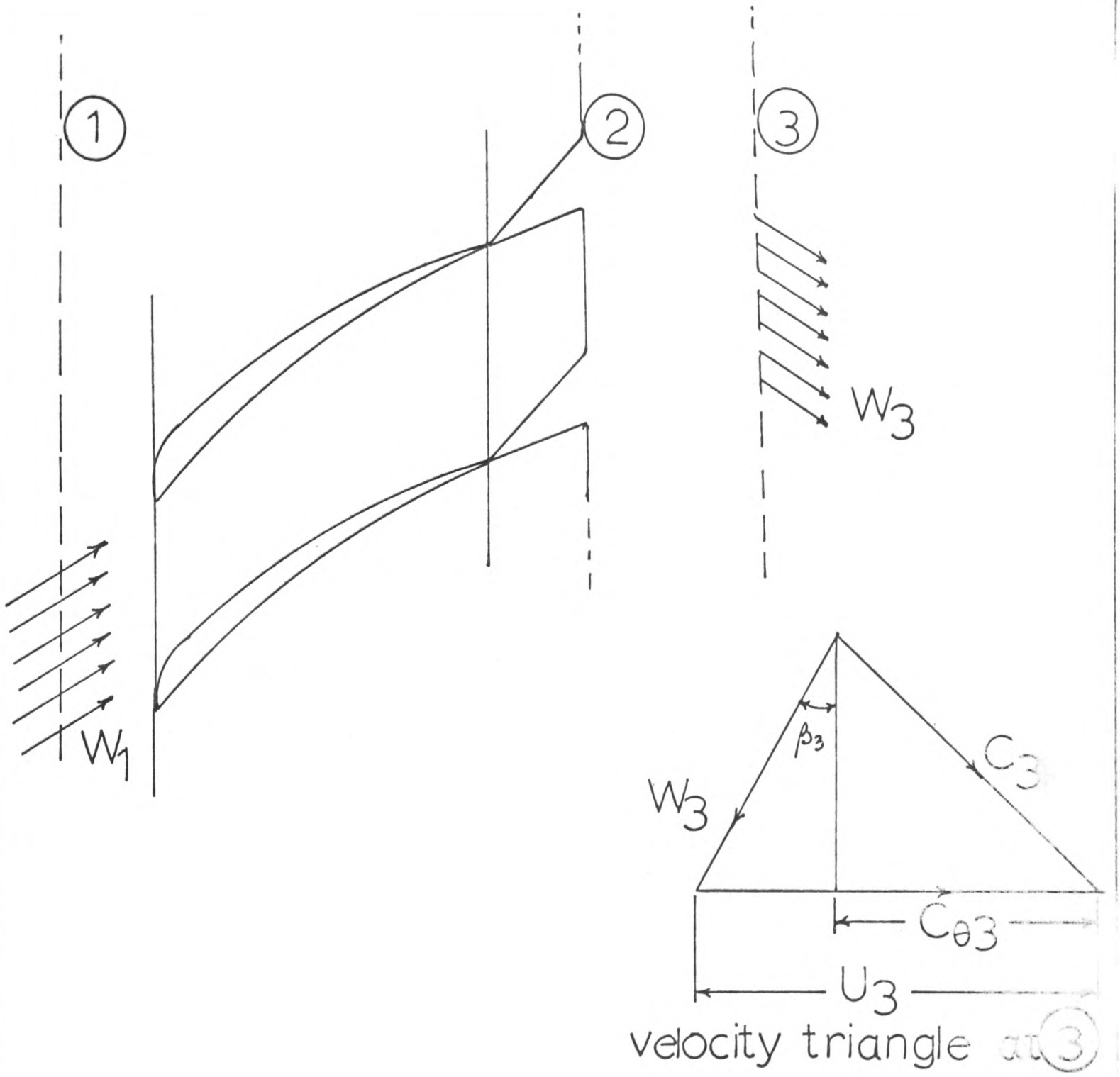

1 upstream plane

2 traversing plane

3 downstream plane withoutwakes

Fig. 6.1

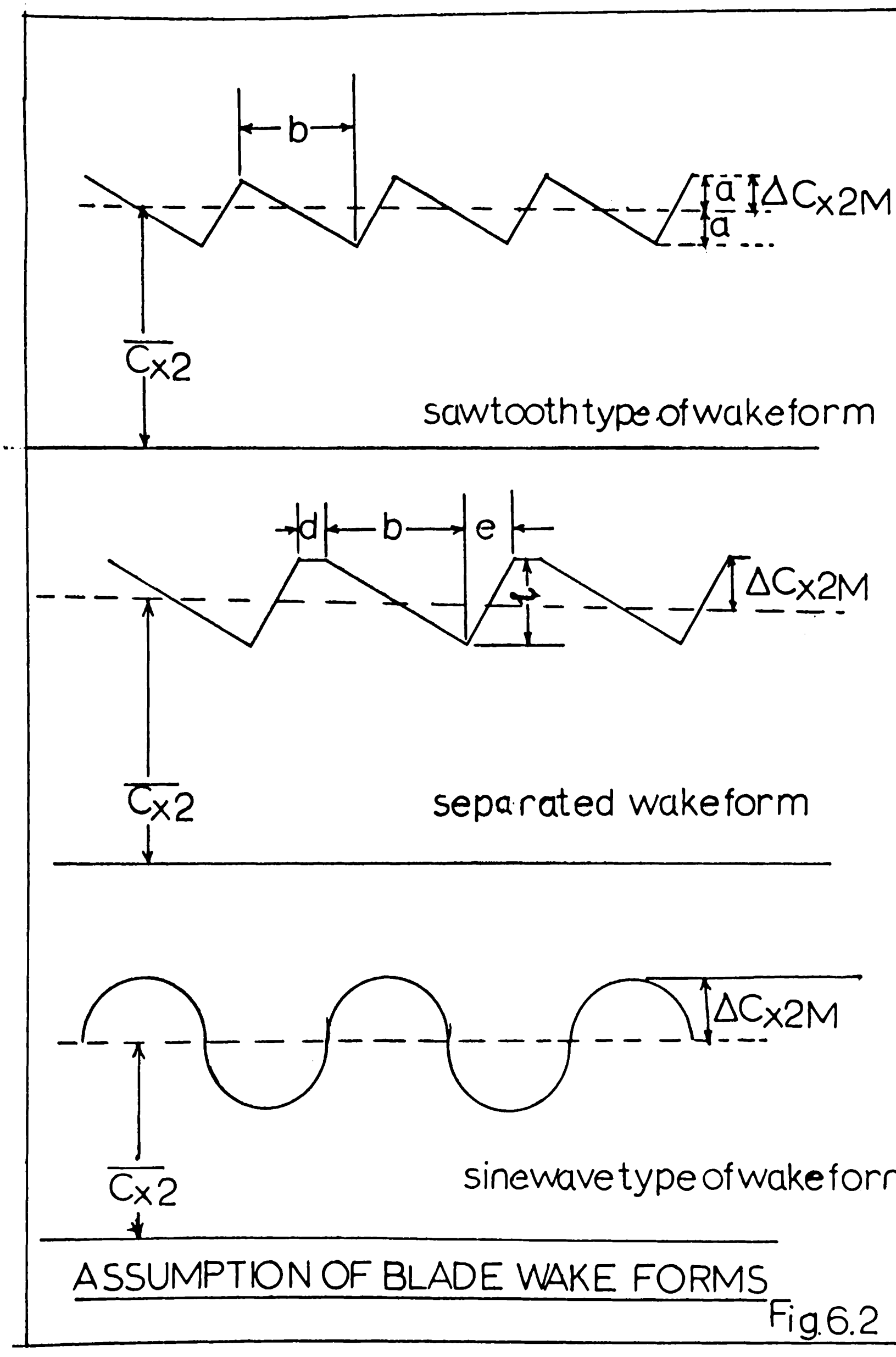

ASSUMPTION OF BLADE WAKE FORMS

Fig. 6.2

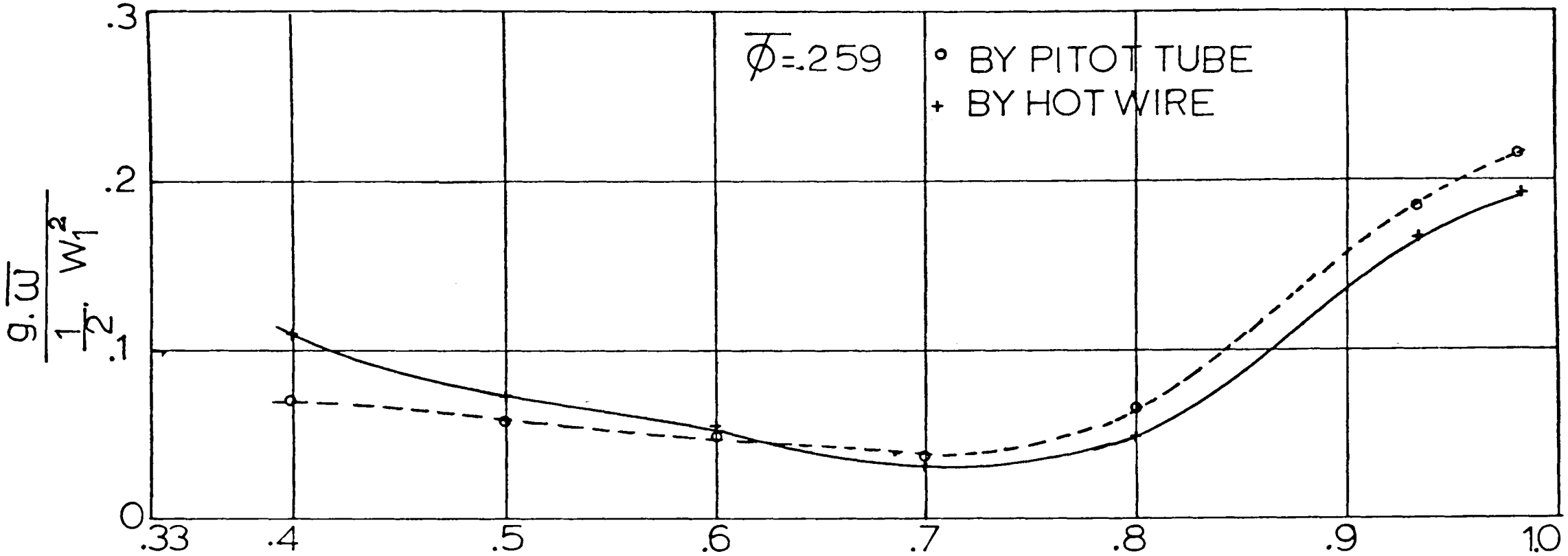

RELATIVE TOTAL HEAD LOSS COEFFICIENT

Fig. 6.3

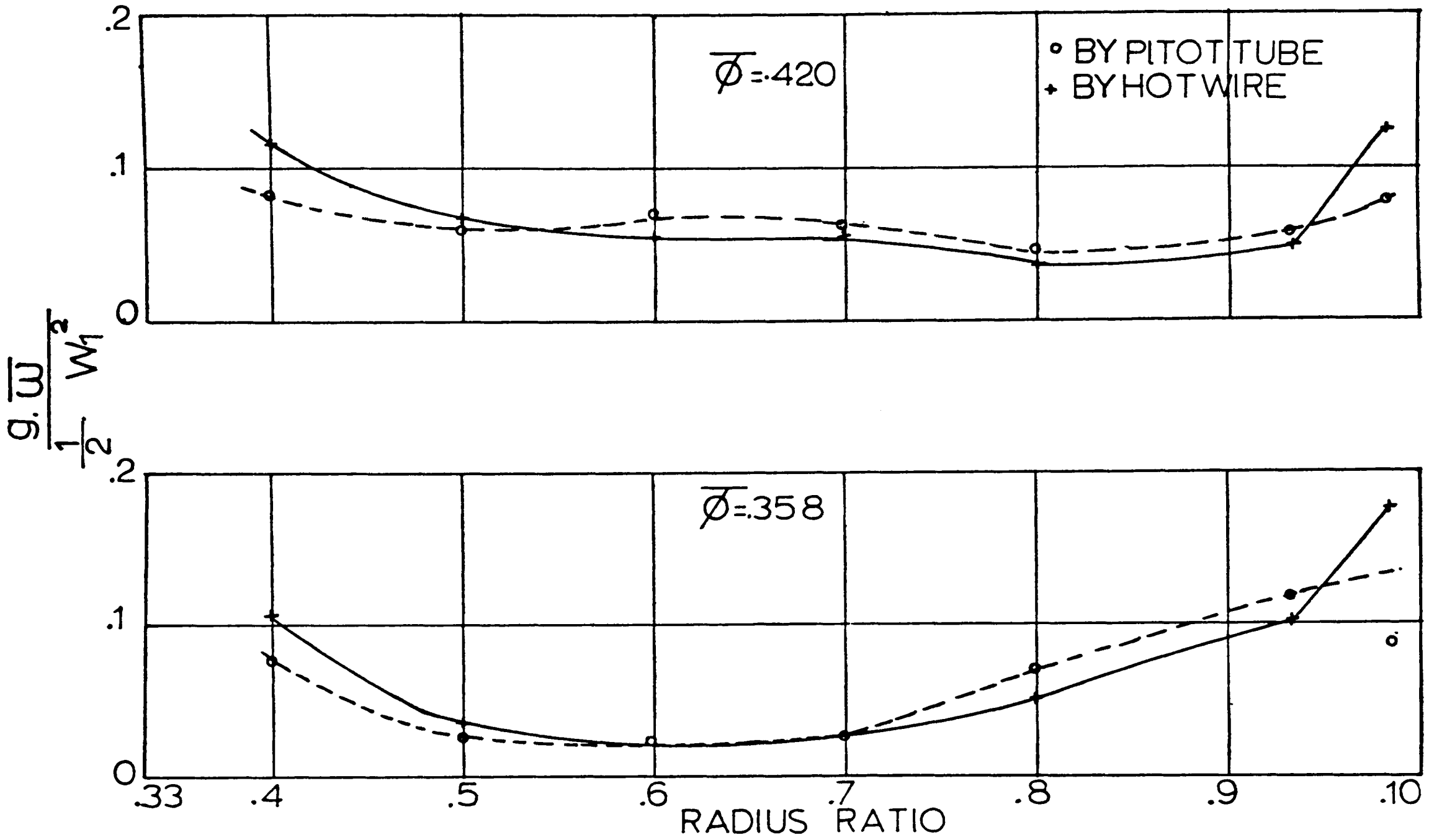

RELATIVE TOTAL HEAD LOSS COEFFICIENT

Fig.6.4

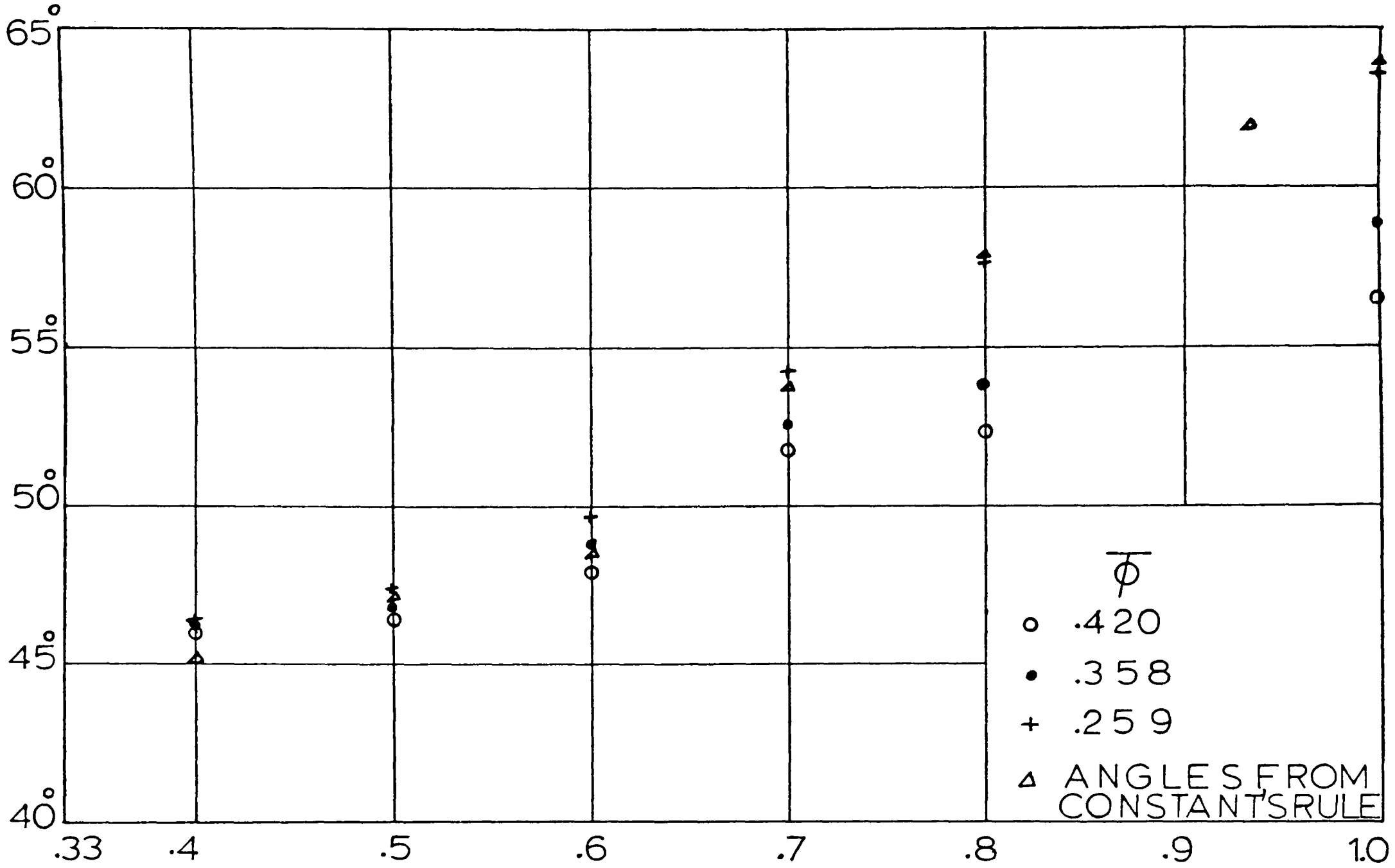

AIR OUTLET ANGLES BY POTENTIAL FLOW SOLUTION

Fig. 7.1

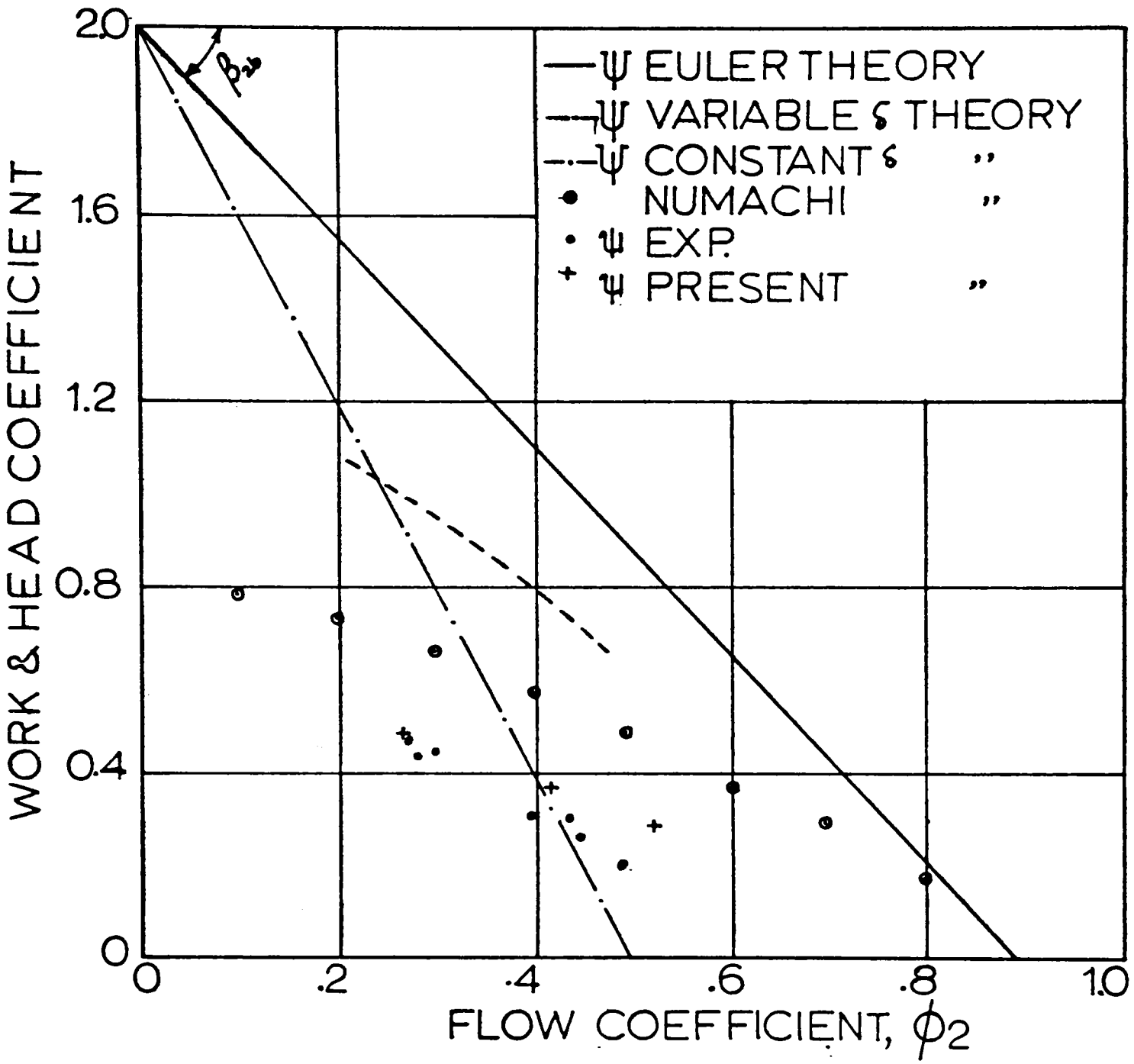

COMPARISON OF PERFORMANCE AT RADIUS RATIO = .933

FIG. 7.2(a)

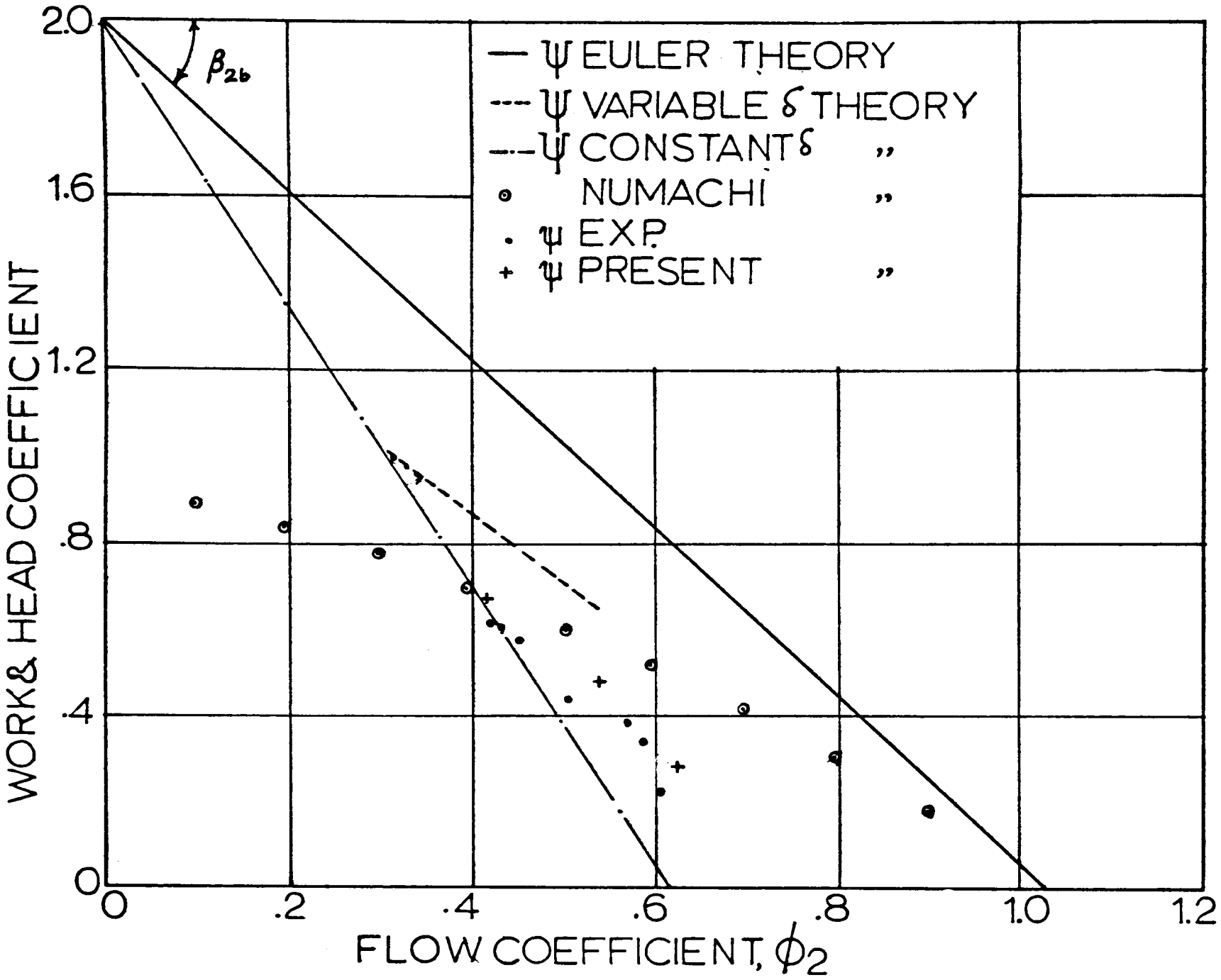

COMPARISON OF PERFORMANCE
AT RADIUS RATIO = .8

Fig. 7.2(b)

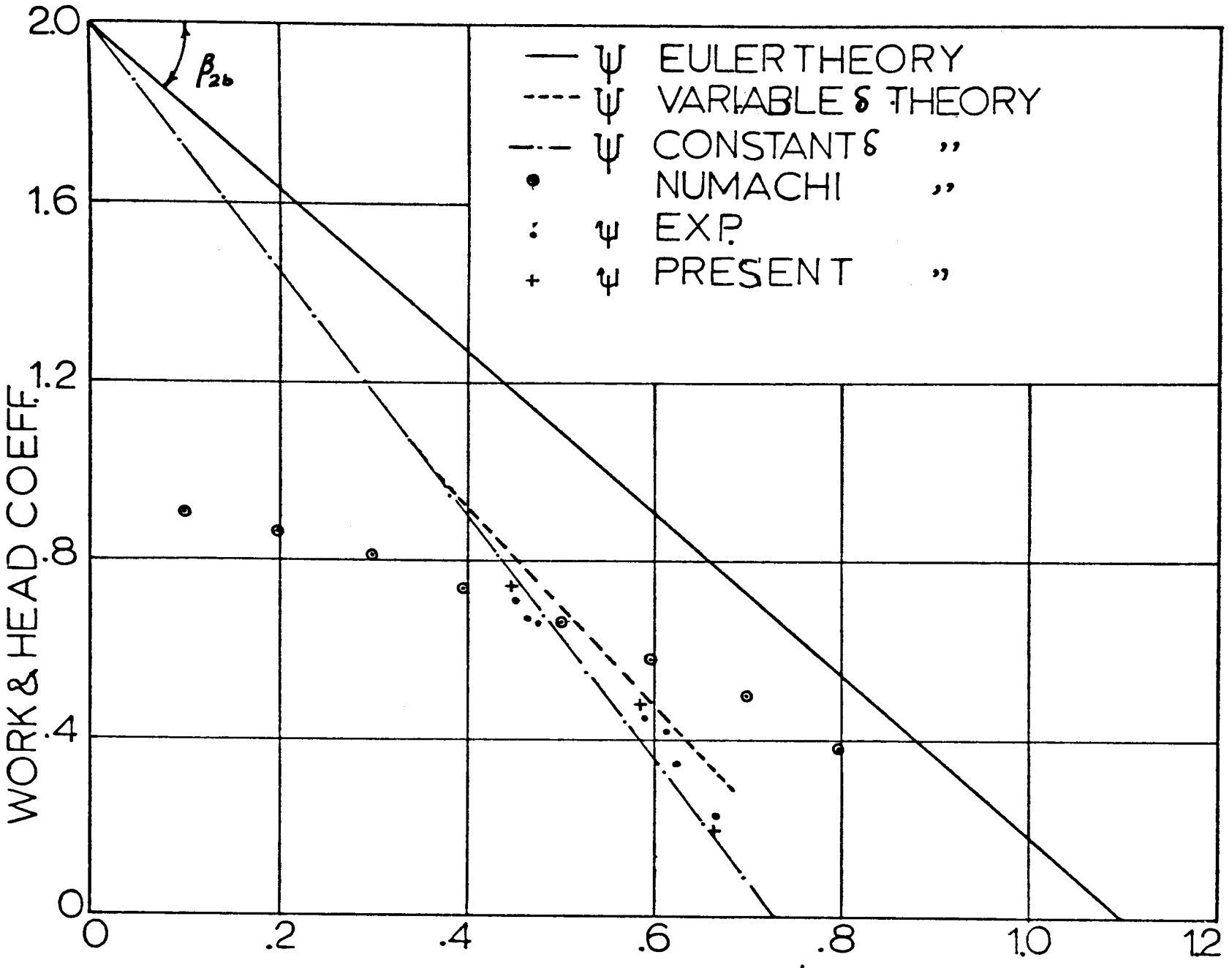

COMPARISON OF PERFORMANCE
AT RADIUS RATIO = .7

Fig. 7.2(c)

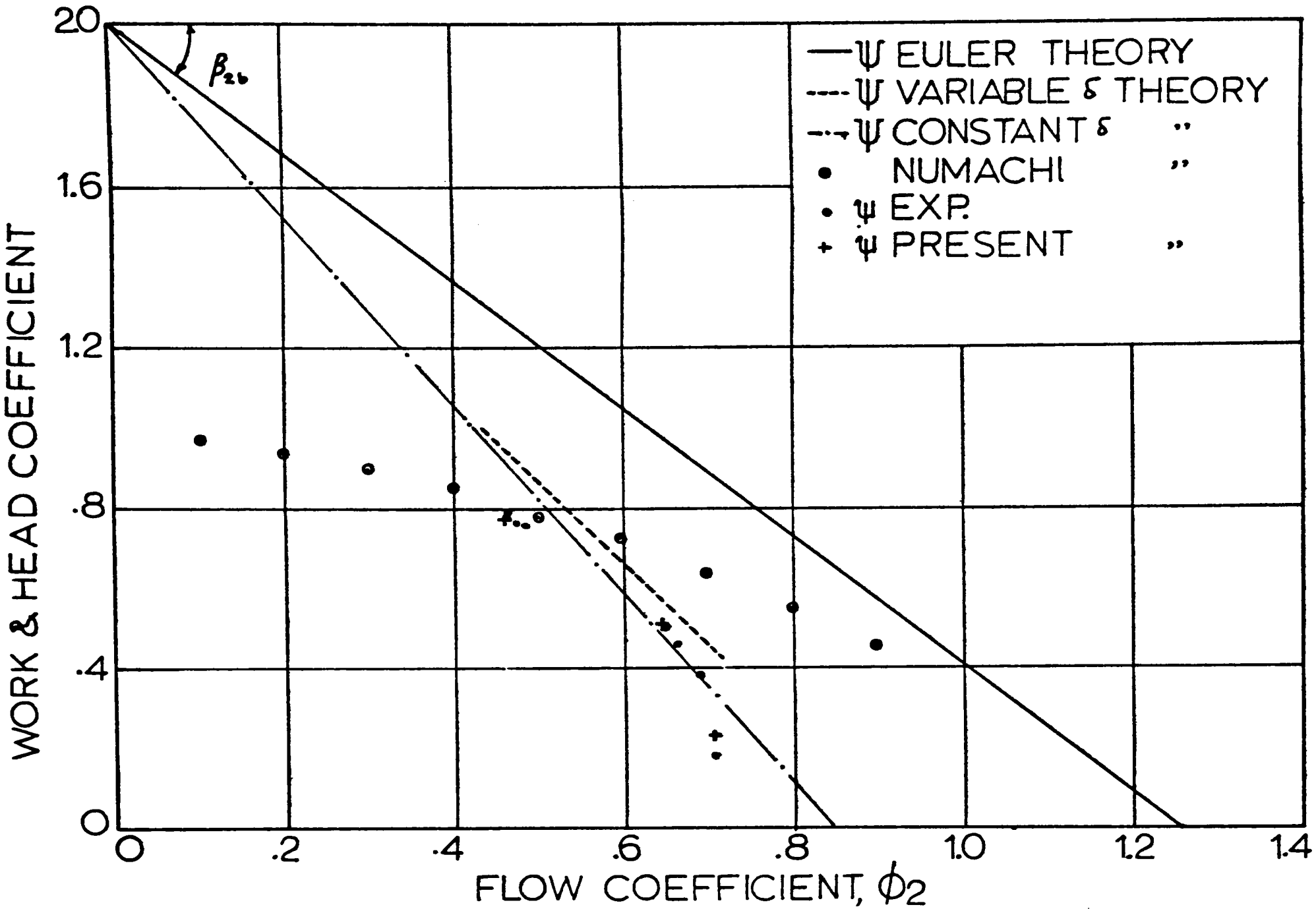

COMPARISON OF PERFORMANCE AT RADIUS RATIO=.6

Fig. 7.2(d)

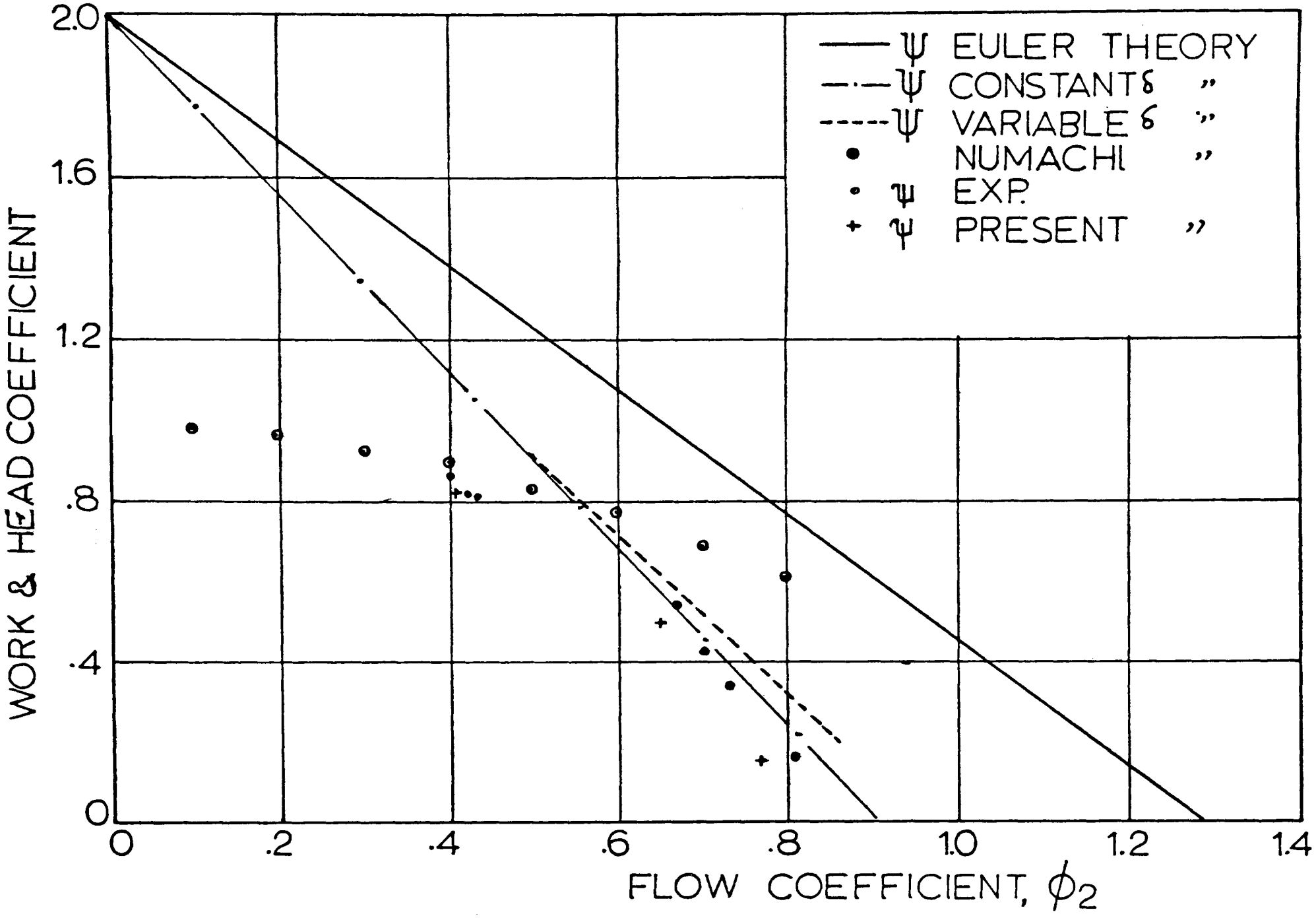

COMPARISON OF PERFORMANCE

AT RADIUS RATIO = .5

Fig. 7.2(e)

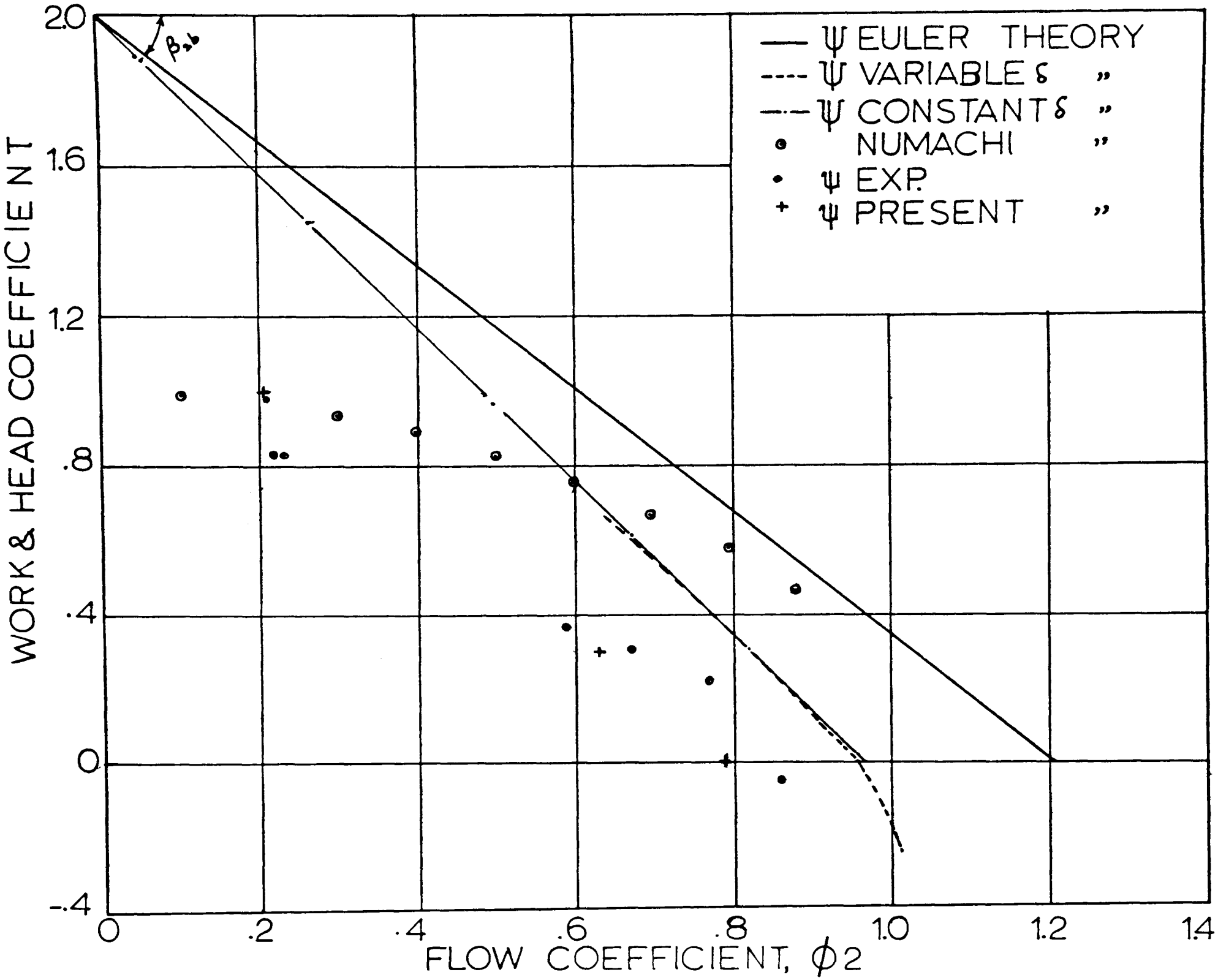

Fig. 7.2(f), COMPARISON OF PERFORMANCE AT RADIUS RATIO = .4

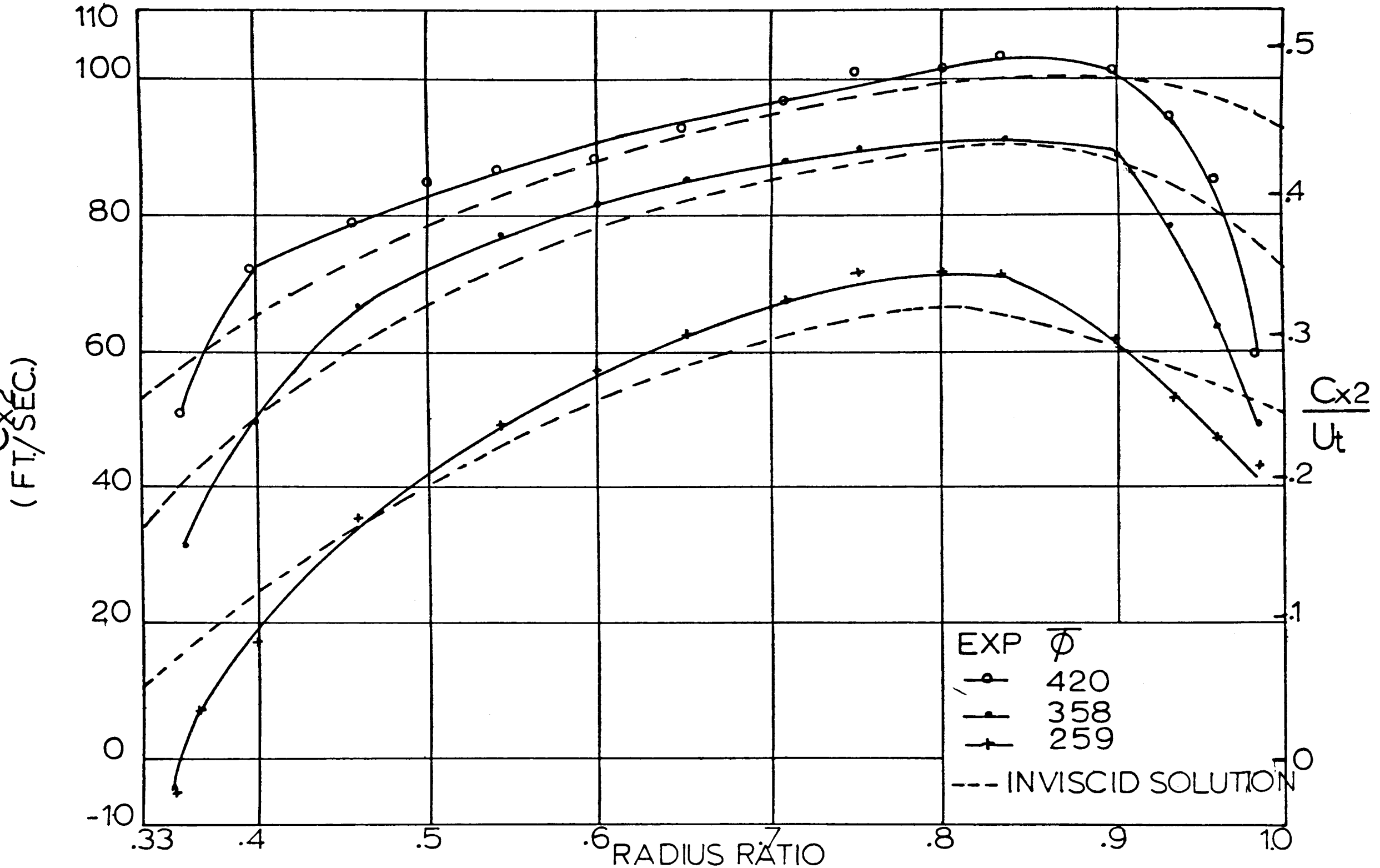

Fig.7.3, OUTLET AXIAL VELOCITY

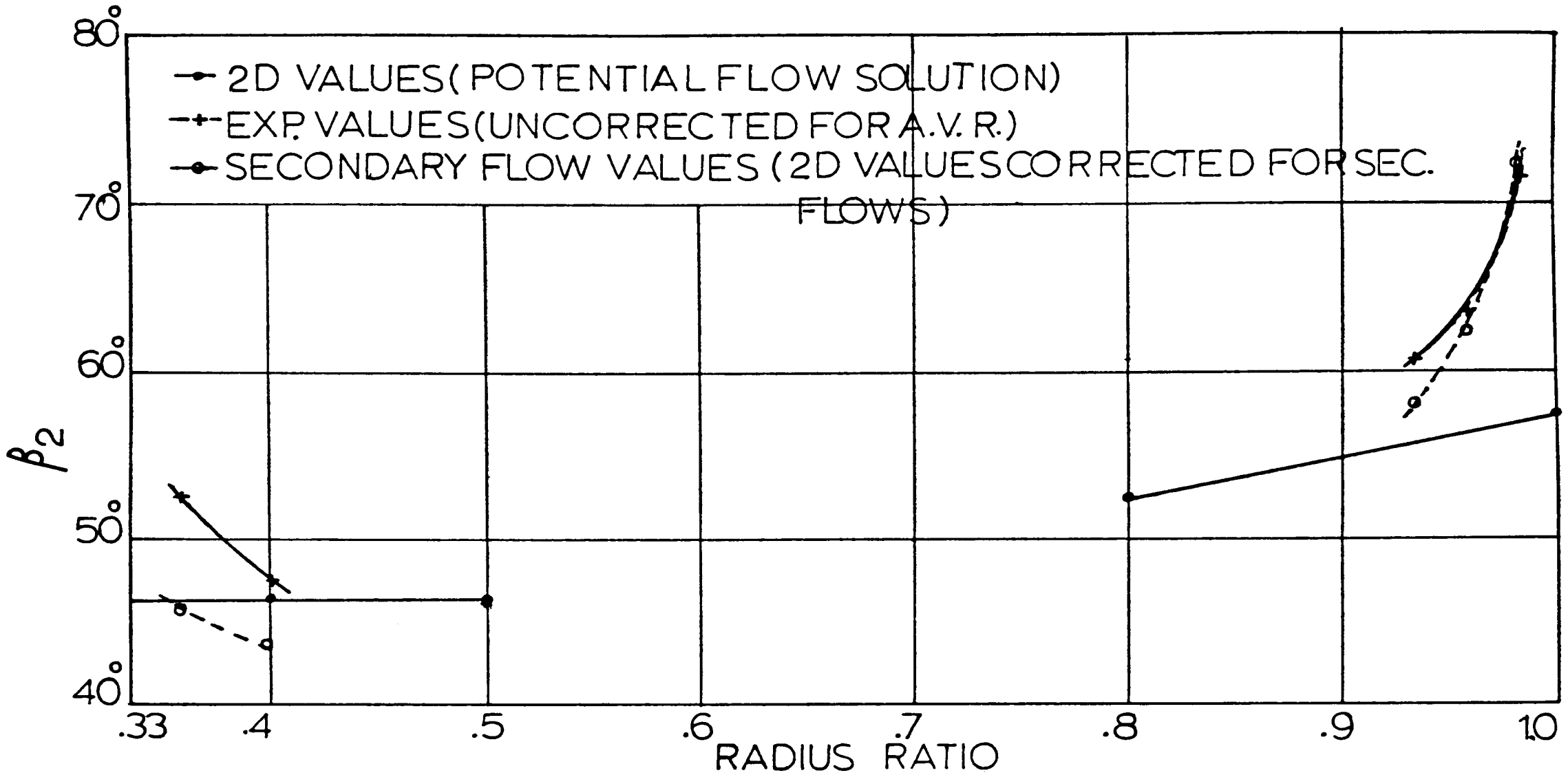

CHANGE IN RELATIVE OUTLET ANGLE DUE TO SECONDARY FLOWS AT $\bar{\phi}$=.420

Fig. 7.4

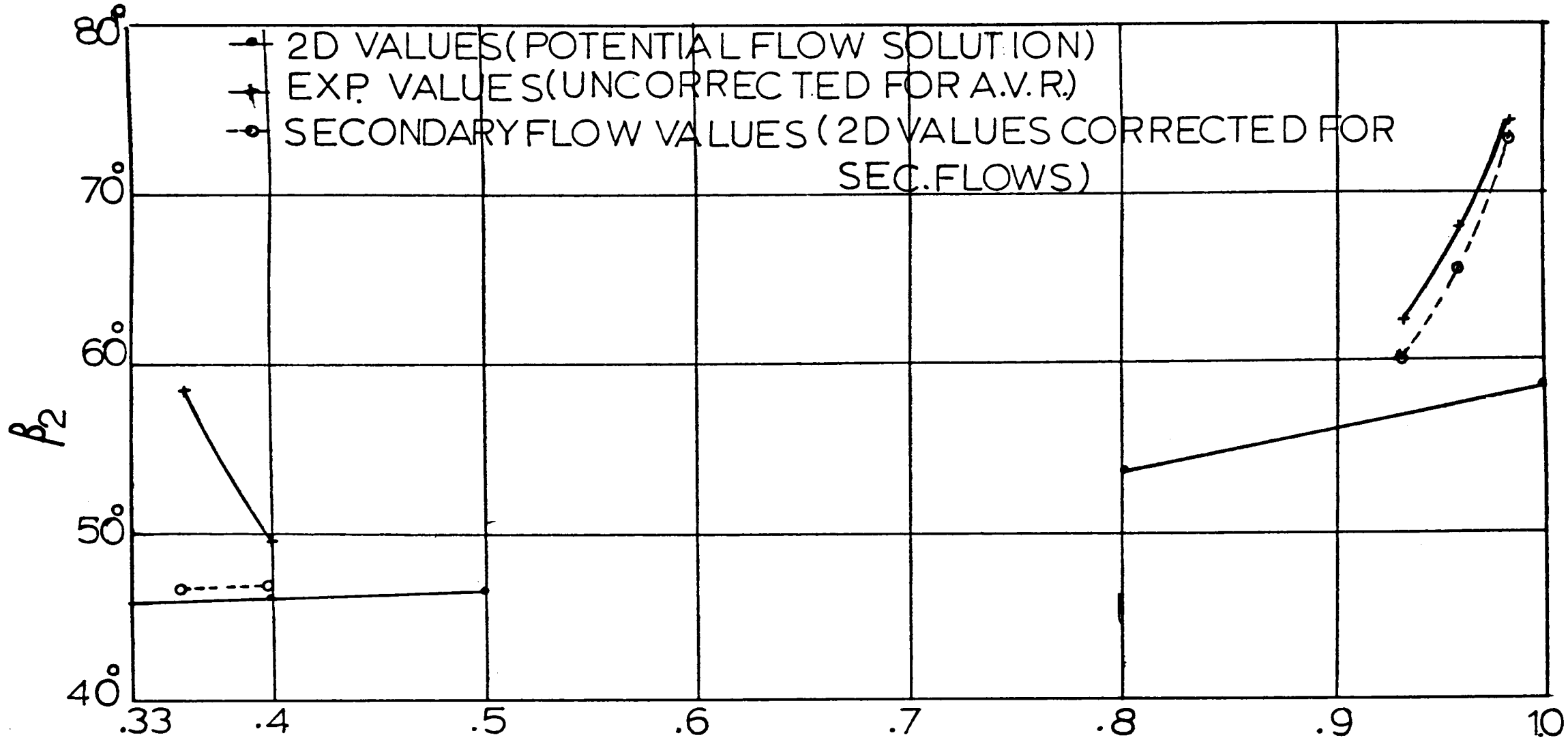

CHANGE IN RELATIVE OUTLET ANGLE DUE TO SECONDARY FLOWS AT $\bar{\phi}$=.358

Fig.7.5

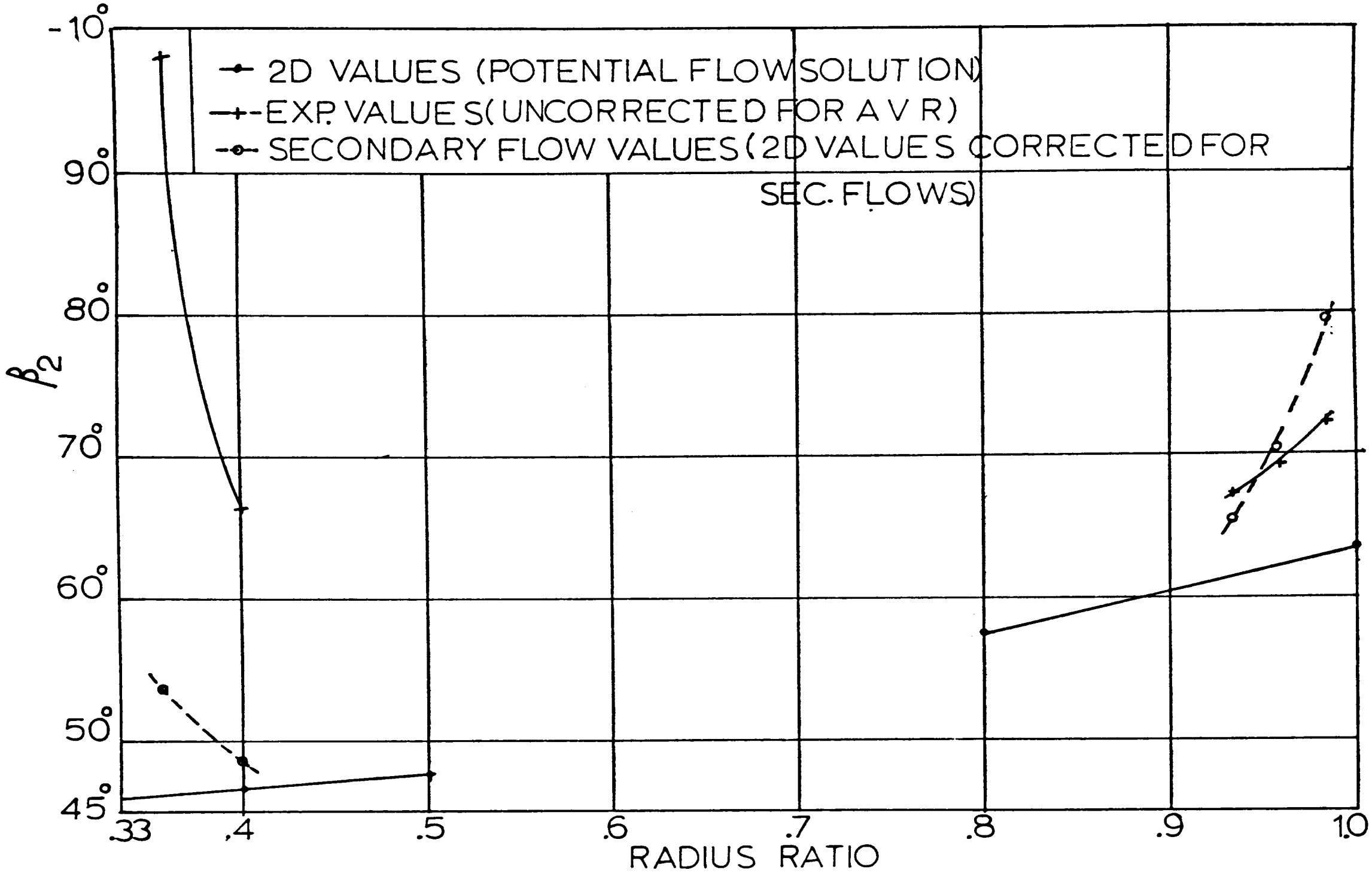

CHANGE IN RELATIVE OUTLET ANGLE DUE TO SECONDARY FLOWS AT $\overline{\phi}$=.259

Fig. 7.6

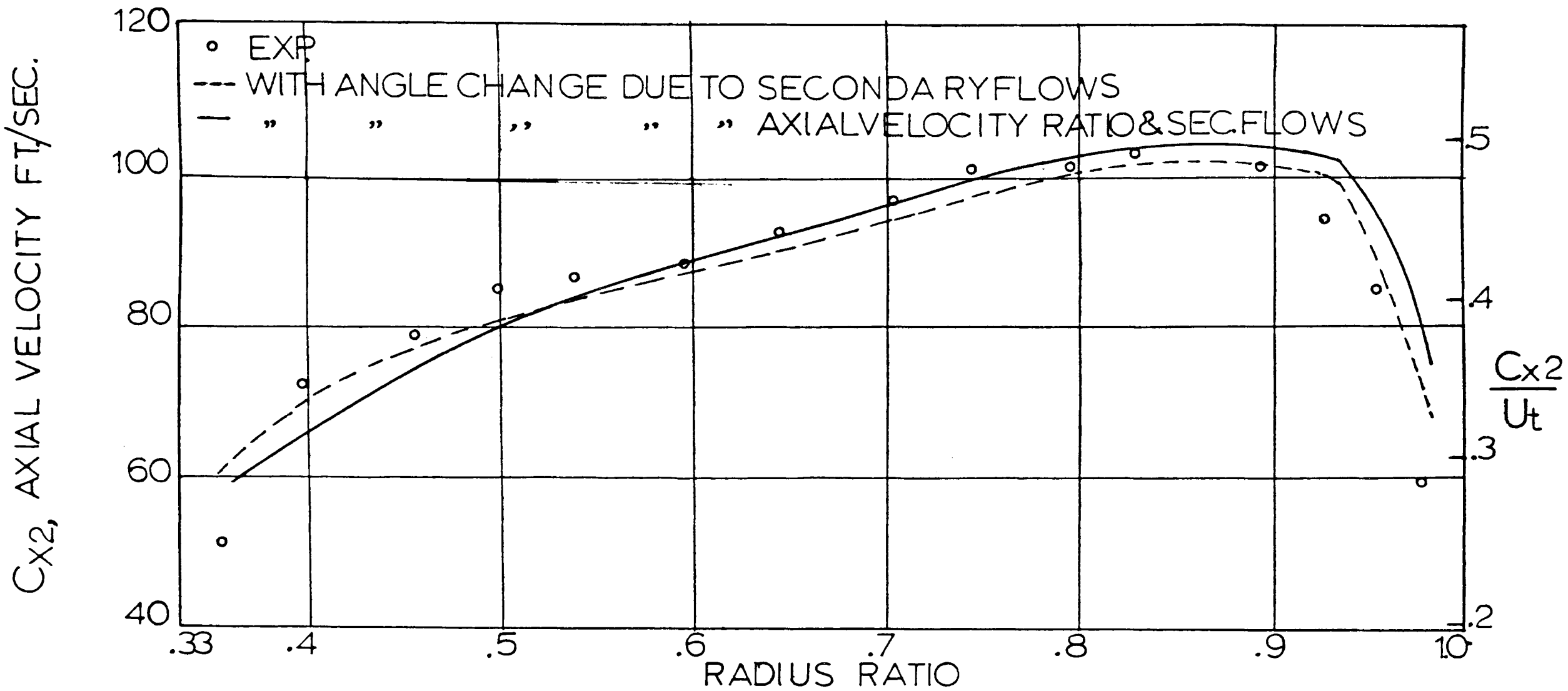

COMPLETE FLOW AT OUTLET OF THE IMPELLER

AT $\bar{\phi} = .420$

Fig. 7.7

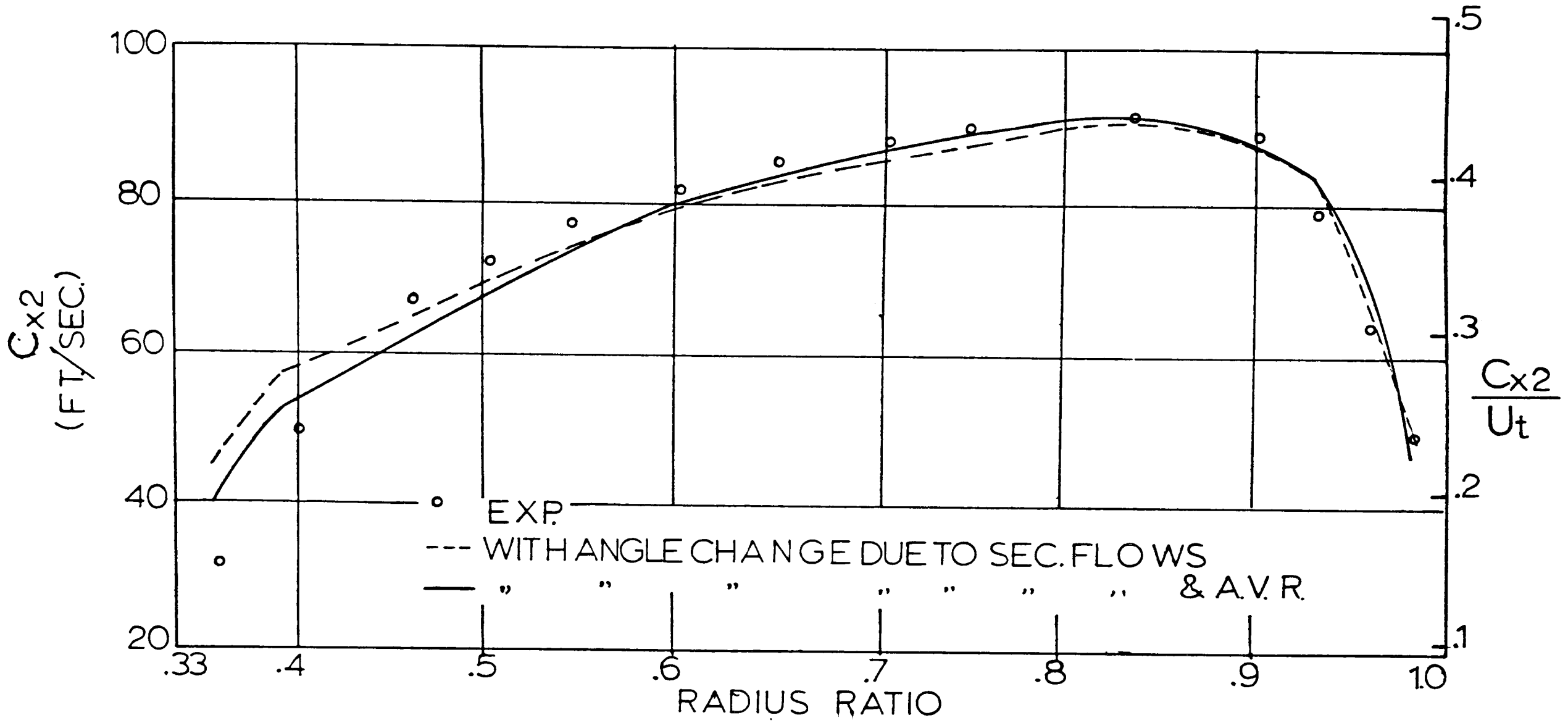

COMPLETE FLOW AT OUTLET OF THE IMPELLER AT $\overline{\phi}$ = .358

Fig. 7.8

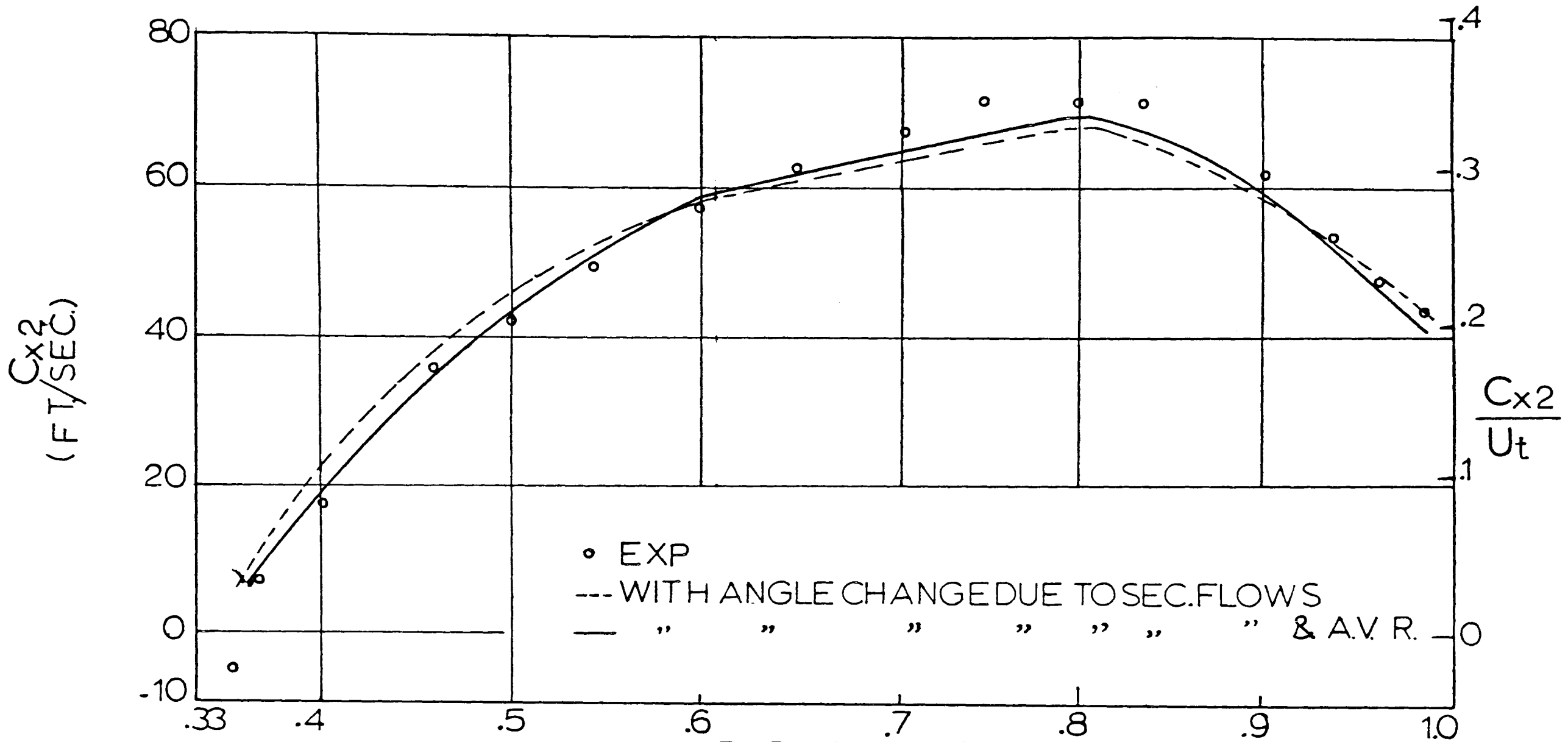

COMPLETE FLOW AT OUTLET OF THE IMPELLER AT $\bar{\phi}$ = .259

Fig. 7.9

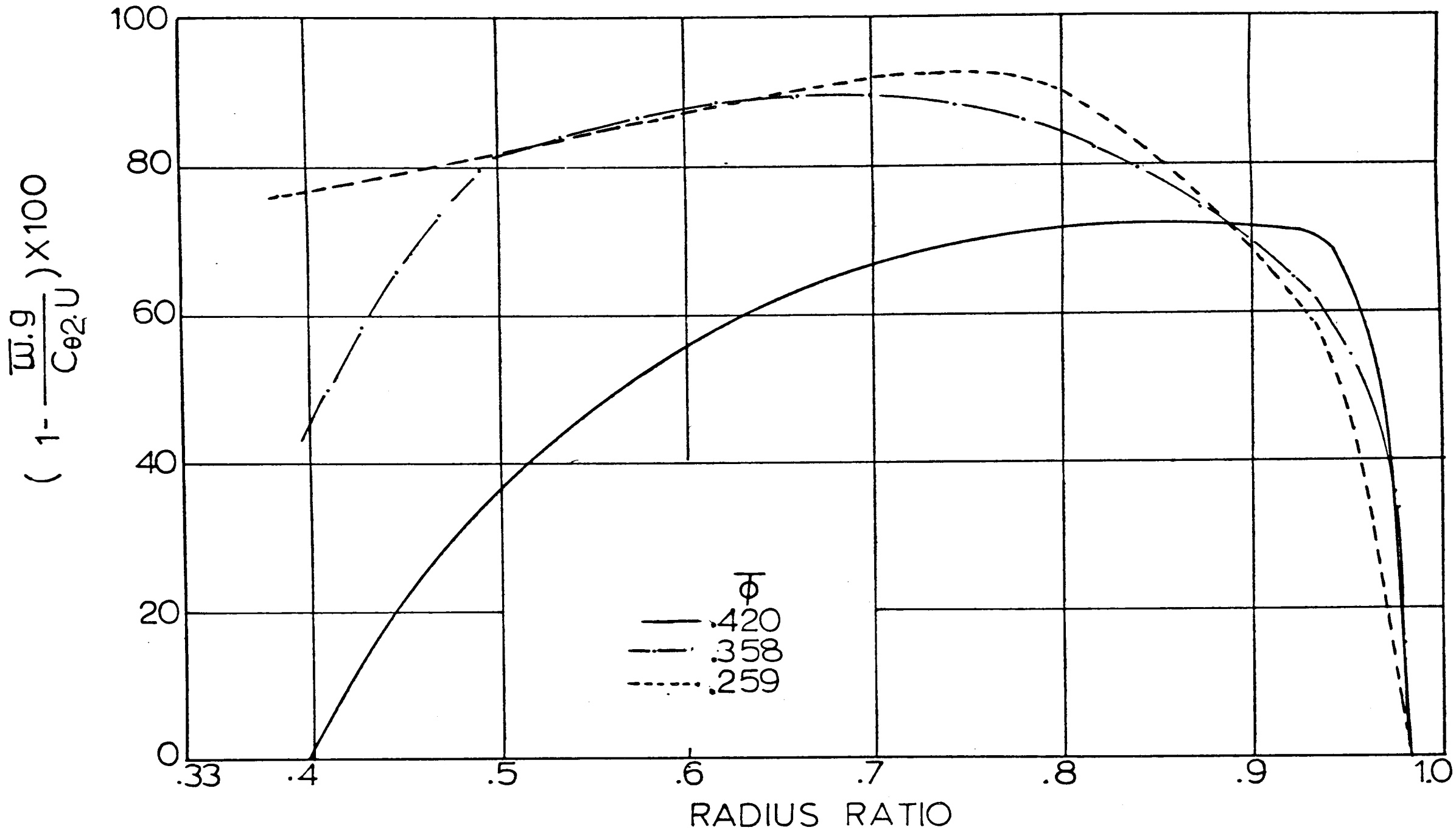

BLADE ELEMENT EFFICIENCY

Fig.7.10

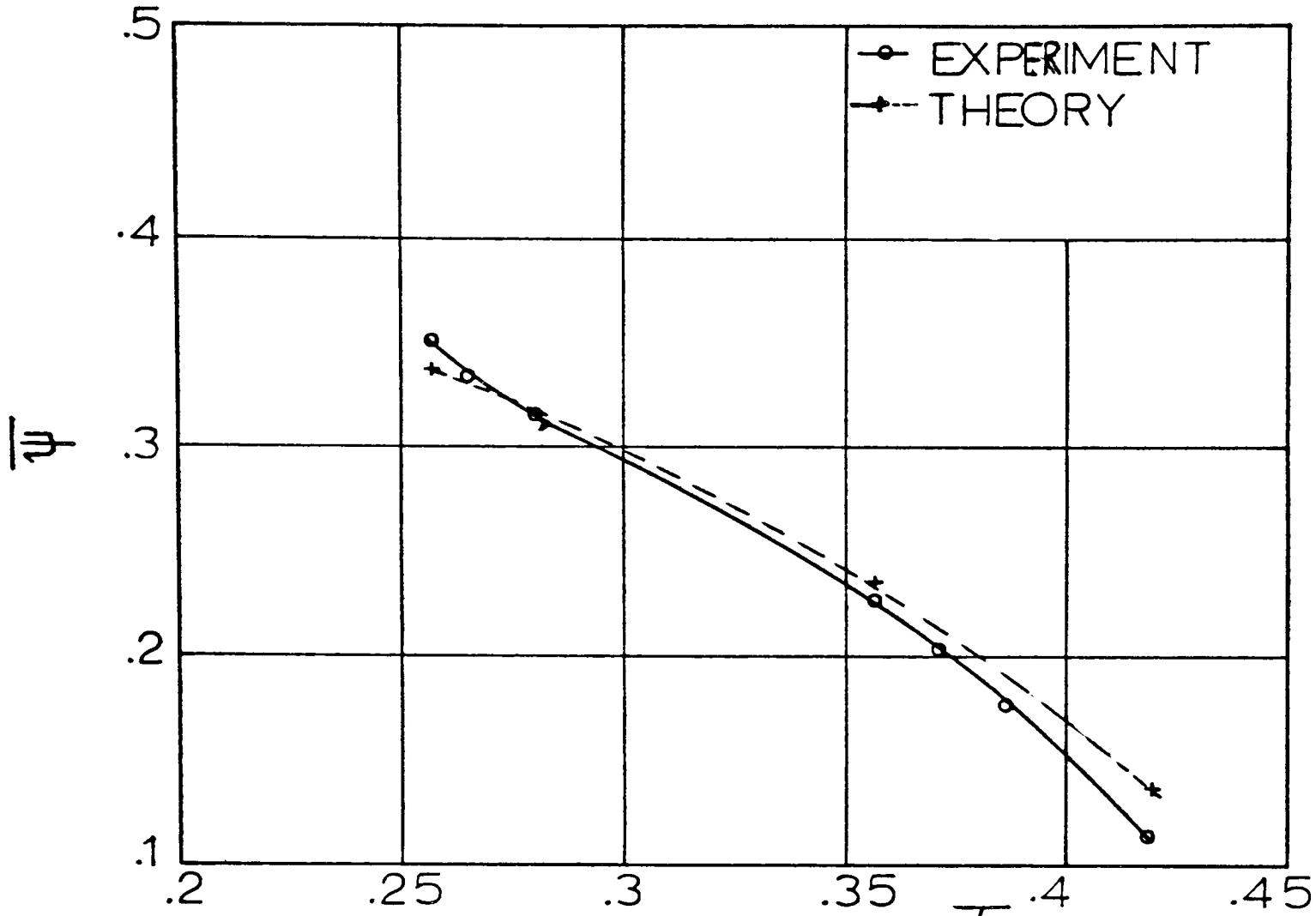

COMPARISON OF INTEGRATED TOTAL HEAD RISE COEFFICIENT

Fig. 7.11

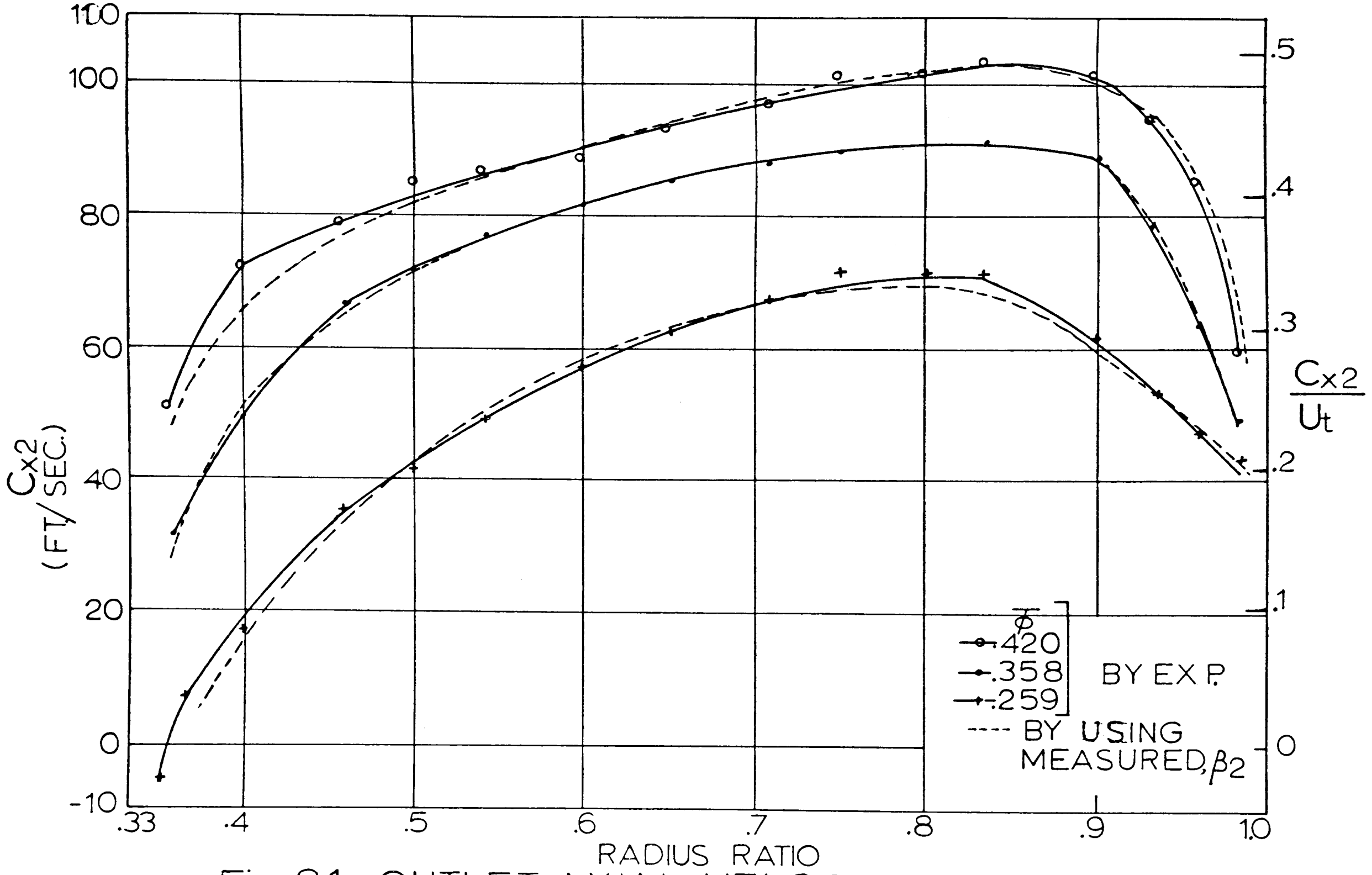

Fig. 8.1 OUTLET AXIAL VELOCITY

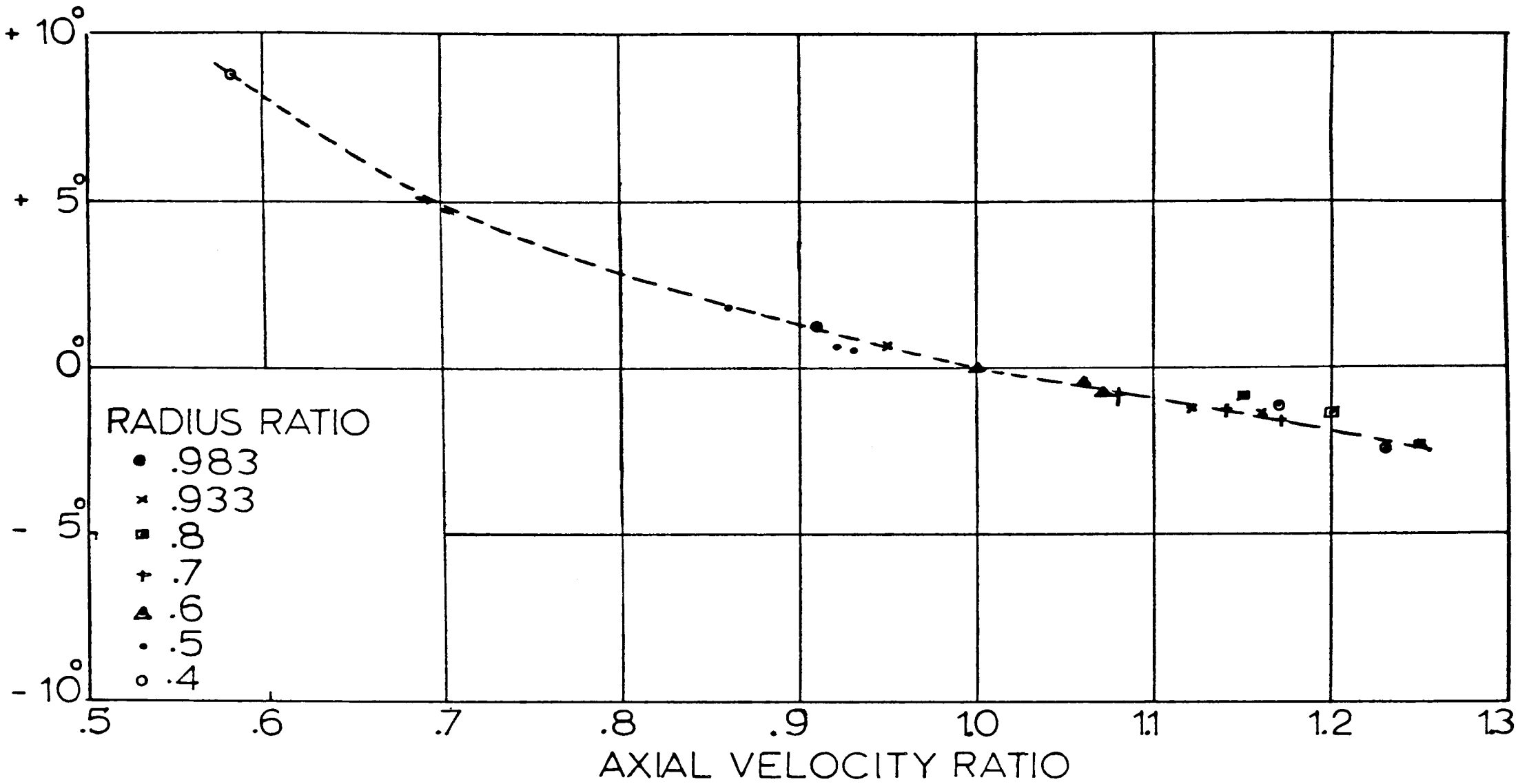

CHANGE IN 2D OUTLET ANGLE DUE TO A.V.R. AT VARIOUS RADIUS RATIOS

Fig. 8.2

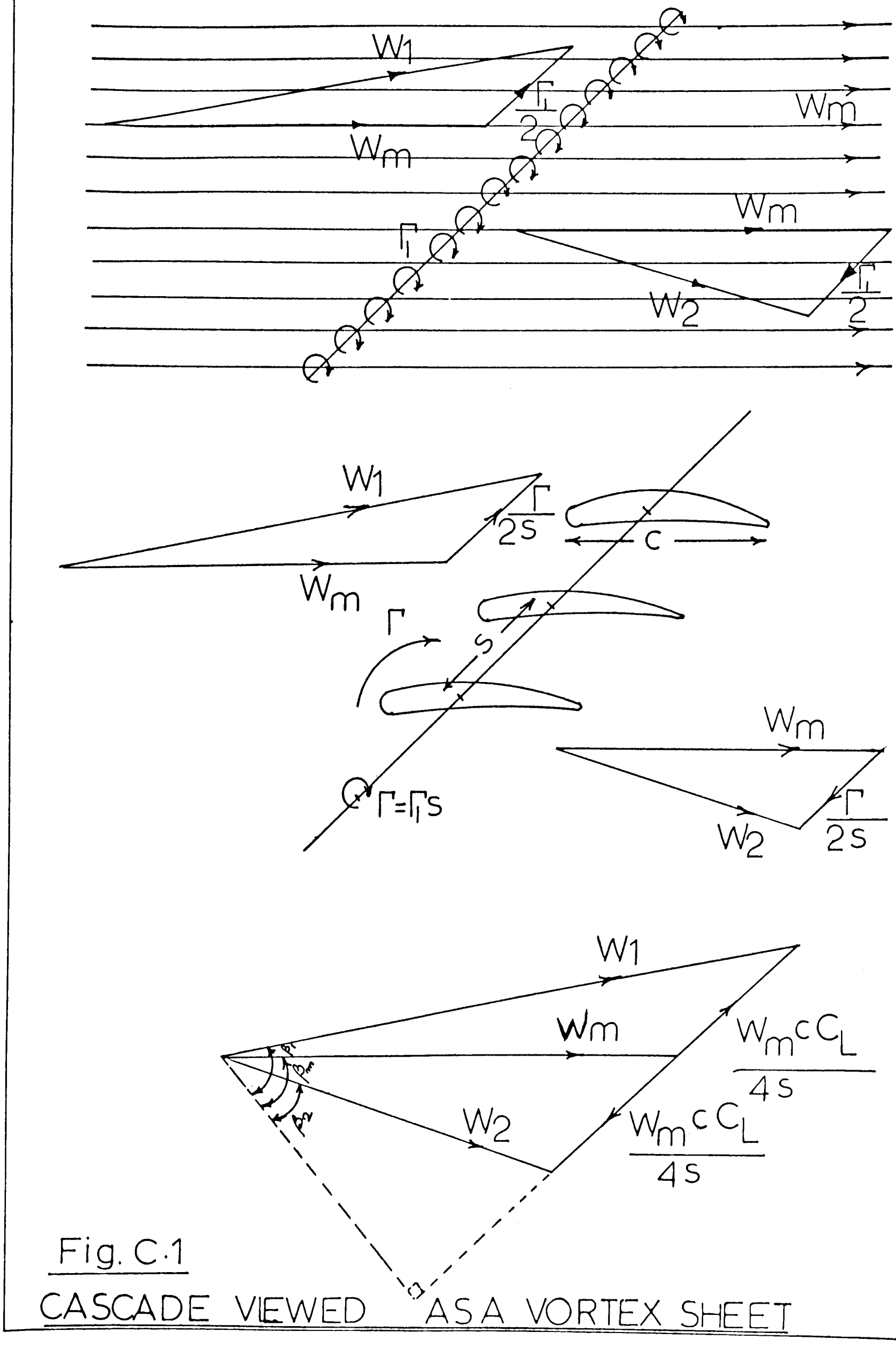

Fig. C·1

CASCADE VIEWED AS A VORTEX SHEET

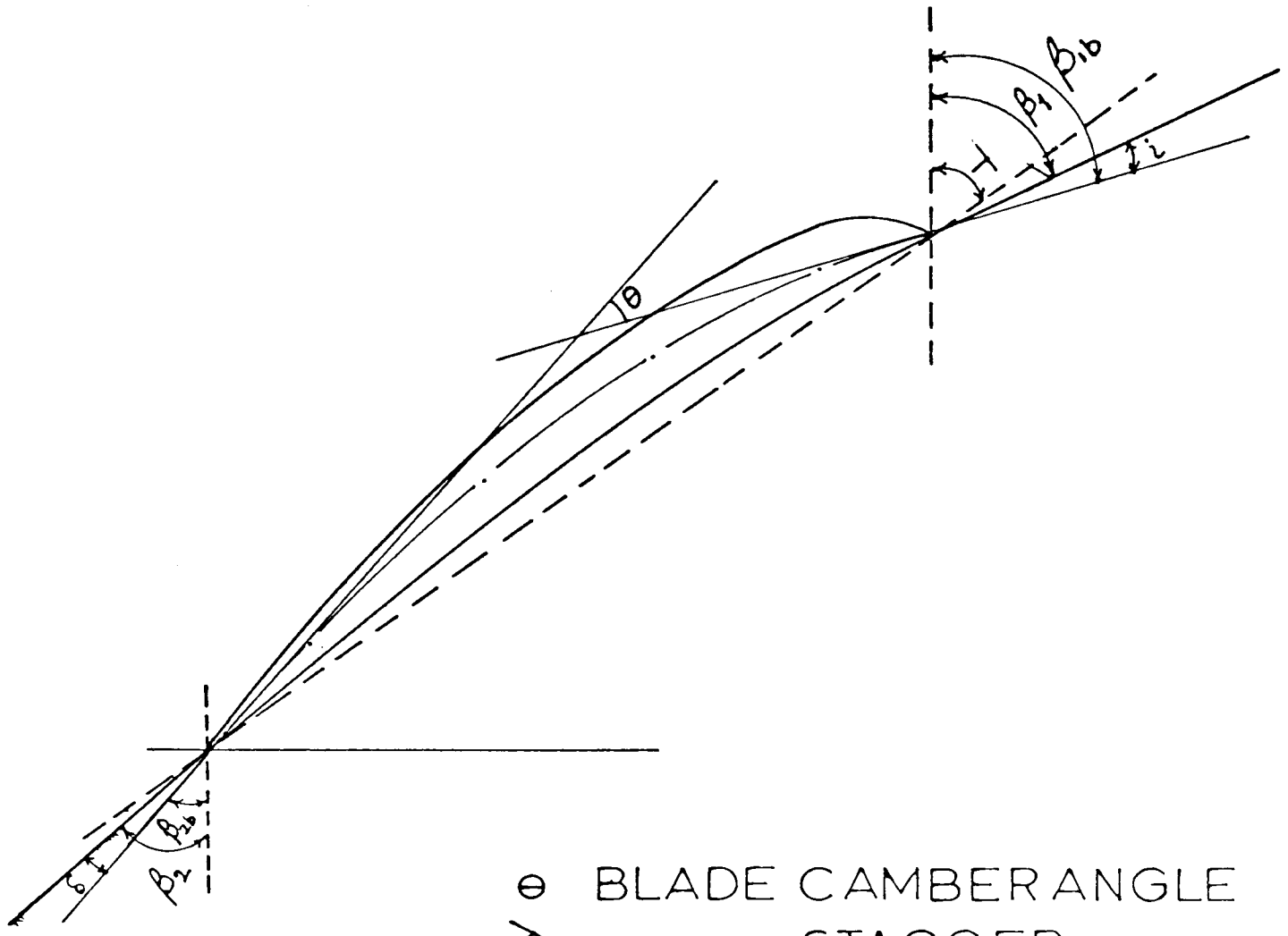

θ BLADE CAMBER ANGLE
γ ,, STAGGER ,,
β_{1b} ,, INLET ,,
β_{2b} ,, OUTLET ,,
β_1 AIR INLET ,,
β_2 ,, OUTLET ,,
i INCIDENCE ,,
δ DEVIATION ,,

BLADE NOMENCLATURE

Fig. D.1

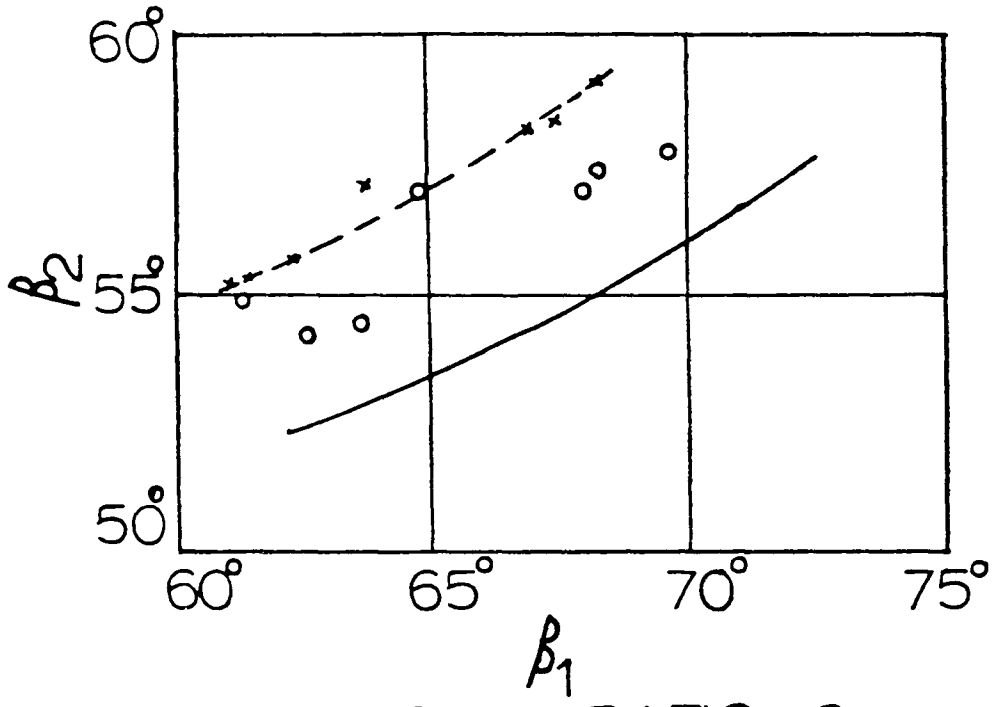

RADIUS RATIO=.8

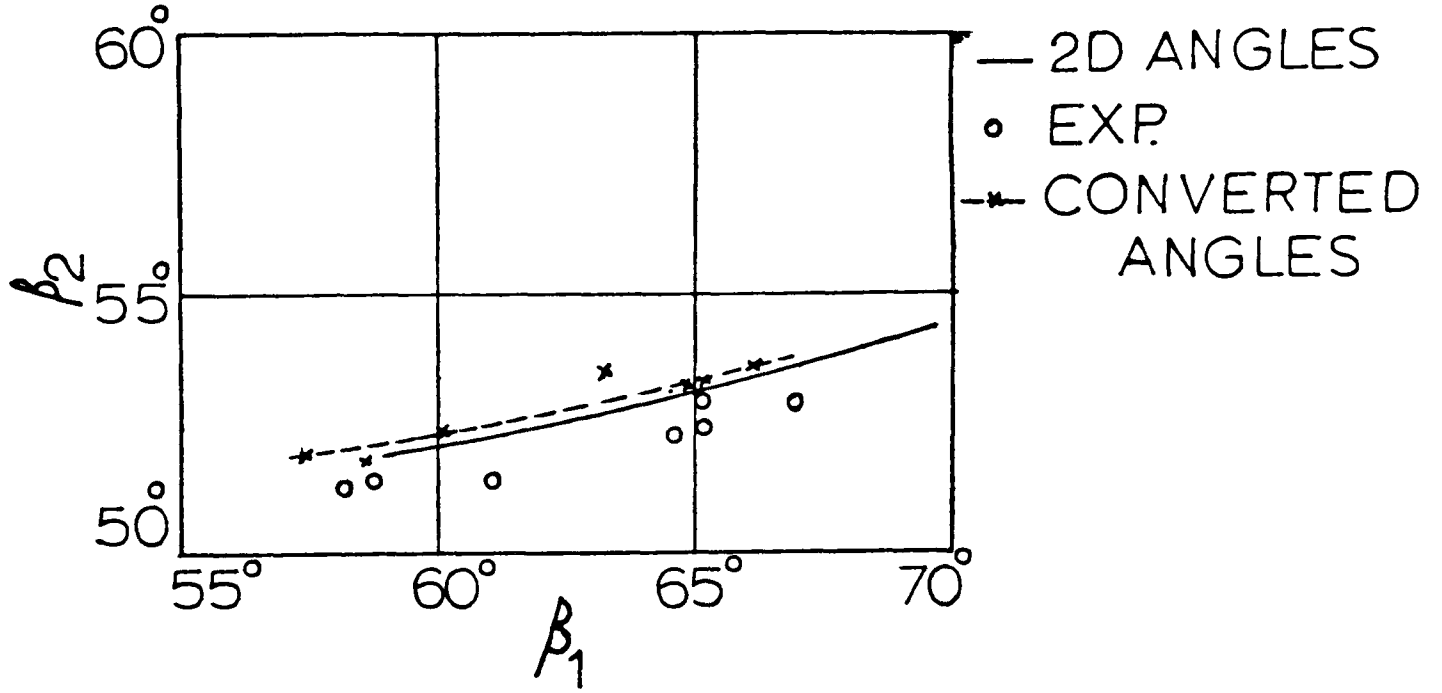

RADIUS RATIO=.7

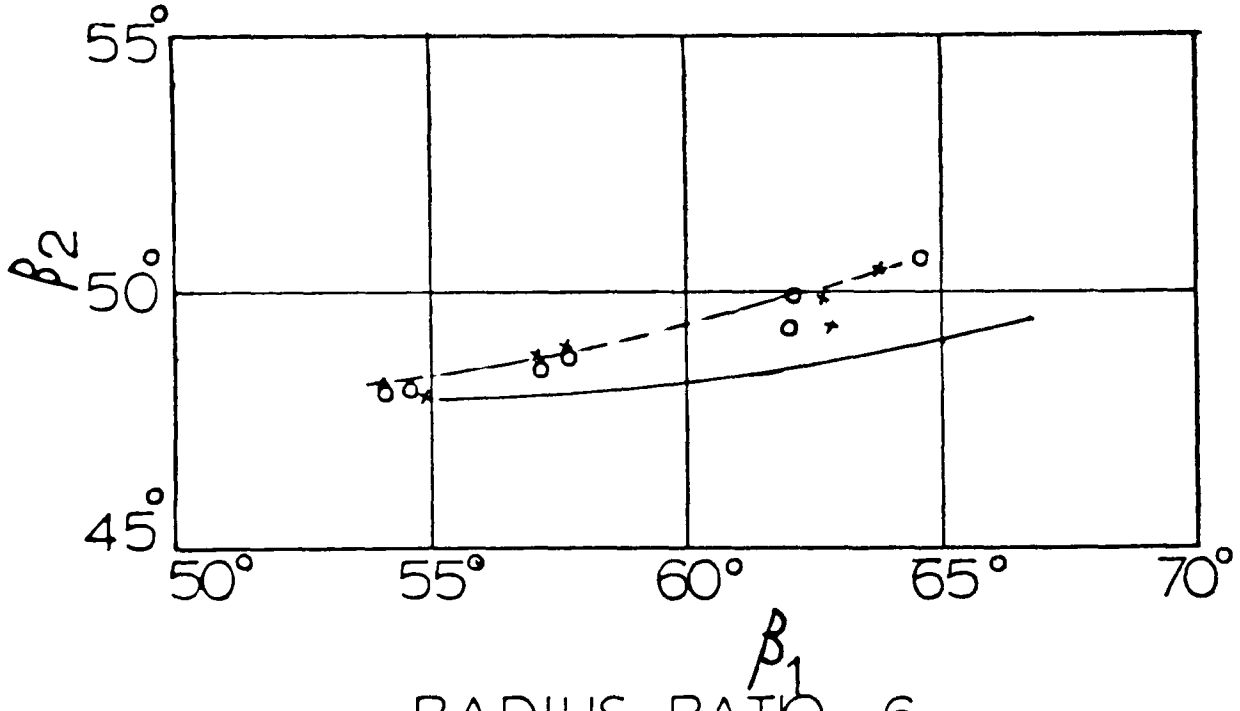

RADIUS RATIO=.6

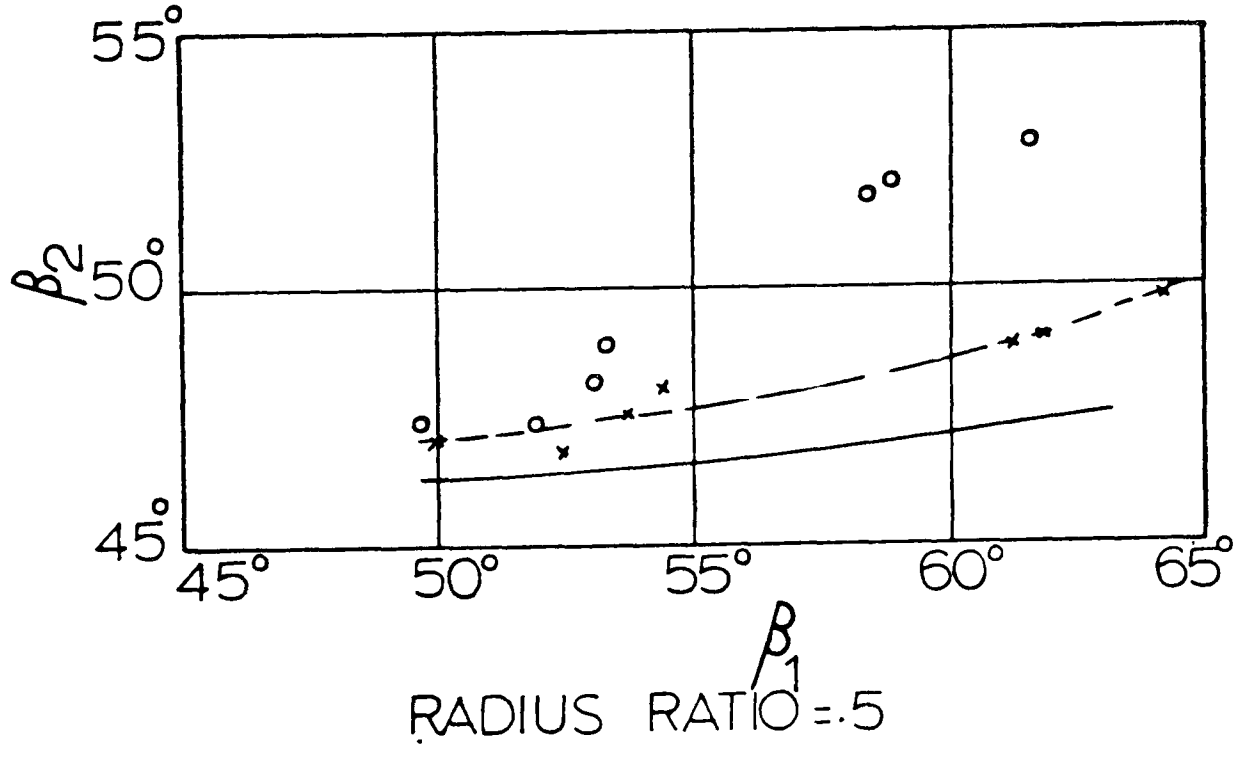

RADIUS RATIO=.5

Fig. F.1, CONVERSION OF RELATIVE OUTLET ANGLE AND RELATIVE INLET ANGLE TO A.V.R.=1

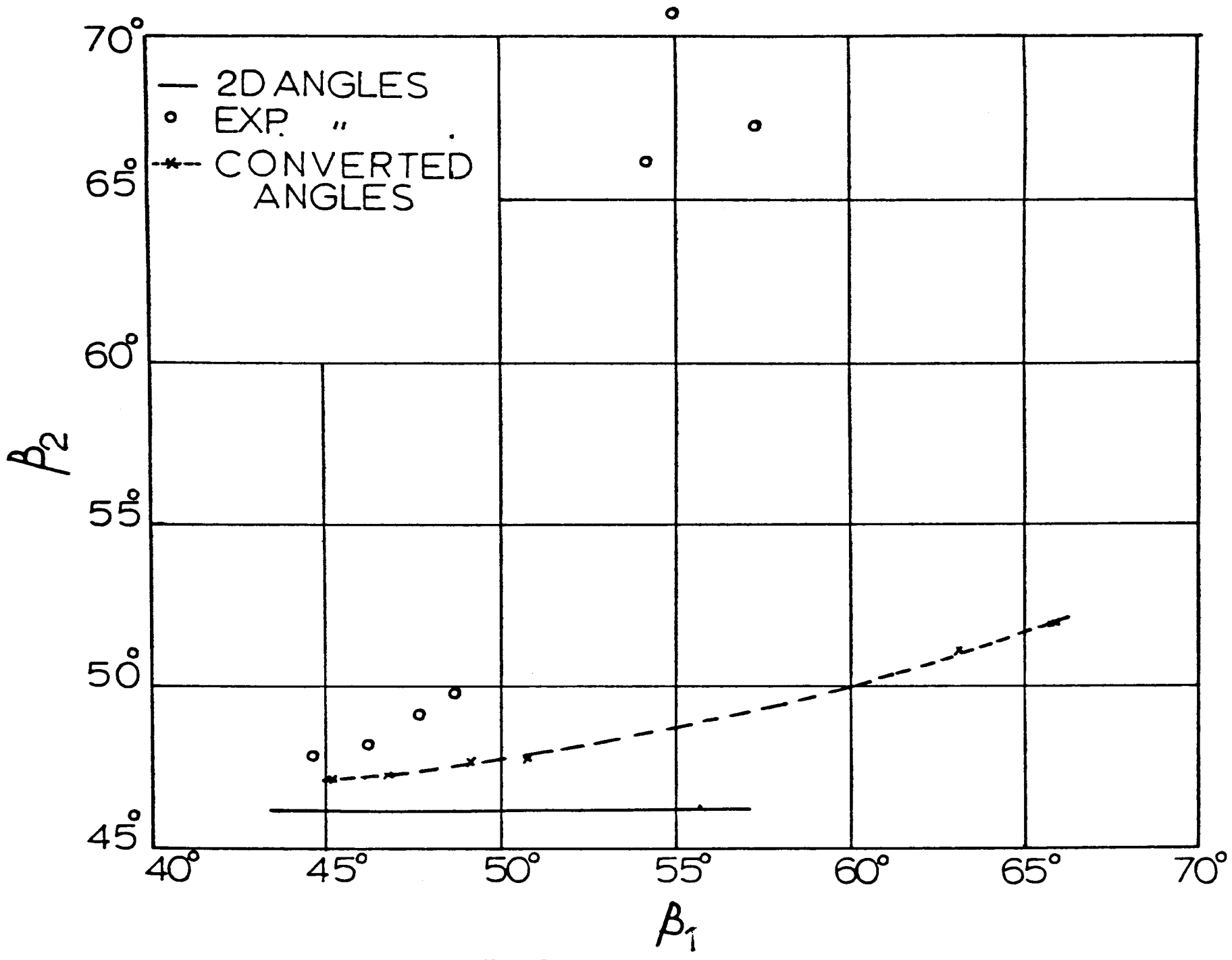

RADIUS RATIO = .4

CONVERSION OF EXP. β_1 & β_2 TO A.V.R. = 1

Fig. F. 2